RUHR-UNIVERSITÄT BOCHUM

Peyman Mianji

Bentonite slurry infiltration in granular soils and its implications for hydroshield tunnelling

Bochum 2026

Heft 91

Schriftenreihe des Lehrstuhls für
Bodenmechanik, Grundbau und Umweltgeotechnik

Herausgeber: Torsten Wichtmann

ISSN 2699-1020

Bentonite slurry infiltration in granular soils

Peyman Mianji

91

ISSN 2699-1020

Ruhr-Universität Bochum
Schriftenreihe Bodenmechanik, Grundbau und Umweltgeotechnik
Heft 91

Herausgeber:
Prof. Dr.-Ing. habil. Torsten Wichtmann
Ruhr-Universität Bochum
Fakultät für Bau- und Umweltingenieurwissenschaften
Lehrstuhl für Bodenmechanik, Grundbau und Umweltgeotechnik
44801 Bochum
Telefon: 0234/ 3226135
Internet: www.bgu.ruhr-uni-bochum.de

ISSN 2699-1020

© 2026 der Herausgeber

Bentonite slurry infiltration in granular soils and its implications for hydroshield tunnelling

Dissertation

as a requirement of the degree of
Doktor-Ingenieur (Dr.-Ing.)

at the Faculty of
Civil and Environmental Engineering
Ruhr-Universität Bochum

submitted by
Peyman Mianji
from Mashhad, Iran

Reviewers
Prof. Dr.-Ing. habil. Torsten Wichtmann
Assoc. Prof. Dr.-Ing. Arash Alimardani Lavasan

Bochum, 2026

Preface of the editor

In mechanized tunneling through water-saturated granular soils, pressurized bentonite slurries are used to stabilize the tunnel face. Depending on the properties of the bentonite suspension and the soil, the suspension penetrates the soil to varying depths. If there is little or no penetration, an outer filter cake forms at the interface between the suspension and the soil. This acts as a kind of membrane through which the excess suspension pressure (i.e., the difference between the suspension pressure and the pore water pressure) is transmitted to the soil's grain skeleton, which is supported by the increased effective stress. In coarser soils, however, the supporting fluid can penetrate to a nearly unlimited extent. In practice, cases often fall between these two extremes, in which the suspension penetrates the soil to a certain depth. As the suspension penetrates, bentonite particles filter out of it, adhere to the solid components of the soil, and thereby reduce the pore space and permeability. As a result of the formation of this so-called internal filter cake, the penetration of the suspension eventually comes to a standstill. In this case, the excess pressure of the bentonite suspension is primarily transferred to the grain skeleton via shear stresses along the penetration path. To verify the stability of the tunnel face and control the tunnel boring machine (TBM), it is crucial to estimate the penetration behavior of the support fluid into the respective ground, the associated transfer of support pressure, and the required suspension volume. This estimation is often based on simple empirical equations. During TBM tunneling, the penetration behavior can be influenced by the controllable parameters of bentonite content in the suspension and excess suspension pressure, while the ground conditions represent a given boundary condition.

The mechanisms and processes involved in the infiltration of bentonite suspensions into granular soils have still not been extensively studied from a quantitative perspective. Both the combined influence of soil particle size distribution, suspension properties, and excess suspension pressure on the penetration depth and the formation of an outer or inner filter cake and the temporal evolution of support pressure transfer within the inner filter cake and its micromechanical structure remain largely unclear. For these reasons, existing empirical prediction models remain relatively inaccurate. Continuum-based approaches for the numerical simulation of the penetration of bentonite suspensions into soils have rarely been the subject of research to date. Comprehensive numerical models of fluid-supported tunnel excavation should also adequately describe the mechanical behavior of the soil infiltrated by the suspension. The extent to which the infiltrated suspension – or

the bentonite adhering to the grains – alters the mechanical behavior of a granular soil remains an open question.

The objective of Peyman Mianji's dissertation was therefore to systematically investigate, through experimentation, the infiltration of bentonite suspensions into granular soils, the formation of outer and inner filter cakes, and the transfer of support pressure for varying properties of the soil and the suspension. This includes studies of the microstructure of the suspension, the filter cake, and the suspension-infiltrated sand. Triaxial tests were conducted to determine the extent to which bentonite infiltration alters the mechanical behavior of the sand under monotonic or cyclic loading. Another objective was to extend a continuum-based approach for the numerical simulation of the infiltration process of bentonite suspensions into granular soils, which was to be calibrated and validated based on the author's own experiments.

A key achievement of Mr. Mianji's dissertation is the development and implementation of the column infiltration test device, which, for the first time, enables the measurement of the temporal evolution of pore pressure at different heights, the post-mortem determination of the bentonite concentration in the pore fluid, and the collection of infiltrated soil samples for subsequent analysis. This enables Mr. Mianji to quantify pressure transmission within the inner filter cake and its temporal evolution. This is carried out in a systematic parameter study varying sand type, bentonite concentration, and excess suspension pressure.

The Cryo-BIB-SEM images provide new insights into the microstructure of suspensions, filter cakes, and suspension-infiltrated sand. An important finding regarding the mechanical behavior of suspension-infiltrated sand is the significantly reduced resistance to liquefaction under cyclic loading, while the behavior under monotonic loading remains largely unaffected. The successful back-analysis of his own column tests confirms the suitability of the extended numerical modeling approach.

This research has been done in the framework of Subproject A6 of Collaborative Research Centre (SFB) 837 "Interaction Modeling in Mechanized Tunneling" at Ruhr-Universität Bochum. The funding of the German Research Foundation (DFG) is gratefully acknowledged.

Bochum, August 2026 Torsten Wichtmann

Acknowledgements

This dissertation represents the culmination of a long academic and personal journey at the Chair of Soil Mechanics, Foundation Engineering and Environmental Geotechnics at Ruhr University Bochum. The research was conducted within Subproject A6 of the Collaborative Research Centre 837, "Interaction Modeling in Mechanized Tunnelling." I gratefully acknowledge the support of the German Research Foundation and the stimulating scientific environment created by the SFB 837 community.

My doctoral journey in Bochum began under the supervision of the late Professor Tom Schanz. I remain sincerely grateful to him for giving me the opportunity to begin this research. His untimely passing occurred at an early stage of my work, but the opportunity and direction he provided formed the foundation of this dissertation.

I am deeply grateful to Professor Torsten Wichtmann for taking over the supervision of my work and enabling me to continue and complete my doctoral research. I greatly appreciate the trust and academic freedom he gave me, as well as his scientific guidance, critical discussions, patience, and continued support throughout the different stages of this work. His commitment was particularly valuable during the demanding final phase of the dissertation.

My very special gratitude goes to Dr.-Ing. Wiebke Baille, under whose close scientific supervision I conducted my doctoral research. She accompanied and supported me throughout the entire PhD, from the planning and execution of the experimental programme to the interpretation of the results and the development of the thesis. Her extensive knowledge, careful guidance, constructive feedback, patience, and constant willingness to help were invaluable at every stage of this work. I am deeply thankful for the time and effort she invested in my research and for the encouragement she provided along the way. This dissertation would not have reached its present form without her support. I also sincerely thank Dr.-Ing. Diethard König for his support during my doctoral research.

I would also like to express my sincere gratitude to Associate Professor Arash Alimardani Lavasan for the important role he played at key stages of my doctoral journey, from its very beginning to the completion of this dissertation. His early confidence in me, guidance, and continued support helped make this path possible. I am particularly grateful that he later served as a reviewer of this dissertation; his careful reading, constructive criticism, and detailed suggestions greatly improved its clarity and scientific quality.

My special thanks go to Dr. Seyed Ali Ghoreishian Amiri for his generous encouragement, guidance, and readiness to help throughout this journey. His advice has been invaluable to me, both academically and personally. I am also deeply grateful to Dr. Habibollah Sadeghi for his generous support and valuable guidance in implementing the model used in this dissertation.

The extensive experimental programme presented in this dissertation would not have been possible without the technical and laboratory support I received at Ruhr University Bochum. I am particularly grateful to Michael Skubisch, Werner Müller, Ralf Schudy, and Stephan Schlechter for their practical expertise, patience, and readiness to find solutions whenever technical difficulties arose. Their assistance with the experimental equipment and laboratory work made an essential contribution to the successful completion of this research.

I am also grateful to my colleagues Debdeep, Manh, Felipe, Meisam, Sudan, Danial, Hossein, Mohammadsadegh, Hanieh, and Alireza for their friendship, support, valuable discussions, and the many experiences we shared during our time at the chair. Their collegiality and companionship made the challenges of doctoral research easier and my years in Bochum more enjoyable. I also thank all the other colleagues and staff members at the chair whose help contributed to a welcoming and stimulating working environment.

Finally, my deepest gratitude belongs to my parents, my brother, and my partner. Their unconditional love, patience, encouragement, and confidence in me sustained me throughout the difficult and uncertain periods of this journey. Their support gave me the strength to persevere and bring this dissertation to completion. This achievement would not have been possible without them.

Bochum, August 2026 Peyman Mianji

Abstract

Slurry-shield tunnelling in sandy soils uses pressurised bentonite slurry to stabilise the excavation face and control fluid losses. The effectiveness of this support depends on the infiltration of bentonite slurry into the granular soil and the resulting pressure transfer within the ground with depth and time. Current models link the controllable parameters, support overpressure Δp and bentonite slurry concentration c, mainly to penetration depth or filter cake thickness. However, predicting pressure transfer as a function of slurry properties, soil characteristics, and applied support conditions remains challenging.

This thesis investigates bentonite slurry infiltration and its effects on tunnel face support through a multi-scale experimental and modelling approach. Infiltration column tests were conducted in different sands under varying support pressures, measuring pore water pressure changes at multiple depths over time together with slurry flow rates. Post-test concentration profiles $c(z)$ identified zones of bentonite retention and the formation of internal filter cakes within the sand. High-resolution imaging (Cryo-BIB-SEM/EDS) revealed microstructures associated with slurry infiltration under different conditions. The mechanical response of infiltration-conditioned sand was investigated through monotonic and cyclic triaxial tests. A numerical model based on an existing continuum formulation was extended to simulate bentonite slurry infiltration and the associated pressure transfer processes.

The experiments identify how slurry infiltration depends on soil grain size, support overpressure Δp, and bentonite slurry concentration c. Depth-resolved pore water pressure measurements and post-test concentration profiles consistently indicate that pressure transfer is closely linked to zones where bentonite particles are retained and internal filter cakes develop. Microstructural observations provide direct evidence of bentonite films, particle accumulations, and bridging structures associated with different infiltration regimes. Triaxial tests indicate systematic changes in dilatancy and cyclic resistance associated with infiltration-induced modifications of the soil fabric, while the critical-state strength remains largely unchanged. The developed numerical model reproduces the observed transitions between deep penetration and internal or external sealing, together with the corresponding pressure distributions within the soil.

This thesis combines experimental observations, microstructural analysis, mechanical testing, and numerical modelling to investigate slurry infiltration in sandy soils. The results

and the calibrated model provide a quantitative basis for evaluating slurry infiltration behaviour under different support overpressures Δp and bentonite slurry concentrations c. This contributes to a better understanding of the conditions governing sealing formation, pressure transfer, and slurry infiltration in granular soils relevant to slurry-shield tunnelling.

Zusammenfassung

Der Hydroschildvortrieb in sandigen Böden nutzt eine druckbeaufschlagte Bentonitsuspension, um die Ortsbrust zu stabilisieren und Flüssigkeitsverluste zu begrenzen. Die Wirksamkeit dieser Stützung hängt vom Eindringen der Bentonitsuspension in den granularen Boden sowie von der daraus resultierenden Druckübertragung im Baugrund mit Tiefe und Zeit ab. Aktuelle Modelle verknüpfen die steuerbaren Parameter Stützüberdruck Δp und Bentonitsuspensionskonzentration c hauptsächlich mit der Eindringtiefe oder der Dicke des Filterkuchens. Die Vorhersage der Druckübertragung in Abhängigkeit von Suspensionseigenschaften, Bodeneigenschaften und den angewandten Stützbedingungen bleibt jedoch weiterhin eine Herausforderung.

Diese Arbeit untersucht die Infiltration von Bentonitsuspension und deren Einfluss auf die Ortsbruststützung im Tunnelbau mithilfe eines multiskaligen experimentellen und modellbasierten Ansatzes. Infiltrationssäulenversuche wurden mit verschiedenen Sanden unter unterschiedlichen Stützdrücken durchgeführt, wobei Porenwasserdruckänderungen in mehreren Tiefen über die Zeit sowie Suspensionsdurchflussraten gemessen wurden. Nachversuchlich bestimmte Konzentrationsprofile $c(z)$ identifizierten Zonen der Bentonitrückhaltung und die Bildung interner Filterkuchen innerhalb des Sandes. Hochauflösende Bildgebung (Cryo-BIB-SEM/EDS) zeigte Mikrostrukturen, die mit der Suspensionsinfiltration unter unterschiedlichen Bedingungen verbunden sind. Das mechanische Verhalten infiltrationsbeeinflusster Sande wurde mithilfe monotoner und zyklischer Triaxialversuche untersucht. Ein numerisches Modell auf Grundlage einer bestehenden kontinuumsmechanischen Formulierung wurde erweitert, um die Infiltration von Bentonitsuspension sowie die damit verbundenen Druckübertragungsprozesse zu simulieren.

Die Experimente zeigen, dass die Suspensionsinfiltration von der Korngröße des Bodens, dem Stützüberdruck Δp sowie der Bentonitsuspensionskonzentration c abhängt. Tiefenaufgelöste Porenwasserdruckmessungen und nachversuchliche Konzentrationsprofile zeigen konsistent, dass die Druckübertragung eng mit Zonen der Bentonitrückhaltung und der Bildung interner Filterkuchen verknüpft ist. Mikrostrukturelle Beobachtungen liefern direkte Hinweise auf Bentonitfilme, Partikelakkumulationen und Brückenstrukturen, die mit unterschiedlichen Infiltrationsregimen verbunden sind. Triaxialversuche zeigen systematische Veränderungen der Dilatanz und der zyklischen Widerstandsfähigkeit infolge infiltrationsbedingter Veränderungen der Bodenstruktur, während die Scherfestigkeit im kritischen Zustand weitgehend unverändert bleibt. Das entwickelte numerische Modell

reproduziert die beobachteten Übergänge zwischen tiefem Eindringen und interner bzw. externer Abdichtung sowie die entsprechenden Druckverteilungen im Boden.

Diese Arbeit verbindet experimentelle Beobachtungen, mikrostrukturelle Analysen, mechanische Untersuchungen und numerische Modellierung zur Untersuchung der Suspensionsinfiltration in sandigen Böden. Die Ergebnisse und das kalibrierte Modell liefern eine quantitative Grundlage zur Bewertung des Infiltrationsverhaltens von Bentonitsuspension unter unterschiedlichen Stützüberdrücken Δp und Bentonitsuspensionskonzentrationen c. Dies trägt zu einem besseren Verständnis der Bedingungen bei, die die Bildung von Abdichtungsstrukturen, die Druckübertragung und die Suspensionsinfiltration in granularen Böden im Kontext des Hydroschildvortriebs bestimmen.

Contents

Preface of the editor i

Acknowledgements iii

Abstract v

Zusammenfassung vii

Contents ix

1 Introduction 1

1.1 Background and motivation 1
1.2 Objectives 3
1.3 Content of the thesis 4

2 State of the art 7

2.1 Face support and pressure transfer in slurry-shield tunnelling 7
2.2 Structure and rheology of bentonite slurry 8
2.3 Infiltration mechanisms in granular soils 11
2.3.1 Slurry–soil interaction regimes 11
2.3.2 Filtration and filter cake formation 11
2.3.3 Pore-size criteria for slurry infiltration regimes 13
2.4 Pressure transfer ahead of a slurry-supported tunnel face 15
2.4.1 Pressure transfer and penetration depth ahead of the face 15
2.4.2 Transient pressure transfer under cyclic excavation 17
2.5 Microstructure of bentonite–sand systems 18
2.6 Monotonic and cyclic behaviour of sand with bentonite infiltration 20
2.6.1 Effect of specimen preparation on the monotonic and cyclic response of sand 20
2.6.2 Monotonic and cyclic behaviour of sand containing bentonite in the pore space 22

2.7 Slurry infiltration in granular soils: empirical relations and continuum modelling . . . 23
2.7.1 Empirical relations for slurry penetration . . . 23
2.7.2 Continuum description at the representative elementary volume (REV) scale . . . 24
2.7.3 Governing equations for slurry infiltration . . . 25
2.7.4 Continuum models for slurry infiltration . . . 26
2.7.5 Pore-scale CFD–DEM models and constitutive relations . . . 28
2.8 Summary and research gaps . . . 29

3 Experimental materials and methods 31
3.1 Introduction . . . 31
3.2 Materials used . . . 31
3.2.1 Sand materials . . . 31
3.2.2 Bentonite . . . 32
3.3 Infiltration column: concept, design, and application . . . 36
3.3.1 Concept . . . 36
3.3.2 Design features . . . 37
3.3.3 Calibration of sensors and monitoring instruments . . . 39
3.3.3.1 Calibration of pore pressure sensors . . . 39
3.3.3.2 Calibration of load cells of the inflow and outflow containers 41
3.3.4 Development of sampling methods . . . 41
3.3.4.1 Sampling for microstructural investigations . . . 42
3.3.4.2 Sampling of bentonite slurry from column tests . . . 42
3.3.4.3 Portable triaxial sampling mould . . . 44
3.3.5 Preparation and assembly of infiltration column test . . . 44
3.3.5.1 Filter materials and design . . . 44
3.3.5.2 Sensor configuration and test preparation considerations . 47
3.3.5.3 Column setup . . . 48
3.3.5.4 CO_2 flowthrough . . . 50
3.3.5.5 Water saturation . . . 50
3.3.5.6 Permeability test procedure . . . 51
3.3.5.7 Infiltration test procedure . . . 52
3.3.6 Dismantling of the column test and sample extraction . . . 53
3.3.6.1 Dismantling of the soil column . . . 53
3.3.6.2 Post-infiltration sampling for bentonite slurry testing . . . 53

3.3.6.3 Post-infiltration sampling for triaxial test 55
3.4 Triaxial test devices 56
3.4.1 Monotonic triaxial device (Wykeham Farrance) 56
3.4.2 Cyclic triaxial device (Wille Geotechnik) 57
3.4.3 System compliance and boundary effects 59
3.5 Triaxial test procedure and sample preparation 59
3.5.1 Installation of samples by air pluviation method 59
3.5.2 Installation of remoulded sand-slurry mixture samples 62
3.5.3 Installation of slurry-infiltrated column samples 63
3.5.4 Saturation procedure for clean, slurry-infiltrated, and remoulded sand-slurry mixture samples 64
3.5.4.1 Clean sand samples 65
3.5.4.2 Slurry-infiltrated column samples and remoulded sand-slurry mixture samples 66
3.5.5 Consolidation procedure 66
3.5.6 Shearing procedure 67
3.5.7 Post-testing procedure 67
3.6 Rheometer device and measurement procedure 68
3.7 Broad Ion Beam Scanning Electron Microscopy (BIB-SEM) investigations . 69
3.7.1 Sample types investigated 70
3.7.2 Sample preparation procedure 71
3.7.3 Sample freezing procedure 72
3.7.4 Sample transport and preservation 73
3.7.5 Cryo-BIB-SEM imaging procedure 74

4 Slurry infiltration into sands: experimental insights for TBM shielding 75
4.1 Objectives of this chapter 75
4.2 Experimental programme of the column infiltration tests 76
4.3 Column test results 77
4.3.1 Effect of soil type 78
4.3.2 Effect of injection pressure: S 0.1–0.5 mm 82
4.3.3 Effect of injection pressure: S 0.5–1.0 mm 85
4.3.4 Effect of bentonite concentration 87
4.4 Slurry infiltration and pressure transfer: implications for TBM shielding . . 89
4.5 Summary 91

5 Soil-bentonite slurry interface properties: microstructural investigation 93
5.1 Objectives of the study . . . 93
5.2 Experimental programme . . . 94
5.3 Microstructural results and interpretation . . . 97
5.3.1 Remoulded bentonite slurries (Set A) . . . 97
5.3.2 Microstructure of external filter cake samples (Set B) . . . 99
5.3.3 Microstructure at sand–slurry interfaces (Set C) . . . 102
5.3.4 Microstructure of internal infiltration structures (Set D) . . . 104
5.3.5 Possible preparation artefacts in Cryo-BIB-SEM images . . . 108
5.4 Summary . . . 110

6 Monotonic and cyclic triaxial behaviour of slurry-infiltrated sand 113
6.1 Objectives . . . 113
6.2 Test programme . . . 113
6.2.1 Monotonic triaxial tests . . . 114
6.2.2 Cyclic triaxial tests . . . 115
6.3 Notation and conventions . . . 116
6.3.1 Notation and sign conventions for presentation of results . . . 116
6.4 Monotonic triaxial response . . . 116
6.4.1 Effect of specimen preparation and slurry infiltration . . . 117
6.4.2 Peak and critical-state friction angles from monotonic triaxial tests 120
6.4.3 Influence of bentonite concentration . . . 124
6.5 Cyclic triaxial response . . . 125
6.5.1 Verification of specimen saturation prior to cyclic loading . . . 125
6.5.2 Effect of specimen preparation and slurry infiltration . . . 126
6.5.3 Effect of bentonite concentration . . . 133
6.5.4 Cycles to thresholds as functions of bentonite concentration, specimen preparation method and amplitude . . . 135
6.5.5 Post-test bentonite mass balance . . . 137
6.6 Response mechanisms . . . 138
6.7 Implications for slurry-shield tunnelling . . . 139
6.8 Limitations and scope . . . 140
6.9 Summary . . . 141

7 Modelling slurry infiltration in porous media 143
7.1 Objectives . . . 143

7.2 Modelling framework and assumptions 144
7.2.1 Kinematic assumptions 146
7.2.2 Flow law 146
7.2.3 Attachment and porosity evolution 147
7.3 Governing equations 148
7.3.1 Phase balances and transport 148
7.3.2 Coupled pressure–transport system 148
7.4 Constitutive relations (baseline and calibrated) 149
7.4.1 Hydraulic properties 149
7.4.2 Deposition law and model constraints 150
7.5 Initial and boundary conditions, and numerical implementation 151
7.5.1 Initial and boundary conditions 151
7.5.2 Initial conditions 151
7.5.3 Boundary conditions 152
7.6 Numerical implementation (1-D) 153
7.6.1 Flow and transport formulation 153
7.6.2 Numerical realization and boundary data 154
7.7 Verification (1-D) 154
7.8 Calibration protocol (1–D) 157
7.9 Predictive validation under changed boundary conditions (1–D) 161
7.10 Parametric study 166
7.10.1 Effect of the prescribed inlet value of c at $\Delta P = 50$ kPa 167
7.10.2 Effect of slurry injection pressure at inlet $c = 0.0500$ 169
7.11 Three-dimensional extension 171
7.12 Limitations 173
7.13 Summary and outlook 174

8 Conclusions and recommendations **177**
8.1 Main findings 177
8.2 Scientific contributions 180
8.3 Future research 181

Bibliography **183**

1 Introduction

1.1 Background and motivation

Mechanized tunnelling with slurry shields uses a pressurised supporting fluid, typically a bentonite suspension, to stabilize the excavation face, transfer pressure from the excavation chamber to the ground, and minimize fluid losses (Maidl et al., 2012). In sandy soils, this process depends on the penetration behaviour of the supporting fluid: it may enter the pore network deeply, form a low-permeability filter cake at or immediately behind the excavation face, or involve a combination of slurry penetration and filter-cake formation, depending on soil permeability and slurry properties (Xu and Bezuijen, 2019; Qin et al., 2023). The prevailing regime and the location of the sealing layer determine how effectively pressure is transmitted, how much is lost to excess pore water pressures, and the volume of slurry consumed (DAUB, 2016). Imbalances can lead to face instability, blowouts, or excessive settlements, along with increased slurry and additive consumption (DAUB, 2016).

Current practice relies largely on empirical rules and short trial phases to adjust key operational parameters, primarily the support overpressure Δp and the bentonite concentration c of the supporting fluid (DAUB, 2016). Sandy soils, however, often exhibit significant variability in grain-size distribution and permeability, while the rheological behaviour of bentonite suspensions is highly sensitive to concentration and chemical composition (Qin et al., 2023). Consequently, relatively small changes in these parameters may substantially influence slurry penetration depth, filter-cake development, and the effectiveness of pressure transfer to the ground (Lu et al., 2022). Quantitative relationships between controllable operational parameters (Δp, c) and soil properties are therefore needed to better anticipate infiltration regimes and the formation of effective sealing conditions at the excavation face.

Slurry infiltration involves not only hydraulic flow through the soil but also microstructural changes at the soil–slurry interface and within the pore space of the sand. The

interaction between bentonite particles and sand grains may lead to the formation of platelet assemblies and particle accumulation that increase hydraulic resistance at the grain scale and may evolve under stress (Xu and Bezuijen, 2019). Such changes may influence the mechanical behaviour of the soil ahead of the excavation face. These observations indicate that face support in slurry-shield tunnelling involves coupled hydraulic and mechanical mechanisms linking slurry infiltration processes with the mechanical response of the soil ahead of the excavation face (Xu and Bezuijen, 2019; Lavasan et al., 2018).

Despite its importance, many existing models rely on simplified descriptions of particle retention and permeability evolution. This provides limited insight into where filtration initiates and how the filter cake develops under varying pressure conditions (Qin et al., 2023). Field measurements rarely identify the location of the filter cake directly, and conventional laboratory tests often disturb the delicate microstructures formed during infiltration. Consequently, there is a need for (i) controlled experiments to capture infiltration regimes and sealing behaviour, (ii) microstructural observations to explain the resulting hydraulic resistance, (iii) mechanical tests to assess implications for soil stability, and (iv) continuum models that can be calibrated from laboratory observations while remaining physically consistent (Lu et al., 2022).

This thesis addresses these needs through a coordinated multi-scale research programme combining infiltration experiments, microstructural investigation of the sand–slurry interface, element-scale mechanical testing, and continuum modelling. Infiltration column experiments equipped with multi-depth pore-water-pressure measurements and post-test composition profiles $c(z)$ are used to characterise slurry penetration behaviour and pressure transfer under controlled soil and slurry conditions. Cryogenic broad-ion-beam scanning electron microscopy (Cryo-BIB-SEM) is employed to investigate the microstructure of the sand–slurry interface and the distribution of retained bentonite within the pore space. The mechanical implications of slurry infiltration are examined through monotonic and cyclic triaxial tests on infiltration-conditioned soils prepared under controlled conditions. Finally, a continuum modelling framework is developed to describe slurry infiltration and pressure transfer using Darcy-scale formulations with particle deposition and evolving pore-space properties.

The main objective of this thesis is to improve the understanding of bentonite slurry infiltration and its implications for face support in slurry-shield tunnelling in sandy soils. This objective is addressed through a coordinated investigation of slurry penetration behaviour, the microstructure of bentonite–sand interactions at the soil–slurry interface,

the shear behaviour and cyclic response of infiltration-conditioned sands, and continuum modelling of slurry infiltration and pressure transfer. By combining controlled infiltration experiments, cryogenic microstructural observations, element-scale shear testing, and continuum modelling, the work examines how operational parameters, slurry properties, and soil characteristics relate to infiltration regimes and face-support behaviour. The thesis seeks to provide a more consistent basis for interpreting slurry infiltration behaviour and its implications for face support in slurry-shield tunnelling.

This thesis was conducted within the Collaborative Research Center 837 (SFB 837) "Interaction Modeling in Mechanized Tunneling" as part of Subproject A6. A6 develops theoretical and numerical models describing the transient penetration of pressurised slurry used for face support into cohesionless ground. These models capture soil-mechanical, hydro-mechanical, and rheological processes occurring during infiltration and filter-cake formation across multiple scales. The present work investigates infiltration regimes and transitions, documents filter-cake microstructures, and calibrates a continuum model to evaluate face-support conditions. This contributes directly to A6's objective of linking infiltration processes to face-stability assessment.

1.2 Objectives

This thesis aims to improve the quantitative understanding of bentonite slurry infiltration in saturated granular soils. It examines how soil type, support overpressure Δp, and bentonite concentration c affect slurry penetration and sealing location, and develops and evaluates a continuum model in a one-dimensional setting, complemented by a three-dimensional proof-of-concept extension, to assess infiltration behaviour across the investigated parameter ranges. To achieve this objective, the thesis pursues the following specific aims:

- Conduct infiltration column tests on representative sands under controlled support overpressure Δp and bentonite concentration c to identify the dominant soil–slurry interaction regime and characterise infiltration dynamics using pore water pressure measurements at multiple depths together with post-test bentonite concentration profiles $c(z)$.
- Use Cryo-BIB-SEM/EDS to document the microstructure of bentonite–sand interactions in pure slurries, at the sand–slurry interface, and within infiltration zones, identifying characteristic particle arrangements and microstructural zones.

- Perform monotonic and cyclic triaxial tests on clean, infiltration-conditioned, and slurry-mixed sands prepared at comparable initial states to assess differences in shear behaviour and cyclic response.
- Develop and evaluate a continuum model to describe slurry infiltration behaviour and pressure transfer in granular soils, verify and calibrate it in the one-dimensional setting against reference solutions and infiltration experiments, and demonstrate its applicability in a three-dimensional proof-of-concept example.

1.3 Content of the thesis

Chapter 1 introduces the background and motivation of the study and defines the objectives and scope of the thesis.

Chapter 2 reviews face support with slurry shields, slurry infiltration and filter-cake formation, relevant microstructural evidence, slurry rheology, and existing modelling approaches. It identifies the research gaps that motivate the experimental and modelling work presented in this thesis.

Chapter 3 describes the materials and experimental methods, including the sands and slurries used, specimen preparation procedures, the infiltration column with pore water pressure monitoring at different depths and post-test $c(z)$ sampling, Cryo-BIB-SEM/EDS microstructural analysis, and monotonic and cyclic triaxial testing.

Chapter 4 presents the results of the infiltration experiments and analyses pressure transfer and bentonite retention using infiltration front advancement, pore water pressure measurements at multiple depths, and post-test $c(z)$ profiles for varying sand and slurry properties and testing boundary conditions.

Chapter 5 investigates the microstructure of bentonite–sand interactions using Cryo-BIB-SEM/EDS to characterise particle arrangements and microstructural features formed during slurry infiltration.

Chapter 6 investigates the mechanical behaviour of sands modified by bentonite infiltration using monotonic and cyclic triaxial tests. Different specimen preparation methods and testing boundary conditions are considered to assess their influence on shear behaviour and cyclic response.

Chapter 7 develops a continuum mixture model describing slurry infiltration into granular soils, applies its one-dimensional formulation to analyse the infiltration exper-

iments and explore parameter effects, and includes a three-dimensional proof-of-concept simulation in a realistic geometry under gravity.

Chapter 8 summarises the main findings and outlines recommendations for future work.

2 State of the art

This chapter reviews the state of the art on bentonite slurry infiltration in granular soils and its relevance to face support in hydroshield tunnelling. It first outlines the principles of face support and pressure transfer in slurry-shield excavation. The composition and rheological behaviour of bentonite suspensions are then summarised, followed by a review of infiltration mechanisms and filtration processes in sands. Hydraulic–mechanical aspects of pressure redistribution, time-dependent behaviour, and microstructural evidence from prior studies are discussed. The chapter concludes with an overview of laboratory approaches and modelling concepts reported in the literature and identifies the research gaps addressed in the subsequent chapters.

2.1 Face support and pressure transfer in slurry-shield tunnelling

Mechanized tunnelling with slurry shields employs a pressurised supporting fluid, typically a bentonite suspension, to stabilise the excavation face in saturated ground. In a slurry-shield machine, the excavation chamber is filled with supporting fluid and maintained at a support overpressure Δp that counteracts earth and hydrostatic pressures at the face. A stable support pressure is essential to ensure face stability and to limit surface settlements during advance (Anagnostou and Kovári, 1994; Kirsch, 2010; Thewes et al., 2016).

From a stress perspective, the normal stress at the tunnel face may be expressed as

$$\sigma_n = \sigma'_n + u, \tag{2.1}$$

where σ'_n is the effective stress acting on the soil skeleton and u is the pore water pressure. The applied support overpressure Δp therefore contributes partly to excess pore water pressure and partly to effective stress mobilisation. The partitioning between these

components depends on the hydraulic interaction between the supporting fluid and the ground.

In permeable sands, support does not act as a purely impermeable boundary. Instead, the supporting fluid may penetrate the pore network ahead of the face, or it may be progressively restricted by filtration and filter cake formation. When penetration dominates, part of Δp is transmitted hydraulically into the ground as excess pore water pressure. When filtration dominates and a low-permeability layer forms, the pressure drop localises near the face and a larger portion of Δp contributes directly to effective stress at the boundary.

This distinction is illustrated schematically in Fig. 2.1. In a membrane-like state, the pressure loss is concentrated at the interface, whereas in a penetration-dominated state the hydraulic gradient is distributed over a finite depth ahead of the face. The spatial extent of this penetration zone governs the magnitude and distribution of excess pore water pressure and thus the effective stress transfer to the soil skeleton.

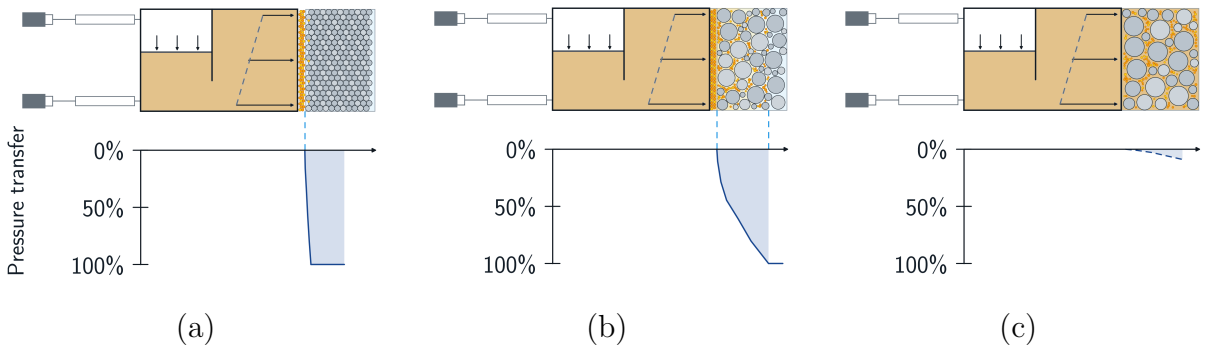

Figure 2.1: Regime schematic for pressure transfer during slurry infiltration in sands: (a) external filter cake; (b) combined penetration with internal or external filter cake; (c) open penetration (adapted from (Žižka, 2019), after (Krause, 1987)).

2.2 Structure and rheology of bentonite slurry

Bentonite suspensions used for slurry-shield tunnelling consist primarily of sodium bentonite dispersed in water, often with additives to adjust rheology and stability (Luckham and Rossi, 1999; Mewis and Wagner, 2012; Praetorius and Schößer, 2017). Their mechanical function at the tunnel face depends strongly on concentration, ionic composition, and mixing state.

The solid phase of bentonite slurry is dominated by montmorillonite platelets, a swelling clay mineral belonging to the smectite group. These platelets have a layered structure with a large specific surface area and carry negative surface charges that promote hydration and swelling when dispersed in water (Grim, 1968; van Olphen, 1977). Depending on electrolyte concentration and mixing conditions, the platelets may form dispersed or flocculated structures in suspension. Figure 2.2 schematically illustrates these arrangements, showing dispersed platelets with approximately parallel orientation (Figure 2.2a) and a flocculated platelet structure (Figure 2.2b). In practical tunnelling applications, additional components such as polymers or weighting agents may be introduced to modify slurry density, stability, and rheological properties.

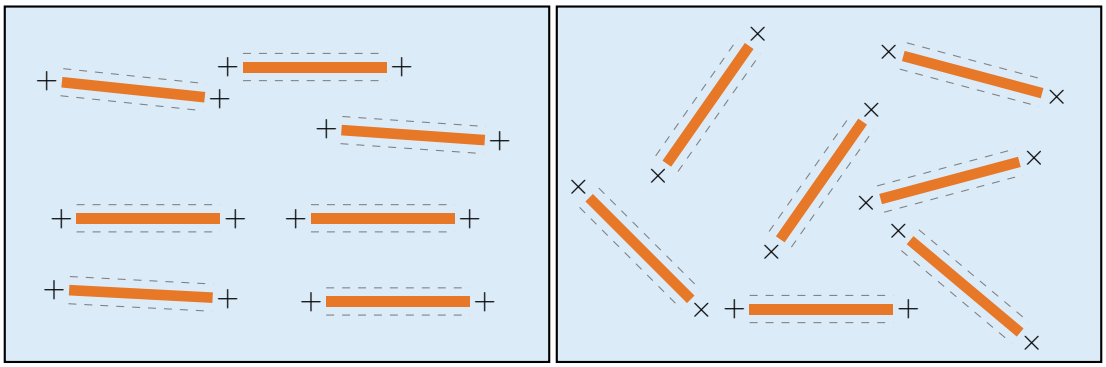

(a) (b)

Figure 2.2: Schematic representation of two platelet arrangements in bentonite suspensions: (a) dispersed platelets with approximately parallel orientation; (b) flocculated platelet arrangement (adapted after (Federation of Piling Specialists, 2006)).

These interactions between suspended clay platelets govern the macroscopic flow behaviour of the slurry. At bentonite concentrations typically used for slurry-shield face support, generally about 4–8% bentonite by mass in the slurry, bentonite suspensions exhibit non-Newtonian flow behaviour (Maidl et al., 2012; Qin et al., 2023). The relationship between shear stress τ and shear rate $\dot{\gamma}$ is commonly represented using yield-stress models such as the Bingham or Herschel–Bulkley formulation. In its simplest form, the Bingham model is expressed as

$$\tau = \tau_y + \mu_p \dot{\gamma}, \tag{2.2}$$

where τ_y is the yield stress and μ_p is the plastic viscosity. The presence of a yield stress implies that a finite shear stress must be exceeded before flow initiates. Increasing ben-

tonite concentration typically increases both yield stress and apparent viscosity, which in turn influences infiltration and filtration behaviour in porous media.

Figure 2.3 summarises schematic rheological idealisations commonly used to represent supporting fluids. While water behaves approximately Newtonian, bentonite slurries are commonly described by yield-stress models. The degree of shear-thinning behaviour, reflected in the flow index of the Herschel–Bulkley model, affects how slurry viscosity changes under varying shear conditions at the tunnel face and within the soil pore network.

Additional insight into the rheological behaviour of bentonite suspensions is provided by studies on clay colloids and time-dependent flow behaviour. Barnes (1997) describes thixotropy as a characteristic feature of structured suspensions, in which the apparent viscosity decreases under shear and gradually recovers when the material is left at rest, reflecting the progressive breakdown and rebuilding of particle networks formed by interacting clay platelets.

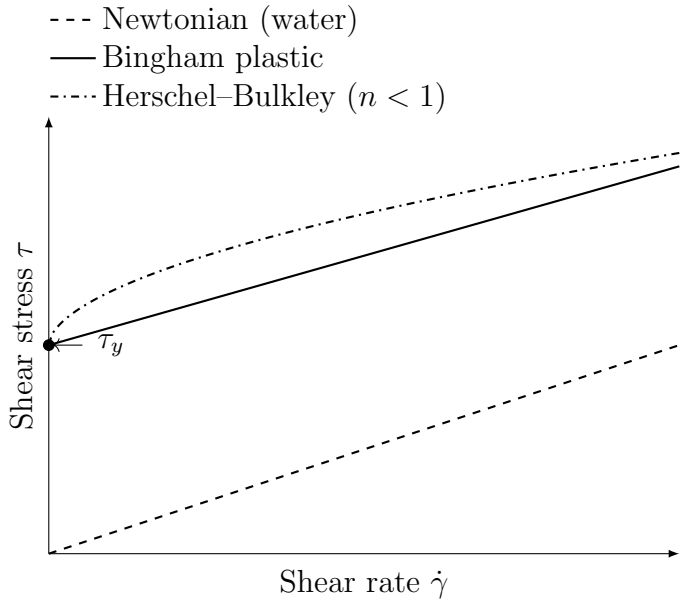

Figure 2.3: Schematic rheological behaviour of supporting fluids. Water is shown as Newtonian (linear), while bentonite slurries are often represented using yield-stress models such as Bingham plastic or Herschel–Bulkley behaviour.

2.3 Infiltration mechanisms in granular soils

2.3.1 Slurry–soil interaction regimes

When pressurised slurry interacts with a permeable granular soil, different slurry–soil interaction regimes may develop depending on soil grading and permeability, slurry rheology, and the applied support overpressure Δp. Based on laboratory observations and field experience reported in the literature, three characteristic regimes are commonly distinguished (Bezuijen and Talmon, 2008; Thewes et al., 2016):

1. External filter cake formation at or immediately behind the excavation face,
2. Open penetration without formation of a distinct filter cake,
3. Combined penetration with internal and/or external cake development.

These regimes represent different modes of interaction between the slurry and the soil pore network and may occur sequentially during tunnelling operations. They are associated with different pressure-transfer characteristics and slurry consumption behaviour. Figure 2.4 schematically illustrates the three regimes.

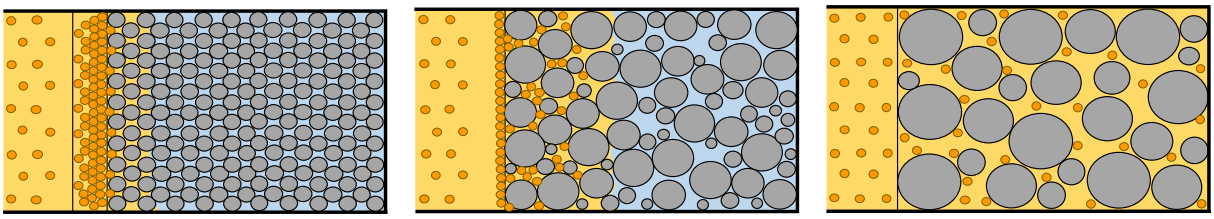

(a) External filter cake (b) Penetration with internal/external cake (c) Pure slurry penetration

Figure 2.4: Regime schematic for pressure transfer during slurry infiltration in sands: (a) external filter cake; (b) penetration with internal/external cake; (c) open penetration (schematic; not to scale).

2.3.2 Filtration and filter cake formation

The slurry–soil interaction regimes described in the previous subsection are closely related to the filtration of suspended particles and the formation of filter cakes at the slurry–soil interface. When slurry infiltrates a permeable granular soil, water and fine particles may enter the pore network, while larger particles or flocculated aggregates can be retained at

pore constrictions. Progressive particle deposition within the pore network reduces the connected pore space and increases hydraulic resistance, leading to localized permeability reduction either at the soil boundary or within the pore network of the soil.

Filtration processes in particle suspensions are commonly described as a two-stage process (Herzig et al., 1970; Tien and Payatakes, 1979). During an initial stage, often referred to as mud spurt, slurry infiltrates relatively freely and the filtrate flow rate is comparatively high. As particle deposition progresses and hydraulic resistance increases, the process transitions to a cake-controlled stage in which the filtrate flow decreases over time.

In laboratory pressure-filtration tests, the cumulative filtrate volume $V_f(t)$ in the cake-controlled regime is frequently observed to increase approximately proportionally to the square root of time,

$$V_f(t) \propto \sqrt{t}, \tag{2.3}$$

reflecting progressive particle deposition and the resulting increase in hydraulic resistance. Figure 2.5 illustrates this two-stage interpretation in a schematic V_f–$\sqrt{t}$ representation.

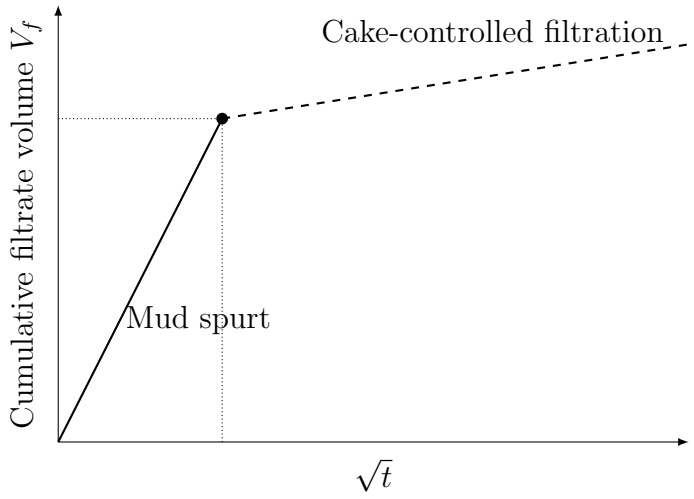

Figure 2.5: Schematic evolution of cumulative filtrate volume V_f during pressure filtration. An initial mud-spurt stage may be followed by a cake-controlled stage in which V_f increases approximately proportionally to $\sqrt{t}$.

In granular soils, filtration may occur not only at a distinct external boundary but also within the pore network, resulting in spatially distributed particle retention and permeability reduction (Talmon et al., 2013; Xu and Bezuijen, 2019). Experimental investigations show that the depth of slurry infiltration and the location of particle retention

depend on slurry properties and soil pore structure. Column and model-scale investigations further demonstrate that the prevailing mechanism depends on the relationship between slurry particle size and characteristic soil pore openings. Min et al. (2013) identified regimes of external filter cake formation, internal filtration, and open penetration based on particle–pore size ratios. Similarly, infiltration experiments conducted by Wang et al. (2022) showed that increasing slurry viscosity or introducing coarser particles into the slurry enhances particle bridging at pore throats and promotes earlier filter cake formation in highly permeable sands.

2.3.3 Pore-size criteria for slurry infiltration regimes

Several studies have attempted to relate the slurry–soil interaction regimes described above to geometric relations between characteristic soil pore openings and slurry particle sizes. Laboratory column experiments have shown that soil pore structure and slurry particle size strongly influence the prevailing infiltration behaviour. Based on experiments in highly permeable sands, Min et al. (2013) distinguished the same three regimes and proposed threshold ranges using size comparisons between characteristic soil pore openings and slurry particle size. Ratios such as $d_{85}/\overline{D_0}$ were proposed to distinguish the three regimes identified by Min et al. (2013) (Type I–III), corresponding to external sealing at the boundary, internal particle retention, and open penetration.

Figure 2.6 illustrates the relationship between the slurry particle size d_{85} and the average soil pore size $\overline{D_0}$, redrawn after Min et al. (2013). The diagram indicates that increasing relative particle size promotes earlier particle bridging and boundary sealing, whereas small particle-to-pore-size ratios favour deeper particle transport and penetration into the pore network.

Because a single size ratio cannot fully describe particle transport and retention processes, additional indicators have been proposed. For example, Lin et al. (2021) introduced a particle retention rate to quantify the fraction of slurry solids retained near the boundary. Their results showed that high retention rates correlate with boundary sealing, while low retention rates correspond to deeper particle transport within the pore network.

Complementary experimental evidence was provided by Wang et al. (2022), who demonstrated that infiltration behaviour in coarse sands can be significantly influenced by slurry composition. Increasing slurry viscosity and incorporating coarser particles enhanced particle bridging at pore throats and promoted boundary sealing under conditions that otherwise led to penetration-dominated behaviour.

Taken together, these studies indicate that slurry infiltration regimes depend on a combined effect of pore geometry, particle size distribution, slurry rheology, and applied pressure. Pore-size related criteria therefore provide useful guidance for regime classification, but they are not fully predictive across different soils and slurry compositions.

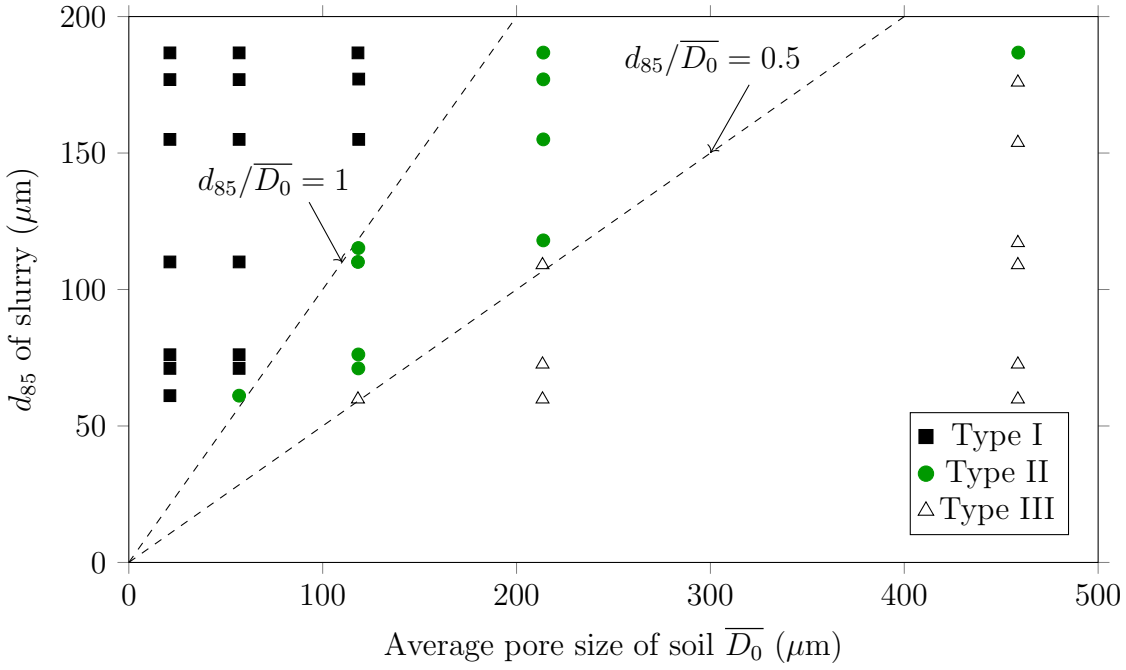

Figure 2.6: Regime indication proposed by Min et al. (2013) based on the ratio $d_{85}/\overline{D_0}$, where $\overline{D_0}$ denotes the average pore size of the soil (redrawn after Min et al. (2013)).

From a parameter viewpoint, several factors influence whether penetration or filtration dominates. Higher applied pressure and longer exposure time favour deeper penetration, whereas higher slurry concentration and stronger non-Newtonian behaviour (larger apparent viscosity and/or yield stress) promote earlier particle retention and a steeper local pressure drop across a thin zone near the face. Soil properties also play an important role: finer and more uniformly graded sands tend to promote particle retention and boundary layer development, while coarser or well-connected pore structures favour open penetration and sustained hydraulic transmission of pressure.

A practical limitation in the literature is the scarcity of depth-resolved measurements of bentonite concentration during infiltration tests. Most studies infer particle retention indirectly from expelled volume and pressure histories or reconstruct it post mortem by slicing the specimen at the end of the experiment (e.g. Xu and Bezuijen, 2019). Real-time

approaches, particularly electrical-resistivity monitoring, can indicate where deposition develops, but they generally provide relative signals rather than calibrated, depth-resolved concentration profiles $c(z,t)$ (Schößer et al., 2023; Kube et al., 2023).

2.4 Pressure transfer ahead of a slurry-supported tunnel face

2.4.1 Pressure transfer and penetration depth ahead of the face

Field measurements in slurry-supported tunnelling show that excess pore water pressures can develop ahead of the excavation face during advance and decay during standstills (Bezuijen, 2004; Bezuijen and Talmon, 2008; Xu and Bezuijen, 2018). Based on instrumented tunnel drives in saturated sand, Bezuijen (2004) proposed an analytical approximation for the excess piezometric head along the tunnel axis,

$$\phi(x) = \phi_0 \left(\sqrt{1 + \left(\frac{x}{R}\right)^2} - \frac{x}{R} \right), \tag{2.4}$$

where ϕ_0 is the excess head at the face, R is the tunnel radius, and x is the distance ahead of the face. This solution was derived by Bezuijen (2004) for steady flow without plastering, assuming a prescribed constant excess head over the tunnel face, homogeneous soil, and negligible influence of the ground surface. Under these assumptions, the normalised excess-head distribution $\phi(x)/\phi_0$ is governed by the geometric ratio x/R. Differentiating this profile gives the magnitude of the hydraulic gradient at the face, $i(0) = \phi_0/R$. The corresponding pore-water velocity is obtained from $v_p = Ki/n$, where K is the hydraulic conductivity [$\mathrm{m\,s^{-1}}$] and n is the porosity. Transient pressure build-up and dissipation additionally depend on the storage properties of the ground.

Figure 2.7 illustrates idealised excess pore water pressure distributions ahead of the face for three characteristic boundary conditions. In the membrane-like case, the pressure drop is strongly localised near the boundary. In the penetration-dominated case, the hydraulic gradient is distributed over a larger depth. The combined case represents penetration with an additional localised pressure loss at a characteristic distance x_k, associated with internal filtration and a concentrated hydraulic resistance within the infiltrated zone.

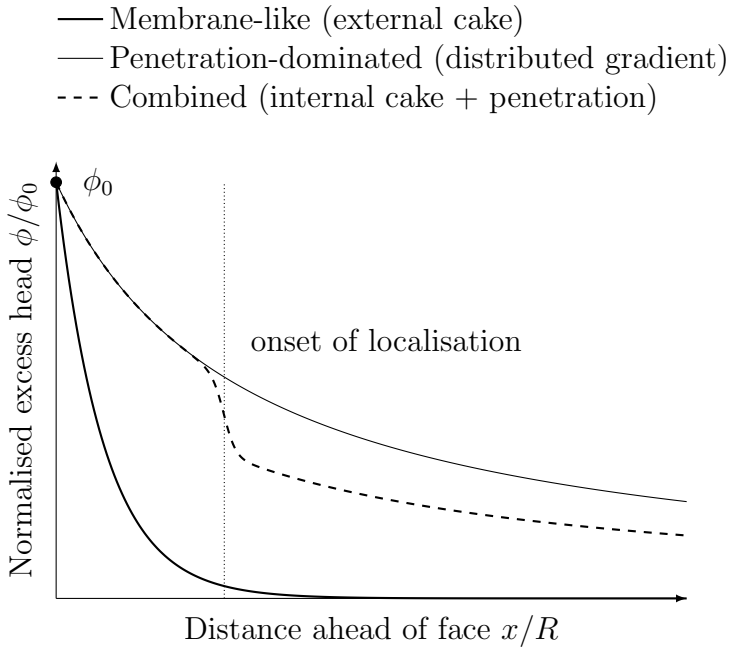

Figure 2.7: Schematic excess pore water pressure (expressed as normalised excess piezometric head ϕ/ϕ_0) ahead of a slurry-supported tunnel face for different near-face boundary conditions. Membrane-like behaviour localises the pressure drop near the face, whereas penetration-dominated behaviour produces a more distributed gradient.

Closely related to the pressure distribution is the penetration depth of the slurry into the soil. Several authors have introduced the concept of a stagnation gradient to describe the limiting penetration depth of slurry into sand (Müller-Kirchenbauer, 1972; Krause, 1987; Žižka et al., 2019). In this interpretation, penetration ceases once the available pressure drop is balanced by hydraulic losses across the invaded zone. Empirical relations of the form

$$x_{\max} = \frac{\Delta p \, d_{10}}{\alpha \, \tau_f}, \tag{2.5}$$

have been proposed, where $x_{\max}$ denotes the maximum penetration length, d_{10} characterises the soil grading, τ_f represents a slurry yield or filtration-related parameter, and α is an empirical coefficient (Krause, 1987; Žižka et al., 2019). Although simplified, such expressions emphasise that penetration depth is controlled jointly by hydraulic loading and material parameters.

Overall, slurry infiltration should be regarded as a coupled hydraulic–mechanical process: the evolving hydraulic resistance governs pore water pressure transfer ahead of the face and thus controls effective stress mobilisation and stability-relevant stress redistribution in the near-face soil.

2.4.2 Transient pressure transfer under cyclic excavation

During slurry-shield tunnelling, the hydraulic boundary condition at the excavation face is inherently non-stationary. The rotating cutterhead repeatedly excavates and disturbs the soil–slurry contact zone, while between cutter passes slurry penetration and filtration continue. Any developing sealing layer may therefore be partially removed or mechanically disrupted and must reform within the available standstill time.

Field observations and physical modelling indicate that this cyclic process governs the hydraulic response ahead of the face. Measurements from instrumented tunnel drives show a characteristic pattern in which excess pore-water pressures increase during active excavation and decrease during short standstill phases, reflecting alternating penetration-dominated and filtration-controlled conditions (Bezuijen, 2004; Xu and Bezuijen, 2018). Consequently, the spatial extent of elevated pore pressures depends not only on soil permeability and support overpressure Δp, but also on the temporal sequence of boundary conditions at the face.

Model-scale investigations further demonstrate that the pressure-transfer behaviour depends strongly on the ratio between excavation time and filtration time (Zhao et al., 2023; Žižka et al., 2019). When the cutterhead rotation is rapid compared to the characteristic sealing time, the support fluid repeatedly penetrates into the soil before a stable low-permeability zone can develop. In contrast, longer standstill periods allow the formation of a more continuous sealing structure, resulting in a stronger localisation of the pressure drop near the tunnel face.

From a porous-media perspective, cyclic excavation can therefore be interpreted as repeated modification of the near-face permeability. During excavation, removal of soil and partial erosion of deposited fines locally increase hydraulic conductivity. During standstill, deposition and bridging reduce pore-throat connectivity and decrease permeability again. The effective hydraulic boundary condition thus oscillates between a higher-permeability penetration state and a lower-permeability filtration state.

Figure 2.8 schematically illustrates this cyclic build-up and decay of excess pore-water pressure ahead of the face. The amplitude of these fluctuations depends on soil per-

meability, slurry rheology, applied support pressure Δp, and the operational excavation cycle.

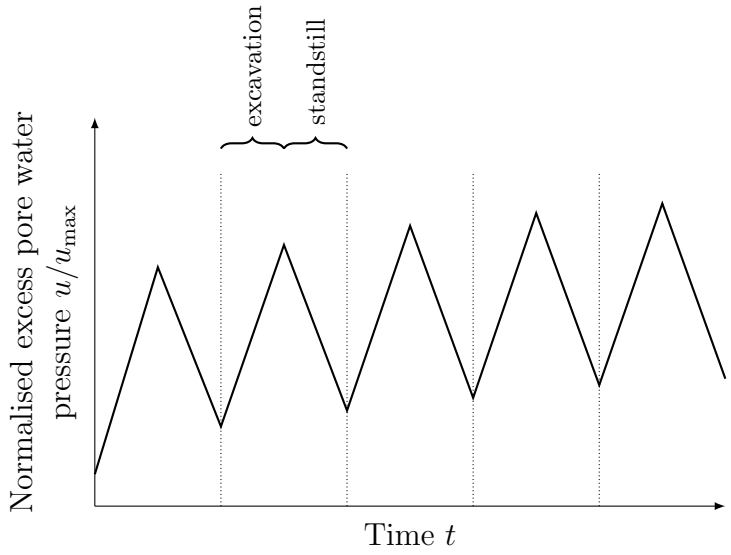

Figure 2.8: Schematic cyclic evolution of excess pore water pressure ahead of a slurry-supported tunnel face. During excavation, penetration may increase pore water pressure, whereas during standstills filtration and dissipation may reduce it.

These observations highlight that support pressure transfer at slurry-supported tunnel faces must be interpreted as a transient hydraulic–mechanical process. A single steady-state pressure distribution may therefore not adequately represent the evolving interaction between excavation, slurry infiltration, and sealing-layer reformation.

2.5 Microstructure of bentonite–sand systems

The hydraulic resistance generated during slurry infiltration is closely related to the microstructural arrangement of bentonite particles within the pore space of granular soils. Clay platelets may assemble into networks that modify pore connectivity and influence permeability and pressure transfer. Fundamental studies on clay suspensions show that platelet interactions are governed by the anisotropic charge distribution of the particles, which promotes edge–face and face–face associations and leads to the formation of aggregated structures in concentrated suspensions (van Olphen, 1964; Luckham and Rossi,

1999). These interactions provide the microstructural basis for the development of clay networks that can partially restrict flow through the pore system.

Microstructural investigations of smectite systems further demonstrate that platelet organisation depends strongly on hydration conditions and stress history. Experimental observations indicate that smectite particles can form stacks and quasi-crystalline aggregates whose internal structure evolves with water content and applied stress (Ben Rhaiem et al., 1987). Such rearrangements modify the internal pore geometry of clay aggregates and therefore influence their hydraulic properties.

Direct observations of clay slurry microstructures have been obtained using cryogenic microscopy techniques. Studies combining high-pressure freezing with cryo-electron microscopy show that hydrated clay suspensions consist of platelet aggregates arranged through face–face and face–edge contacts rather than forming regular cellular networks (Deirieh et al., 2018). These particle associations create heterogeneous networks of aggregates and inter-aggregate pores within the slurry.

At sand–slurry interfaces, particle deposition during filtration can lead to the development of thin clay films and graded boundary layers that progressively reduce pore-throat connectivity. Experimental studies of slurry infiltration into granular soils have shown that such boundary layers can develop near the soil surface as particles accumulate and rearrange during filtration processes (Min et al., 2013). These structures localise hydraulic resistance near the interface and influence the transfer of pressure from the slurry to the soil skeleton.

Characterisation of such microstructures requires preparation techniques that preserve delicate clay fabrics while minimising preparation artefacts. Broad ion beam (BIB) milling combined with scanning electron microscopy enables the preparation of smooth cross-sections suitable for high-resolution imaging of pore structures in fine-grained geomaterials (Sinn et al., 2017; Hemes et al., 2015). The combination of BIB–SEM imaging with focused ion beam (FIB) tomography further allows multi-scale investigation of pore networks and their connectivity.

Cryogenic preparation techniques are particularly important for imaging hydrated clay systems. Cryo-SEM observations demonstrate that thin wetting films and hydrated clay fabrics can be preserved during preparation when freezing procedures are carefully controlled, allowing direct observation of clay–fluid interfaces (Schmatz et al., 2017).

For quantitative analysis of such images, backscattered electron (BSE) imaging combined with energy-dispersive X-ray spectroscopy (EDS) mapping can be used to distinguish

mineral phases and analyse microstructural features at sub-micron resolution. Segmentation workflows integrating BSE contrast with elemental information enable automated identification of phases and measurement of particle geometries and spatial distributions (Jiang et al., 2022).

Despite these advances, direct microstructural observations of bentonite particles within the pore space of sand after slurry infiltration remain limited. While previous studies have characterised the organisation of clay particles in suspensions and the behaviour of clay aggregates, fewer investigations have resolved how bentonite particles are arranged within the pore network of granular soils. Imaging such configurations is challenging because hydrated clay fabrics are easily disturbed during conventional sample preparation. Consequently, the pore-scale arrangement of bentonite within infiltrated sands and its interaction with sand grains remain insufficiently documented.

2.6 Monotonic and cyclic behaviour of sand with bentonite infiltration

2.6.1 Effect of specimen preparation on the monotonic and cyclic response of sand

The mechanical behaviour of sand in laboratory testing is strongly influenced by the method of specimen preparation, as different reconstitution techniques generate distinct initial fabrics and inherent anisotropy. Common preparation methods include air pluviation (dry deposition under gravity), water pluviation or sedimentation, moist or wet tamping, vibration, and slurry deposition (Miura and Toki, 1982; Tatsuoka et al., 1986a; Vaid and Sivathayalan, 2000). Although specimens prepared by these techniques may share the same global void ratio or relative density I_D, their particle orientation, contact distribution, and degree of fabric anisotropy can differ substantially.

Air pluviation typically produces cross-anisotropic fabrics associated with gravitational settling, whereas moist or wet tamping introduces layer-wise compaction and may reduce inherent anisotropy while potentially inducing density non-uniformities if compaction energy is not carefully controlled (Miura and Toki, 1982). Experimental observations indicate that such fabric differences influence the monotonic stress–strain response. Sands prepared by pluviation frequently exhibit stronger peak dilatancy and higher peak stress

ratios than tamped specimens at comparable densities (Tatsuoka et al., 1986a). Plane-strain compression studies further demonstrate that the preparation method affects strain localisation and peak strength, even when the critical-state condition remains essentially unchanged (Wanatowski and Chu, 2008).

Within the framework of critical-state soil mechanics, clean sands prepared by different methods generally converge toward a common critical-state line (CSL) at large strains, suggesting that the critical-state friction angle is governed primarily by intrinsic characteristics of the sand skeleton, including mineralogy, grain-size distribution, and grain shape, rather than by preparation history (Been and Jefferies, 1985; Schofield and Wroth, 1968). However, the pre-peak regime is sensitive to initial fabric. Differences in particle orientation and contact distribution influence dilatancy rate, peak strength, and stiffness, particularly in dense specimens where fabric effects are amplified.

The influence of the preparation method becomes even more pronounced under cyclic loading. Cyclic undrained triaxial and torsional shear tests have shown that cyclic resistance depends not only on density but also on fabric generated during specimen preparation (Tatsuoka et al., 1986a). Classic liquefaction studies by Mulilis et al. (1977) demonstrated that specimens prepared by moist tamping exhibit lower resistance to liquefaction than water-pluviated specimens at similar densities, reflecting differences in pore-pressure generation behaviour. Vaid and Sivathayalan (2000) reported that preparation-induced anisotropy affects early-cycle contractiveness and the rate of pore-pressure build-up, thereby altering the number of cycles required to reach a defined pore-pressure threshold.

Differences in cyclic response are commonly observed in terms of pore-pressure development rate, effective stress-path evolution, and deformation mode (cyclic mobility versus flow-type behaviour) (Yoshimine et al., 1998). More recent experimental databases confirm that cumulative strain accumulation under cyclic loading is sensitive to the specimen preparation method and associated fabric anisotropy, even when density and confining stress are held constant (Wichtmann et al., 2005, 2020).

Overall, the literature consistently indicates that specimen preparation governs the initial fabric of sand, which in turn controls dilatancy, peak shear strength, and pore-pressure development during both monotonic and cyclic loading. While the critical-state condition tends to be relatively insensitive to preparation history for clean sands, pre-peak and cyclic behaviour can vary significantly, underscoring the importance of consistent and well-documented preparation procedures when comparing experimental results.

2.6.2 Monotonic and cyclic behaviour of sand containing bentonite in the pore space

Clay particles within the pore space of sand can influence the mechanical behaviour mainly by modifying drainage conditions and local soil fabric. While the intrinsic frictional resistance of the sand grains generally remains unchanged, clay occupying pore throats or grain surfaces can alter dilatancy, stiffness, and pore pressure generation during loading.

In mechanically mixed sand–clay systems, clay particles are distributed throughout the specimen and may participate in the load-bearing skeleton. Laboratory triaxial tests show that increasing clay content typically suppresses dilatancy and promotes contractive behaviour. Polito and Martin (2001) reported faster pore pressure build-up and reduced cyclic resistance in sands containing clay fines, while Carraro et al. (2009) showed that stiffness and peak strength can also change depending on clay type and initial state.

When bentonite is introduced into sand by permeation, the granular skeleton is largely preserved and bentonite particles are introduced primarily within the pore space. Laboratory tests reported by El Mohtar et al. (2012) showed that small bentonite contents (approximately 3–5% by dry mass of sand) did not significantly modify the friction angle in monotonic triaxial tests, although the early stress–strain response was affected. Under cyclic loading, specimens permeated with bentonite exhibited an increased number of cycles to liquefaction after sufficient hydration time, which the authors associated with delayed pore pressure generation in the bentonite–water suspension.

Despite the available literature on specimen preparation effects and on sand–clay mixtures, experimental data specifically addressing the mechanical behaviour of slurry-infiltrated sands remain limited. In particular, systematic triaxial investigations examining the monotonic and cyclic response of sands containing bentonite introduced through slurry infiltration are scarce. Most existing studies consider mechanically mixed sand–clay systems, in which clay particles are distributed throughout the specimen during preparation. As discussed above, such mixtures may not adequately represent infiltration-conditioned sands because specimen preparation modifies the granular fabric and the spatial distribution of clay within the pore space. Consequently, the mechanical response of sands containing bentonite introduced by slurry infiltration remains insufficiently documented.

2.7 Slurry infiltration in granular soils: empirical relations and continuum modelling

Slurry infiltration into granular soils has been described using both empirical relations and continuum formulations. Empirical approaches provide simplified estimates of penetration distance, pressure gradients, and sealing conditions based on operating pressure, slurry properties, and soil parameters. Continuum descriptions treat the slurry–soil system at the representative elementary volume (REV) scale and derive governing equations for fluid flow, particle transport, and pore-space evolution.

2.7.1 Empirical relations for slurry penetration

Empirical relations have been proposed to approximate the extent of slurry penetration into granular soils using simplified representations of the governing variables. These relations typically connect the applied support overpressure Δp, slurry rheological properties, and soil characteristics such as grain size to observable penetration behaviour. In practice, attention focuses on quantities such as the penetration length reached before filtration becomes dominant, the pressure gradient within the soil during penetration, and the characteristic time scale associated with the transition from open penetration to sealing.

Early engineering descriptions of slurry penetration consider the balance between the applied support pressure and the hydraulic resistance of the soil. In this framework, penetration is assumed to continue until the pressure gradient within the soil reaches a limiting value often referred to as the stagnation gradient f_{so} (Krause, 1987; Huisman, 1998). Under this assumption, the maximum penetration length $x_{\max}$ can be expressed as

$$x_{\max} = \frac{\Delta p}{f_{\mathrm{so}}}. \tag{2.6}$$

The stagnation gradient has been related empirically to slurry rheological properties and soil grain size. A commonly used approximation expresses the gradient as (Krause, 1987; Huisman, 1998)

$$f_{\mathrm{so}} = a\frac{\tau_f}{d_{10}}, \tag{2.7}$$

where τ_f denotes the yield stress of the slurry, d_{10} is the representative grain size of the soil, and a is an empirical coefficient accounting for soil structure and filtration conditions. Combining these expressions yields an estimate for the penetration length

$$x_{\max} = \frac{\Delta p \, d_{10}}{a \, \tau_f}. \tag{2.8}$$

In addition to the maximum penetration distance, empirical descriptions have also been proposed for the time evolution of the penetration front. A commonly cited relation describes the penetration distance as (Krause, 1987)

$$x(t) = \frac{x_{\max} \, t}{t + a}, \tag{2.9}$$

where t denotes time and a is an empirical time constant. This relation describes a rapid initial advance of the slurry front followed by a gradual approach toward the limiting penetration length $x_{\max}$ as filtration processes progressively restrict flow.

Similar penetration expressions have been discussed in tunnelling studies addressing slurry infiltration in sandy soils under pressurised conditions (Talmon et al., 2013). In such applications, empirical penetration relations are often used to obtain approximate estimates of the potential depth of slurry invasion based on operating pressure and slurry rheology.

In addition, slurry infiltration may lead to the formation of a filter cake at the soil–slurry interface as bentonite particles accumulate and progressively reduce permeability. The formation and hydraulic behaviour of such filter cakes have been extensively investigated in the filtration literature, beginning with early theoretical formulations of cake filtration dynamics (Ruth, 1935) and subsequent developments of conventional filtration theory (Tiller and Cooper, 1960). More recent analyses and reviews of cake filtration mechanisms and modelling approaches are provided by Tien and Bai (2003) and Olivier et al. (2007). However, a detailed treatment of filter-cake formation processes and their modelling is beyond the scope of the present section.

2.7.2 Continuum description at the representative elementary volume (REV) scale

Continuum descriptions of slurry infiltration treat the slurry–soil system at the scale of a representative elementary volume (REV), where pore-scale heterogeneity is replaced by averaged quantities describing the behaviour of the porous medium. In this framework,

the granular soil is represented by an equivalent continuum characterised by averaged properties such as porosity, permeability, and the concentration of suspended particles within the pore fluid.

The theoretical basis of such continuum descriptions is commonly derived from volume averaging and mixture theory. Classical references include the works of Bear (1972) and Whitaker (1999), which establish the averaged balance equations governing fluid flow and transport processes in porous media. Extensions to multiphase and multi-constituent systems were developed by Hassanizadeh and Gray (1979a,b, 1980, 1990), providing a rigorous framework for describing mixtures of fluids and suspended particles within porous structures.

Within the REV framework, the slurry–soil system is therefore described using averaged fields such as fluid pressure $p(z,t)$, Darcy flux $q(z,t)$, porosity $\phi(z,t)$, and, when required, the concentration of mobile particles $c(z,t)$. These quantities allow the infiltration process to be represented using continuum balance equations that link fluid flow, particle transport, and the evolution of pore-space properties.

2.7.3 Governing equations for slurry infiltration

Continuum descriptions of slurry infiltration represent the soil–slurry system at the scale of a representative elementary volume (REV), where pore-scale heterogeneity is replaced by averaged quantities such as porosity, permeability, and particle concentration. Within this framework, fluid flow through the porous medium is commonly described using Darcy's law, which relates the Darcy flux q to the pressure gradient (Bear, 1972; Whitaker, 1999)

$$q = -\frac{k}{\mu}\frac{\partial p}{\partial z}, \tag{2.10}$$

where k denotes the intrinsic permeability of the porous medium, μ the dynamic viscosity of the slurry, and p the fluid pressure.

Mass conservation of the pore fluid leads to the continuity equation

$$\frac{\partial \phi}{\partial t} + \frac{\partial q}{\partial z} = 0, \tag{2.11}$$

where ϕ denotes the porosity of the porous medium.

In addition to fluid flow, slurry infiltration involves the transport of suspended particles within the pore fluid. At the continuum scale this process is commonly described by an advection–reaction equation for the particle concentration c

$$\frac{\partial(\phi c)}{\partial t} + \frac{\partial(qc)}{\partial z} = -r_{\mathrm{dep}}, \tag{2.12}$$

where r_{dep} represents the rate of particle deposition within the pore space.

Particle deposition progressively alters the pore structure of the soil and therefore modifies its hydraulic properties. The evolution of porosity associated with particle retention can be expressed as

$$\frac{\partial \phi}{\partial t} = -\frac{1}{\rho_s} r_{\mathrm{dep}}, \tag{2.13}$$

where ρ_s denotes the density of the deposited solid phase.

These averaged balance relations form the basis of continuum models used to describe slurry penetration into granular soils. The theoretical framework for multiphase and multi-constituent transport in porous media has been developed using mixture theory and volume averaging (Hassanizadeh and Gray, 1979a, 1980, 1990), providing a consistent basis for coupling fluid flow, particle transport, and the evolution of pore-space properties in infiltration models. Different continuum models adopt specific constitutive relations for permeability, slurry rheology, and deposition kinetics. Examples of such models applied to slurry infiltration are reviewed in the following subsection.

2.7.4 Continuum models for slurry infiltration

Building on the continuum framework described above, several studies have developed models to analyse slurry infiltration into granular soils and the associated pressure transfer mechanisms. These models typically couple Darcy-scale flow with particle transport and deposition processes in order to represent the progressive reduction of permeability caused by bentonite retention within the pore space.

For example, Schaufler et al. (2013) developed a thermodynamically consistent four-phase continuum model for suspension infiltration into cohesionless granular media. Although the formulation is general, its principal engineering motivation was the infiltration of annular-gap grouting mortar into the surrounding soil during annular-gap backfilling in mechanised tunnelling. The model distinguishes between the fluid phase, the granular

skeleton, and mobile and immobilised particle fractions, leading to a multi-constituent description of the suspension–soil system. A schematic representation of this continuum mixture formulation is shown in Fig. 2.9.

In this representation, the classical two-phase description distinguishes between the solid skeleton φ^s and the liquid phase φ^l, as shown on the left of Fig. 2.9. In the extended continuum mixture formulation proposed by Schaufler et al. (2013), the porous medium is further decomposed into several volume fractions describing the different constituents present within the REV. The native soil skeleton is denoted by φ^{sn}, while the pore space may contain pore fluid φ^f as well as particle fractions transported with the fluid. Mobile particle aggregates are represented by φ^a, whereas particles that become immobilised within the pore structure are described by the attached or deposited fraction φ^{sa}. Such a multi-constituent description enables the modelling of particle transport and retention during suspension infiltration.

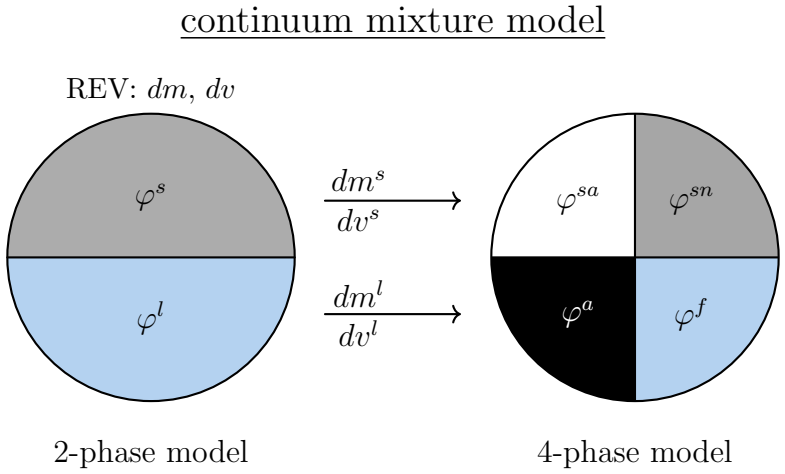

Figure 2.9: Four-phase continuum representation for suspension infiltration into cohesionless granular media, adapted from Schaufler et al. (2013) . The original tunnelling application concerned annular-gap grout infiltration; the framework is adapted in this thesis for bentonite-slurry infiltration.

In these models, particle deposition is often represented using a first-order kinetic retention law of the form

$$r_{\mathrm{dep}} = \lambda\, c\, q, \tag{2.14}$$

where λ is an empirical deposition coefficient representing the combined effects of particle attachment, straining, or bridging within the pore structure, c is the concentration of suspended particles, and q is the Darcy flux.

The reduction of permeability caused by particle accumulation is typically represented using empirical relations linking permeability to porosity, for example

$$k = k_0 \left(\frac{\phi}{\phi_0} \right)^n , \tag{2.15}$$

where k_0 and ϕ_0 denote the initial permeability and porosity, respectively, and n is an empirical exponent.

Numerical simulations based on such formulations have been used to investigate the evolution of infiltration fronts, permeability reduction, and pressure transfer during slurry infiltration into sandy soils (Zhou et al., 2018; Lu et al., 2022). These studies show that particle deposition can significantly reduce soil permeability near the slurry interface and strongly influence the spatial distribution of pore pressure. However, the complexity of slurry–soil interactions and the limited availability of experimental data mean that simplified assumptions are often required in practical modelling approaches.

2.7.5 Pore-scale CFD–DEM models for cake morphology and constitutive-relation development

Here, constitutive relations denote material-specific equations required to complete the averaged balance laws, such as the particle-retention law $r_{\mathrm{dep}} = \lambda c q$ and the permeability–porosity relation $k(\phi)$. Where these relations remain uncertain, pore-scale simulations provide morphology-resolved insight and support parameter selection. Coupled CFD–DEM approaches resolve the granular geometry and explicitly track particle motion and deposition within pore constrictions.

For example, Zhang and Yin (2018) performed CFD–DEM simulations under slurry-shield conditions, resolving grain throats and tracking bentonite particles to reproduce regimes ranging from external filter-cake formation to mixed external–internal clogging. Zhang et al. (2019) extended this approach to filtration-column configurations representative of tunnel-face conditions, analysing the evolution of cake thickness, porosity distribution, and pressure drop.

High-resolution simulations by Yin et al. (2021) further related cake morphology to pressure-filtration characteristics and clarified transitions from spurt loss to the development of a self-sealing cake. More recently, Chen et al. (2023) examined the impermeability and stability of filter cakes under varying hydraulic and chemical conditions.

These pore-scale investigations provide mechanistic insight into particle deposition, clogging behaviour, and cake structure. Although such simulations are computationally intensive and typically restricted to small domains, they provide valuable information for selecting constitutive relations, such as particle-retention laws and permeability–porosity relations, for REV-scale infiltration models.

Despite these advances, several challenges remain in the numerical description of slurry infiltration into granular soils. Continuum models rely on simplified constitutive relations for particle retention and permeability evolution, which are often introduced empirically and remain difficult to constrain from available data. Although pore-scale CFD–DEM simulations provide detailed insight into particle deposition and clogging mechanisms, their computational cost restricts their application to small domains and short time scales. Consequently, developing continuum models with practical constitutive relations for particle retention and permeability evolution remains an important aspect of slurry infiltration modelling.

2.8 Summary and research gaps

This chapter reviewed face-support mechanisms, slurry composition and rheology, penetration–filtration behaviour, interface microstructure, and the hydro-mechanical response of sands modified by fines or slurry infiltration. While the qualitative pathway from pressurised infiltration to sealing and pressure transfer is well established, several aspects required for quantitative interpretation and modelling remain insufficiently documented.

Few studies resolve where filtration initiates and how pressure drop is distributed with depth during slurry infiltration, or quantify the time required to re-establish an effective sealing layer after disturbance. This thesis addresses this gap through an instrumented experimental programme combining multi-depth pore-water-pressure measurements with the determination of post-test composition profiles $c(z)$ across controlled soil grading, permeability, support overpressure Δp, and slurry concentration c.

Detailed descriptions of the sand–slurry interface remain limited. Although preserved hydrated sections have been reported, the pore-scale morphology of this interface is still

insufficiently documented. This thesis therefore investigates the interface using cryogenic preparation and high-resolution imaging to provide a predominantly qualitative characterisation of the pore-scale arrangement of bentonite and sand particles.

Systematic investigations of the mechanical consequences of slurry infiltration remain limited when preparation route and initial state are controlled consistently. In particular, systematic comparisons between the mechanical behaviour of sands modified by bentonite infiltration and that of clean sand remain scarce. This thesis addresses this gap through monotonic and cyclic triaxial tests on clean and infiltrated samples conducted at identical p'_0 and similar density. Furthermore, infiltrated and mechanically mixed samples with the same bentonite content are compared.

Finally, continuum models describing slurry infiltration require constitutive relations for particle retention and permeability evolution whose parameters can be calibrated against experimental observations. However, experimentally supported formulations remain limited in the literature.

The following chapters address these gaps in sequence: development of the experimental methods; column infiltration tests examining slurry penetration, particle retention, and pressure transfer; microstructural investigation of sand–slurry interfaces; monotonic and cyclic triaxial testing of clean, infiltrated, and mechanically mixed specimens; and finally continuum modelling of slurry infiltration and pressure transfer in granular soils.

3 Experimental materials and methods

3.1 Introduction

This chapter presents the materials and experimental methods employed in the present work. A major part of the experimental programme is dedicated to the development and application of an infiltration column device, which enabled the acquisition of depth-resolved pore-water pressure and concentration data for subsequent model calibration and validation.

In addition to the column investigations, various element tests were conducted to examine the hydro-mechanical behaviour of clean, slurry-infiltrated, and slurry-mixed sands. These include monotonic and cyclic triaxial tests. The following sections describe the materials used, the experimental setups, and the corresponding testing procedures.

3.2 Materials used

3.2.1 Sand materials

Three uniformly graded quartz sands were used in the experimental programme. These materials represent coarse granular soils typically encountered in slurry-shield tunnelling in permeable ground conditions. The grain size distribution curves of the sands are shown in Fig. 3.1, and their physical properties are summarised in Table 3.1. Photographs of the three sands are presented in Fig. 3.2.

All sands were supplied by *EUROQUARZ GmbH* (Dorsten, Germany). According to the manufacturer, the materials consist predominantly of quartz.

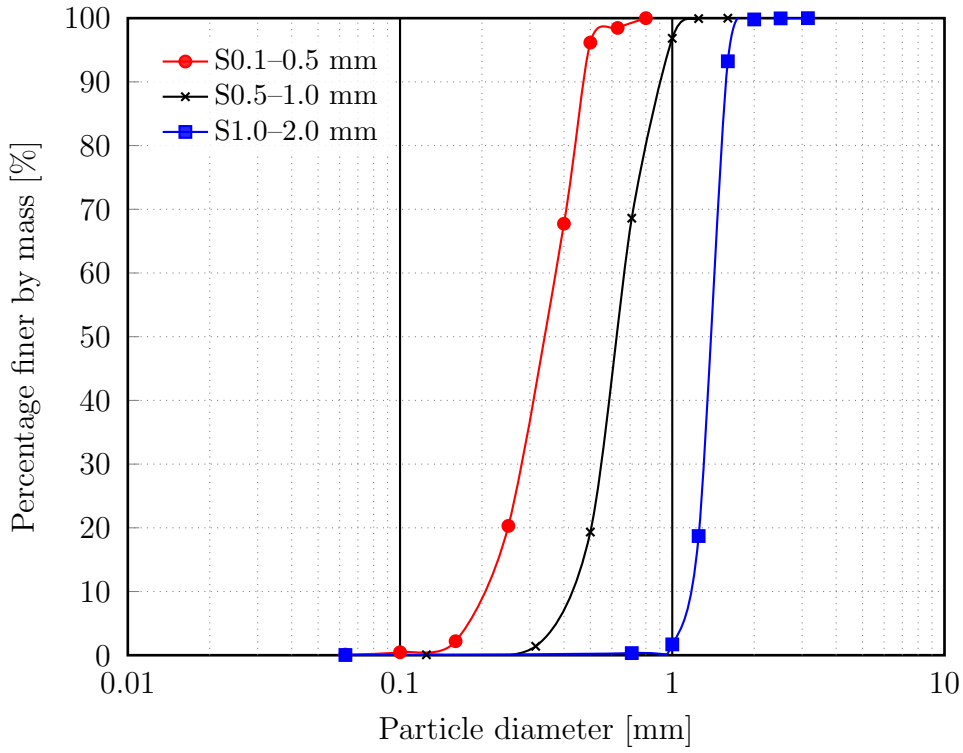

Figure 3.1: Grain size distribution curves of the tested sands

Table 3.1: Physical properties of the three sands considered in the testing programme

Sand	$\rho_{d,\max}$ (g/cm^3)	$\rho_{d,\min}$ (g/cm^3)	$e_{\max}$ (−)	$e_{\min}$ (−)	G_s (−)
0.1–0.5 mm	1.685	1.335	0.97	0.56	2.63
0.5–1.0 mm	1.721	1.415	0.86	0.53	2.64
1.0–2.0 mm	1.667	1.407	0.87	0.58	2.63

3.2.2 Bentonite

A sodium-activated bentonite powder (IBECO S) was used to prepare the bentonite slurry. According to the manufacturer, the bentonite is characterised by a liquid limit of $w_L = 317\%$ and a plasticity index of $I_P = 253\%$, corresponding to a plastic limit of $w_P = 64\%$.

Bentonite slurries were prepared by mixing the powder with tap water at nominal concentrations of 20, 40, 60, and 80 g/L, denoted B20, B40, B60, and B80, respectively. Each batch was stirred for 10 minutes and then left to hydrate for 16–18 hours in a temperature-controlled room before testing. The rheological response of the B60 slurry

(a) 0.1 - 0.5 mm (b) 0.5 - 1.0 mm (c) 1.0 - 2.0 mm



Figure 3.2: Sands used for the experiments

at 20 °C was measured with a rotational rheometer (MCR 102e, Anton Paar GmbH, Austria). Figure 3.3 shows the shear stress τ as a function of shear rate $\dot{\gamma}$. Compared with water, the slurry exhibits a strongly non-linear τ–$\dot{\gamma}$ relation, consistent with shear-thinning behaviour and the presence of a pronounced stress level at low shear rates.

For additional interpretation, the apparent viscosity $\mu_{\text{app}} = \tau/\dot{\gamma}$ derived from the same measurements is presented in Fig. 3.4. The B60 slurry shows a marked decrease in μ_{app} with increasing $\dot{\gamma}$, whereas water is shown as a constant-viscosity reference at 20 °C.

In addition to the rheometer measurements, classification tests were performed on each prepared slurry batch prior to its use in the experiments in accordance with DIN Deutsches Institut für Normung e. V. (2014). An overview of the applied methods is shown in Fig. 3.5.

The static yield point was determined using the ball-harp method (Fig. 3.5b). The device consists of calibrated balls with defined critical yield values. When placed on the slurry surface, balls with a lower yield value than the suspension float, whereas those with a higher yield value sink. The static yield point of the slurry is identified between the largest floating ball and the smallest sinking ball. For each prepared slurry batch, the resulting yield values were averaged and later compared with the rheometer-derived stress levels at low shear rates.

The dynamic viscosity was evaluated using the Marsh funnel test (Fig. 3.5a). The test determines the efflux time of defined slurry volumes (1000 mL and 1500 mL), from which flow characteristics such as dynamic yield stress (τ_F) and differential viscosity (η') can be derived. The measurements were repeated for each slurry batch to verify consistency of the flow behaviour.

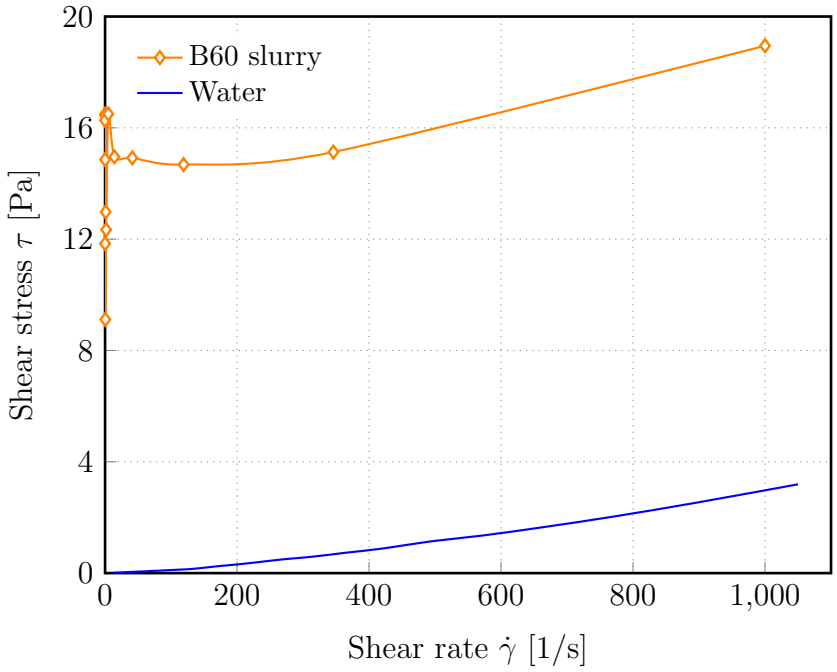

Figure 3.3: Rheological response of the B60 slurry at 20 °C shown as shear stress τ versus shear rate $\dot{\gamma}$, compared with water.

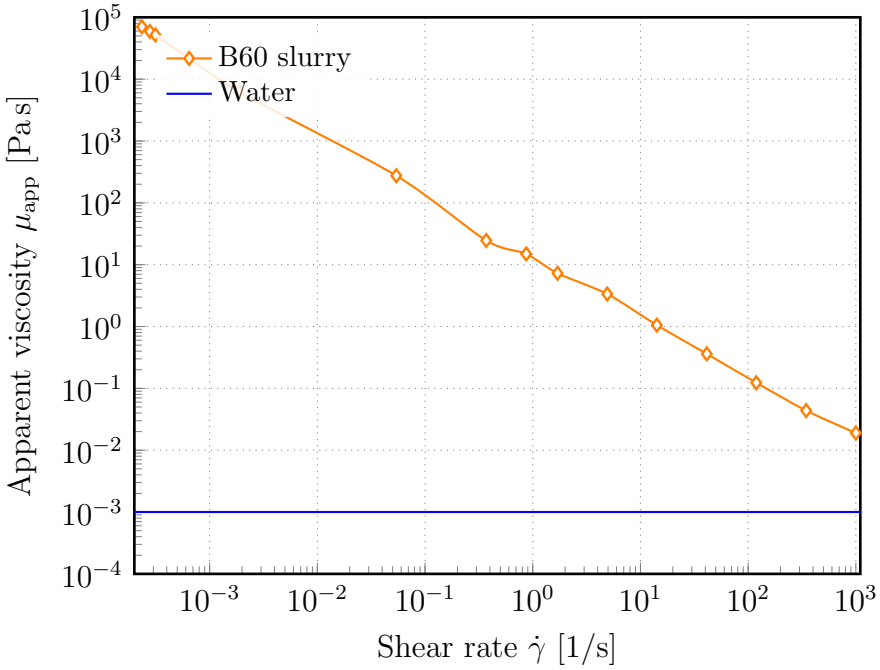

Figure 3.4: Apparent viscosity $\mu_{app} = \tau/\dot{\gamma}$ of the B60 slurry at 20 °C derived from the measured τ–$\dot{\gamma}$ data. Water is shown as a constant-viscosity reference with $\mu_w = 1.002 \times 10^{-3}$ Pa s at 20 °C.

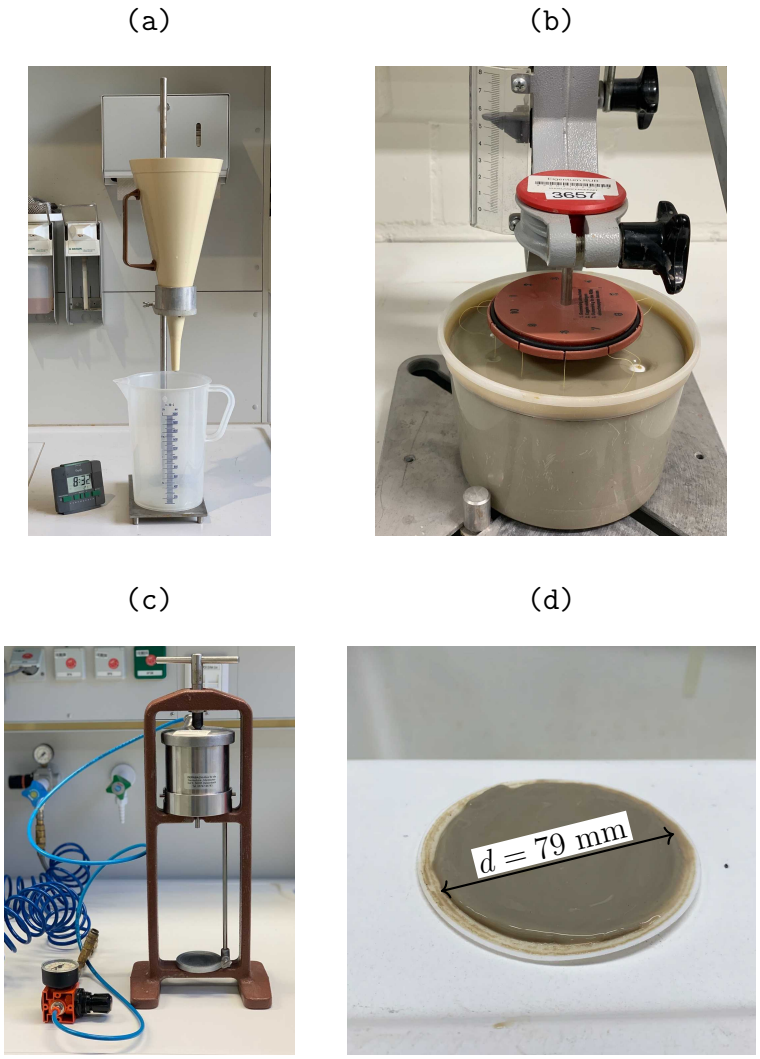

Figure 3.5: (a) Marsh funnel method; (b) Ball-harp method; (c) filter press device (all according to DIN Deutsches Institut für Normung e. V. (2014)); (d) filter cake for the B60 slurry with measured diameter $d = 79$ mm.

Filter-cake formation characteristics were assessed using a standard filter press device (Fig. 3.5c). Under a controlled pressure of 7.0 ± 0.35 bar, the filtrate volume released within 7.5 minutes was measured, and the resulting filter-cake thickness was determined (example shown in Fig. 3.5d). These measurements provide an index of slurry filtration behaviour relevant to sealing performance. In addition, slurry density and temperature were measured prior to testing to ensure consistent experimental conditions.

The suspension density was determined using a calibrated measuring flask (Fig. 3.6). The filled and empty flask masses were measured with an accuracy of 0.01 g, and the density was calculated as

$$\rho_f = \frac{m_{\text{filled}} - m_{\text{flask}}}{V_{\text{flask}}} \tag{3.1}$$

where m_{filled} and m_{flask} denote the masses of the filled and empty flask, and V_{flask} is the calibrated flask volume at the measurement temperature (typically 20 °C).

The suspension temperature was measured using a digital thermometer prior to testing and recorded together with density to ensure consistent reference conditions.



Figure 3.6: Measuring flask for suspension density determination.

3.3 Infiltration column: concept, design, and application

A central component of the experimental programme is a vertical infiltration column designed to reproduce slurry infiltration under controlled boundary conditions. The device enables depth-resolved pore water pressure measurements and the recovery of infiltration-conditioned specimens for subsequent element testing. The overall configuration and its main components are described in the following section.

3.3.1 Concept

The experimental set-up was developed to reproduce controlled slurry infiltration under laboratory conditions while enabling continuous hydraulic monitoring and specimen recovery. An overview of the complete infiltration system is shown in Fig. 3.7.

The system consists of a central vertical infiltration column connected to an inflow container and an outflow container. A pressure regulator controls the applied support overpressure Δp, while a data acquisition system records pore water pressures and the mass changes of the containers during testing. The inflow and outflow connections allow a defined pressure difference to be imposed across the sand specimen.

This integrated configuration enables controlled infiltration, monitoring of pressure transfer, and recovery of infiltration-conditioned samples for subsequent microstructural and mechanical investigations.

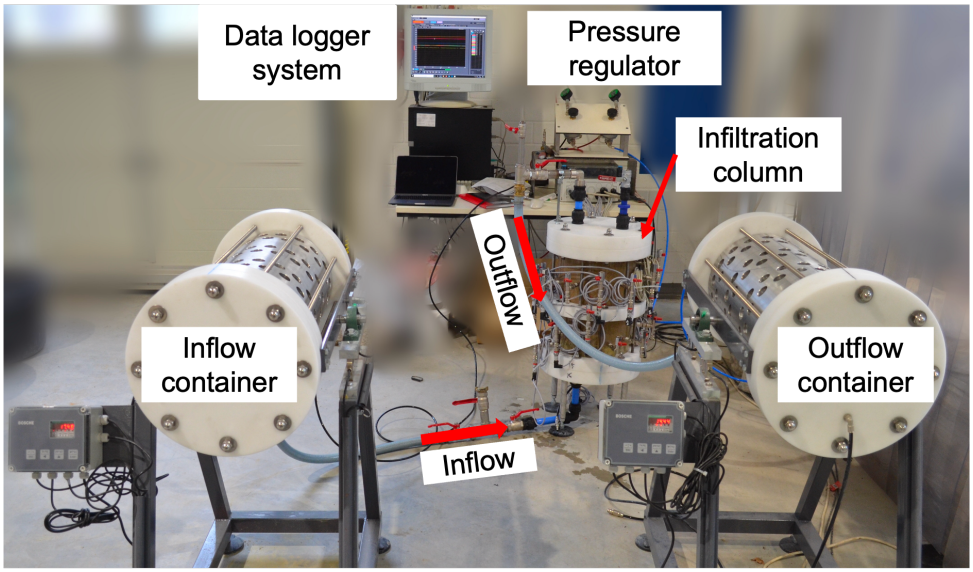

Figure 3.7: Full experimental set-up of the infiltration system showing the central infiltration column, inflow and outflow containers, pressure regulator, and data acquisition system.

3.3.2 Design features

The cylindrical column has an inner diameter of 27 cm and a total height of 44 cm. It is designed for pressures up to 10 bar. A cross-sectional view of the column and its internal configuration is shown in Fig. 3.8.

Along its height, 24 pressure ports are arranged to allow depth-resolved pore water pressure measurements within the sand specimen. The openings on the specimen side are covered with water-permeable glass fibre to prevent sand intrusion while maintaining hydraulic contact between the pore water and the sensors. Each pressure-port assembly

includes a quick-connect valve for attaching the pore water pressure transducer and a separate saturation valve used to fill the connecting line between the column and the transducer with water before measurement. Sixteen Keller 21Y piezoresistive pressure sensors (measurement range 0–4 bar, response time < 5 ms) (Keller AG, 2020) are connected to selected ports for monitoring the pressure evolution during infiltration.

Embedded within the sand body, removable moulds enable targeted sampling during and after infiltration. The column dimensions provide sufficient internal space for the free placement of sampling moulds at different heights and radial positions within the sand specimen. The red element (a) in Fig. 3.8 represents a sample extractor used for microstructural investigations. The grey mould (b) corresponds to the triaxial specimen mould, allowing recovery of infiltration-conditioned specimens for subsequent element testing. The perforated hollow cylinders (c) permit slurry sampling at different elevations within the column and enable the determination of concentration profiles $c(z)$.

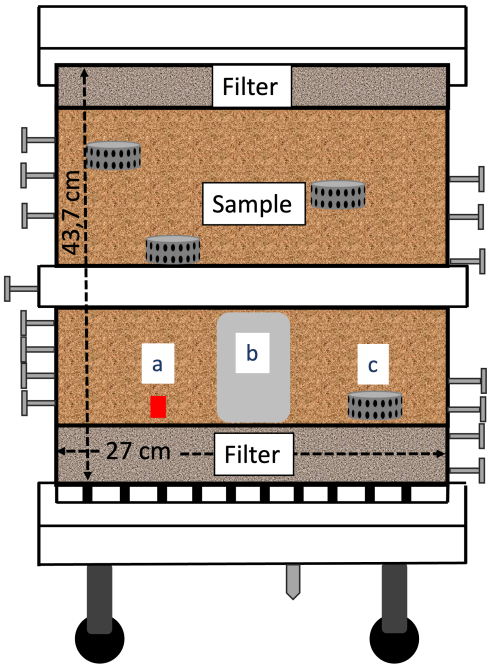

Figure 3.8: Schematic overview of the infiltration column with embedded sampling moulds (a–c) and depth-resolved pressure ports.

The column is hydraulically connected to an inflow container and an outflow container, each equipped with S40S load cells for gravimetric monitoring of mass changes during testing (precision ±0.03% of full scale) (Bosche GmbH & Co. KG, 2020). The container capacity is 27 L.

A pressure regulator controls the applied support overpressure Δp, and a Graphtec GL820 data acquisition system records pore water pressures and container mass signals at up to 5 Hz (Graphtec Corporation, 2020).

3.3.3 Calibration of sensors and monitoring instruments

Prior to each experimental series, the pore water pressure sensors and the load cells in the containers were calibrated. Controlled air and water pressures were applied to establish calibration relationships between the electrical output signals (mV) and the corresponding physical quantities.

For the pressure sensors, the millivolt signal was related to applied pressure in kilopascals (kPa). For the load cells, the electrical signal was related to applied mass in kilograms (kg). The resulting calibration factors were implemented in the data acquisition system for direct conversion during testing.

3.3.3.1 Calibration of pore pressure sensors

i) Calibration using air

Over a pressure range of 50–400 kPa, increments of 50 kPa were applied to the column pore water pressure sensors using a pressure regulator. At each pressure level, the stabilised electrical output signal (mV) of the sensor was recorded.

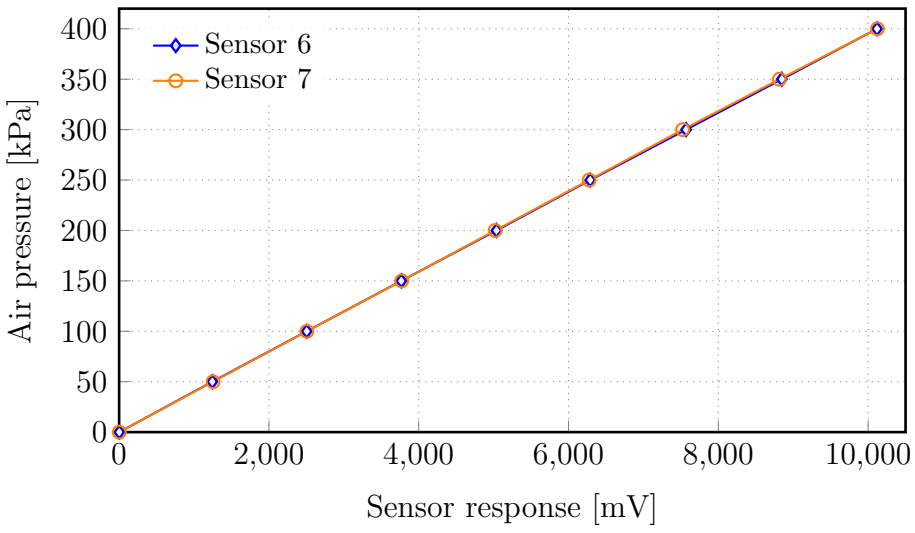

Figure 3.9: Calibration of pore pressure sensors of the infiltration column

A linear calibration relationship between applied pressure (kPa) and measured signal (mV) was obtained for all sensors. The slope of the calibration curve was determined from the linear fit and used as the conversion factor for subsequent measurements. A consistent slope of approximately 25 mV/kPa was found for all pore water pressure sensors. Examples for two sensors are shown in Fig. 3.9.

ii) Calibration using water

A hydrostatic validation of the column pore water pressure sensors was performed using water filling of the column. The sensors were installed at predetermined elevations along the column, and the water level was raised in two stages. For each filling level, the electrical output signal (mV) of the sensors was recorded.

Based on the known sensor elevations and the measured water level, the corresponding hydrostatic head at each sensor location was determined from geometry. The measured sensor response was then compared with the hydrostatic head to evaluate the consistency of the previously established air-based conversion factor. The results for two representative sensors are shown in Fig. 3.10.

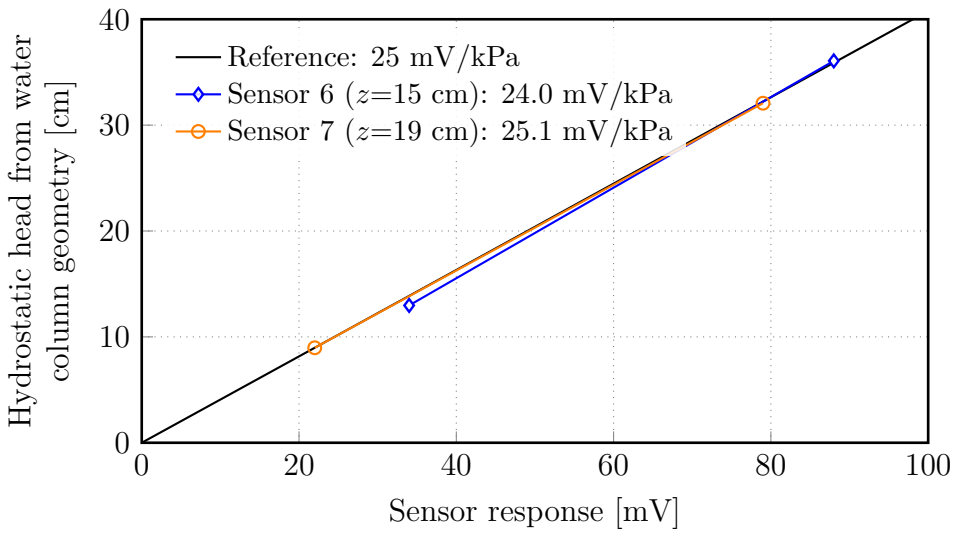

Figure 3.10: Water-column calibration check for two pore water pressure sensors installed at different elevations z.

The slopes derived from the water-column check corresponded to conversion factors in the range of 24.0 to 25.6 mV/kPa. A uniform conversion factor of 25 mV/kPa was therefore adopted for all sensors in subsequent analyses.

3.3.3.2 Calibration of load cells of the inflow and outflow containers

The containers were tared in the empty condition, and incremental solid weights were applied in 5 kg steps. The corresponding voltage response was recorded and compared with the applied mass to verify the linear relationship between load and electrical output signal. Figure 3.11 shows the linear calibration relationship between applied mass and sensor response for the inflow and outflow containers.

The calibration data yield a factor of approximately 0.005 kg/mV for converting the voltage signal to mass. This is equivalent to a load-cell sensitivity of approximately 200 mV/kg. The mass-per-voltage factor is implemented in the data acquisition system. Prior to each experimental series, it was verified by dividing the reference mass of each container displayed on the BOSCHE digital weighing indicator by the corresponding voltage signal displayed in the data acquisition software on the PC.

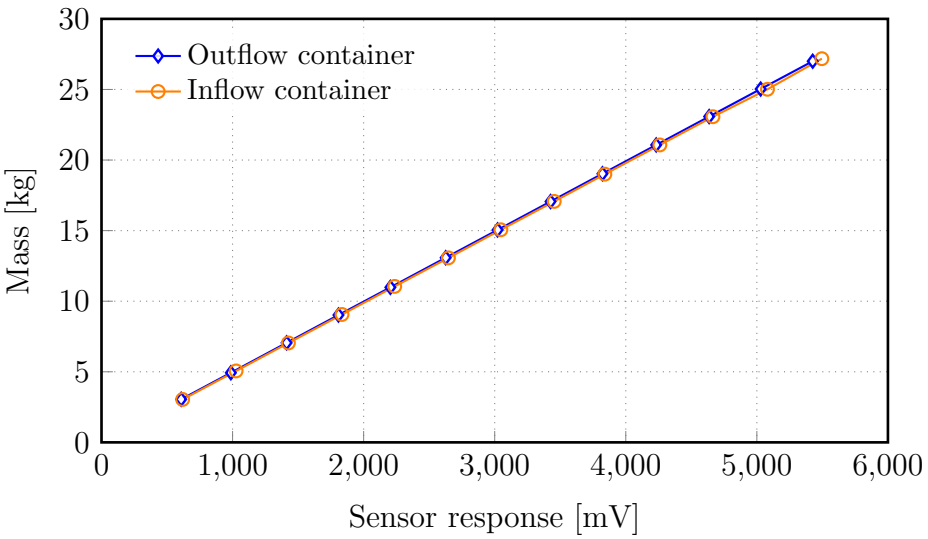

Figure 3.11: Calibration of the load cells of the inflow and outflow containers.

3.3.4 Development of sampling methods

One objective of the present work was to investigate samples obtained from the infiltration column after bentonite infiltration in triaxial tests. In addition, microstructural investigations were performed on column-derived samples at various infiltration stages.

As illustrated in Fig. 3.8, dedicated sampling moulds (a–c) were embedded within the sand body at predefined locations. Based on this configuration, specific extraction procedures were developed to recover infiltration-conditioned specimens while preserving their

internal structure and spatial position within the column. These methods were designed to maintain specimen integrity and ensure compatibility with the subsequent mechanical and microstructural analyses. The detailed procedures are described in the following subsections.

3.3.4.1 Sampling for microstructural investigations

Microstructural analyses were conducted on samples extracted from the infiltration column after bentonite infiltration and on filter cake specimens prepared in the filter press test. A primary challenge was to recover infiltration-conditioned specimens without disturbing the internal fabric formed during slurry penetration and retention.

Initial attempts using manual cutting with fine scalpels or paper moulds frequently resulted in local disturbance and loss of structural integrity. After multiple trials, 3D-printed cubic split moulds were identified as the most effective solution for producing intact samples for microstructural testing.

The overall principle consisted of embedding the split moulds within the sand body prior to the infiltration process or within the filter press device prior to filter cake formation. After completion of the column test or the filter press test, the moulds were dismantled together with the enclosed soil or filter cake, thereby preserving the infiltration-induced structure at the respective location.

The mould dimensions ($4 \times 8 \times 12$ mm) were selected to meet the requirements of Broad Ion Beam Scanning Electron Microscopy (BIB-SEM). Following extraction, the specimens were subjected to freeze-drying and subsequent preparation for cryogenic BIB–SEM analysis.

Figure 3.12a shows the 3D-printed split moulds used for obtaining filter cake samples, while Fig. 3.12b illustrates their embedded placement within the sand body of the infiltration column for extracting infiltration-conditioned sand specimens.

3.3.4.2 Sampling of bentonite slurry from column tests

For measuring local and depth-dependent bentonite concentration and rheological properties, slurry samples were collected from defined locations within the infiltration column. For this purpose, perforated cylindrical metal containers were embedded at selected positions within the sand body.

(a) (b)



Figure 3.12: 3D-printed split moulds for obtaining filter cake samples (a) and their embedded placement within the sand body of the infiltration column for extracting infiltration-conditioned sand specimens (b).

The cylinders had external dimensions of 60 mm in diameter and 22 mm in height, with internal dimensions of 54 mm in diameter and 19 mm in height, corresponding to a sample volume of approximately 43.5 cm^3. Each cylinder consisted of a screw-connected base and lid. A 10 mm opening at the top allowed slurry extraction using a pipette. Figure 3.13a shows an open cylinder.

To prevent sand particles from entering the container during testing, glass fiber layers were fitted to the lid, base, and cylindrical body to cover the perforations. The prepared and sealed cylinders are shown in Fig. 3.13b.

(a) (b)



Figure 3.13: Perforated cylinder for slurry sampling inside the infiltration column: open cylinder (a) and prepared cylinders sealed for testing (b).

3.3.4.3 Portable triaxial sampling mould

A plastic split mould was developed to extract infiltration-conditioned specimens from the infiltration column for subsequent monotonic and cyclic triaxial testing. The mould was used in combination with a portable vacuum pump to stabilise the specimen during extraction and transfer. The vacuum acted in the annular space between the latex membrane and the mould, thereby preventing disturbance of the specimen.

The mould has an inner diameter of 5 cm and a height of 10 cm, corresponding to the standard dimensions of triaxial specimens. It consists of two split mould parts that are screwed together to form a cylindrical body for sample containment during handling and transport. The mould is shown in Fig. 3.17f–g.

3.3.5 Preparation and assembly of infiltration column test

3.3.5.1 Filter materials and design

Gravel materials were used exclusively as filter layers within the infiltration column to prevent sand loss and to ensure uniform flow conditions. These materials are not part of the investigated soil matrix but form a structural component of the column setup. Photographs of the filter materials are shown in Fig. 3.14.

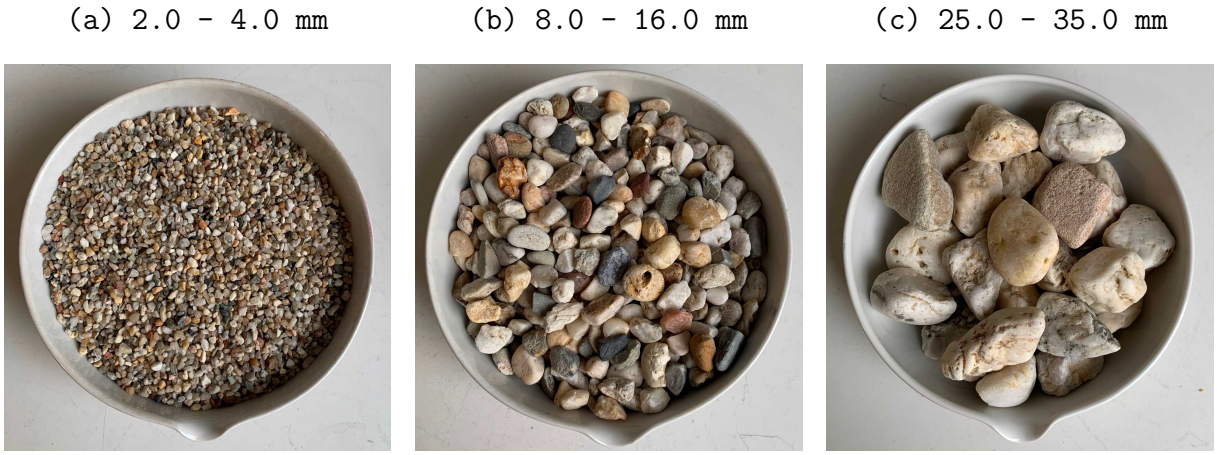

Figure 3.14: Gravel materials used as filter layers in the infiltration column

Table 3.2 summarises the granular characteristics of the filter layers and the tested sands, including the particle diameters corresponding to 15%, 50%, and 85% passing (d_{15}, d_{50}, and d_{85}), as well as the coefficients of uniformity (C_u) and curvature (C_c).

Table 3.2: Granular characteristics of the tested sands and filter layers used in the column infiltration tests

Material	d_{15} (mm)	d_{50} (mm)	d_{85} (mm)	C_u (−)	C_c (−)
Tested sands					
S 0.1–0.5	0.21	0.33	0.46	1.76	1.01
S 0.5–1.0	0.55	0.75	0.96	1.47	0.97
S 1.0–2.0	1.16	1.50	1.86	1.30	1.04
Filter layers					
F 2.0–4.0	2.17	3.00	3.71	1.47	0.97
F 8.0–16.0	10.0	13.45	15.65	1.42	0.96
F 25.0–35.0	25.5	30.0	34.0	1.22	0.98

Based on these materials, a graded filter system was designed for the infiltration column to ensure both hydraulic compatibility and mechanical stability of the sand specimen.

An effective filter was required to ensure a uniform distribution of the bentonite slurry and to provide a stable support for the sand specimen. The filter system was installed above the perforated metal base plate of the column device. The base plate contains perforations with a diameter of 20 mm and serves as mechanical support for the filter layers. A water-permeable geotextile, subsequently referred to as the filter mat, was placed directly above the perforated base plate to retain the overlying granular filter material while allowing fluid flow through the base.

The filter design followed the classical Terzaghi criteria for soil retention and permeability, as reviewed by Fannin (2008). These criteria can be expressed as

$$4D_{85b} > D_{15f} > 4D_{15b} \tag{3.2}$$

with

D_{85b} : Grain diameter of the base soil at which 85% of the particles (by weight) are finer.

D_{15b} : Grain diameter of the base soil at which 15% of the particles (by weight) are finer.

D_{15f} : Grain diameter of the filter material at which 15% of the particles (by weight) are finer.

To provide a gradual transition between the perforated base plate and the main sand layer, a series of granular filter layers was introduced. For the medium and coarse sands (S 0.5–1.0 mm and S 1.0–2.0 mm), three filter layers were sufficient. For the finer sand (S 0.1–0.5 mm), an additional intermediate layer was required above the F 2.0–4.0 mm filter layer. In this case, sand S 1.0–2.0 mm was used as a fourth transition layer to ensure a proper gradation between the filter layers and the base sand.

A schematic representation of the two filter configurations used in the column infiltration tests is shown in Fig. 3.15.

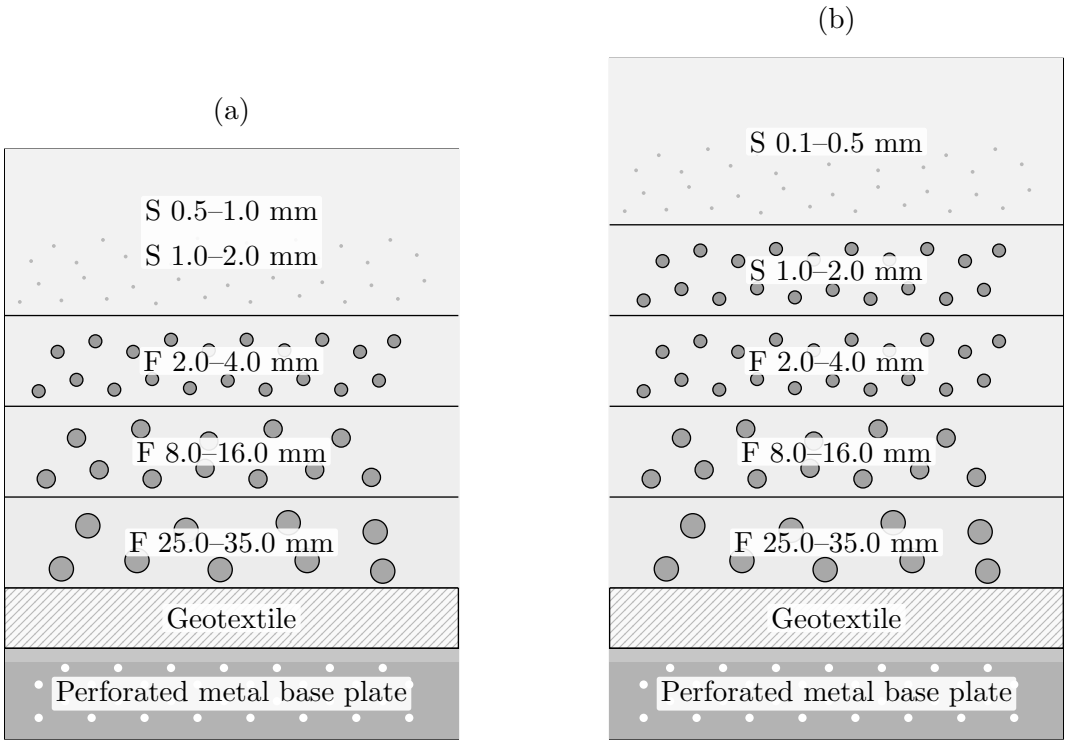

Figure 3.15: Schematic vertical cross-sections of the filter configurations used in the column infiltration tests: (a) configuration used for sands S 0.5–1.0 mm and S 1.0–2.0 mm; (b) configuration used for sand S 0.1–0.5 mm.

This layered filtering system ensured both mechanical stability and hydraulic compatibility between the base plate and the sand specimen. In addition, the graded filter structure enabled a uniform distribution of the bentonite slurry over the cross-section while maintaining adequate drainage conditions during the infiltration tests.

3.3.5.2 Sensor configuration and test preparation considerations

As described in Section 3.3.2, the infiltration column was equipped with 16 pore water pressure (PWP) sensors distributed over 24 available slots. The sensor placement followed the considerations outlined below:

- Sensor (S_1) was connected to the bottom slot to monitor the applied injection pressure.
- Sensor (S_2) was installed within the filter layer to verify that no filtration of bentonite particles occurred within the filter stack.
- Sensor (S_3) was positioned at the interface between the filter layer and the sand layer to detect potential external filter-cake formation.
- The minimum vertical spacing between any two sensors was maintained at 2 cm, in accordance with the spatial resolution limits of the sensors.
- In each test, two sensors (S_6 and S_7) were installed at identical elevations to verify the assumption of one-dimensional flow conditions.

The schematic configuration of the sensors, including their identifiers and corresponding slot positions, is illustrated in Fig. 3.16.

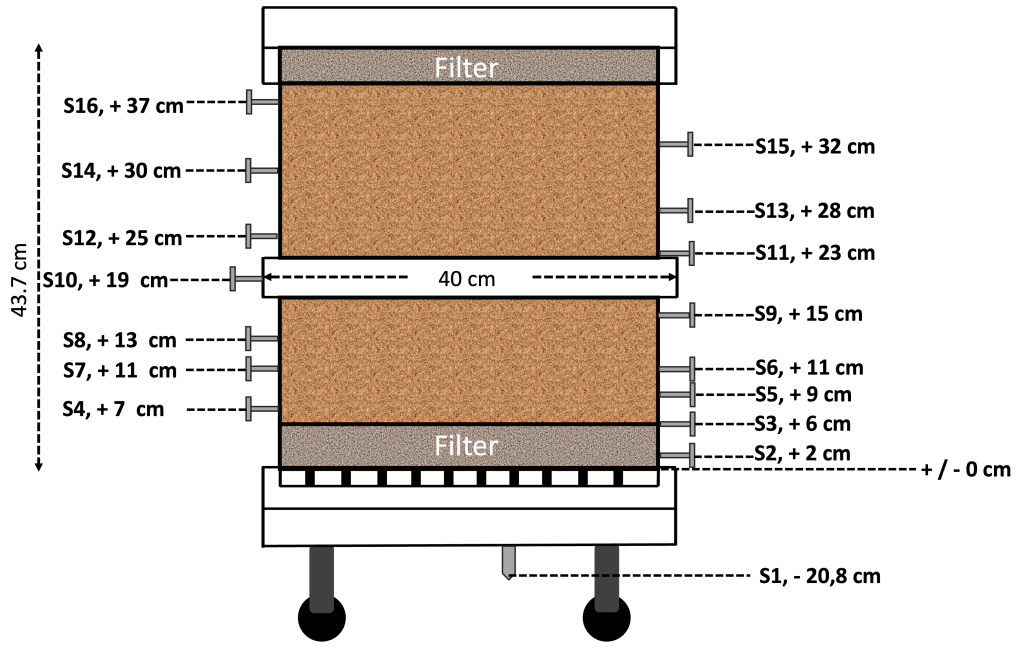

Figure 3.16: Schematic configuration of pore water pressure sensors and slot positions in the infiltration column device.

3.3.5.3 Column setup

Figure 3.17 shows the sequence of steps required for column test sample installation. Firstly, all pore pressure ports in the column, as visible for example in Fig. 3.17d and Fig. 3.17l, are covered with small squares of water-permeable glass fiber secured with tape. This prevents sand intrusion while maintaining hydraulic contact between the pore water and the pressure sensors. The ports at the column base are sealed in the same manner. Plastic rulers are attached vertically to the inner wall of the column at three circumferential positions using adhesive and reinforced with tape to facilitate layer height measurements. A filter grid and the geotextile filter mat are placed at the bottom of the column to prevent the filter material from falling and obstructing the slurry inflow path.

The setup begins with the placement of the bottom filter material, and its height is recorded in a protocol. The first layer consists of coarse gravel (25–35 mm), followed by medium gravel (8–16 mm) and fine gravel (2–4 mm) (Fig. 3.17a–d). Subsequently, the sand layer is placed using a dry-pluviation method with a dropping height between 10 and 35 mm, adjusted according to sand grain size and target density to achieve a uniform density distribution over the specimen height.

At predefined heights, the respective sampling moulds are installed. The first perforated mould is positioned 2 cm above the upper fine gravel layer (2–4 mm), within the lower 2 cm of the host sand. It is placed near the outer circumference at a horizontal distance of approximately 2-3 cm from the plexiglass column wall to reduce boundary effects (Fig. 3.17e). The vertical position of the mould is recorded. Sand is subsequently added until the perforated mould is fully covered (approximately 2.2 cm). The filling process continues until the target elevation for the portable triaxial split mould is reached. The split mould is centred and connected to a vacuum pump, which applies suction in the annular space between the latex membrane and the inner mould surface to stabilise the specimen. The portion of the latex membrane folded over the upper rim of the split mould is covered with protective masking tape to prevent damage and contamination during column filling and subsequent excavation. The vertical position of the split mould is then recorded (Fig. 3.17f–g).

Sand pluviation continues both outside and inside the split mould to embed it within the surrounding sand matrix. This procedure is repeated until the column is filled to approximately 39 cm (Fig. 3.17h–i). Subsequently, the upper filter layers are installed, starting with fine gravel (2–4 mm), followed by medium gravel (8–16 mm), and finally coarse gravel (25–35 mm) (Fig. 3.17j–k). During placement of the coarse gravel, the

portable mould is disconnected from the vacuum pump, and the hose is positioned between the gravel particles. At this stage, the surrounding sand is assumed to provide sufficient lateral support to keep the latex membrane in place after the vacuum line is disconnected.

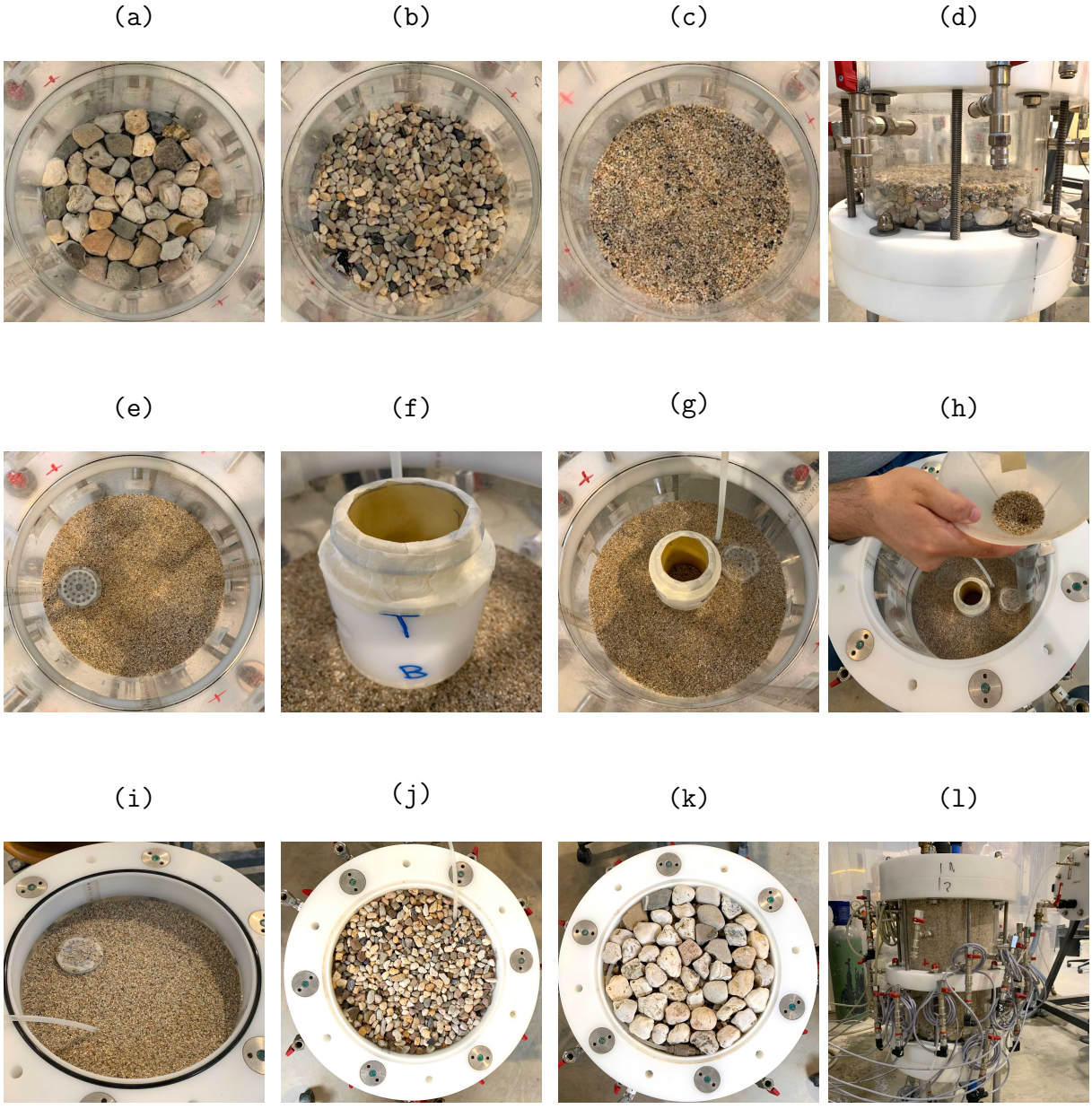

Figure 3.17: Infiltration column sample preparation

Before sealing the column, the rim is cleaned and a rubber O-ring is inserted. The column lid is then positioned and secured with screws. For the subsequent water-saturation and permeability stages, both the inflow and outflow containers are filled with water; bentonite slurry is introduced into the inflow container only after the permeability test. The water

used for saturation is vacuum-treated to remove entrapped air. The pore water pressure sensors are connected to their respective ports (Fig. 3.17l). Connecting hoses are installed between the column and the containers, with the inflow container connected to the lower port and the outflow container to the upper port of the infiltration column (see Fig. 3.18). Finally, the sand specimen is flushed with CO_2 prior to water saturation.

During sample preparation, the mass of sand installed and the number of embedded perforated moulds are recorded. Using the measured sand mass and the corresponding specimen volume, and accounting for the volumes of the installed moulds (triaxial and perforated), the resulting bulk density of the prepared sand specimen can be determined.

This method provides a systematic and reproducible preparation procedure for infiltration experiments and subsequent testing of the specimens in the post-infiltration state.

3.3.5.4 CO_2 flowthrough

Prior to water saturation, a CO_2 flowthrough is performed to facilitate subsequent water saturation of the sand specimen. During this procedure, all pore pressure ports are closed to prevent preferential gas escape and to ensure vertical flow through the entire specimen. Valve V1 at the free end of the hose connected to the column lid is kept slightly open to allow displaced air to exit.

Before initiating the flowthrough, the CO_2 flow rate is adjusted by submerging the outlet hose in water and observing the bubble formation. After setting the desired flow rate, the CO_2 hose is connected to the lower saturation port of the column, and the specimen is flushed from bottom to top for approximately 45–60 minutes.

3.3.5.5 Water saturation

After completion of the CO_2 flowthrough, the hose is disconnected and water saturation is initiated.

All pore pressure ports and the valves on the column lid are reopened. The water used for saturation has been vacuum-treated to remove entrapped air. Before starting the saturation process, the mass-per-voltage conversion factor of the water container is verified from the reference mass displayed on the BOSCHE digital weighing indicator and the corresponding mV signal displayed in the data acquisition software on the PC.

The data acquisition system is set to a recording interval of 10 s and activated. The water-filled inflow container is connected to the lower saturation port of the soil column.

During saturation, the hose attached to V1 is also connected to the water container. The inflow rate is adjusted via valve V7 (Fig. 3.18) to maintain a slow saturation rate of approximately 2–4 $\mathrm{mL\,s^{-1}}$. As water reaches the pore pressure ports, the respective valves are gradually closed. Once water reaches the hose attached to V1 and valve V3 on the column lid (Fig. 3.18), V1 and V3 are closed, marking completion of the saturation phase. The recording is stopped and the data are saved.

After saturation, the conversion factor of the water container is rechecked and documented. The entire process requires approximately 2.5–3 hours.

3.3.5.6 Permeability test procedure

Prior to bentonite slurry infiltration, the permeability of the fully water-saturated sand specimen is determined using water only. Before the permeability test, the inflow container is filled with 26 kg of water, whereas the outflow container is adjusted to 5 kg. A fluid mass of 5 kg is the minimum permissible level in either container because a lower mass would allow air to enter the hydraulic system. Starting the outflow container at this minimum level also provides sufficient capacity for collecting the transferred water. The pressure hoses are connected to the inflow and outflow containers. For the test configuration, valves V1–V5 remain closed, while valves V6, V7, and V8 are opened (see Fig. 3.18). The connecting hose between the soil column and the inflow container is filled with water before the test; no bentonite slurry is present in the inflow path at this stage.

Before the test, the conversion factor of each container is verified from the BOSCHE digital weighing indicator and the corresponding PC voltage reading. The data acquisition interval is set to 250 ms. A pressure of 30 kPa is applied to the inflow container and 20 kPa to the outflow container, resulting in a constant pressure difference of 10 kPa. The lower valve (V4), connecting the inflow container to the column, is gradually opened, followed by opening of valve V2 to stabilise the applied pressures.

The permeability test is terminated when the water mass in the inflow container decreases to the minimum permissible value of 5 kg. Thus, the fluid transferred during this test is water rather than bentonite slurry. Valve V2 is closed first, followed by V4. The applied pressures are released and data recording is stopped. The remaining water is then removed from the inflow container, and the water collected in the outflow container is removed until its mass again reaches 5 kg.

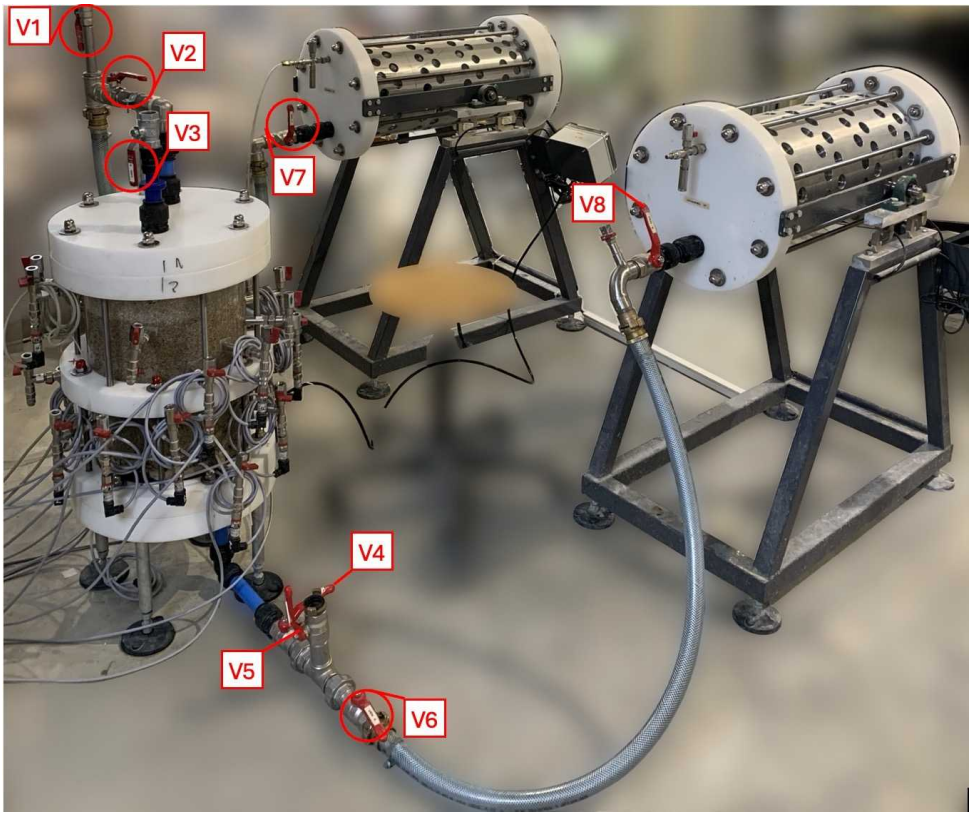

Figure 3.18: Column experiment setup with valve configuration

3.3.5.7 Infiltration test procedure

For each infiltration test, approximately 25 L of bentonite slurry is prepared in advance and allowed to hydrate for 16–18 hours prior to use.

After completion of the permeability test and removal of the remaining inflow water, the pre-hydrated slurry is transferred to the inflow container. A vacuum is applied to remove entrapped air, and the water remaining in the connecting hose to the soil column is replaced by slurry before infiltration begins. Valves V1–V5 remain closed, while valves V6, V7, and V8 are opened, following the same configuration as in the permeability test (see Fig. 3.18). The mass-per-voltage conversion factor for each container is then reverified by dividing the reference mass displayed on the BOSCHE digital weighing indicator by the corresponding mV signal displayed in the data acquisition software on the PC, and the data acquisition interval is set to 250 ms.

For a net injection pressure of 50 kPa, the inflow container is pressurised to 90 kPa and the outflow container to 40 kPa. For higher net injection pressures (e.g., 100 or 200 kPa),

the outflow container pressure remains at 40 kPa, while the inflow container pressure is increased to 140 or 240 kPa, respectively.

The test is initiated by gradually opening the lower valve (V4), followed by opening of valve V2 to stabilise the pressure difference between inflow and outflow containers at the prescribed values.

The infiltration phase typically lasts approximately 45 minutes and is terminated by first closing valve V2 and subsequently valve V4. Data recording is then stopped and the conversion factors of both containers are rechecked.

For coarser sands (e.g., S 1.0–2.0 mm) or lower slurry concentrations (e.g., B20 or B40), the test duration may be reduced, as the inflow container empties more rapidly under these conditions. The test is therefore monitored and terminated earlier when required to prevent air entry into the system.

3.3.6 Dismantling of the column test and sample extraction

3.3.6.1 Dismantling of the soil column

The hoses and pore water pressure sensors were disconnected from the column. The column lid was removed, and the hose connected to the triaxial split mould was attached to a vacuum pump to maintain firm contact between the latex membrane and the inner surface of the split mould during the excavation process. The upper filter layers were carefully removed and placed in a tray for washing and reuse. The bentonite-infiltrated sand was then excavated in a controlled manner until the top edge of the first perforated mould became visible.

3.3.6.2 Post-infiltration sampling for bentonite slurry testing

Depending on the infiltration behaviour and sample consistency, two extraction methods were applied. Fluid-like samples, such as water or diluted slurry, were extracted using a pipette (Fig. 3.19a,b). At higher bentonite concentrations, where the consistency becomes too firm for pipette extraction, the perforated mould was removed from the column, the four securing screws were loosened, and the sample was extracted using a spoon (Fig. 3.19c,d).

After extraction, the samples were transferred into glass or plastic bottles (Fig. 3.19e) and subsequently used for determining rheological properties and bentonite concentration. For

concentration determination, each recovered slurry sample was weighed in its wet state and again after oven-drying to constant mass. The dry residue provided the bentonite mass, while the difference between the wet and dry masses provided the water mass; the resulting dry-bentonite-to-water ratio was expressed in g/L using the density of water.

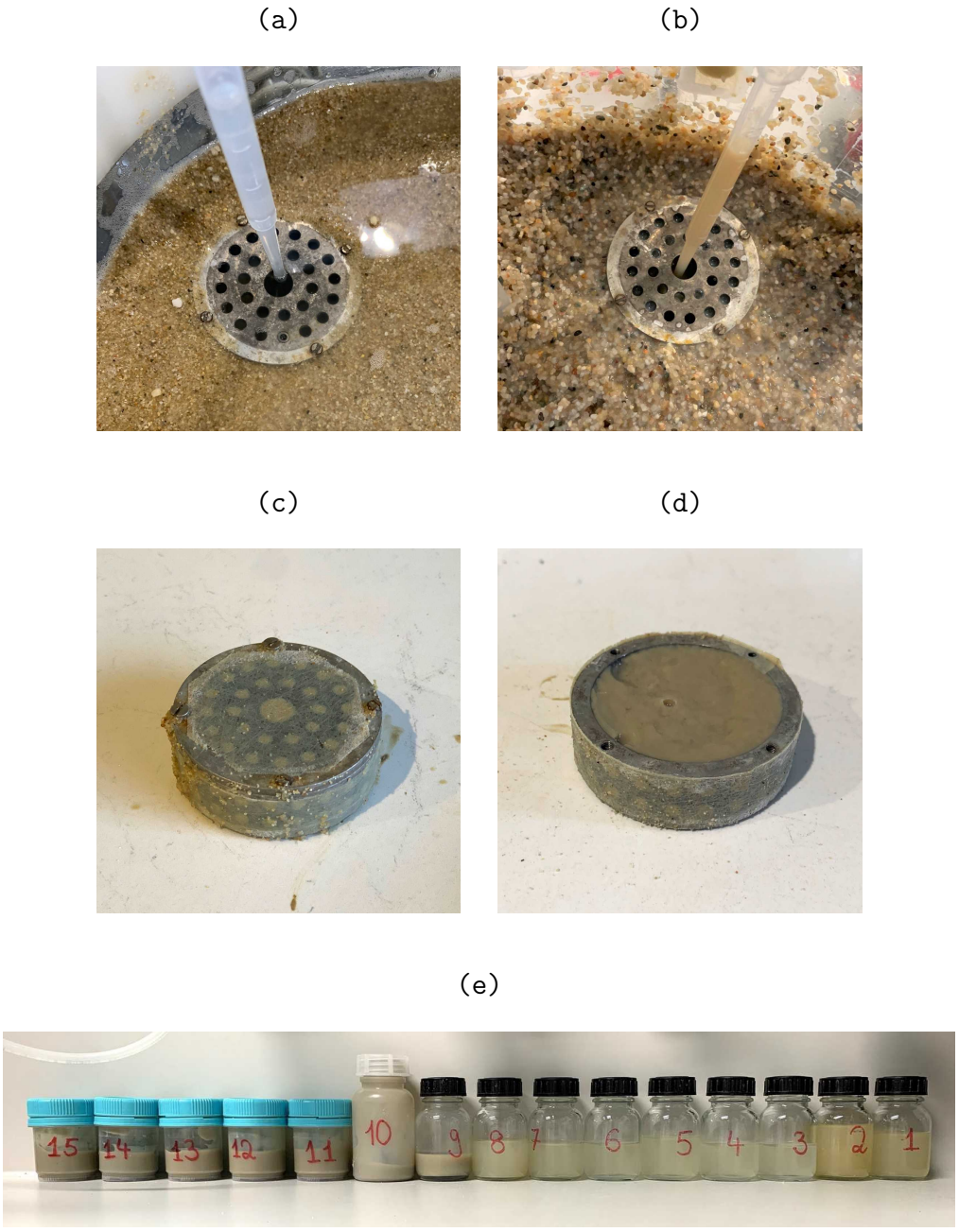

Figure 3.19: Slurry sampling and storage: pipette-based sampling (a,b), sampling by opening the perforated cylinder (c,d), and collected samples prepared for rheological testing and bentonite concentration determination (e).

3.3.6.3 Post-infiltration sampling for triaxial test

As sand excavation proceeds from top to bottom, the perforated moulds are removed sequentially to collect slurry samples from different elevations. Once the embedded triaxial split mould becomes visible, the surrounding sand is carefully removed until the bottom edge of the split mould is exposed (Fig. 3.20a). The split mould containing the infiltrated sand specimen is then separated from the column by inserting a thin metal plate with sharpened edges beneath the mould (Fig. 3.20b). The plate, together with the mould and enclosed specimen, is gently lifted and placed on a stable surface.

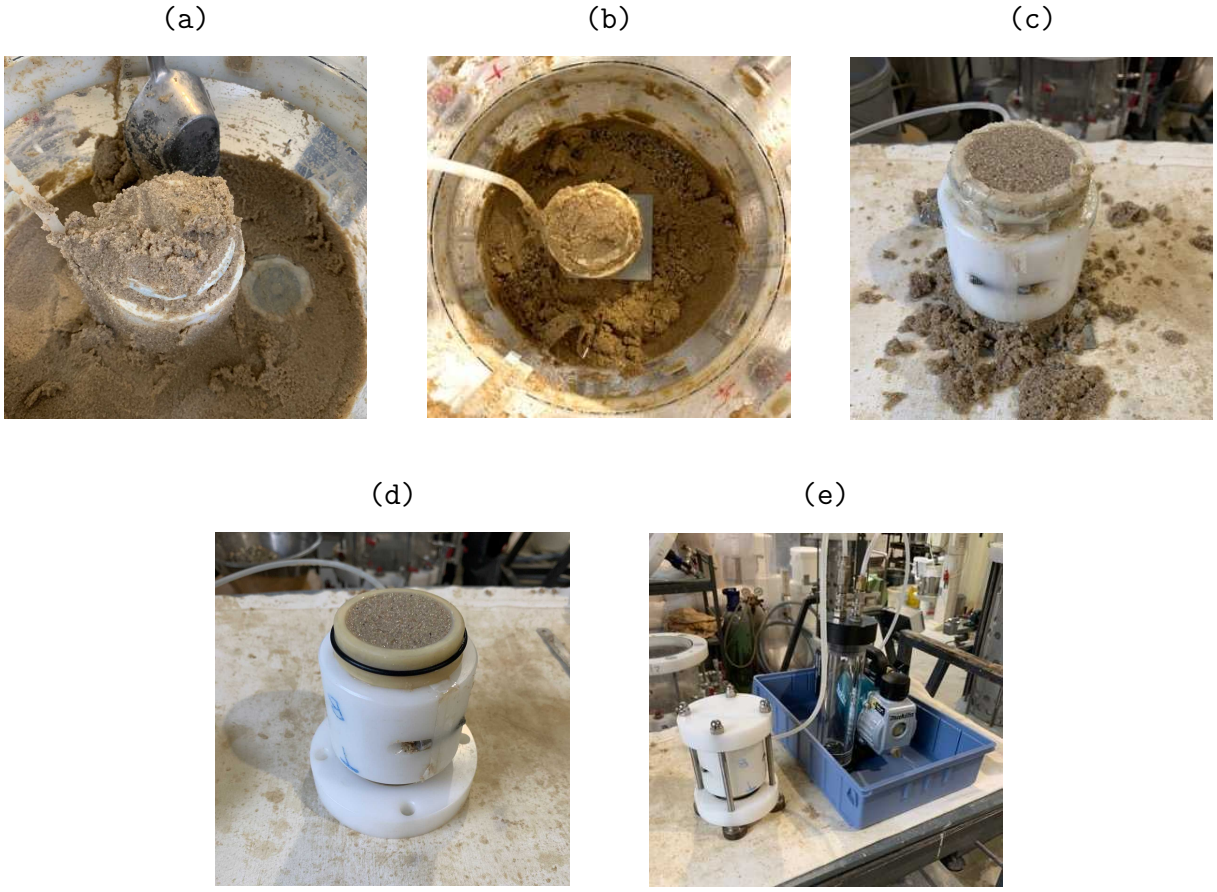

Figure 3.20: Post-infiltration sampling procedure for triaxial testing: excavation of the embedded mould (a–c), specimen preparation and capping (d), and sealed, vacuum-stabilised specimen prepared for transport (e)

Excess sand above the mould is levelled using a ruler (Fig. 3.20c) to obtain a smooth surface, and residual particles along the exterior are removed with a brush. The protective masking tape covering the latex membrane is carefully removed. After preparation of the upper surface, a cap is installed and the specimen is inverted. The bottom surface is

cleaned and levelled, followed by installation of a second cap (Fig. 3.20d). The specimen is then secured by fastening the caps together (Fig. 3.20e). Finally, the vacuum line is transferred to a portable vacuum system to maintain specimen stabilisation during transport and subsequent installation in the triaxial apparatus.

3.4 Triaxial test devices

The triaxial experiments were performed using two testing systems for monotonic and cyclic loading conditions. The devices and their calibration procedures are described below.

3.4.1 Monotonic triaxial device (Wykeham Farrance)

The triaxial testing apparatus is a widely used geotechnical laboratory tool for evaluating the intermediate- and large-strain behaviour of geomaterials. The apparatus used for the monotonic tests in this study is shown in Fig. 3.21. The overall test setup was originally presented by Wichtmann (2005). The strain-controlled loading machine was manufactured by Wykeham Farrance Engineering Ltd. (England).

The cylindrical specimens had a diameter of 5 cm and a height of 10 cm. Axial loading was applied by displacement-controlled upward movement of the base plate towards the top piston fixed to the loading machine. The displacement rate, set to 0.05 mm/min in this study, could be adjusted by repositioning the loading gears. This axial deformation rate ensured a uniform development of pore-water pressure within the specimen during undrained shearing. For drained shearing, it allowed drainage to occur throughout the test. Axial deformation was measured using a linear variable differential transformer (LVDT) mounted on the load piston.

Specimen volume changes were monitored using a connected burette system, where variations in the burette water level correspond to volume changes in the specimen. A differential pressure transducer measured these water-level changes by comparing the pressure in the measuring burette with that in a reference burette maintained at a constant water level.

The device was equipped with a 14 bar cell pressure transducer and a 7 bar back pressure transducer installed at the outlets of the pressure cell and the drainage system, respectively. The axial force was measured with a 5 kN load cell located inside the pressure

cell below the specimen base. Data from all sensors were recorded continuously using HP-VEE software on a PC, allowing continuous monitoring and analysis throughout the test.



Figure 3.21: Triaxial device used for the monotonic triaxial experiments

3.4.2 Cyclic triaxial device (Wille Geotechnik)

The undrained cyclic triaxial tests were carried out using an electromechanically driven load press manufactured by *Wille Geotechnik GmbH*, Germany. A triaxial cell similar to that used in the monotonic tests was employed. The cyclic loading followed a triangular pattern, with the loading direction reversed after the prescribed maximum or minimum deviatoric stress amplitude was reached (Fig. 3.23). Vertical displacement was determined

from the movement of the loading piston. Geosys software was used for data acquisition and general control of the triaxial device, including movement of the loading piston and measurement of vertical deformation. A burette system similar to that used in the monotonic tests was employed for applying back pressure and measuring volume changes during consolidation; no volume-change measurements were performed during undrained cyclic loading. The cyclic triaxial device is shown in Fig. 3.22.



Figure 3.22: Cyclic triaxial device used for the undrained cyclic tests

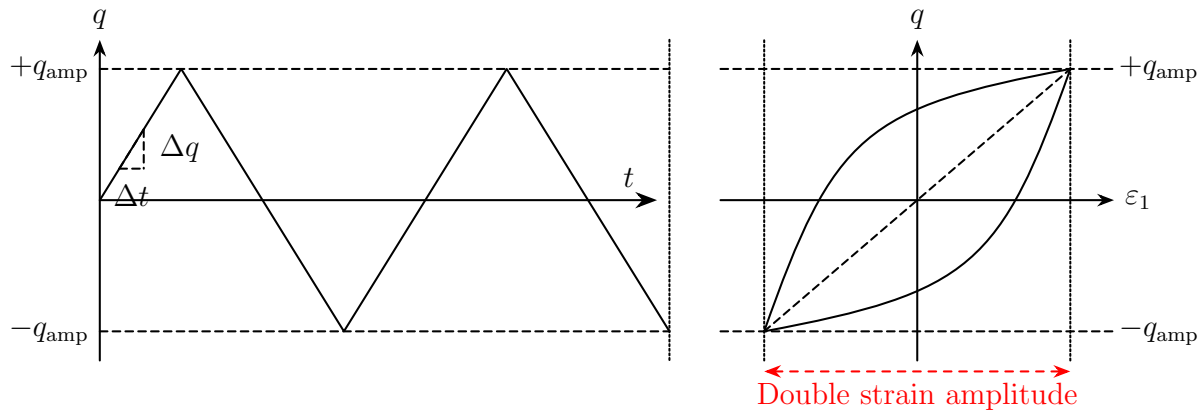

Figure 3.23: Triangular deviatoric loading against time t used for the cyclic tests (left) and the resulting relationship between deviatoric stress q and axial strain ε_1 (right).

3.4.3 System compliance and boundary effects

Prior to testing, the compliance of the triaxial system was evaluated using a steel dummy specimen with a diameter of 5 cm and a height of 10 cm in order to quantify system deformation associated with the loading frame and measurement devices.

A membrane thickness of 0.7 mm was used for all monotonic and cyclic triaxial tests conducted in this study. The potential influence of membrane penetration and membrane resistance was evaluated and found to be negligible due to their small magnitude. End-bearing friction was minimised by using rigid stainless steel platens equipped with a small central porous stone (10 mm in diameter), which reduces restraint at the specimen ends and limits the influence of boundary friction on the measured response (Tatsuoka et al. 1986b; Omar and Sadrekarimi 2014).

3.5 Triaxial test procedure and sample preparation

3.5.1 Installation of samples by air pluviation method

Figure 3.24 shows the sequence of sample installation in the triaxial device. The procedure begins with the application of a thin grease layer to the base plate, followed by placement of a rubber disk, to reduce friction between the specimen and the plate. The base plate is inserted into the triaxial device and the drainage hoses are connected. The membrane is pulled over the base plate and sealed with two O-rings (Fig. 3.24a,b), and the split

mould consisting of two aluminium parts is assembled around it (Fig. 3.24c). The excess membrane is pulled over the upper rim of the split mould, and a vacuum is applied to draw the membrane against the inner surface of the split mould (Fig. 3.24d,e). A three-component raining guard is then installed to minimise sand loss and control specimen density (Fig. 3.24f).

Prior to filling, the sand and its container are weighed. After deposition, the container is weighed again to determine the mass of sand placed in the mould. The mass and specimen dimensions are recorded for subsequent determination of relative density. The funnel has interchangeable openings; although additional sizes are available, only openings of 4, 6, and 10 mm are used in this study, depending on grain size. For specimens prepared at a prescribed drop height, the funnel is moved horizontally across the specimen cross-section while maintaining a constant vertical distance from the growing sand surface, thereby keeping the surface level throughout deposition. For preparation of the loosest state, the funnel is raised vertically without maintaining a prescribed drop height (Fig. 3.24g).

After filling, the surface is levelled with a straightedge and excess sand is removed. The raining guard is removed and the collected surplus sand is returned to the container for re-weighing.

Subsequently, the top plate is installed and the drainage hoses are connected (Fig. 3.24h). The membrane is pulled over the top plate and sealed with two O-rings (Fig. 3.24i). A vacuum of approximately -40 kPa is applied to stabilise the specimen. After disassembly of the split mould, the membrane and drainage system are checked for leakage (Fig. 3.24j,k). Leakage is assessed by sequentially closing the drainage paths and observing the vacuum stability; a pressure drop indicates membrane or connection leakage.

Once membrane integrity is confirmed, the specimen dimensions are measured. The diameter is determined from five measurements at different heights, repeated at two additional orientations, resulting in 15 diameter values. The specimen height is obtained from the measured distance between the top of the load piston and the top surface of the triaxial cell, along with a corresponding measurement on a dummy with known height. Finally, the triaxial cell is assembled, secured with tie rods, and positioned beneath the loading piston of the load press (Fig. 3.24l), completing the preparation for testing.

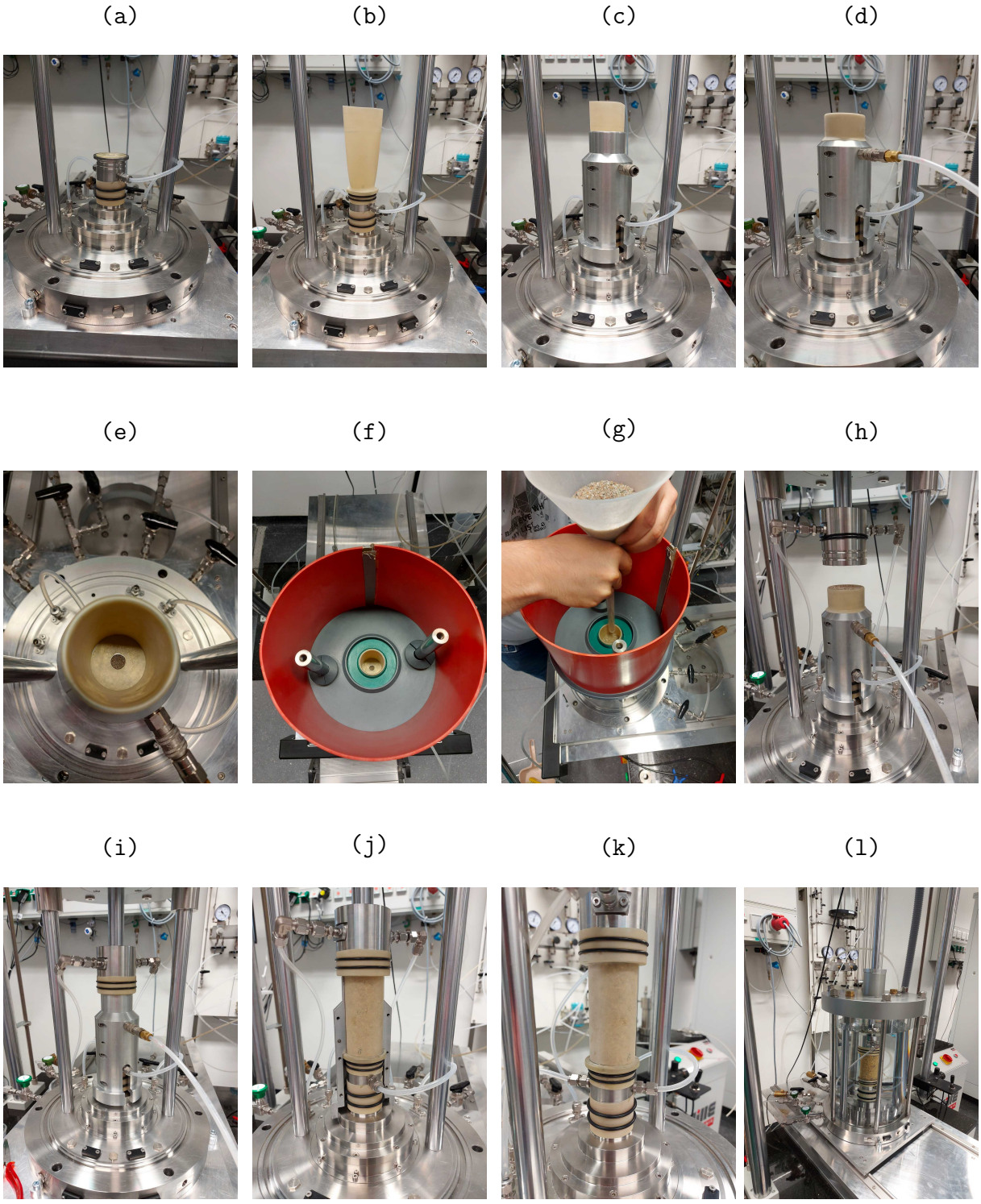

Figure 3.24: Air pluviation method for preparation of a clean sand sample in the triaxial device

3.5.2 Installation of remoulded sand-slurry mixture samples

The initial installation steps up to mounting the membrane and mould onto the base plate are identical to those described for the sand specimens prepared using the air pluviation method (Fig. 3.24a,b). A pre-mixed combination of sand and bentonite slurry was used. To ensure uniformity, the mixture was divided into three portions and placed layer by layer into the mould. Each layer was compacted to target heights of 3.33 cm, 6.66 cm, and 9.99 cm, resulting in a cylindrical specimen approximately 10 cm high (Fig. 3.25c,d).

After filling the mould, installation generally followed the procedure for the air-pluviated specimens. The top plate was installed and the membrane was folded over and sealed with O-rings (Fig. 3.25e,f). A vacuum of approximately −40 kPa stabilised the specimen during mould removal (Fig. 3.25g–h). Membrane integrity was checked and the specimen dimensions required for density determination were measured as described above. Finally, the triaxial cell was assembled, secured with tie rods, and positioned beneath the loading piston of the load press.

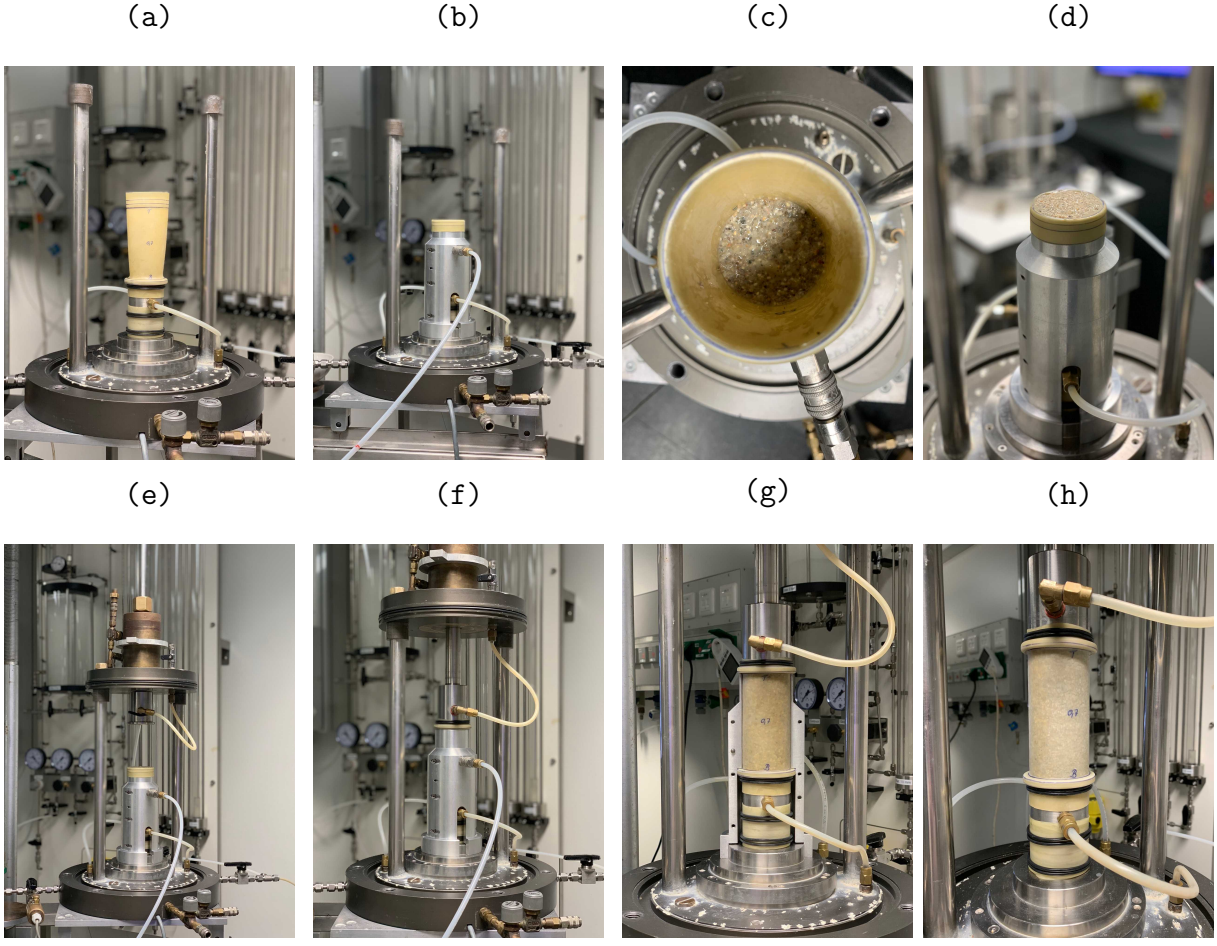

Figure 3.25: Installation of remoulded sand-slurry mixture samples in the triaxial device

3.5.3 Installation of slurry-infiltrated column samples

The slurry-infiltrated specimen, extracted and vacuum-stabilised as described in Section 3.3.6.3 (Fig. 3.26a), was subsequently prepared for installation in the triaxial device. The installation generally followed the same sequence as for air-pluviated specimens and remoulded sand-slurry mixture specimens, with adjustments specific to the slurry-infiltrated specimen. After one end of the specimen was exposed while it remained confined in the split mould (Fig. 3.26b), the lower platen was placed against the specimen (Fig. 3.26c), and the latex membrane was pulled over this platen and sealed with two O-rings (Fig. 3.26d).

The volume-change measurement system was prepared by connecting the back pressure (BP) line and initiating the monitoring software. The assembly of the specimen, mould, and lower platen was then rotated and positioned in the triaxial device (Fig. 3.26e). The drainage lines were connected; the upper platen was installed and the membrane was sealed to it with two O-rings (Fig. 3.26f). A vacuum of approximately -40 kPa was applied through the volume-change measurement system to maintain specimen stability.

Following stabilisation, the split mould was removed (Fig. 3.26h). System tightness was verified by closing the drainage lines and monitoring the BP response. A stable BP value indicated intact membrane sealing and drainage connections, whereas pressure decay signalled leakage requiring correction.

The remaining assembly steps were common to air-pluviated specimens, remoulded sand-slurry mixture specimens, and slurry-infiltrated specimens. The specimen dimensions were measured, and the triaxial cell was assembled by installing the sealing ring, plexiglas cylinder, and lid, which were secured using tie rods (Fig. 3.26i). The cell was filled with water to approximately 5 cm below the top edge (Fig. 3.26j), and the cell pressure sensor was connected and saturated.

A cell pressure of 50 kPa was applied gradually by simultaneously reducing the specimen vacuum and increasing the cell pressure in 5 kPa increments to maintain constant effective stress. The triaxial cell was then aligned beneath the loading piston of the load press, after which saturation and consolidation procedures were initiated.

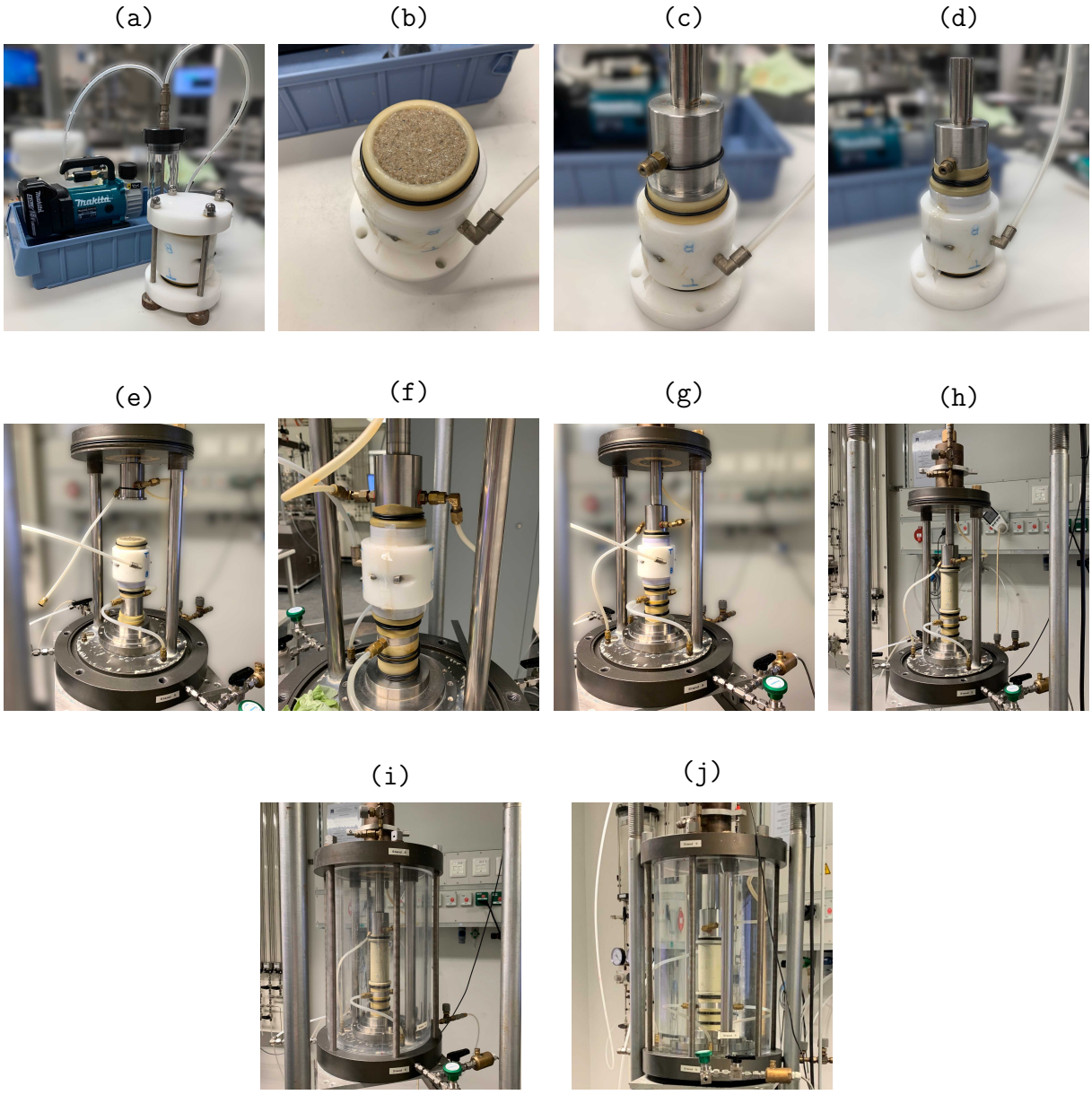

Figure 3.26: Installation of the bentonite-infiltrated sand samples in the triaxial device

3.5.4 Saturation procedure for clean, slurry-infiltrated, and remoulded sand-slurry mixture samples

Since slurry shield tunnelling occurs under saturated soil conditions and undrained triaxial tests require fully saturated specimens, a saturation stage was performed in all triaxial tests conducted in this study. The saturation procedure for clean sand differs from that applied to slurry-infiltrated sand or sand-slurry mixture specimens. Both procedures are described below.

3.5.4.1 Clean sand samples

The saturation procedure consisted of three stages: (1) removal of air in the pore space by flushing with carbon dioxide (CO_2), which is more soluble in water than air; (2) saturation by flushing with de-aired and de-ionized water over several hours (typically 3–4 hours); and (3) back pressure saturation, the longest stage, lasting approximately 10–12 hours, typically overnight.

CO_2 was supplied through a line connected to the central CO_2 gas cylinder in the geotechnical laboratory. The flow rate was controlled to approximately 1–2 bubbles per second, as verified by submerging the outlet hose in water. Under a constant cell pressure of 50 kPa, CO_2 was first circulated through both drainage lines in the bottom platen. After several minutes, one of the bottom drainage lines was closed and the top drainage line was opened, allowing CO_2 to flow upward through the specimen. This stage lasted approximately 1 hour to replace the air within the specimen pore space with CO_2.

The second stage consisted of saturation by flushing with de-aired and de-ionized water. The de-ionized water in a supply tank located at the triaxial device was first de-aired for approximately 1 hour using CO_2 and subsequently vacuum-treated. The prepared water was then circulated through the bottom platen by introducing it through one bottom drainage line and allowing it to leave through the other, which served as the outlet line. The water flow rate was maintained at approximately 1–2 drops per second throughout both circulation configurations. This initial circulation was continued for 10–15 minutes until no CO_2 bubbles were visible in the outlet line; during this period, water entered the pore space in the lower part of the specimen. The outlet line in the bottom platen was then closed and the top drainage line was opened, allowing the water to flow upward through the specimen at the same rate. This flushing stage lasted approximately 3 hours, during which approximately 2 litres of de-aired water flowed through the specimen.

In the final stage, the drainage lines were connected to the burettes of the volume-change measurement system. After the burettes were filled to the same water level as the water supply tank, the water inflow was stopped. Back pressure and cell pressure were then gradually increased to 200 kPa and 240 kPa, respectively. After approximately 10 minutes under these conditions, saturation was evaluated using Skempton's B-value test, which typically yielded B-values between 0.92 and 0.96. To avoid negative back pressure during shearing, a higher back pressure of 600 kPa was applied. Consequently, the back pressure and cell pressure were increased to 600 kPa and 640 kPa, respectively, and maintained overnight. After this period, the B-value was checked again.

In all tests, a B-value of at least 0.98 was reached, indicating sufficient saturation and allowing the consolidation phase to begin.

3.5.4.2 Slurry-infiltrated column samples and remoulded sand-slurry mixture samples

The slurry-infiltrated column specimens and the remoulded sand-slurry mixture specimens already exhibited a high degree of saturation after preparation. Additional flow of CO_2 or de-aired water through the specimens would have altered their state by washing out the slurry and thereby compromising specimen integrity. Therefore, only the top and bottom drainage lines were saturated separately using de-aired and de-ionized water.

To achieve this, an additional drainage line was installed in the top end plate, allowing the top drainage system to be saturated without inducing water flow through the specimen from the bottom drainage. During saturation of either the top or bottom drainage line, the opposite drainage line remained closed to prevent water flow through the specimen. After both drainage systems were saturated, the pre-filled burette system was connected to the drainage lines. Subsequently, the back pressure and cell pressure were increased following the same procedure described previously for the clean sand specimens.

3.5.5 Consolidation procedure

After obtaining an acceptable B-value, the specimens were isotropically consolidated under a target mean effective stress. To maintain isotropic stress during the increase in cell pressure, an additional vertical force was applied through the loading piston to compensate for the absence of cell pressure over the piston cross-sectional area. The additional correction force was applied manually for the monotonic tests performed with the Wykeham Farrance loading press, whereas it was automatically controlled by the Wille loading press during the cyclic triaxial tests. During this process, the drainage from both ends was opened to allow flow of pore water into the burette of the volume-change measurement system. Specimens were allowed to consolidate for 1 hour, while the vertical deformation and volume change were continuously monitored throughout this process. The process of consolidation was deemed complete once the specimen volume remained almost unchanged over a longer period of time. The volume and height changes during consolidation were recorded and the actual sample dimensions, void ratio and relative density corresponding to the end of consolidation and the start of the shearing phase were determined.

3.5.6 Shearing procedure

After completion of the consolidation stage, the shearing phase was initiated. Depending on the test type, specimens were subjected to either monotonic or cyclic loading under drained or undrained conditions. The tests were performed in strain-controlled mode by applying axial deformation through the loading piston while maintaining the prescribed cell pressure and back pressure conditions. For monotonic triaxial tests, axial deformation was applied at a constant displacement rate of 0.05 mm/min until the target strain level was reached or the specimen exhibited clear post-peak behaviour. Throughout monotonic shearing, axial force, axial deformation, cell pressure, and pore-water pressure were recorded continuously. During undrained shearing, the drainage lines were closed, whereas during drained shearing they remained open and specimen volume change was additionally measured throughout the test.

For cyclic triaxial tests, cyclic deviatoric loading was applied according to the predefined loading program, with the selected amplitude and frequency. All cyclic tests were conducted under undrained conditions. Each cyclic test was terminated when either the mean effective stress p' approached zero or the axial strain reached 10%, whichever occurred first. Throughout the cyclic shearing stage, axial force, axial deformation, cell pressure, and pore-water pressure were recorded continuously. These measurements were subsequently used to determine the stress–strain behaviour, pore-pressure response, and effective stress path of the specimens.

3.5.7 Post-testing procedure

After completing the testing phase (both monotonic and cyclic), the HP-VEE or Geosys program was terminated and the axial loading piston was disengaged from the loading frame. Both the top and bottom drainage lines were then opened before the cell pressure and back pressure were gradually reduced, thereby allowing the back pressure within the specimen to dissipate through the open drainage lines. The water within the plexiglas cylinder was subsequently released. The plexiglas cylinder was then removed, the top drainage line was disconnected, and the top cap of the triaxial cell together with the top platen was carefully taken off. The specimen was then gently extracted and collected in a container.

For slurry-infiltrated specimens or sand-slurry mixtures, the material was washed several times to separate the bentonite from the sand. The separated components were oven-dried at 105°C. The sand was dried for 24 hours, while the washed bentonite was dried

for several days depending on the remaining moisture content, in order to prepare both materials for potential reuse.

The measured dry sand mass was used to calculate the relative density and void ratio of the sand skeleton, from which the absolute pore volume in cm^3 or mL was obtained. The recovered dry bentonite mass was then compared with the amount expected from the moisture-corrected inlet concentration and the calculated pore volume as an approximate specimen-scale recovery check; this mass-per-pore-volume comparison was not treated as a direct measurement of the local post-test slurry concentration.

3.6 Rheometer device and measurement procedure

The rheological properties of the bentonite suspensions were determined using a Modular Compact Rheometer MCR 102e (Anton Paar GmbH, Austria) equipped with a coaxial cylinder measuring system (bob–cup geometry), as shown in Fig. 3.27. This geometry is suitable for suspension-type materials such as bentonite slurries, as the sample is contained between a rotating inner cylinder (bob) and a stationary outer cup, allowing reliable measurement of shear stress and viscosity.



Figure 3.27: Modular Compact Rheometer MCR 102e equipped with a coaxial cylinder (bob–cup) measuring system used for rheological measurements of the bentonite suspensions.

All measurements were performed at a constant temperature of 20 °C. The rheometer was operated in controlled shear-rate mode, with the shear rate ranging from 0.001 to 3000 s^{-1}. For each test, 100 data points were recorded across the applied shear-rate range. Before each test, the slurry sample was placed in the measuring cup, which was then installed in the rheometer. After completion of each measurement, the recorded data were stored for subsequent evaluation, and the measuring system was cleaned before preparing the next sample.

3.7 Broad Ion Beam Scanning Electron Microscopy (BIB-SEM) investigations

One part of this study focuses on the microstructural investigation of bentonite slurry, both in its initial state and after being subjected to applied pressure, resulting in filter cake formation or interaction with sand. The microstructural characterization was performed using the Cryo-BIB-SEM technology (Broad Ion Beam polishing combined with scanning electron microscopy under cryogenic conditions), which is recognised as an effective technique for imaging pore-fluid distributions in porous media (Schmatz et al., 2017). The method builds on the Cryo-BIB-SEM approach described by Desbois et al. (2013).

The investigations were carried out at MAP Microstructure and Pores GmbH, Aachen, using a Zeiss Supra 55 scanning electron microscope equipped with a Leica VCT100 cryo-transfer system (Fig. 3.28), enabling high-resolution imaging of cryogenically preserved sample cross-sections. Cryogenic conditions were maintained throughout the sample preparation and imaging stages to preserve the original microstructure. Sample cross-sections were prepared using Broad Ion Beam (BIB) milling with a Leica TIC3X system, which produces smooth, flat, and damage-free surfaces suitable for detailed microstructural analysis. Multiple detectors, including SE2 (secondary electrons), BSE (backscattered electrons), and EDS (energy dispersive spectroscopy), were used to obtain complementary structural and compositional information.



Figure 3.28: Cryo-BIB-SEM device used for microstructural investigation.

3.7.1 Sample types investigated

To investigate the microstructure of bentonite suspensions and their interaction with granular soil, eight representative specimens were analysed using the Cryo-BIB-SEM technique. The specimens were organised into four experimental categories (Sets A–D) to represent remoulded pure bentonite slurry, external filter cake, the sand-slurry interface, and internal infiltration within the sand skeleton.

(A) Remoulded pure bentonite slurry (S1, S2). Pure bentonite suspensions were investigated in their initial state to characterise the microstructure of the slurry prior to interaction with porous media. These samples provide a reference state for the particle arrangement and pore-fluid distribution of the bentonite suspension.

(B) External filter cake (S3.1, S3.2). Filter cake specimens were generated using a filter press device under controlled pressure conditions. These samples represent the consolidated bentonite structure that forms when slurry is subjected to filtration and pressure gradients during slurry shield tunnelling.

(C) Sand-slurry interface (S4, S5). These specimens were obtained at the infiltration front during tests conducted using the separate small-scale infiltration column described in Section 5.2; they capture the boundary structure formed where the slurry contacted the host sand.

(D) Internal infiltration and remoulded control (S6, S7, S8). Samples S6 and S7 were obtained behind the infiltration front in the same small-scale infiltration column to capture bentonite retained within the internal pore network of the sand skeleton. Sample S8 was manually remoulded to reproduce the bulk state of Sample S6 without an infiltration history and served as the control specimen.

3.7.2 Sample preparation procedure

The preparation procedures differed depending on the investigated specimen type. For each sample category defined in the experimental programme, specific preparation methods were applied in order to obtain representative specimens for Cryo-BIB-SEM investigation.

(A) Bentonite slurry samples. For the investigation of the initial slurry microstructure, small droplets of bentonite slurry were directly sampled from the prepared suspension. Due to the liquid nature of the material, moulds were not used for this sample type.

(B) Filter cake samples. Filter cake specimens were produced using a filter press device. For this purpose, specially designed 3-D printed moulds were attached to the filter paper placed inside the filter press (Fig. 3.29a). Bentonite slurry was then poured onto the filter paper, and the filtration process was carried out under controlled pressure and time conditions. During filtration, well-defined filter cakes formed within the moulds, providing samples suitable for subsequent microstructural analysis. After completion of filtration, the specimen moulds were recovered from the surrounding filter cake for further preparation (Fig. 3.29c,d).

(C) Sand–slurry interface samples (S4, S5). For the investigation of sand–slurry interfaces, the 3-D printed moulds were positioned at the infiltration front within the sand

column prior to the infiltration tests (Fig. 3.29b). During infiltration, the moulds captured the boundary structure formed where the slurry contacted the host sand. After completion of the experiments, the moulds containing the interface specimens were carefully extracted for further preparation.

(D) Internal-infiltration and remoulded-control samples (S6, S7, S8). For Samples S6 and S7, the split moulds were embedded within the host sand behind the infiltration front before slurry injection. Sample S6 was positioned approximately 45 mm behind the interface in fine sand (0.1–0.5 mm), whereas Sample S7 was positioned approximately 49 mm behind the interface in medium sand (0.5–1.0 mm). After infiltration, the moulds containing the internal-infiltration specimens were recovered from the column. Sample S8 was prepared without infiltration by manually mixing B60 slurry and fine sand (0.1–0.5 mm) to reproduce the bulk state of Sample S6 and compacting the mixture directly into a split sampler.

3.7.3 Sample freezing procedure

After preparation, all specimens were rapidly frozen in liquid nitrogen in order to preserve their original microstructure prior to Cryo-BIB-SEM analysis. Rapid freezing prevents structural rearrangement of particles and pore fluids, thereby maintaining the microstructural state of the specimens.

(A) Bentonite slurry samples. For pure slurry samples, small droplets of bentonite suspension were directly introduced into liquid nitrogen. Due to the fluid nature of the material, the use of moulds was not practical for this sample type. The rapid freezing process ensured preservation of the initial slurry microstructure.

(B) Filter cake samples. Filter-cake specimens formed in the filter-press moulds were trimmed before freezing only in the vertical direction; their lateral dimensions were defined by the mould. The resulting specimens measured $4 \times 8 \times 12$ mm (Fig. 3.29e). The specimens were removed completely from the split moulds before immersion in liquid nitrogen.

(C) Sand–slurry interface samples (S4, S5). For the interface specimens, the moulds containing the bentonite-infiltrated sand were first extracted from the column (Fig. 3.29f). These specimens were not trimmed. One half of the split mould was removed, after which the specimen was gently pushed out of the remaining half and released directly into liquid nitrogen. Consequently, both mould halves were removed before freezing.

(D) Internal-infiltration and remoulded-control samples (S6, S7, S8). The internal-infiltration specimens S6 and S7 were not trimmed and followed the same complete-demoulding and direct-immersion procedure as the interface specimens: one half of the split mould was removed and each specimen was gently pushed out of the remaining half directly into liquid nitrogen. Sample S8 was prepared as a remoulded control in a split sampler. After compaction, it was removed from the sampler and rapidly frozen in liquid nitrogen; because it was prepared without infiltration, no column-extraction step was required.

Before freezing, the liquid nitrogen was stabilised by placing it in a desiccator under vacuum. This procedure removed trapped gases and reduced surface turbulence, producing a calm liquid nitrogen bath suitable for sample immersion (Fig. 3.29g). All specimens were kept in the liquid nitrogen for at least one minute to ensure complete freezing.

3.7.4 Sample transport and preservation

After freezing, the specimens were transferred to pre-cooled sample holders while maintaining cryogenic conditions. All samples were then stored in a liquid nitrogen container to preserve their frozen state prior to microstructural analysis.

The frozen specimens were transported from Bochum to Aachen in the liquid nitrogen transport container (Fig. 3.29h). This procedure ensured that the samples remained continuously submerged in liquid nitrogen during transport, preventing thawing and preserving the original microstructure of the bentonite slurry, filter cakes, and bentonite-infiltrated sand specimens.

Maintaining cryogenic conditions during storage and transport was essential to avoid structural changes caused by melting or redistribution of pore fluids prior to Cryo-BIB-SEM imaging.

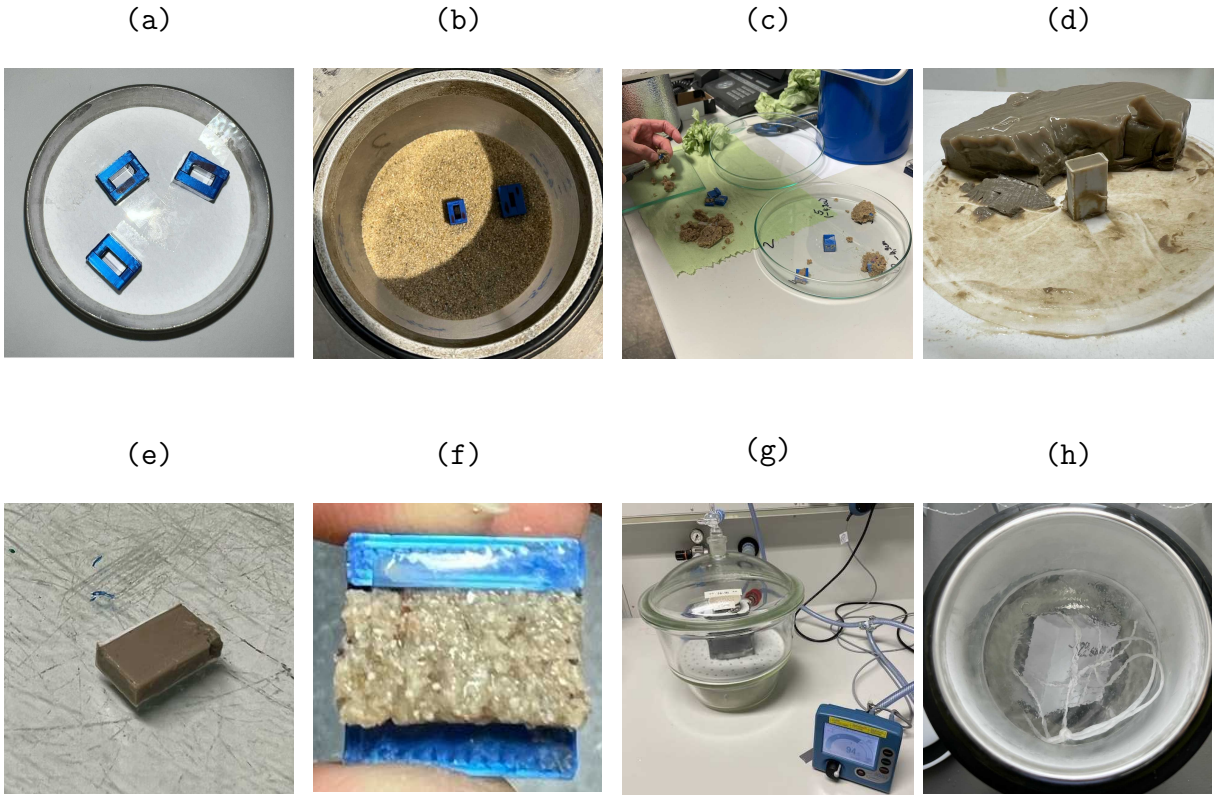

Figure 3.29: Preparation and cryogenic preservation of specimens for Cryo-BIB-SEM investigation.

3.7.5 Cryo-BIB-SEM imaging procedure

After transport to the microscopy laboratory, the frozen specimens were transferred to the cryo-preparation chamber using the Leica VCT100 cryo-transfer system while maintaining cryogenic conditions. The samples were subsequently mounted in the Leica TIC3X Broad Ion Beam (BIB) milling system.

BIB milling was applied to produce smooth and flat cross-sections of the frozen samples. This preparation step exposes the internal microstructure of the bentonite slurry, filter cakes, and bentonite-infiltrated sand specimens without introducing mechanical damage.

Following milling, the specimens were transferred directly into the chamber of the Zeiss Supra 55 scanning electron microscope for imaging. Secondary electron (SE2) and backscattered electron (BSE) detectors were used to capture microstructural features and phase contrast, while energy dispersive spectroscopy (EDS) was used for elemental analysis of selected regions of the samples.

4 Slurry infiltration into sands: experimental insights for TBM shielding

This chapter investigates the influence of support overpressure Δp, soil type, and slurry concentration c on bentonite slurry infiltration in saturated sands using column experiments performed with the setup described in Section 3.3.5. Pore water pressure was monitored continuously at multiple depths, and post-test bentonite concentration profiles $c(z)$ were analysed to identify infiltration behaviour and particle retention within the soil. These measurements provide quantitative information on pressure transfer and the spatial distribution of bentonite particles during infiltration.

In slurry-shield tunnelling, face support can be maintained either by the formation of a low-permeability filter cake at the excavation face or by slurry penetration into the pore network until filtration occurs. Both mechanisms control how support pressure is transferred into the ground and therefore influence stability conditions and slurry losses in permeable sands (Anagnostou and Kovári, 1994; Min et al., 2013).

4.1 Objectives of this chapter

The experiments presented in this chapter aim to clarify how injection pressure Δp, soil grain size, and slurry concentration c influence slurry infiltration and pressure transfer in saturated sands. The objectives are to evaluate how these parameters govern the infiltration depth and the development of filtration zones, to relate the evolution of pore water pressure (PWP) to the retention of bentonite along the column depth, and to identify consistent patterns governing support-pressure transfer in permeable sands. The experimental results further provide a quantitative dataset that supports the subsequent modelling of slurry infiltration processes.

4.2 Experimental programme of the column infiltration tests

Table 4.1 summarises the first experimental series performed with the column device, which was dedicated to investigating the influence of soil type and support overpressure. Three primary sand types (S 0.1–0.5 mm, S 0.5–1.0 mm, and S 1.0–2.0 mm) were tested in medium-dense to dense states.

Table 4.1: Experimental programme of the first series of column infiltration tests: influence of soil type and injection pressure ($\Delta p = p_{\text{in}} - p_{\text{out}}$)

Sand (mm)	I_D (%)	c_{prepared} (g/L)	c_{actual} (g/L)	Δp (kPa)	p_{in} (kPa)	p_{out} (kPa)	k_s (m/s)
1.0–2.0	78.4	60	53.3	50	90	40	1.04×10^{-3}
0.5–1.0	69.0	60	53.9	30	70	40	5.77×10^{-4}
0.5–1.0	77.6	60	52.2	50	90	40	7.18×10^{-4}
0.5–1.0	71.0	60	53.6	100	140	40	5.84×10^{-4}
0.5–1.0	73.0	60	54.0	200	240	40	1.69×10^{-3}
0.1–0.5	65.0	60	53.6	30	70	40	4.25×10^{-4}
0.1–0.5	61.0	60	53.3	50	90	40	3.98×10^{-4}
0.1–0.5	56.0	60	53.8	100	140	40	3.98×10^{-4}
0.1–0.5	66.0	60	53.7	200	240	40	3.91×10^{-4}

Four effective injection pressures were applied ($\Delta p = 30, 50, 100$, and 200 kPa). The outflow container was maintained at a constant pressure ($p_{\text{out}} = 40$ kPa), while the slurry container pressure (p_{in}) was adjusted accordingly. In the test identifiers and figure legends, Δp denotes the prescribed boundary-pressure difference $p_{\text{in}} - p_{\text{out}}$ listed in Table 4.1. The PWP curves, in contrast, show local sensor pressures within the hydraulic system and specimen; they therefore do not directly represent the imposed boundary-pressure difference and need not equal the Δp value used in the test identifier. The listed injection pressures were applied to the fine and medium sands (S 0.1–0.5 mm and S 0.5–1.0 mm). For the coarse sand (S 1.0–2.0 mm), injection pressure differences Δp higher than 50 kPa were not investigated. Table 4.1 also lists the coefficient of permeability to water (k_s), measured prior to each infiltration test.

In a second set of column infiltration tests, the effect of slurry concentration was investigated. Coarse sand (S 1.0–2.0 mm) was selected because its relatively open pore network

allowed B60 slurry to penetrate the full column under the selected hydraulic condition. B20 and B40 were therefore included to obtain fully infiltrated sand specimens at lower bentonite concentrations; B60 provided the common reference to the soil-type series, and B80 extended the series to determine whether filtration would occur at a higher concentration even in the coarse sand. The B20, B40, B60, and B80 grades correspond to nominal preparation dosages of 20 g/L, 40 g/L, 60 g/L, and 80 g/L and moisture-corrected inlet concentrations of 17.8, 35.2, 53.3, and 71.2 g/L, respectively. The nominal preparation dosages and moisture-corrected inlet concentrations, together with the applied pressure conditions and the water-permeability values measured prior to each infiltration test, are listed in Table 4.2.

Table 4.2: Experimental programme of the second series of column infiltration tests: influence of bentonite concentration

Sand (mm)	I_D (%)	c_{prepared} (g/L)	c_{actual} (g/L)	Δp (kPa)	p_{in} (kPa)	p_{out} (kPa)	k_s (m/s)
1.0–2.0	87.9	20	17.8	50	90	40	1.12×10^{-3}
1.0–2.0	84.2	40	35.2	50	90	40	1.09×10^{-3}
1.0–2.0	78.4	60	53.3	50	90	40	1.04×10^{-3}
1.0–2.0	83.9	80	71.2	50	90	40	1.06×10^{-3}

4.3 Column test results

The infiltration behaviour of bentonite slurry in granular soils is influenced by soil type, injection pressure, and slurry concentration, each playing a key role in penetration depth, filtration processes, and pore-water pressure (PWP) response. While soil type determines the permeability and resistance to flow of the porous medium, injection pressure provides the driving force for slurry movement, and slurry concentration affects fluid properties such as viscosity and the retention of bentonite particles within the sand matrix. To examine these effects, the experiments were organised into series in which soil type, injection pressure, or slurry concentration was treated as the principal variable. The results are therefore presented in three parts: the effect of soil type, the effect of injection pressure, and the effect of slurry concentration, highlighting their influence on infiltration behaviour and filter-cake formation.

4.3.1 Effect of soil type

The experimental programme distinguished two observed infiltration responses: internal filter-cake formation and full slurry penetration. Three sand types were tested under an effective pressure difference of $\Delta p = 50\,\mathrm{kPa}$ using a B60 slurry. The results are presented in Figs. 4.1 and 4.2, where penetration depth, pore-water pressure (PWP) distribution, and slurry concentration profiles are analysed together to identify correlations among these key measures.

Figure 4.1 illustrates the temporal evolution of pore-water pressure (PWP) profiles for the three sands at selected times ($t = 0, 5, 30$, and $600\,\mathrm{s}$). These profiles provide insight into the progression of the infiltration mechanisms from test initiation towards a stable response. For S 1.0–2.0 mm, the PWP profiles quickly approach a nearly linear gradient, indicating rapid pressure transmission through the sand column and consistent full penetration of the slurry. In contrast, S 0.5–1.0 mm and S 0.1–0.5 mm develop increasingly nonlinear PWP profiles over time, with localised changes in slope reflecting an increasing resistance to flow and the gradual development of internal filtration zones. The evolution of these profiles therefore provides early indications of the filtration behaviour that later becomes evident in the stabilized pressure and penetration results discussed below.

The common initial decrease visible in the $t = 5\,\mathrm{s}$ profiles is attributed mainly to start-up compliance of the apparatus. Following pressure application, slight elastic expansion of the test cell and connected hydraulic components increased the fluid-filled system volume; rapid filling of this additional volume produced a short-lived PWP decrease. This response is therefore treated as an apparatus-related transient rather than a separate filtration stage.

The transient evolution of PWP is shown in Fig. 4.1. In the combined comparisons below, profiles recorded at $t = 600\,\mathrm{s}$ represent the stabilized stage; subsequent measurements showed only minor fluctuations and no further material evolution of the PWP-profile shape. For tests with durations shorter than 600 s, the last undisturbed PWP profile recorded immediately before the test was stopped is shown. All concentration profiles are destructive post-test measurements.

Figure 4.2a shows the penetration behaviour of the three sands plotted against the square root of time ($\sqrt{t}$), revealing distinct infiltration patterns. The penetration depth represents the averaged infiltration depth calculated as V_{in}/A, where V_{in} is the cumulative infiltrated slurry volume measured in the inflow container and A is the column cross-sectional area (see Section 3.3.5). This quantity is an equivalent volume-based depth,

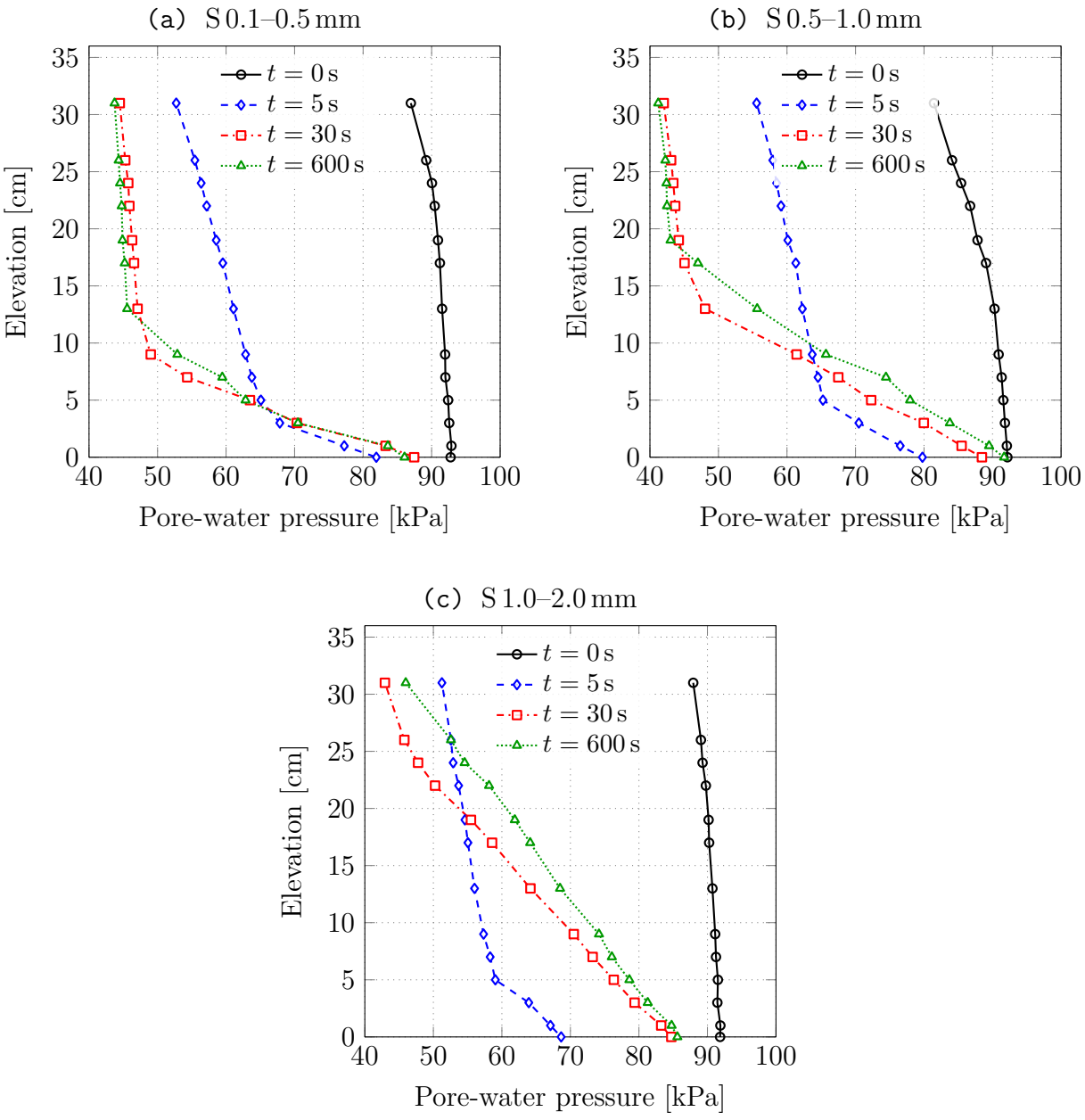

Figure 4.1: Pore-water pressure profiles at selected times for (a) S 0.1–0.5 mm, (b) S 0.5–1.0 mm, and (c) S 1.0–2.0 mm under $\Delta p = 50\,\mathrm{kPa}$ and B60.

not a direct measurement of filter-cake thickness or of a sharp infiltration-front position. The $\sqrt{t}$ representation is motivated by the approximate $V_f \propto \sqrt{t}$ scaling of cumulative filtrate volume during cake-controlled pressure filtration (Fig. 2.5); because the equivalent penetration depth is proportional to cumulative inflow volume, this transformation helps identify changes in infiltration rate as filtration develops, without implying that every test follows an exact square-root law. S 1.0–2.0 mm (coarse sand, green) exhibits the fastest and deepest penetration, consistent with full penetration where no substantial obstruction limits slurry flow. S 0.5–1.0 mm (medium sand, red) shows intermediate penetration, which slows markedly as internal filter cake formation develops within the sand column at a depth of about 18–22 cm. S 0.1–0.5 mm (fine sand, blue) exhibits the smallest penetration depth, which is attributed to earlier clogging of the pore network at a depth of about 11–15 cm, where an internal filter cake forms and restricts further slurry advance.

The stabilized PWP profiles at $t = 600$ s shown in Fig. 4.2b reveal a close link between pressure transfer and penetration behaviour. Subsequent measurements showed only minor fluctuations and no further material evolution of the profile shapes. For S 1.0–2.0 mm, a nearly linear PWP gradient confirms pressure transmission through the full column height. This is consistent with full penetration without appreciable localised filtration resistance, while the finite pressure gradient indicates that hydraulic resistance through the sand remains. In contrast, for S 0.5–1.0 mm and S 0.1–0.5 mm, inflection points appear at about 19 cm and 13 cm, respectively, marking the location of internal filter cake formation. These depths coincide with the change in slope of the penetration curves, confirming that filtration governs infiltration resistance.

Figure 4.2c further supports these findings through the post-test slurry concentration profiles, which provide insight into bentonite particle retention and filter-cake zones:

- For S 1.0–2.0 mm, the slurry concentration remains nearly unchanged over the measured depth, confirming full penetration with negligible bentonite particle filtration.
- For S 0.5–1.0 mm, the concentration remains between approximately 51 and 54 g/L up to 17.5 cm and then decreases to near zero by approximately 23–25 cm, identifying internal filtration. The intermediate values at approximately 19.7 and 21.5 cm may arise because each 2 cm-high sample spatially averages a non-planar filtration front; they therefore do not establish a separate clogging phase.
- For S 0.1–0.5 mm, a sharper drop between 11 and 15 cm confirms earlier cake formation; the concentration decreases gradually in the first 10 cm (from about 50 g/L

to about 42 g/L) before the steep decline, indicating stronger filtration at finer pore scales.

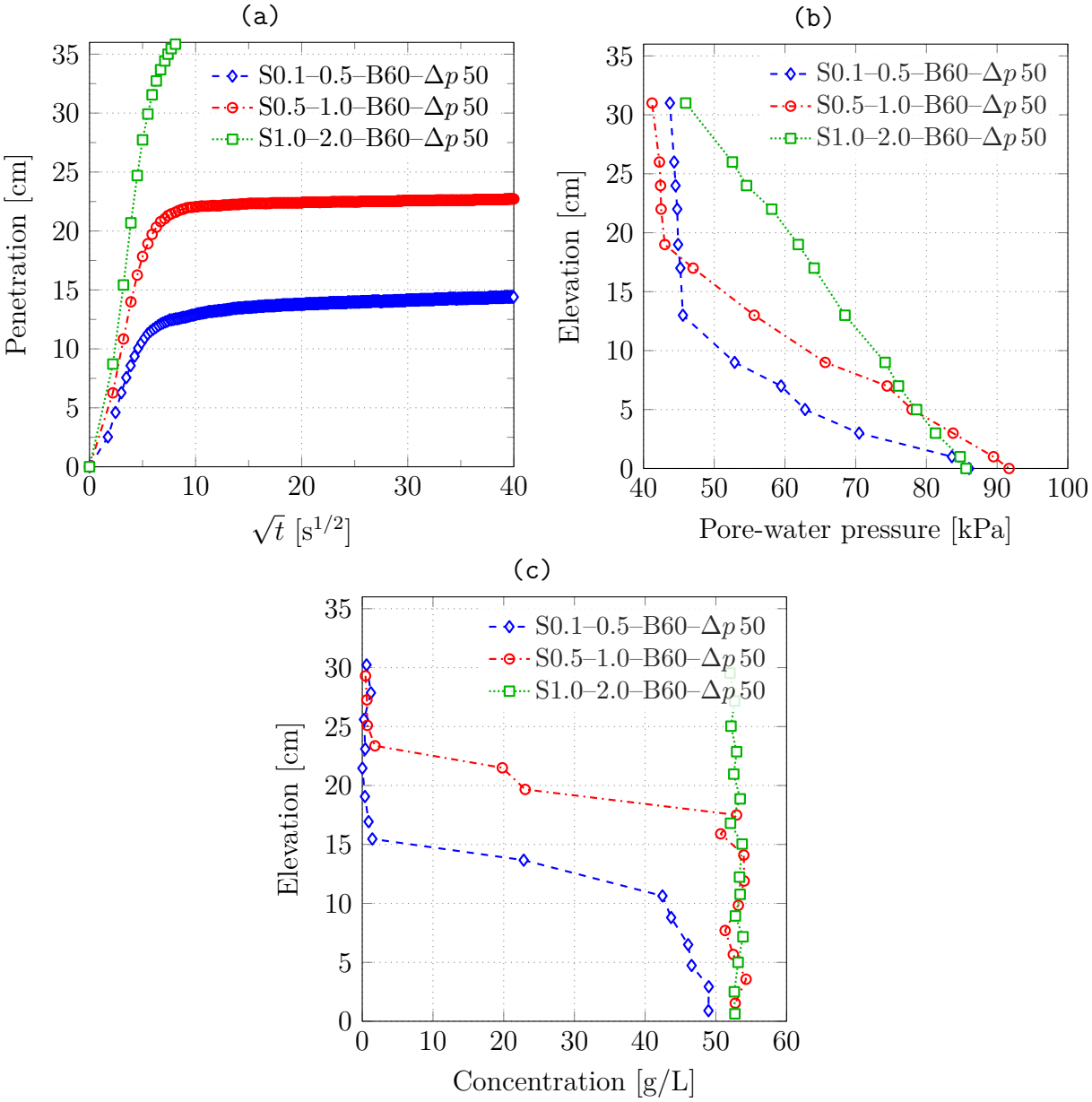

Figure 4.2: Effect of soil type on (a) equivalent slurry penetration depth versus $\sqrt{t}$, (b) stabilized pore-water pressure (PWP) profiles at $t = 600$ s, and (c) post-test slurry concentration profiles for S 0.1–0.5 mm, S 0.5–1.0 mm, and S 1.0–2.0 mm under $\Delta p = 50$ kPa and B60.

The agreement among the penetration curves, stabilized PWP profiles, and post-test concentration profiles indicates that penetration behaviour and pressure transfer are directly

linked and that PWP and concentration profiles identify the same filtration zones. For S 0.5–1.0 mm, the concentration transition is consistent with internal filtration over approximately 18–23 cm; the two intermediate values may reflect spatial averaging across a non-planar filtration front rather than a distinct clogging phase. Under the B60 and $\Delta p = 50$ kPa condition used for this soil-type comparison, S 1.0–2.0 mm exhibited full slurry penetration with negligible bentonite retention, whereas the medium and fine sands developed internal filter cakes that controlled both penetration and pressure transfer.

Under this fixed B60 and $\Delta p = 50$ kPa condition, the finer sands filtered earlier and showed less penetration, while the coarsest sand remained in a full-penetration regime. These trends are consistent with other column-scale observations reported for bentonite slurries in sands (Min et al., 2013; Yin et al., 2016).

4.3.2 Effect of injection pressure: S 0.1–0.5 mm

According to the experimental programme presented in Table 4.1, the injection pressure was varied between $\Delta p = 30$, 50, 100, and 200 kPa using the same nominal B60 preparation grade as the inlet slurry in every test. The results for the fine sand S 0.1–0.5 mm are summarised in Fig. 4.3, which presents the equivalent penetration depth versus $\sqrt{t}$, stabilized pore-water pressure (PWP) profiles at $t = 600$ s, and post-test slurry concentration profiles.

Figure 4.3a shows the penetration behaviour plotted against the square root of time ($\sqrt{t}$). Increasing Δp leads to deeper penetration before filtration begins. At $\Delta p = 30$ kPa, filtration initiates almost immediately, resulting in very shallow penetration. Increasing the pressure to $\Delta p = 50$ kPa produces a moderate increase in penetration depth, although filtration still occurs close to the inlet boundary. At $\Delta p = 100$ kPa, the onset of filtration is clearly delayed and penetration increases further. For $\Delta p = 200$ kPa, the maximum penetration depth approaches approximately 19 cm before stabilising. Although the higher hydraulic gradient reduces the initial resistance to slurry movement, it does not eliminate the depth limitation imposed by filtration processes in the pore network.

The location and length of the filtration zone vary with injection pressure. As indicated in Fig. 4.3a, filtration occurs between approximately 2 and 9 cm for $\Delta p = 30$ kPa and between about 11 and 15 cm for $\Delta p = 50$ kPa. For higher pressures, $\Delta p = 100$ kPa and $\Delta p = 200$ kPa, the filtration zones extend to approximately 7–19 cm and 6–20 cm, respectively. Thus, the filtration front generally shifts farther from the inlet as pressure

rises, but the transition-zone width does not increase monotonically across every pressure increment.

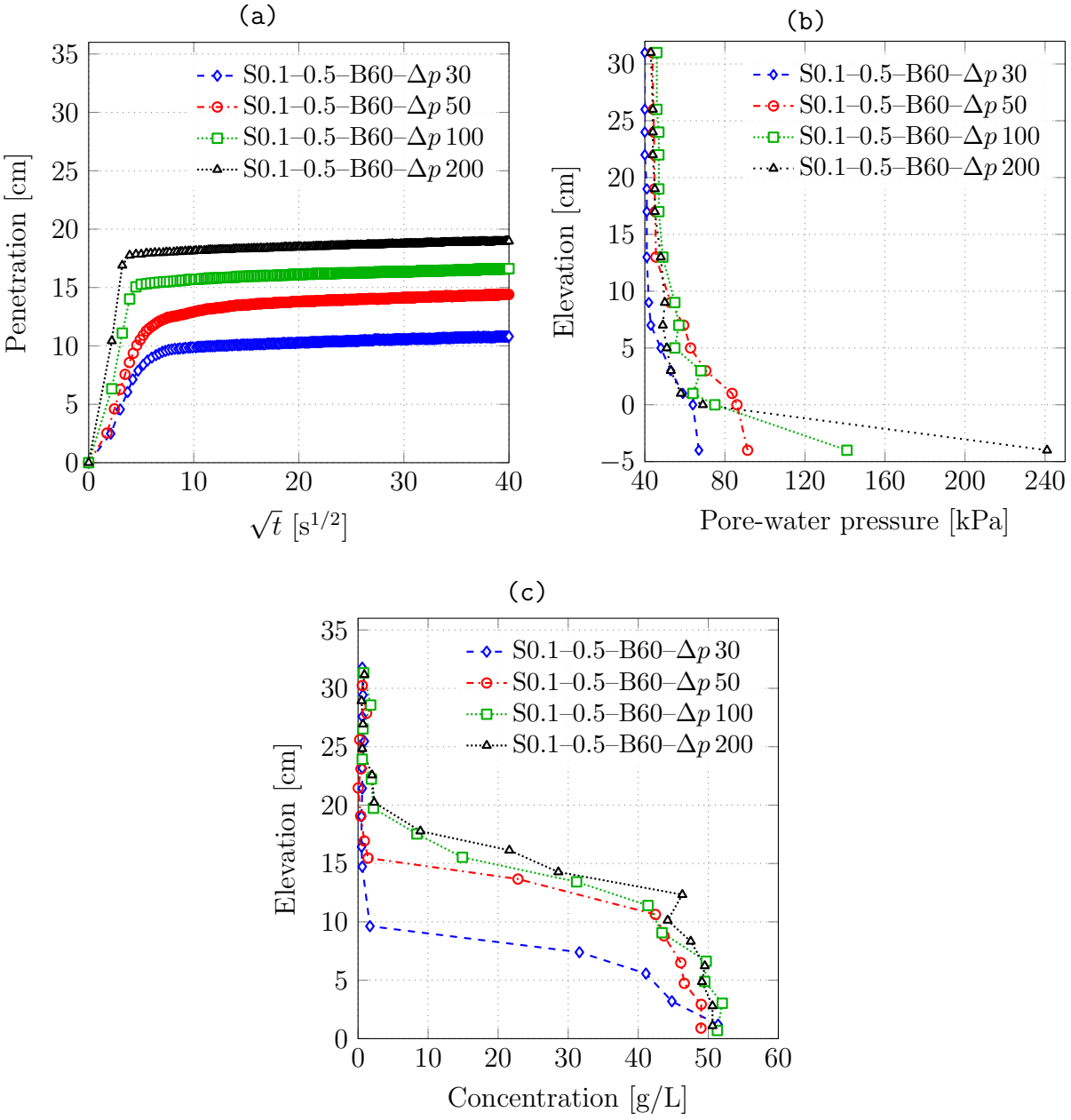

Figure 4.3: Effect of slurry injection pressure on (a) equivalent slurry penetration depth versus $\sqrt{t}$, (b) stabilized pore-water pressure (PWP) profiles at $t = 600\,\mathrm{s}$, and (c) post-test slurry concentration profiles in S 0.1–0.5 mm for $\Delta p = 30$, 50, 100, and 200 kPa (B60).

The stabilized PWP profiles at $t = 600\,\mathrm{s}$ shown in Fig. 4.3b reveal how pressure transmission changes with injection pressure. Subsequent measurements showed only minor fluctuations and no further material evolution of the profile shapes. In this plot, the elevation 0 cm corresponds to the bottom level of the sand specimen, while the PWP sensor located at the sand–filter interface is plotted slightly below this level in order to illustrate the pressure gradient across the boundary. Consequently, values appearing below 0 cm represent measurements within the filter layer rather than within the sand specimen.

At lower pressures ($\Delta p = 30$ and $50\,\mathrm{kPa}$), the pressure drop across the filter layer and lower sand–filter interface is small, and most of the pressure decrease occurs within the lower part of the sand. At higher pressures ($\Delta p = 100$ and $200\,\mathrm{kPa}$), most of the pressure drop occurs between the filter-layer sensor and the lower boundary of the sand, while only a smaller pressure gradient remains within the sand specimen. Thus, the high-pressure profiles indicate that hydraulic resistance is concentrated near the lower inlet interface.

The slurry concentration profiles shown in Fig. 4.3c show that the concentration transition shifts farther from the inlet as Δp increases, while its width varies with injection pressure. At $\Delta p = 30\,\mathrm{kPa}$, the concentration decreases from about $51\,\mathrm{g/L}$ near an elevation of 1 cm to below $2\,\mathrm{g/L}$ by approximately 10 cm. At $\Delta p = 50\,\mathrm{kPa}$, it remains above approximately $42\,\mathrm{g/L}$ up to an elevation of about 11 cm and then decreases to about $1.4\,\mathrm{g/L}$ by 15.5 cm. At $\Delta p = 100\,\mathrm{kPa}$, the decrease is more gradual, from about $41\,\mathrm{g/L}$ at 11.4 cm to about $2\,\mathrm{g/L}$ at 19.7 cm. At $\Delta p = 200\,\mathrm{kPa}$, a broadly similar transition occurs slightly farther from the inlet, from about $46\,\mathrm{g/L}$ at 12.3 cm to about $2\,\mathrm{g/L}$ at 20.2 cm.

Overall, increasing Δp increases the maximum penetration depth and generally shifts the filtration front farther from the inlet, while the measured concentration-transition width varies non-monotonically. The measured pressure-loss pattern also changes with increasing pressure: at low Δp, most of the pressure decrease develops within the lower part of the sand and broadly overlaps the concentration-transition zone, whereas at higher Δp the dominant pressure loss is concentrated across the filter layer and lower sand–filter interface, with a smaller gradient remaining within the sand. The concentration transitions at $\Delta p = 100$ and $200\,\mathrm{kPa}$ are broadly similar, with the latter extending only slightly farther from the inlet; because the profiles are based on discrete spatial samples, their relative sharpness should be interpreted qualitatively. This pressure-loss pattern is consistent with analytical descriptions of pressure transmission and filtration onset in slurry infiltration systems (Xu and Bezuijen, 2018).

4.3.3 Effect of injection pressure: S 0.5–1.0 mm

For S 0.5–1.0 mm, the effect of slurry injection pressure on penetration, filtration, and pore-water pressure (PWP) response was also assessed at $\Delta p = 30$, 50, 100, and 200 kPa using the same nominal B60 preparation grade as the inlet slurry in every test, according to the experimental programme in Table 4.1. The results are summarised in Fig. 4.4, which presents the equivalent penetration depth versus $\sqrt{t}$, selected PWP profiles, and post-test slurry concentration profiles for the different injection pressures.

Figure 4.4a shows that increasing Δp produces progressively deeper penetration before filtration begins. At $\Delta p = 30$ kPa and $\Delta p = 50$ kPa, the slurry front encounters resistance within the specimen and internal filter cakes develop. For $\Delta p = 30$ kPa, the filtration zone appears at approximately 10–15 cm, whereas for $\Delta p = 50$ kPa it occurs deeper in the column, at elevations of approximately 17–23 cm. Compared with the finer sand S 0.1–0.5 mm tested under the same pressures, the filtration depth is greater here, reflecting the lower hydraulic resistance of the coarser pore structure.

The PWP profiles shown in Fig. 4.4b correspond to the stabilized stage at $t = 600$ s for $\Delta p = 30$, 50, and 100 kPa; subsequent measurements showed only minor fluctuations and no further material evolution of the profile shape. For the shorter $\Delta p = 200$ kPa test, the last undisturbed profile, recorded at $t = 38$ s immediately before the test was stopped, is shown. At $\Delta p = 30$ and $\Delta p = 50$ kPa, the pore-water pressure decreases progressively over the penetrated part of the specimen and approaches a plateau above it. The pressure loss is therefore distributed over the penetration zone rather than concentrated at a single elevation. Compared with the finer sand S 0.1–0.5 mm, the response is less localised, reflecting a more distributed hydraulic resistance within the coarser pore structure.

At higher injection pressures ($\Delta p = 100$ and $\Delta p = 200$ kPa), the behaviour changes markedly. The slurry penetrates through the entire sand column without forming an internal cake within the specimen height. Consequently, no significant bentonite retention is observed within the sand. The corresponding PWP profiles exhibit a gradual pressure decrease along the column height, indicating a distributed hydraulic gradient through the specimen rather than localised transfer of slurry pressure to the grain skeleton through an internal filter cake.

The slurry concentration profiles in Fig. 4.4c follow the same pattern. At $\Delta p = 30$ and $\Delta p = 50$ kPa, the concentration decreases gradually with depth before a sharp drop occurs across the filtration zone, reflecting progressive bentonite retention followed by abrupt clogging. In contrast, at $\Delta p = 100$ and $\Delta p = 200$ kPa the concentration remains close to

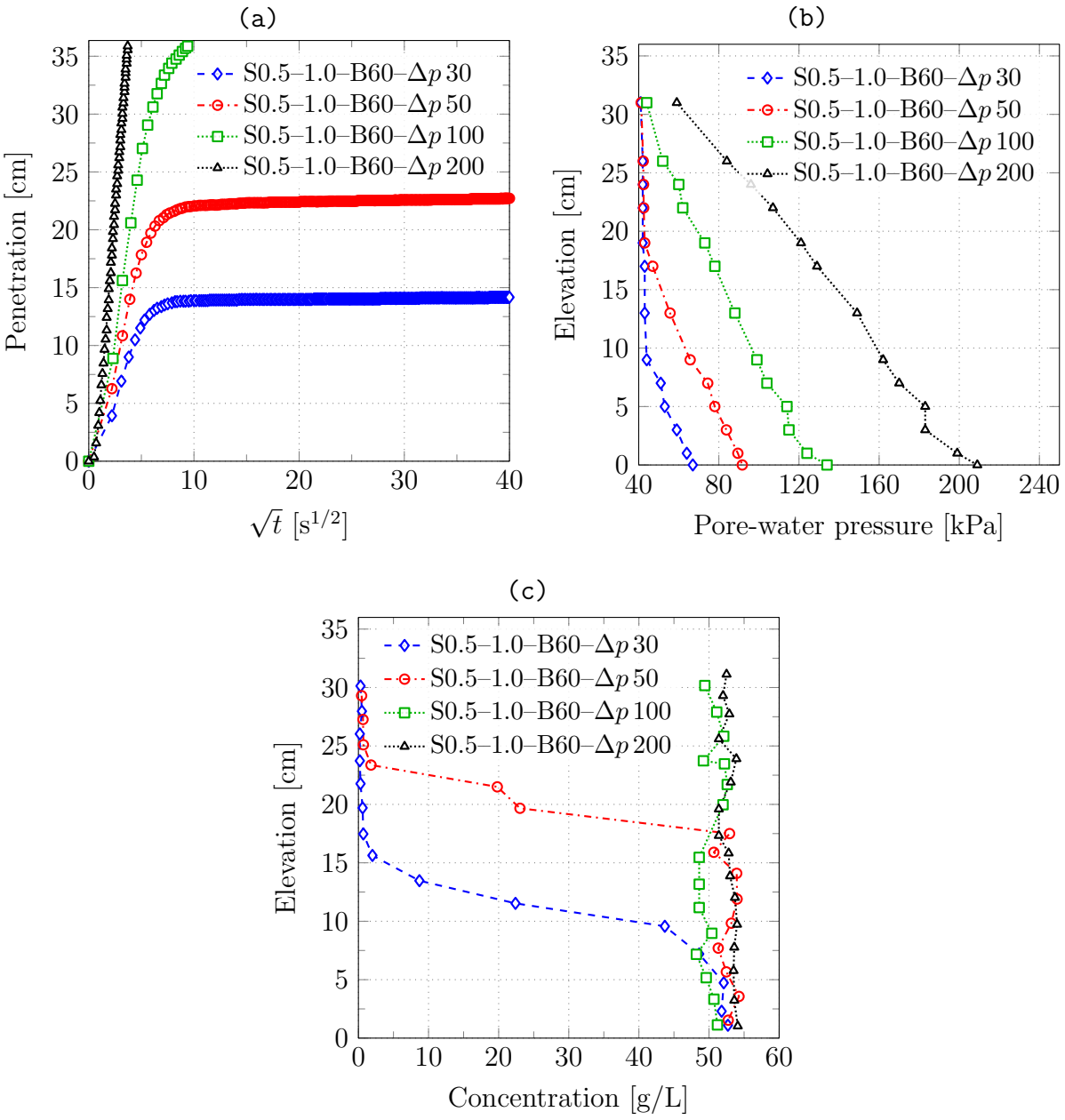

Figure 4.4: Effect of slurry injection pressure on (a) equivalent slurry penetration depth versus $\sqrt{t}$, (b) stabilized pore-water pressure (PWP) profiles at $t = 600\,\mathrm{s}$ for $\Delta p = 30$, 50, and 100 kPa and the last undisturbed profile before test termination at $t = 38\,\mathrm{s}$ for $\Delta p = 200\,\mathrm{kPa}$, and (c) post-test slurry concentration profiles in S 0.5–1.0 mm (B60).

the initial value throughout the measured depth, confirming that the slurry penetrates the specimen without significant filtration.

The similarity of the PWP and concentration profiles at $\Delta p = 100$ and $\Delta p = 200\,\mathrm{kPa}$ indicates that, at these pressure levels, filtration resistance associated with bentonite retention is small within the tested height and the response approaches full-penetration conditions. In fact, the resulting profiles are comparable to those observed for the coarser sand S 1.0–2.0 mm at $\Delta p = 50\,\mathrm{kPa}$.

Overall, the results demonstrate that the combined influence of grain size and injection pressure controls the infiltration mechanism. For S 0.5–1.0 mm, lower pressures lead to internal filtration within the sand column, whereas sufficiently high pressures promote complete penetration with minimal bentonite retention. This transition reflects the increasing dominance of pressure-driven flow over particle retention as the hydraulic gradient increases.

4.3.4 Effect of bentonite concentration

The effect of slurry concentration on penetration behaviour, filtration, and pore-water pressure (PWP) response was analysed for S 1.0–2.0 mm using B20, B40, B60, and B80 at a constant injection pressure of $\Delta p = 50\,\mathrm{kPa}$. The results are summarised in Fig. 4.5, which presents the equivalent penetration depth versus $\sqrt{t}$, selected PWP profiles, and post-test slurry concentration profiles for the different slurry concentrations.

Figure 4.5a shows that the slurries B20, B40, and B60 penetrate the entire sand column without forming an internal filter cake. The penetration curves for these concentrations are very similar, indicating that the slurry advances rapidly through the coarse sand matrix and reaches the top of the column. In contrast, the B80 slurry exhibits a significantly shallower penetration depth. In this case, the slurry front stabilizes at approximately 8–15 cm, indicating the formation of an internal filter cake that prevents further advancement of the slurry.

The PWP profiles shown in Fig. 4.5b reflect these differences in infiltration behaviour. For the shorter B20 and B40 tests, the last undisturbed profiles were recorded at $t = 34$ and 57 s, respectively, immediately before each test was stopped. For B60 and B80, the $t = 600\,\mathrm{s}$ profiles represent the stabilized stage; subsequent measurements showed only minor fluctuations and no further material evolution of the profile shape. For B20, B40, and B60 the PWP profiles display nearly linear gradients through the specimen,

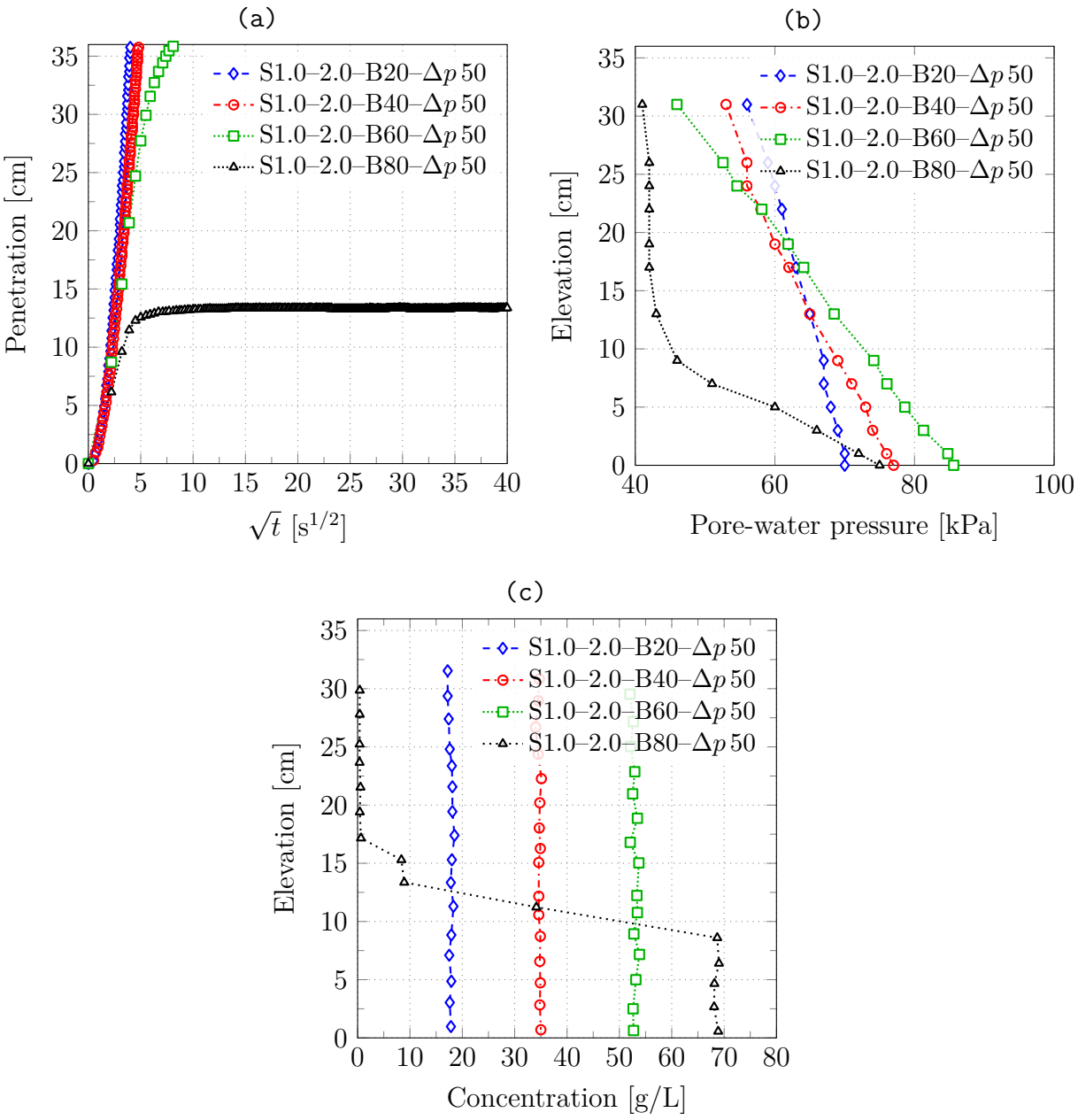

Figure 4.5: Effect of slurry concentration on (a) equivalent slurry penetration depth versus $\sqrt{t}$, (b) the last undisturbed pore-water pressure (PWP) profiles before test termination at $t = 34\,\mathrm{s}$ for B20 and $t = 57\,\mathrm{s}$ for B40 and stabilized profiles at $t = 600\,\mathrm{s}$ for B60 and B80, and (c) post-test slurry concentration profiles in S 1.0–2.0 mm at $\Delta p = 50\,\mathrm{kPa}$.

indicating that the applied pressure is transmitted through the entire sand column. This behaviour is consistent with complete penetration of the slurry without significant particle retention. For B80, however, a pronounced but continuous pressure decrease occurs over the same elevation range as the observed penetration zone. This distributed pressure decrease indicates the hydraulic resistance associated with bentonite retention throughout the developing internal filter cake.

The slurry concentration profiles in Fig. 4.5c confirm these observations. For B20, B40, and B60 the concentration remains nearly constant along the specimen height, indicating negligible bentonite particle retention within the sand matrix. In contrast, the B80 profile shows a strong decrease in concentration across the same elevation range where the penetration front stabilizes, confirming the formation of an internal filter cake and the associated retention of bentonite particles.

Although S 1.0–2.0 mm is the coarsest sand investigated in this study, the B80 slurry still forms an internal filter cake within the column. This indicates that, at sufficiently high bentonite concentrations, the viscosity and particle interaction effects dominate the infiltration process and reduce the effective permeability even in relatively coarse sands. The internal filter cake therefore extends throughout the infiltrated zone, as indicated by the progressive concentration decrease across several consecutive samples. The maximum penetration depth marks the downstream end of this filtration zone, where the measured bentonite concentration approaches zero or has decreased considerably relative to the initial slurry concentration.

These observations are consistent with the trends observed for the other sands investigated in this study. They also agree with findings reported in the literature: increasing bentonite concentration promotes earlier filtration and stronger resistance to slurry penetration, whereas lower concentrations allow full penetration with negligible bentonite retention (Min et al., 2013; Xu and Bezuijen, 2019).

4.4 Slurry infiltration and pressure transfer: implications for TBM shielding

The infiltration and filter-cake mechanisms observed in the column experiments provide insight into the pressure transfer processes governing slurry-supported tunnel faces. In slurry shield tunnelling, the applied support pressure must be transmitted effectively to the surrounding soil while limiting fluid losses. This pressure transfer may occur either

through a low-permeability filter cake formed at the excavation face or, if infiltration proceeds, through a penetration zone within the soil until filtration initiates. Once a sufficiently low-permeability filtration zone develops, the slurry pressure can be transmitted to the soil skeleton while excessive seepage into the ground is limited (DAUB, 2016; Anagnostou and Kovári, 1994).

The experiments presented in Section 4.3 revealed two characteristic infiltration mechanisms: (i) full slurry penetration without filtration and (ii) internal filter-cake formation within the soil mass. External filter-cake formation at the soil boundary is described in the literature but was not directly demonstrated by the present column experiments. The two observed mechanisms determine the efficiency of pressure transfer during slurry TBM operation and depend on the combined influence of soil permeability, injection pressure, and slurry rheology.

The measured pore-water pressure (PWP) distributions show that increasing slurry penetration leads to pressure being transmitted further into the soil column. For S 0.5–1.0 mm at the higher tested pressure differences ($\Delta p = 100$ and 200 kPa), the slurry penetrated the full specimen height, and the corresponding PWP profiles showed a gradual pressure decrease along the column. In highly permeable formations, such full-penetration behaviour may increase slurry losses and reduce the fraction of chamber pressure transferred to the soil skeleton as effective support unless operational parameters are adjusted (Xu and Bezuijen, 2018; Bezuijen et al., 2006). In practice, injection pressure and slurry properties are therefore controlled to limit penetration depth while maintaining adequate support pressure at the tunnel face (DAUB, 2016).

When filtration occurs, the experiments show that the pressure gradient becomes concentrated across the developing filter cake. This is reflected by steeper PWP gradients across the zones in which internal filter cakes develop. In such cases, the low-permeability filtration zone concentrates the hydraulic gradient, so a larger fraction of the applied slurry pressure acts on the soil skeleton as effective support instead of propagating farther into the specimen as pore-water pressure.

From an operational perspective, it is advantageous if a low-permeability filtration zone develops close to the tunnel face, because this transfers the slurry pressure to the soil skeleton near the potential shear failure wedge while limiting deep slurry penetration and fluid loss. In the present tests, lower injection pressures and higher slurry concentrations promoted earlier filtration and shallower filtration zones, whereas higher Δp delayed filtration and allowed deeper slurry penetration.

Another important operational consideration is the time available for filter-cake formation between consecutive cutter passes. If tool passages occur too frequently relative to the filtration time, the excavation face may remain partly in a penetration state, allowing a larger fraction of the chamber-pressure influence to propagate farther into the ground as elevated pore-water pressure rather than being mobilized near the face as effective stress in the soil skeleton. Conversely, once a filter cake is established, a larger fraction of the support pressure is mobilized on the soil skeleton (Thewes et al., 2016; Žižka et al., 2015). This highlights the need to balance advance rate and pressure settings with the filtration characteristics of the slurry.

The test series with varying slurry concentration, performed using S 1.0–2.0 mm, further emphasises the role of slurry rheology. While B20–B60 resulted in full penetration without appreciable bentonite retention, the more concentrated B80 slurry developed an internal filter cake across the approximately 8–15 cm infiltrated zone and significantly reduced permeability. This behaviour is consistent with field practice, where more viscous slurries are used in coarse sands and gravels to suppress seepage and enhance face stability (Min et al., 2013; Xu and Bezuijen, 2019).

In finer sands (S 0.1–0.5 mm and S 0.5–1.0 mm), increasing Δp extended the penetration zone and delayed filtration, reducing the effectiveness of cake formation. These observations highlight the importance of adapting slurry properties and injection pressure to the permeability of the ground in order to maintain stable support conditions (Xu and Bezuijen, 2018).

Overall, the laboratory results demonstrate how infiltration depth, pressure transfer, and filter-cake formation interact to control slurry-supported face stability. These findings provide a mechanistic basis for selecting slurry properties and operational pressures that promote timely cake formation near the excavation face while avoiding excessive slurry penetration and fluid loss.

4.5 Summary

This chapter investigated how injection pressure Δp, soil grain size, and slurry concentration c influence bentonite–slurry infiltration and pressure transfer in sands using column experiments with continuous pore-water pressure (PWP) measurements and the determination of post-test concentration profiles.

The results show that infiltration behaviour is governed by the interaction between soil permeability, driving pressure, and slurry rheology. In the coarse sand (S 1.0–2.0 mm), B20–B60 penetrated the full column, whereas B80 developed an internal filtration zone. The effect of injection pressure depended on grain size: in S 0.5–1.0 mm, internal filtration occurred at $\Delta p = 30$ and 50 kPa, whereas full penetration occurred at $\Delta p = 100$ and 200 kPa; in S 0.1–0.5 mm, internal filtration occurred at all four tested pressure differences, although the filtration front generally shifted farther from the inlet as Δp increased. Higher slurry concentrations promoted earlier filtration and reduced effective permeability even in coarse sand.

The combined interpretation of equivalent penetration depth, selected PWP profiles, and post-test concentration distributions consistently identified the location of the filtration zone and the prevailing infiltration regime. These results provide experimental insight into the mechanisms governing slurry pressure transfer and filter-cake formation relevant to slurry-supported TBM operations.

The experiments represent controlled one-dimensional infiltration conditions and therefore provide mechanistic guidance for face-support control, while additional field factors such as excavation disturbance and groundwater chemistry require consideration in practice.

5 Soil-bentonite slurry interface properties: microstructural investigation

In this chapter, the microstructural interactions between bentonite slurry and granular soils during slurry infiltration into the sand skeleton are investigated. A specialised scanning electron microscopy technique, Cryo-Broad Ion Beam SEM (Cryo-BIB-SEM), was employed to obtain detailed and undisturbed images of slurry structures from their initial hydrated states to their transformation under pressure and subsequent infiltration into the sand. The high-resolution images reveal pore geometry, particle alignment, and the formation of sealing layers at sand–slurry interfaces at the microscale.

Eight sample preparations representing different slurry and infiltration states yielded nine specimens for Cryo-BIB-SEM analysis at MAP Microstructure and Pores GmbH, Aachen by Dr. Joyce Schmatz (see for example Schmatz et al. (2017)). The investigated samples represent four characteristic regimes: pure slurry structures, external filter cakes, soil–slurry interfaces, and internal infiltration zones within the sand skeleton.

5.1 Objectives of the study

The objective of this chapter is to investigate the microstructural evolution of bentonite slurry during slurry infiltration into granular soils. Particular attention is given to the interaction between bentonite particles and the sand skeleton and to the resulting structural changes within the slurry and the surrounding pore space.

The specific objectives are to characterise the microstructure of bentonite slurry in its initial state, to examine the formation and structure of filter cakes and boundary zones at the bentonite–sand interface during infiltration, and to analyse the distribution and

arrangement of bentonite within the infiltrated sand skeleton. In addition, the influence of slurry composition and infiltration history on the resulting microstructure is investigated.

5.2 Experimental programme

The experimental programme comprised eight preparations yielding nine analysed specimens (S1, S2, S3.1, S3.2, and S4–S8), organised into four thematic sets (A–D) to investigate different microstructural regimes of bentonite slurry and its interaction with granular soils. Specimens S3.1 and S3.2 were subsamples obtained from the same filter-cake preparation. The investigated sample conditions are summarised in Table 5.1, while the corresponding bulk state parameters of the specimens are listed in Table 5.2. The sets represent distinct states ranging from pure slurry structures to external filter cakes, soil–slurry interfaces, and internal infiltration zones within the sand skeleton.

Specimens belonging to Set A were prepared as remoulded pure slurry samples, while the remaining specimens were generated either in a filter press (Set B) or in a separate small-scale infiltration column (Sets C and D). The cylindrical test section of this column was 22 cm high and 10 cm in internal diameter. The sand layer occupied the central part of the column, with the slurry placed above it and a filter stone below it to allow water to drain through the basal outlet. This top-to-bottom arrangement was selected so that the slurry reached the sampling positions over the shortest practical flow path and the specimens could be recovered with minimal disturbance; the geometry of the small column did not permit bottom-to-top operation. After each test, the specimen-containing moulds were recovered and prepared using the sample-specific procedures described in Section 3.7. Details of the Cryo-BIB-SEM preparation and imaging procedures are therefore not repeated here.

Set A: Remoulded pure bentonite slurry (S1, S2). This set represents reference microstructures of bentonite slurry without interaction with porous media. Two slurry states were prepared: a dense slurry near the liquid limit (S1) and a fluid B60 slurry (S2). Both Set A slurry samples were prepared with distilled water, whereas tap water was used for the remaining specimens. Although water chemistry can affect bentonite fabric, this difference was not expected to dominate the structural changes caused by filtration and infiltration; comparisons between Set A and the remaining specimens are therefore interpreted primarily in terms of these mechanisms. Small quantities of slurry were frozen directly by dropping them into liquid nitrogen to preserve the hydrated slurry structure and minimise structural disturbance.

Table 5.1: Summary of conditions for microstructural investigation

Sample	Slurry composition	Host sand (mm)	Δp (kPa)	Time (h)	Remarks
Set A: Remoulded pure bentonite slurry					
S1	1.1×LL	—	—	—	Dense slurry reference (near liquid limit)
S2	B60	—	—	—	Fluid slurry reference (high water content)
Set B: External filter cake					
S3.1	B60	—	400	48	External filter cake, 12 mm above bottom drainage
S3.2	B60	—	400	48	External filter cake, 6 mm above bottom drainage
Set C: Sand–slurry interface					
S4	B60	0.1–0.5	50	1	Bentonite slurry–fine sand interface at the infiltration front
S5	B40 + S	1.0–2.0 0.1–0.5	50	1	Sand-loaded slurry (10 $\mathrm{g\,L^{-1}}$) at coarse-sand interface
Set D: Internal infiltration					
S6	B60	0.1–0.5	50	1	Internal filter cake, 45 mm behind interface in fine sand
S7	B60	0.5–1.0	50	1	Internal filter cake, 49 mm behind interface in medium-coarse sand
S8	B60	0.1–0.5	—	—	Remoulded slurry–sand mixture

Set B: External filter cake (S3.1, S3.2). External filter-cake samples were produced using a filter press device. Pure B60 slurry was placed onto filter paper and subjected to a constant pressure of 400 kPa for approximately 48 h, resulting in the formation of a compact bentonite filter cake. Two specimens were extracted from different vertical positions relative to the drainage boundary: Sample S3.1 from approximately 12 mm above the bottom drainage and Sample S3.2 from approximately 6 mm above the bottom drainage. These samples represent consolidated filter-cake structures formed under sustained filtration conditions.

Before freezing, only the external filter-cake specimens were trimmed where necessary, and only in the vertical direction. They were then completely removed from both halves of the split mould and immersed in liquid nitrogen.

Set C: Sand–slurry interface (S4, S5). This set investigates the formation of filter cakes and interface structures at the infiltration front between bentonite slurry and sand. The sampling moulds were positioned directly at the slurry–sand interface within the infiltration column so that they captured the microstructure developing at the infiltration front.

Sample S4 represents infiltration of pure B60 slurry onto a fine sand layer (0.1–0.5 mm) under a pressure difference of $\Delta p = 50$ kPa for 1 h. In contrast, Sample S5 examines the influence of sand particles present within the slurry itself. For this specimen, the slurry was pre-loaded with fine sand particles (B40 slurry containing 10 $\mathrm{g\,L^{-1}}$ of 0.1–0.5 mm sand) and infiltrated onto a coarser sand layer (1.0–2.0 mm) under identical pressure and time conditions. After infiltration, the specimen-containing split moulds were recovered from the column. The specimens were not trimmed; one mould half was removed, and each specimen was gently pushed from the remaining half directly into liquid nitrogen. Both mould halves were therefore removed before freezing.

Set D: Internal infiltration (S6, S7, S8). The final set focuses on microstructures formed within the internal infiltration zone of the sand skeleton. In these tests, the sampling moulds were embedded within the host sand skeleton prior to slurry infiltration. Sample S6 was positioned approximately 45 mm behind the slurry–sand interface within fine sand (0.1–0.5 mm), while Sample S7 was located approximately 49 mm behind the interface within medium-coarse sand (0.5–1.0 mm). In both cases, slurry infiltration occurred under a pressure difference of $\Delta p = 50$ kPa for 1 h, resulting in the formation of internal filter cakes within the pore space of the sand skeleton.

Sample S8 served as a remoulded control specimen. In this case, slurry and sand were manually mixed to reproduce the bulk state corresponding to Sample S6 and the mixture was compacted directly into the sampler without undergoing infiltration. Comparison between this remoulded specimen and the infiltrated samples allows isolation of microstructural changes associated specifically with the infiltration process.

Samples S6 and S7 were not trimmed and followed the same complete-demoulding and direct-immersion procedure as Samples S4 and S5. Sample S8 was removed from its split sampler without trimming before freezing. All specimens were rapidly frozen in liquid nitrogen after their sample-specific preparation to preserve the original microstructure prior to Cryo-BIB-SEM imaging.

Table 5.2: Bulk state parameters of the Cryo-BIB-SEM samples

Sample	C_b^* (-)	w (-)	e (-)	I_D (-)
S1	0.286	3.49	–	–
S2	0.058	17.33	–	–
S3.1	–	5.09	–	–
S3.2	–	5.07	–	–
S4	–	–	0.76	0.31
S5	–	–	0.65	0.67
S6	–	–	0.72	0.60
S7	–	–	0.64	0.68
S8	–	–	0.72	0.60

$C_b^* = m_{b,d}/m_w = 1/w$ is the dry bentonite-to-water mass ratio, where $m_{b,d}$ is the dry bentonite mass, m_w is the water mass, and $w = m_w/m_{b,d}$ is the gravimetric water content.

5.3 Microstructural results and interpretation

5.3.1 Remoulded bentonite slurries (Set A)

The microstructure of the two remoulded slurry samples S1 and S2 is shown in Fig. 5.1. The images were obtained using the secondary electron detector (SE2) of the scanning electron microscope (SEM), which provides topographic contrast between the bentonite solid matrix and the pore space.

Samples S1 and S2 correspond to the two reference slurry states defined in Section 5.2. S1 represents a dense slurry at approximately 1.1× the liquid limit (w = 3.49), while S2 corresponds to the B60 slurry (w = 17.33). The 1.1LL slurry is used here as a soil-mechanics reference state for clay suspensions with documented microstructural fabric (Ben Rhaiem et al., 1987).

The overview micrographs in Fig. 5.1a–b reveal pronounced differences in the spatial arrangement of the bentonite solid matrix. In Sample S1 (Fig. 5.1a), the microstructure appears relatively dense and heterogeneous, forming a network-like fabric in which elongated and irregular pores are distributed between interconnected clay aggregates. The pore space is generally narrow and tortuous, with characteristic dimensions on the order of a few micrometres. Although many pores appear elongated and aligned with the surrounding particle framework, nearly circular pore shapes can also be observed locally.

In contrast, the B60 slurry in Sample S2 (Fig. 5.1b) exhibits a considerably more open structure. The bentonite solid matrix appears less compact and the pore network is wider and more continuous. Individual pores and channels are visibly larger than in S1 and frequently extend over several micrometres between adjacent solid domains. This observation is consistent with classical descriptions of particle interactions in clay suspensions, where increasing water content promotes separation of platelet aggregates and expansion of the pore network (van Olphen, 1964).

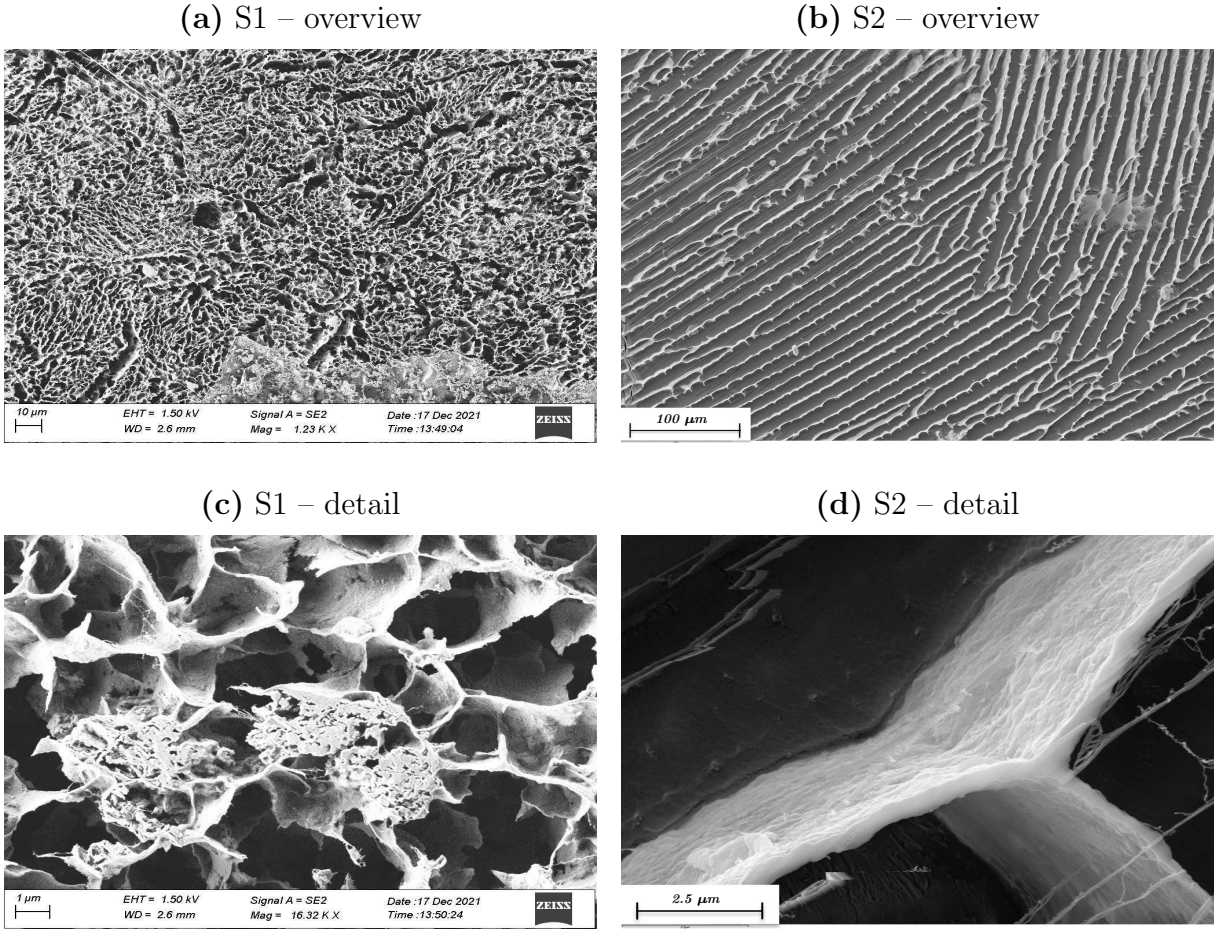

Figure 5.1: Microstructure of remoulded bentonite slurries at two hydration states. (a) Overview of slurry S1 ($w = 3.49$) showing a relatively dense network of bentonite aggregates with narrow and elongated pores. (b) Overview of slurry S2 ($w = 17.33$) exhibiting a more open structure with wider interconnected pores. (c) Higher-magnification view of S1 showing an interwoven platelet fabric forming narrow slit-like pores. (d) Higher-magnification view of S2 showing thicker platelet stacks separated by wider pore channels. Scale bars as indicated. Solid bentonite appears in light grey, whereas pores and water-filled regions appear darker.

Higher-magnification images provide additional insight into the internal fabric of the bentonite aggregates. The detailed micrograph of Sample S1 (Fig. 5.1c) shows an interwoven network of bentonite platelets forming irregular aggregates. Individual particles are difficult to distinguish within this structure because they are tightly stacked and interlocked, creating narrow slit-like pores between adjacent platelet stacks. The pore space between the network-like walls typically ranges from roughly one to a few micrometres. Localised denser clusters of particles can occasionally be observed; these may result either from incomplete homogenisation during slurry preparation or from minor artefacts produced during the ion-beam milling step of the BIB preparation.

The detailed view of Sample S2 (Fig. 5.1d) shows a markedly different arrangement. Instead of the dense interwoven fabric seen in S1, the structure consists of thicker platelet stacks forming the walls of larger pore channels. These solid domains appear as bright laminar structures separating darker pore regions. The thickness of the platelet stacks is typically on the order of one to a few micrometres, while the adjacent pore space is substantially wider than in Sample S1. Similar expanded microstructures of hydrated bentonite suspensions have been reported using cryogenic electron microscopy techniques (Deirieh et al., 2018).

Overall, the comparison between Samples S1 and S2 demonstrates that the dominant control on the observed slurry microstructure is the large difference in water content and solids concentration between the two suspensions. The dense slurry S1 forms a compact network of bentonite aggregates with narrow pores, whereas the highly hydrated B60 slurry develops a more open structure with larger interconnected voids.

5.3.2 Microstructure of external filter cake samples (Set B)

Samples S3.1 and S3.2 originate from the same bentonite filter cake, which was sliced horizontally after the filtration test. Sample S3.1 represents the upper part of the cake, located farther from the drainage boundary, whereas Sample S3.2 was taken from the lower part of the cake in close proximity to the drainage boundary at the filter paper. Although both samples consist of the same bentonite material, their microstructures differ markedly as a consequence of their position within the filter cake.

The overview micrographs in Fig. 5.2a–b illustrate these differences. In Sample S3.1 (Fig. 5.2a), the pore structure appears relatively coarse, with interconnected voids and channels that locally exceed several micrometres in width. In contrast, the overview image of Sample S3.2 (Fig. 5.2b) reveals a considerably finer and more compact structure, in

which the pores are smaller and the solid matrix appears more densely packed. The higher-magnification images further emphasise this contrast. In Sample S3.1 (Fig. 5.2c), the bentonite platelets form loosely arranged aggregates separated by relatively wide pore spaces. In contrast, the microstructure of Sample S3.2 (Fig. 5.2d) shows a denser arrangement of platelet stacks with narrower pores and a more compact solid framework.

The observed differences reflect the progressive development of the filter cake during the filtration process. In the vicinity of the drainage boundary, pore pressure dissipates more rapidly, resulting in stronger compression of the bentonite matrix and therefore a denser microstructure. At larger distances from the drainage boundary, the effective stress acting on the cake is lower and the solid structure remains more open. This results in a graded pore structure within the filter cake, with smaller pores and a denser fabric near the filter paper and larger pores farther away from the drainage boundary.

Such a structural gradient is consistent with the mechanics of filtration and consolidation under one-sided drainage conditions. The denser microstructure observed in S3.2 therefore reflects the stronger consolidation near the drainage boundary, whereas the more open structure in S3.1 corresponds to the less compressed region of the cake located farther from the drainage surface.

(a) S3.1 – overview

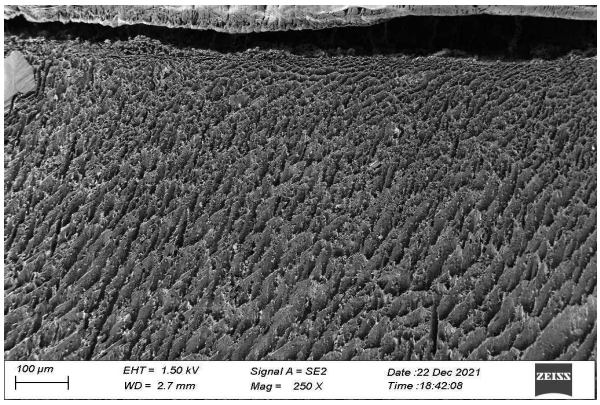

(b) S3.2 – overview

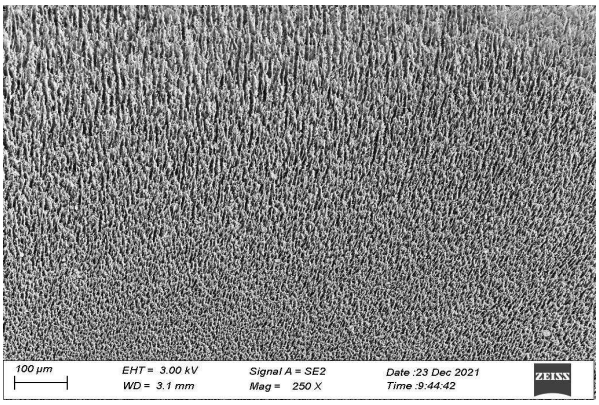

(c) S3.1 – detail

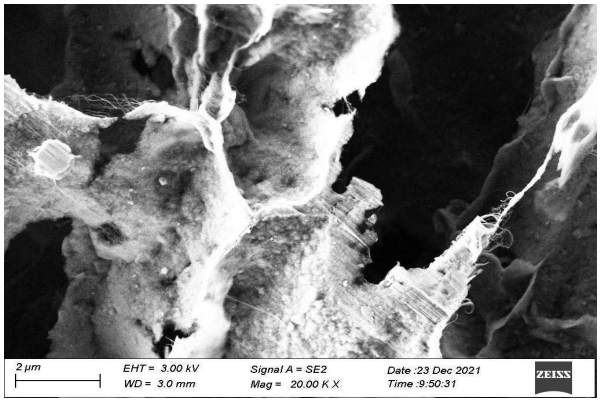

(d) S3.2 – detail

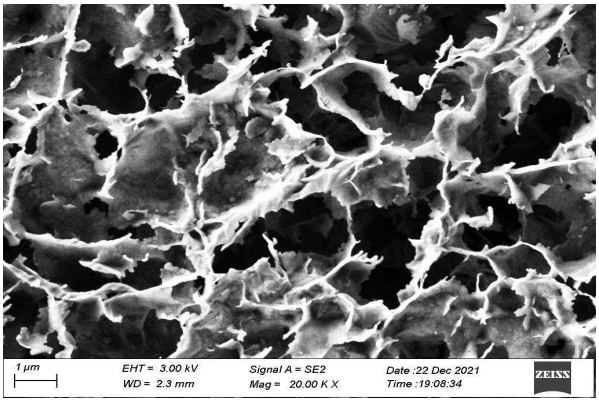

Figure 5.2: Microstructure of two sub-samples taken from the same bentonite filter cake. (a) Overview of the upper region S3.1, located farther from the drainage boundary, showing a coarser and less compact pore structure. (b) Overview of the lower region S3.2, located closer to the drainage boundary, showing a finer and denser fabric. (c) Higher-magnification view of S3.1 revealing larger pores between bentonite aggregates. (d) Higher-magnification view of S3.2 showing a denser solid matrix with smaller pores. Scale bars as indicated. Solid bentonite appears in light grey, whereas pores and water-filled regions appear darker.

5.3.3 Microstructure at sand–slurry interfaces (Set C)

Samples S4 and S5 represent bentonite slurry interaction with granular soil at the infiltration front. Figure 5.3 presents Cryo-BIB-SEM observations of the corresponding sand–slurry interfaces. Panels (a,c,e) correspond to Sample S4, representing pure B60 slurry infiltrating fine quartz sand (0.1–0.5 mm), whereas panels (b,d,f) correspond to Sample S5, where a sand-loaded B40 slurry interacts with coarse quartz sand (1–2 mm).

In Sample S4, the SE image (Fig. 5.3a) shows angular quartz grains separated by relatively narrow intergranular pores. These pores are largely filled by a thin bentonite layer forming a continuous coating on the grain surfaces. The corresponding BSE image (Fig. 5.3c) highlights the compositional contrast between bright quartz grains and the darker bentonite matrix, confirming that the bentonite film closely follows the sand surface and locally bridges small pore throats.

The EDS elemental map (Fig. 5.3e) supports this interpretation. The elemental colour legend for the EDS signals is shown above the map. Quartz grains are characterised by strong Si signals, while the bentonite layer shows combined signals of Si, Al and Na, which are characteristic of smectitic clay minerals. Because several elements are mapped simultaneously, mixed colours may occur where elemental signals overlap. The elemental distribution confirms that the intergranular region is dominated by bentonite with only limited quartz inclusions. This thin coating indicates that slurry penetration into the fine sand matrix is limited and that sealing occurs mainly through the formation of a bentonite film at the sand surface.

In contrast, Sample S5 exhibits a markedly different interface structure. In the SE image (Fig. 5.3b), larger pores between coarse sand grains are visible, allowing the slurry to intrude into the voids and form irregular bentonite tongues extending into the pore space. The corresponding BSE image (Fig. 5.3d) reveals bentonite bridges connecting neighbouring quartz grains, indicating that the slurry occupies a larger portion of the pore network than observed in S4. The EDS map (Fig. 5.3f) shows a more heterogeneous distribution of bentonite within the pore space, consistent with a thicker and more irregular clay structure between the coarse grains.

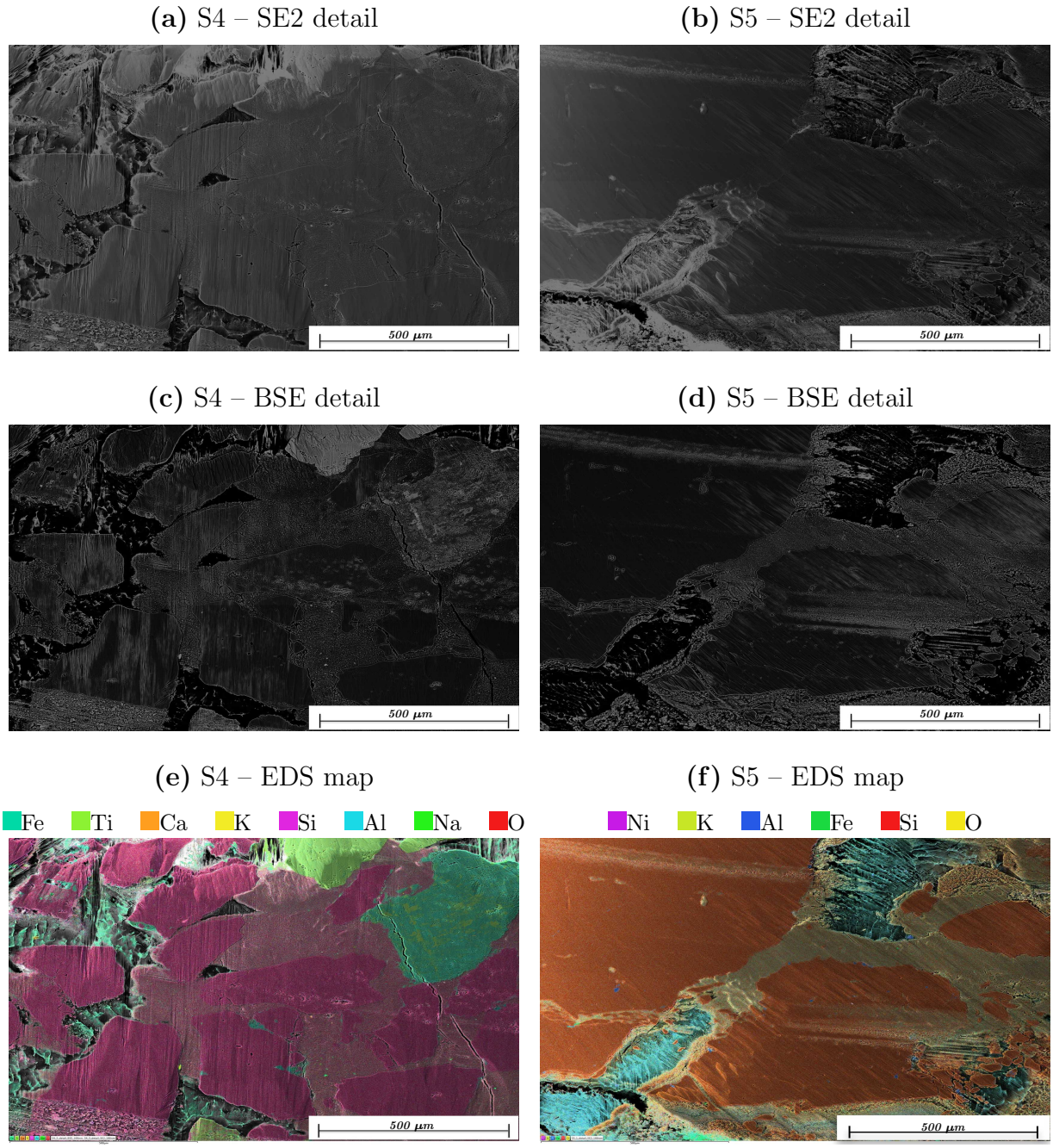

Figure 5.3: Cryo-BIB-SEM micrographs of the bentonite–sand contact zones in Samples S4 and S5. Panels (a,c,e) show the interface in Sample S4, representing pure B60 slurry on fine quartz sand, whereas panels (b,d,f) show the interface in Sample S5, representing sand-loaded B40 slurry on coarse quartz sand. The first row shows secondary electron (SE) images, the second row corresponding backscattered electron (BSE) images, and the third row energy-dispersive spectroscopy (EDS) elemental maps. The elemental colour legends are shown in panels (e) and (f); mixed colours correspond to overlapping elemental signals. Scale bars as indicated.

These observations show that the different interface morphologies of S4 and S5 reflect the combined effects of host-sand pore geometry and slurry composition. In S4, the smaller pore throats of the fine host sand restrict B60 slurry penetration, leading to a thin bentonite coating at the pore entrances. In S5, the larger pores of the coarse host sand permit deeper intrusion of the B40 slurry, while the added fine sand (10 g L^{-1}, 0.1–0.5 mm) could be retained together with bentonite at pore constrictions and contribute to local bridging and to the more heterogeneous interfacial structure. However, because slurry concentration, fine-sand loading, and host-sand size were varied simultaneously between S4 and S5, the contribution of each factor cannot be isolated from this comparison. The thicker, more spatially variable interface observed in S5 should therefore be interpreted as the combined outcome of these differences rather than as an effect of host-sand grain size alone.

5.3.4 Microstructure of internal infiltration structures (Set D)

Samples S6 and S7 represent bentonite slurry structures formed inside the sand skeleton several centimetres behind the infiltration front. In contrast to the interface samples of Set C, these specimens capture the internal microstructure that develops after slurry has penetrated the pore network of the host sand.

Figure 5.4 presents Cryo-BIB-SEM observations of the internal infiltration zone. Panels (a,c,e) correspond to Sample S6, taken approximately 45 mm behind the infiltration front within fine sand (0.1–0.5 mm), whereas panels (b,d,f) correspond to Sample S7, taken approximately 49 mm behind the infiltration front within medium-coarse sand (0.5–1.0 mm).

In Sample S6 (Fig. 5.4a,c), quartz grains form the host skeleton while bentonite occupies a large portion of the intergranular pore space. The BSE image clearly distinguishes the brighter quartz grains from the darker bentonite matrix. The EDS map (Fig. 5.4e) confirms this interpretation: quartz grains are dominated by silicon signals, whereas the bentonite phase exhibits overlapping signals of silicon, aluminium, and sodium characteristic of smectitic clay minerals. Minor signals of potassium, iron, calcium, magnesium, and titanium occur locally as trace components. Because several elements contribute simultaneously to the detected signal, colours in the EDS map often appear as mixed shades rather than pure elemental colours.

Structurally, the bentonite in S6 forms a three-dimensional network within the pore space between sand grains. The clay phase fills much of the available pore volume and lo-

cally forms connections between adjacent grains, producing a relatively compact internal structure within the fine sand skeleton.

The microstructure observed in Sample S7 differs due to the larger pore geometry of the host sand. In the SE2 image (Fig. 5.4b), bentonite occurs as strands and sheet-like structures extending across wider intergranular pores formed by the medium-coarse sand grains. The corresponding BSE image (Fig. 5.4d) again highlights the compositional contrast between quartz grains and bentonite. The EDS map (Fig. 5.4f) confirms the same mineralogical composition as in S6, while the bentonite distribution appears more heterogeneous within the larger pore network.

Compared with S6, the internal structure in S7 is visibly more open, with larger pores remaining partially unfilled and bentonite forming irregular bridges and sheets between grains. This difference reflects the influence of the host-sand grain size: the smaller pore space in fine sand promotes a denser bentonite structure (S6), whereas the larger pores of the medium-coarse sand allow a more open clay network (S7). These observations illustrate how the pore geometry of the host sand controls the spatial distribution and connectivity of bentonite within the infiltrated sand skeleton.

Figure 5.5 presents Cryo-BIB-SEM observations of Sample S8, which was prepared by manually mixing B60 slurry with fine sand to reproduce the bulk state of Sample S6 (Table 5.2), but without any infiltration history. The sample therefore represents a remoulded slurry–sand mixture that has not been subjected to filtration or infiltration processes.

The secondary electron image (Fig. 5.5a) shows a relatively dense and uniform clay matrix in which quartz grains are embedded within the bentonite mass. Only small voids are visible, and the overall structure appears comparatively homogeneous. The corresponding backscattered electron image (Fig. 5.5b) confirms this interpretation: quartz grains appear as brighter regions, while the surrounding bentonite matrix forms a continuous darker phase. Grain boundaries are less clearly expressed than in the infiltrated samples, indicating that the sand particles are dispersed within the clay matrix rather than forming a connected granular skeleton.

The energy-dispersive spectroscopy elemental map (Fig. 5.5c) further illustrates the chemical distribution within the remoulded material. Quartz grains are characterised by strong silicon signals, whereas the bentonite matrix shows overlapping signals of Si, Al, and Na associated with smectitic clay minerals. Minor signals from Ca, Fe, and K occur locally as trace phases. Because the EDS colours represent individual elemental signals, mixed colours may appear where several elements overlap within the same region.

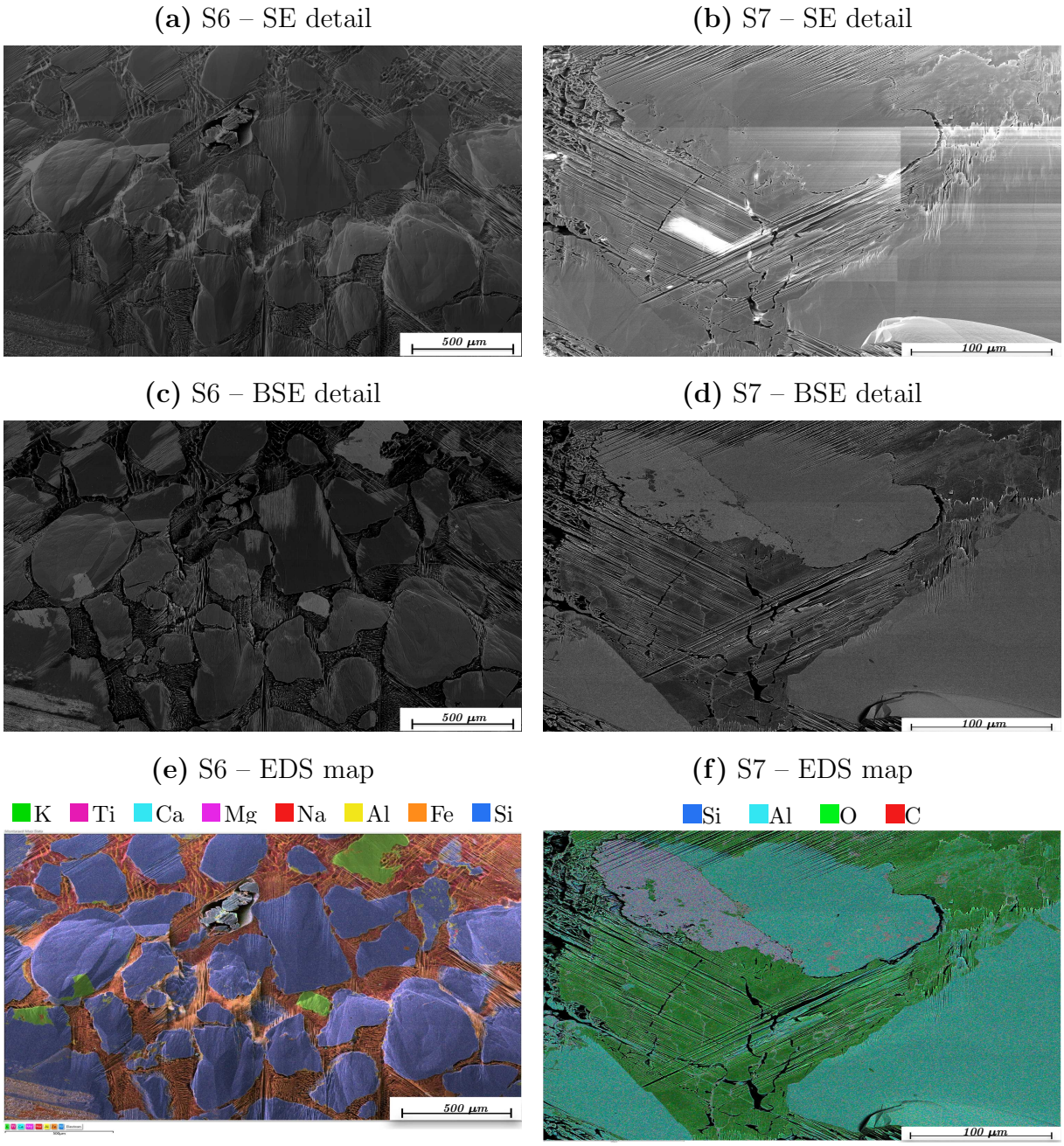

Figure 5.4: Cryo-BIB-SEM micrographs of the internal infiltration zone in Samples S6 and S7. Panels (a,c,e) correspond to Sample S6, taken 45 mm behind the infiltration front in fine sand (0.1–0.5 mm) after infiltration with pure B60 slurry, whereas panels (b,d,f) correspond to Sample S7, taken 49 mm behind the infiltration front in medium-coarse sand (0.5–1.0 mm) after infiltration with pure B60 slurry. The first row shows secondary electron (SE2) images, the second row corresponding backscattered electron (BSE) images, and the third row energy-dispersive spectroscopy (EDS) elemental maps. The elemental colour legends are shown above the EDS panels. Scale bars as indicated.

(a) S8 – SE detail

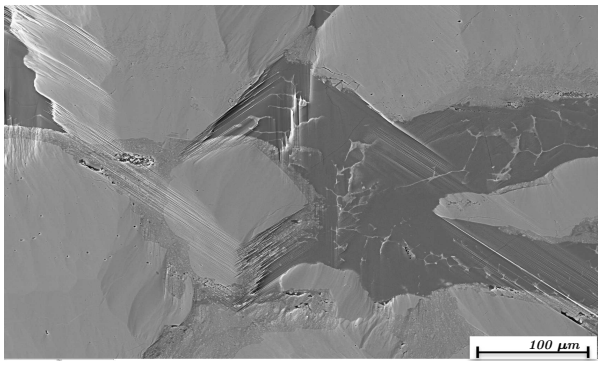

(b) S8 – BSE detail

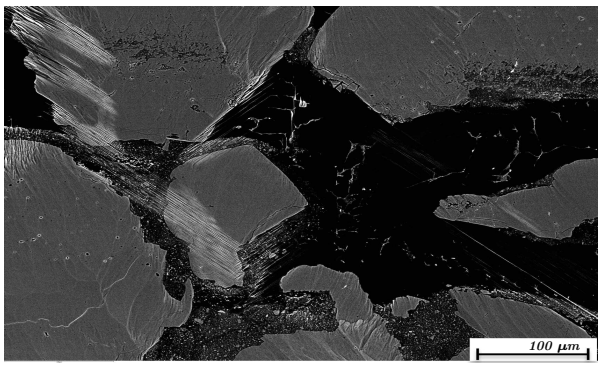

(c) S8 – EDS map

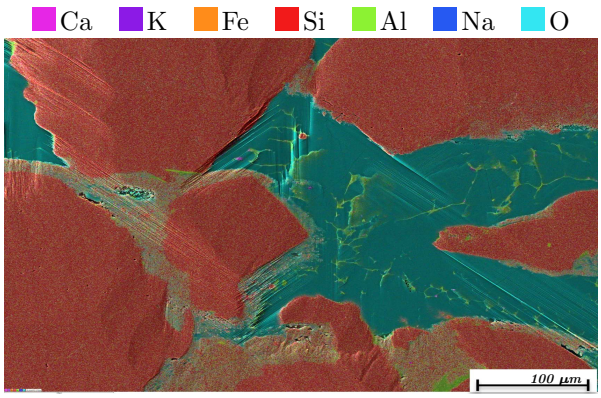

Figure 5.5: Cryo-BIB-SEM micrographs of Sample S8, a remoulded B60 slurry prepared to reproduce the composition of Sample S6 without an infiltration history. (a) Secondary electron (SE2) image. (b) Corresponding backscattered electron (BSE) image. (c) Energy-dispersive spectroscopy (EDS) elemental map. The elemental colour legend is shown above panel (c). Scale bars as indicated.

Compared with the infiltrated samples, the remoulded specimen lacks the organised pore network and grain-to-grain bridges observed in the internal infiltration structures. Instead, quartz grains are dispersed within a continuous bentonite matrix without a preferred orientation or distinct pore channels. This microstructure reflects the absence of flow-induced particle rearrangement and consolidation.

The comparison between Samples S8 and S6 therefore highlights the influence of infiltration history on the internal structure of bentonite–sand mixtures. While both samples share the same slurry composition and host sand (Table 5.2), Sample S8 represents a mechanically mixed reference state with a relatively isotropic clay fabric. In contrast, the infiltrated Sample S6 exhibits a structured internal arrangement in which bentonite forms bridges between sand grains and develops open intergranular pathways. These differences demonstrate that slurry infiltration processes can significantly reorganise the internal clay fabric within the pore network of the host sand.

5.3.5 Possible preparation artefacts in Cryo-BIB-SEM images

During the inspection of several Cryo-BIB-SEM images, features were observed that are interpreted as preparation-related artefacts rather than intrinsic microstructural elements of the bentonite–soil system. Such artefacts may arise during cryogenic freezing, specimen transfer, trimming of frozen samples, or during the final broad-ion-beam milling step used to prepare flat observation surfaces.

One type of feature consists of straight, parallel channels that appear predominantly near specimen edges (Fig. 5.6a,c). These channels are aligned in a uniform direction and differ from the irregular pore networks observed within the interior of the samples. Similar structures have been reported in BIB-SEM investigations of porous materials and attributed to minor beam chatter or surface instabilities during the final stages of ion-beam milling (Holzer and Cantoni, 2012).

A second type of feature consists of broader sheet-like cracks occurring in regions with high water content (Fig. 5.6b). These structures resemble freezing-induced artefacts described in cryogenic SEM investigations of hydrated clay systems (Desbois et al., 2013). Rapid freezing may locally redistribute pore water or generate stresses during ice formation, producing planar cracks that are not representative of the original slurry microstructure. Comparable preparation effects have also been discussed for bentonite suspensions investigated by cryogenic electron microscopy (Deirieh et al., 2018).

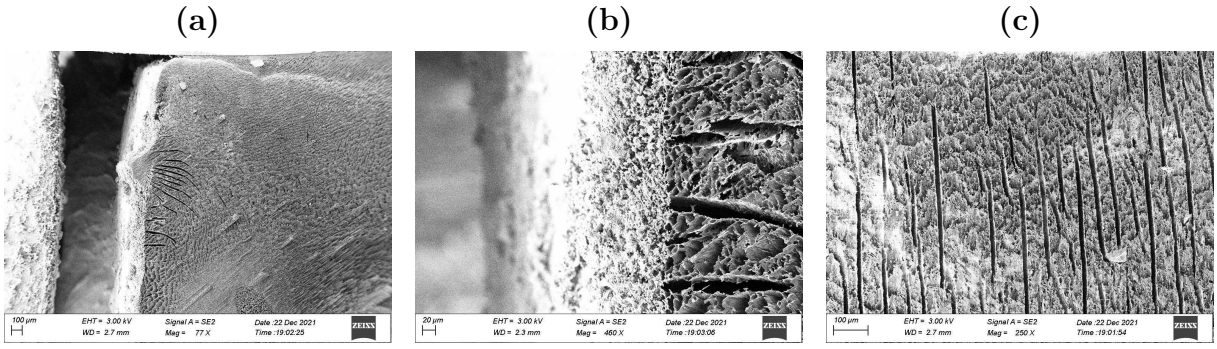

Figure 5.6: Examples of possible preparation artefacts observed in Cryo-BIB-SEM images. (a,c) Straight, parallel channels located near specimen edges; (b) sheet-like cracking observed in a region with high water content. These structures occur locally near specimen boundaries and are interpreted as preparation-related artefacts rather than intrinsic pore structures.

Additional Cryo-BIB-SEM images obtained from Sample S7 show complex clay textures that illustrate the three-dimensional morphology of bentonite structures within larger pores of the sand skeleton. Selected examples are presented in Fig. 5.7. Panel (a) shows a pore wall where bentonite forms parallel plate-like ribs. Panel (b) illustrates a honeycomb-like clay network filling a pore corner. Panel (c) shows clay sheets and thin bridges surrounding a quartz grain.

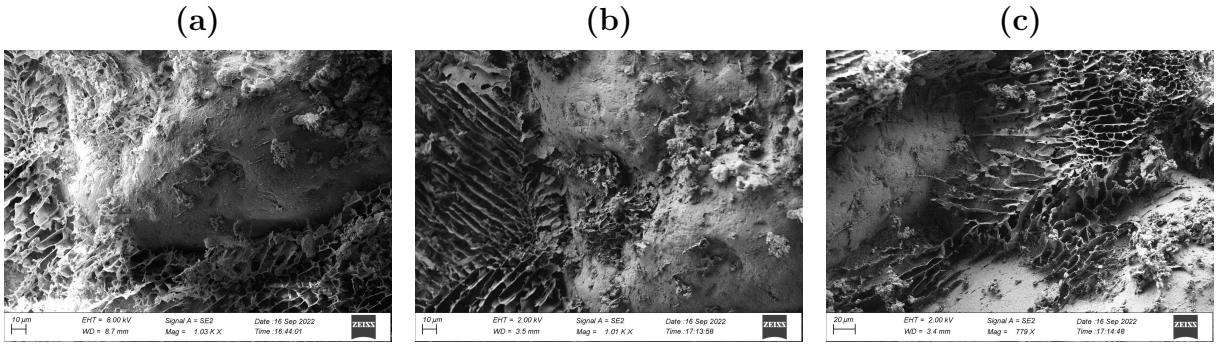

Figure 5.7: Selected secondary electron (SE2) micrographs illustrating three-dimensional clay textures within Sample S7. (a) Parallel bentonite ribs along a pore wall; (b) honeycomb-like clay structure within a pore corner; (c) clay sheets and thin bridges surrounding a quartz grain. Scale bars as indicated.

Although such images provide useful visualisation of possible clay arrangements within larger pores, some observed features may also be influenced by specimen preparation. Fragmented ribs, open slots, or thin connecting bridges may partly result from sample

trimming, fracture preparation, or proximity to specimen edges. Consequently, these images should be regarded as illustrative examples of possible clay textures rather than statistically representative features of the internal infiltration zone.

To minimise the influence of preparation-related artefacts, all pore-size and platelet-gap observations presented in the preceding sections were derived from regions interpreted as representative of the intrinsic microstructure. In particular, areas located near specimen edges or containing clearly aligned channel-like features were excluded from the analysis.

5.4 Summary

This chapter presented a Cryo-BIB-SEM investigation of bentonite slurry interacting with quartz sand under different infiltration conditions. The analysed specimens represent four characteristic regimes: pure slurry structures, external filter cakes, sand–slurry interface zones, and internal infiltration structures within the sand skeleton. These observations provide microstructural insight into the mechanisms governing slurry penetration and filter-cake formation in granular soils.

The main findings can be summarised as follows:

- **Pure slurry structures (S1, S2).** The microstructure of bentonite slurry depends strongly on its hydration state. The near-liquid-limit slurry (S1) forms a dense platelet fabric with narrow, elongated pores, whereas the fluid B60 slurry (S2) exhibits a more open, gel-like network with larger and more interconnected pores. These differences reflect the higher water content and lower solids concentration in S2, resulting in a more permeable and deformable structure.
- **External filter-cake structures (S3.1, S3.2).** The filter cake exhibits a vertical microstructural gradient: S3.2, located closer to the drainage boundary, has a denser fabric and smaller pores than S3.1 farther from the drainage boundary.
- **Sand–slurry interface structures (S4, S5).** At the sand–slurry contact, bentonite forms interfacial structures whose geometry depends on slurry composition and grain size. Pure B60 slurry (S4) forms a thin and relatively uniform bentonite coating along fine sand grain surfaces, effectively sealing pore entrances. In contrast, the sand-loaded B40 slurry (S5) produces a thicker and more heterogeneous interface zone in which bentonite occupies larger pore spaces and forms bridges between grains. Although initially more permeable, this structure can compact under stress and develop into an effective filter cake.

- **Internal infiltration structures (S6, S7) and remoulded reference (S8).** Within the sand skeleton, infiltrating bentonite forms three-dimensional bridge networks connecting adjacent grains. In fine sand (S6), the bentonite structure appears relatively compact with narrower channels, whereas in medium-coarse sand (S7) larger pore spaces allow the formation of wider intergranular channels and a more open network. The remoulded reference sample (S8) lacks these infiltration-related features and shows a dense, homogeneous clay matrix with dispersed quartz grains.
- **Chemical composition and preparation artefacts.** EDS maps confirm that bentonite structures are dominated by Si–Al–Na signals characteristic of smectitic clay minerals, whereas quartz grains are identified by their strong Si signal. Minor elements (Fe, Ca, K, Mg, Ti) occur locally but do not control the overall fabric. Preparation-related artefacts such as milling-induced channels or freezing cracks were identified near specimen edges and excluded from the microstructural interpretation.

Overall, the Cryo-BIB-SEM observations demonstrate how slurry composition, sand grain size, and infiltration history control the formation of bentonite sealing structures in granular soils. Surface films tend to develop at sand–slurry interfaces, while deeper infiltration produces bentonite bridge networks within the pore space. These mechanisms explain the permeability reduction and filter-cake development observed in filtration and column infiltration experiments relevant to slurry-shield tunnelling.

6 Monotonic and cyclic triaxial behaviour of slurry-infiltrated sand

Monotonic and cyclic triaxial tests were conducted to examine how bentonite slurry infiltration affects the mechanical behaviour of sand. The chapter is organised into two parts. The first presents monotonic triaxial tests performed under drained and undrained conditions to investigate the stress–strain response and critical-state characteristics of slurry-infiltrated sand. The second part presents cyclic undrained triaxial tests used to assess the influence of bentonite infiltration on the cyclic resistance and liquefaction behaviour of the material.

6.1 Objectives

The objective of this chapter is to clarify how bentonite slurry infiltration modifies the mechanical response of sand and how these changes depend on specimen preparation and bentonite content within the sand skeleton. The study aims to relate the monotonic and cyclic triaxial behaviour of the material to infiltration-induced changes in soil fabric and to interpret the experimental observations within the framework of critical-state soil mechanics.

6.2 Test programme

The experimental programme comprises monotonic and cyclic triaxial tests performed on clean sand, slurry-infiltrated sand, and sand–slurry mixtures prepared using different specimen preparation methods.

The slurry grades B20, B40, B60, and B80 denote nominal preparation dosages of 20, 40, 60, and 80 g of as-received bentonite powder per litre of added mixing water, as defined in

Chapter 3. Numerical concentrations reported for the triaxial specimens are the moisture-corrected dry-bentonite-to-mixing-water mass ratios, $C_{\mathrm{bentonite}} = 100 m_{b,d}/m_{w,\mathrm{mix}}$, where the dry bentonite mass $m_{b,d}$ is obtained from the measured wet and oven-dry powder masses and $m_{w,\mathrm{mix}}$ is the mass of added mixing water. Using the density of water, this is the mass-ratio representation of the moisture-corrected inlet concentration reported in g/L in Chapter 4; batch-specific values may differ slightly from the nominal B grade.

6.2.1 Monotonic triaxial tests

A series of monotonic triaxial tests was conducted to investigate the influence of bentonite concentration and specimen preparation methods on the mechanical shear response of sand. The programme included isotropically consolidated drained (CID) and isotropically consolidated undrained (CIU) tests and was organised into two groups. The first group examined the effect of bentonite concentration in infiltrated sand specimens obtained from the column infiltration experiments, while the second group investigated the influence of specimen preparation and initial stress conditions by comparing clean sand prepared by air pluviation, specimens extracted from the infiltration column, and slurry–sand mixtures prepared by wet tamping. The corresponding test matrix is summarised in Table 6.1.

Table 6.1: Overview of monotonic triaxial tests.

Test ID	Specimen type	Preparation method	I_D [–]	$C_{\mathrm{bentonite}}$ [%]	Type	σ_{cell} [kPa]	σ_{BP} [kPa]	p'_0 [kPa]
Effect of bentonite concentration								
MT1	Clean sand	Column	0.71	0.00	CIU	700	600	100
MT2	Infiltrated sand	Column	0.79	1.79	CIU	700	600	100
MT3	Infiltrated sand	Column	0.69	3.47	CIU	700	600	100
MT4	Infiltrated sand	Column	0.64	5.33	CIU	700	600	100
MT5	Infiltrated sand	Column	0.68	7.10	CIU	700	600	100
Effect of specimen preparation and other parameters								
MT6	Clean sand	Air-pluviation	0.63	0.00	CIU	700	600	100
MT7	Clean sand	Column	0.66	0.00	CIU	700	600	100
MT8	Clean sand	Column	0.78	0.00	CIU	700	600	100
MT9	Clean sand	Column	0.85	0.00	CIU	800	600	200
MT10	Clean sand	Column	0.85	0.00	CIU	900	600	300
MT11	Clean sand	Column	0.76	0.00	CID	700	600	100
MT12	Infiltrated sand	Column	0.80	5.20	CIU	700	600	100
MT13	Infiltrated sand	Column	0.81	5.20	CIU	800	600	200
MT14	Infiltrated sand	Column	0.80	5.20	CIU	900	600	300
MT15	Infiltrated sand	Column	0.81	5.20	CID	700	600	100
MT16	Remoulded sand–slurry mixture	Wet tamping	0.75	5.20	CIU	700	600	100
MT17	Remoulded sand–slurry mixture	Wet tamping	0.80	5.20	CIU	800	600	200
MT18	Remoulded sand–slurry mixture	Wet tamping	0.84	5.20	CIU	900	600	300
MT19	Remoulded sand–slurry mixture	Wet tamping	0.82	5.20	CID	700	600	100
MT20	Remoulded sand–slurry mixture	Wet tamping	0.82	5.20	CID	800	600	200

6.2.2 Cyclic triaxial tests

In addition to the monotonic tests, cyclic undrained triaxial tests were conducted to investigate the cyclic resistance and deformation behaviour of the previously described specimen types under repeated loading conditions. The cyclic test matrix is summarised in Table 6.2.

Repeated loading conditions of this type are relevant for tunnel face stability in slurry-shield tunnel boring machines (TBMs), where the rotating cutterhead repeatedly passes over the same area of the excavation face and causes fluctuations in the applied support pressure. Cyclic triaxial loading in the laboratory can therefore be interpreted as a small-scale analogue for these repetitive stress conditions at the tunnel face.

The cyclic loading is characterised using the cyclic stress ratio (CSR), defined as

$$\mathrm{CSR} = \frac{q_{\mathrm{amp}}}{2\,p'_0}, \tag{6.1}$$

where q_{amp} is the cyclic deviatoric stress amplitude and p'_0 is the initial mean effective stress. For example, at $p'_0 = 100$ kPa, a stress amplitude of $q_{\mathrm{amp}} = 60$ kPa corresponds to $\mathrm{CSR} = 0.30$, while $q_{\mathrm{amp}} = 80$ kPa results in $\mathrm{CSR} = 0.40$.

The cyclic response is evaluated in terms of the imposed CSR, the initial effective stress state, and the number of loading cycles required to reach specified reductions in mean effective stress. The cycle counts $N_{0.9}$ and $N_{0.95}$ denote the number of cycles required for the mean effective stress p' to decrease by 90% and 95%, respectively, relative to the initial mean effective stress p'_0.

Table 6.2: Overview of cyclic triaxial tests.

Test ID	Specimen type	Preparation method	I_D [–]	$C_{\mathrm{bentonite}}$ [%]	p'_0 [kPa]	q_{amp} [kPa]	CSR [–]
CT1	Clean sand	Air pluviation	0.80	0.0	100	80	0.40
CT2	Clean sand	Air pluviation	0.82	0.0	100	60	0.30
CT3	Clean sand	Infiltration column	0.84	0.0	100	80	0.40
CT4	Clean sand	Infiltration column	0.80	0.0	100	60	0.30
CT5	Slurry-infiltrated sand	Infiltration column	0.81	5.2	100	80	0.40
CT6	Slurry-infiltrated sand	Infiltration column	0.81	5.2	100	60	0.30
CT7	Remoulded sand–slurry mixture	Wet tamping	0.85	5.1	100	80	0.40
CT8	Remoulded sand–slurry mixture	Wet tamping	0.85	5.3	100	60	0.30
CT9	Slurry-infiltrated sand	Infiltration column	0.81	1.8	100	80	0.40
CT10	Slurry-infiltrated sand	Infiltration column	0.85	3.7	100	80	0.40
CT11	Slurry-infiltrated sand	Infiltration column	0.82	7.1	100	80	0.40

6.3 Notation and conventions

6.3.1 Notation and sign conventions for presentation of results

Unless stated otherwise, all stresses are effective. Pressures applied by the apparatus are written explicitly as the cell pressure σ_{cell} and the back pressure σ_{BP}. The pore-water pressure within the specimen is denoted by u.

Compression stress is positive. Under axisymmetric triaxial conditions ($\sigma'_2 = \sigma'_3$), the mean effective stress is defined as

$$p' = \frac{\sigma'_1 + \sigma'_2 + \sigma'_3}{3} = \frac{\sigma'_1 + 2\sigma'_3}{3}. \tag{6.2}$$

The initial mean effective stress is denoted by p'_0.

The deviatoric stress is

$$q = \sigma'_1 - \sigma'_3. \tag{6.3}$$

Axial strain is reported as engineering strain in %. Consistent with the monotonic and cyclic plots in this chapter, compression is taken as positive axial strain ($\varepsilon_1 > 0$) and extension as negative axial strain ($\varepsilon_1 < 0$).

For the drained test results, volumetric strain is calculated as $\varepsilon_v = \varepsilon_1 + \varepsilon_2 + \varepsilon_3$ and is reported using the convention that contraction is positive ($\varepsilon_v > 0$) and dilation is negative ($\varepsilon_v < 0$).

Pore-water pressure u is measured relative to atmospheric pressure. The excess pore pressure is defined as

$$\Delta u = u - u_0, \tag{6.4}$$

where u_0 is the initial pore-water pressure at the start of shearing or cyclic loading. In the saturated specimens used here, u_0 corresponds to the applied back pressure σ_{BP}.

6.4 Monotonic triaxial response

The monotonic triaxial test results are presented and discussed in the following subsections, focusing on the influence of specimen preparation method and bentonite concentration on the shear behaviour of the sand.

6.4.1 Effect of specimen preparation and slurry infiltration

Figure 6.1 compares clean sand prepared by air pluviation in the triaxial device (MT6) with clean sand extracted from the column (MT7) at an initial mean effective stress of $p'_0 = 100$ kPa in isotropically consolidated undrained triaxial tests. The results are presented in terms of the effective stress path (q–p') and the stress–strain relationship (q–ε_1). Higher deviatoric stress q and mean effective stress p' are mobilised by the column specimen along the stress path. In the stress–strain view, the column specimen exhibits a clear peak followed by softening, whereas the specimen prepared by air pluviation remains at lower q across the whole strain range. At the same initial mean effective stress, the column specimen shows a stronger and more dilatant response than the air-pluviated specimen, although this comparison is based on one specimen per preparation route.

The difference may be associated with the slightly different initial states of the two specimens. The column specimen has a slightly higher initial relative density ($I_D = 0.66$) than the air-pluviated specimen ($I_D = 0.63$), which may partly contribute to its higher peak strength and more dilatant response. Extraction, transfer, and installation may also alter the fabric of the column specimen in ways not fully captured by relative density. On the available data, density and fabric effects cannot be separated.

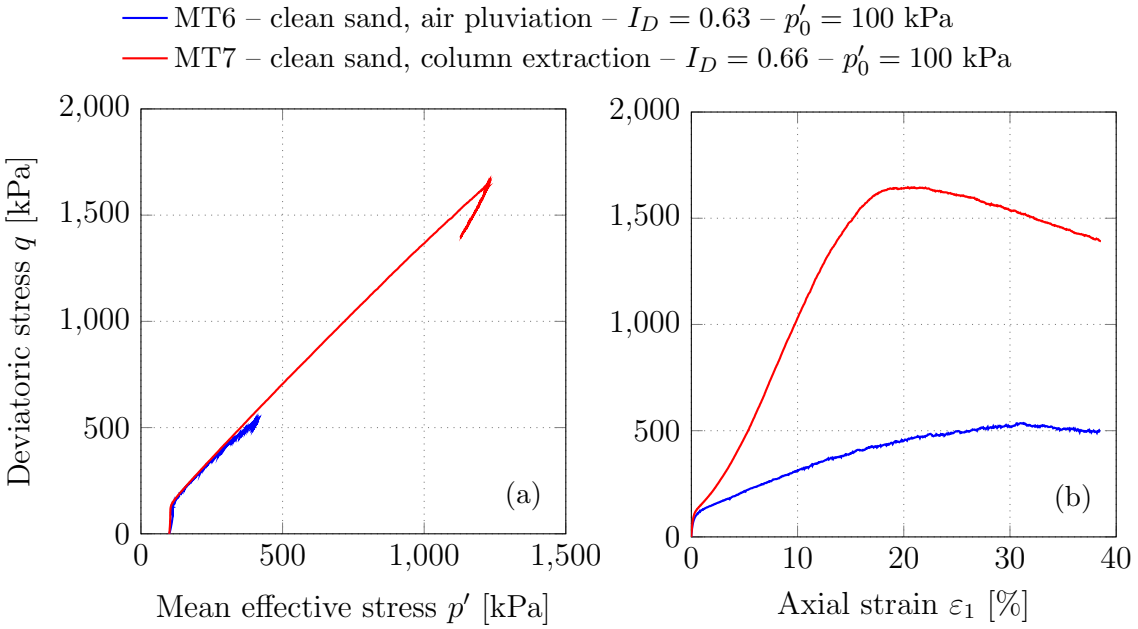

Figure 6.1: Clean sand at $p'_0 = 100$ kPa (CIU): effect of specimen preparation method. (a) Effective stress path in the q–p' plane. (b) Stress–strain response in the q–ε_1 plane.

Figure 6.2, panels (a,b), show CIU tests at $p'_0 = 100\,\mathrm{kPa}$ for three preparation routes. The clean column specimen and the infiltrated column specimen follow nearly the same effective stress path in the q–p' plane in the approach to peak and exhibit similar stress–strain curves. In contrast, the mixed specimen prepared by wet tamping reaches a lower peak and begins to soften earlier, remaining below the other two specimens over the entire strain range.

Figure 6.2, panels (c,d), show the corresponding CIU tests at $p'_0 = 200\,\mathrm{kPa}$. The three effective stress paths in the q–p' plane are similar in the approach to peak stress ratio. The infiltrated specimen reaches the highest peak q and maintains it over a broader strain interval, the clean specimen is slightly lower, and the mixed specimen remains clearly below and softens earlier.

Figure 6.2, panels (e,f), show the corresponding CIU tests at $p'_0 = 300\,\mathrm{kPa}$. The curves of the clean and infiltrated specimens remain close around peak strength and both lie clearly above the mixed specimen. The peak deviatoric stress q increases with initial mean effective stress for all three preparation routes, while the relative ordering of the curves remains unchanged.

Figure 6.3 presents the results of drained triaxial tests (CID) at $p'_0 = 100\,\mathrm{kPa}$. In the stress–strain plot, the infiltrated specimen reaches the highest peak deviatoric stress q, the remoulded specimen is intermediate, and the clean specimen shows the lowest peak response. The lower peak strength of the clean specimen may partly reflect its lower initial relative density ($I_D = 0.76$) compared with the infiltrated and remoulded specimens ($I_D =$ 0.81 and 0.82, respectively). The volumetric-strain plot shows that all three specimens undergo slight initial contraction followed by dilation. The infiltrated specimen develops the largest dilation over most of the strain range, while the remoulded specimen develops dilation more gradually but approaches a comparable value at large strain. All specimens subsequently soften with increasing axial strain ε_1.

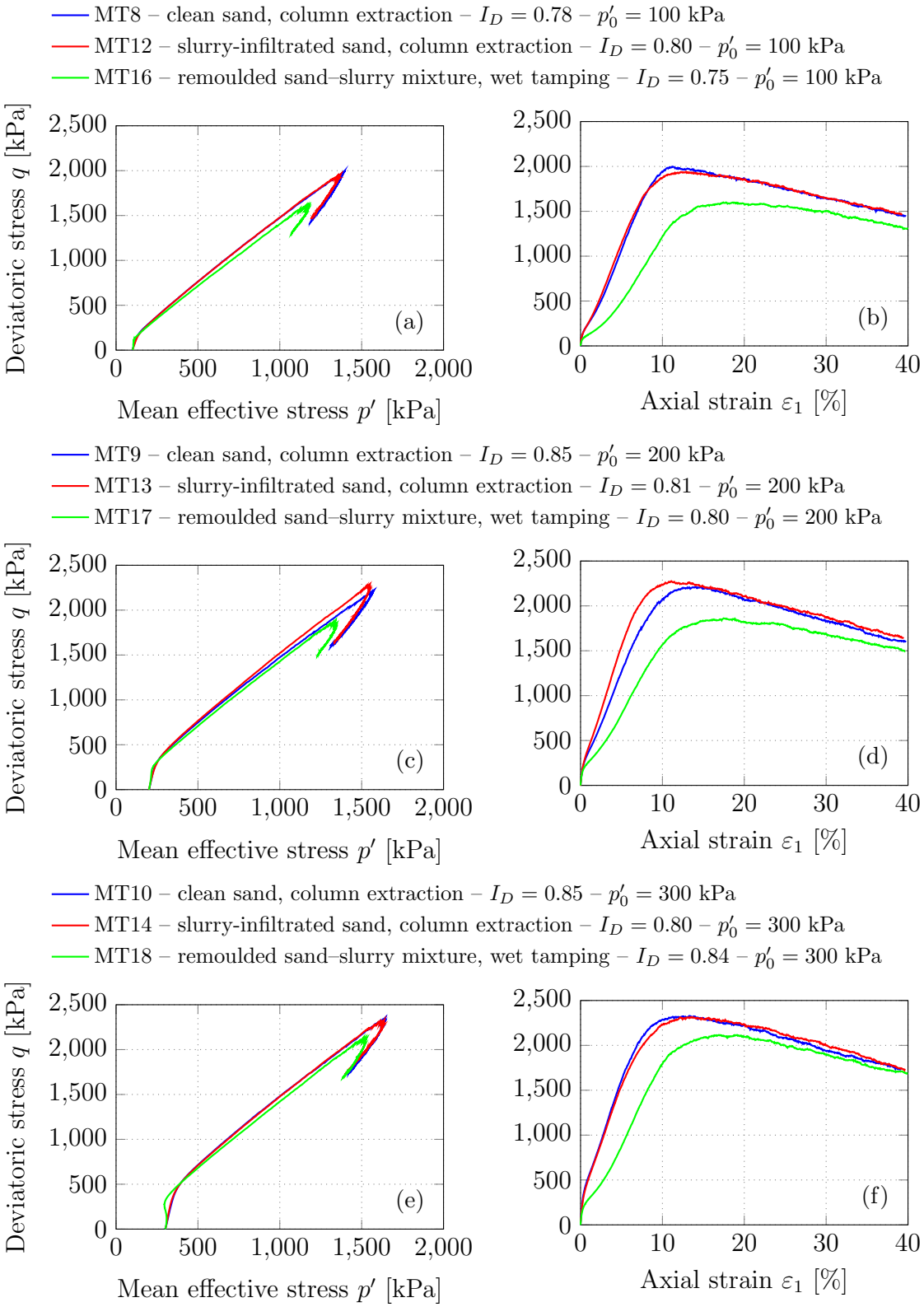

Figure 6.2: CIU results for three preparation routes at different initial mean effective stresses. Panels (a), (c), and (e) show the effective stress paths in the q–p' plane for $p'_0 = 100$, 200, and 300 kPa, respectively. Panels (b), (d), and (f) show the corresponding stress–strain responses in the q–ε_1 plane.

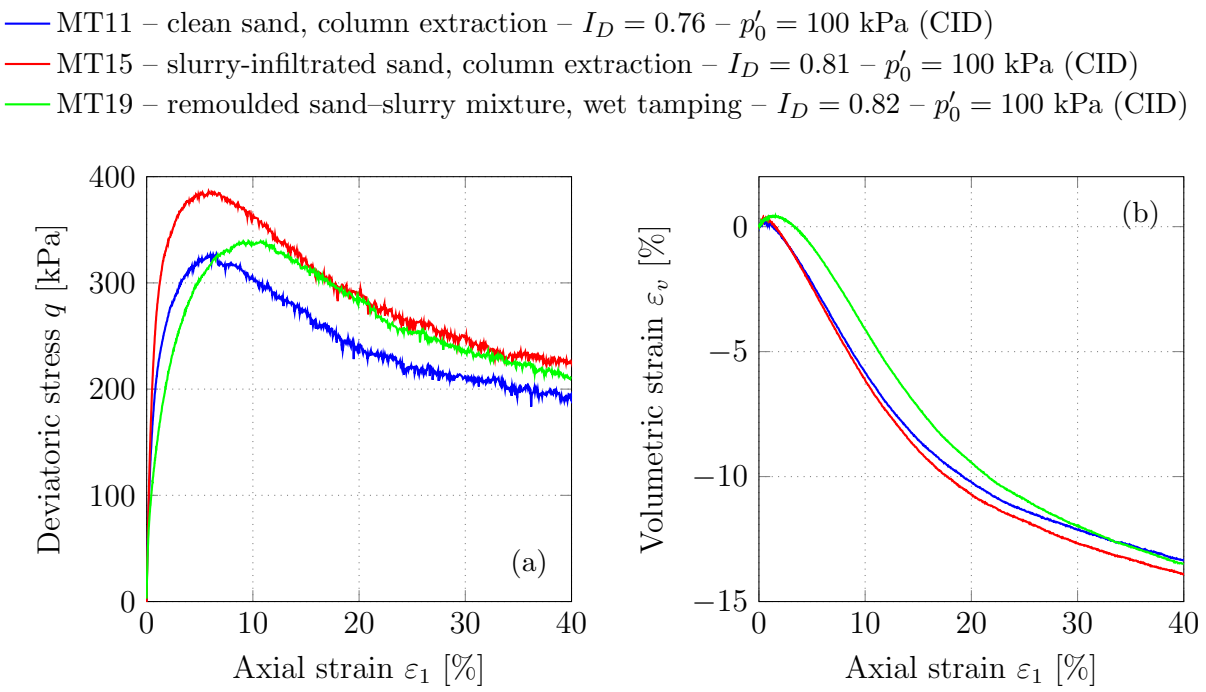

Figure 6.3: CID results at $p'_0 = 100\,\text{kPa}$ for three preparation routes. (a) Deviatoric stress–axial strain response in the q–ε_1 plane. (b) Volumetric strain–axial strain response in the ε_v–ε_1 plane, with contraction positive and dilation negative.

6.4.2 Peak and critical-state friction angles from monotonic triaxial tests

The critical-state friction angle was estimated from the monotonic triaxial tests by identifying representative large-strain stress states in the q–p' plane and fitting the critical-state line (CSL). In the q–p' representation the CSL can be written as

$$q = M\,p', \tag{6.5}$$

and the corresponding critical-state friction angle φ'_{cs} follows from

$$\sin\varphi'_{cs} = \frac{3M}{6+M}, \tag{6.6}$$

according to classical critical-state soil mechanics (Schofield and Wroth, 1968).

From each monotonic test, five representative stress states (data points in the q–p' plane) were selected from the final portion of the stress path where the response had approached

a stable large-strain condition. In the CIU tests these points correspond to axial strains of approximately $\varepsilon_1 \approx 35$–40%, representing the terminal part of the post-peak effective stress path. In the CID tests the selected points were taken from the final portion of the drained shearing stage, typically within $\varepsilon_1 \approx 30$–40%.

Five points were selected rather than a single final stress state in order to reduce the influence of measurement noise and small fluctuations in the terminal part of the stress path. Using several neighbouring late-stage stress states provides a more robust representation of the terminal stress ratio q/p' while still representing the same large-strain condition. These states therefore represent the closest experimental approximation to the critical state and were used to construct the critical-state line, following, for example, Schanz and Vermeer (1996).

The selected points at the available values of initial mean effective stress p'_0 within each preparation route were pooled and a least-squares fit of a linear function through the origin was performed to determine the CSL slope M. The CSL was determined from the CIU tests, which provide a consistent set of specimens across all p'_0 levels for each preparation route. The CID tests are included in the figures for comparison but were not used in the regression because they are available only at limited p'_0 levels and would therefore introduce uneven weighting in the regression. Figure 6.4 shows the selected late-stage stress states and the resulting CSL fits for the three specimen preparation routes: clean sand (column), infiltrated sand (column), and remoulded sand–slurry mixture (wet tamping).

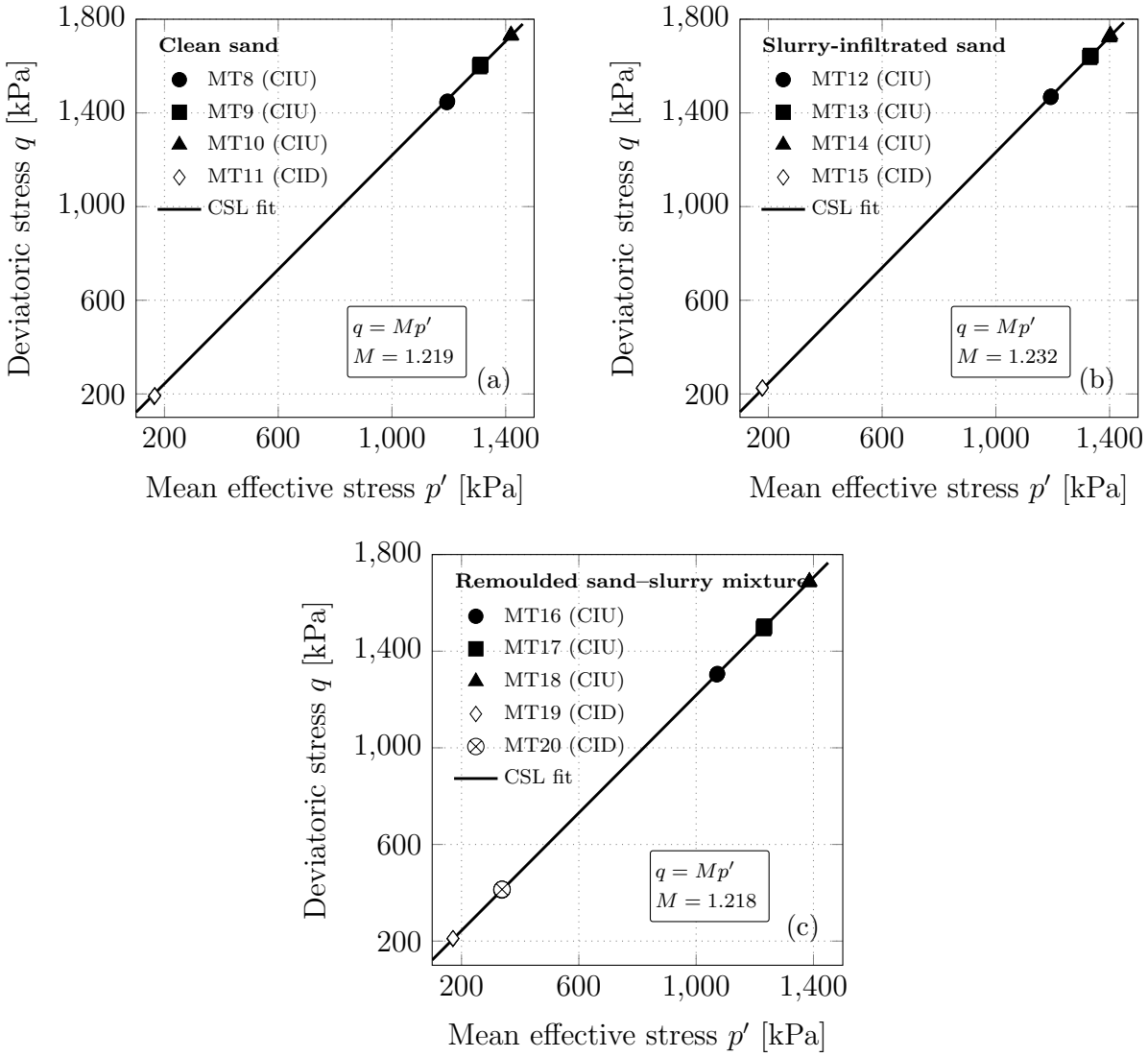

Figure 6.4: Critical state line estimations in the q–p' plane for the three specimen preparation routes based on selected large-strain stress states from monotonic CIU tests. Panels (a), (b), and (c) correspond to clean sand, slurry-infiltrated sand, and remoulded sand–slurry mixture, respectively. Large-strain stress states from the corresponding drained tests are shown for comparison.

In addition to the critical-state strength, the peak friction angle was evaluated from the maximum stress state reached in each monotonic test. Table 6.3 lists the peak stress states $(p'_{\mathrm{peak}}, q_{\mathrm{peak}})$ together with the corresponding peak friction angles φ'_{peak} derived from these values. The peak friction angles obtained from the CIU tests lie in a narrow range between approximately 34° and 36° for all specimen types. The CID tests mobilise higher peak friction angles, approximately 38°–41°, consistent with their drained dilative response.

Table 6.3: Peak stress states and corresponding peak friction angles derived from the monotonic triaxial tests.

Test ID	Specimen type	Test type	p'_{peak} [kPa]	q_{peak} [kPa]	ϕ'_{peak} [°]
MT8	Clean sand (column)	CIU	1396.5	1996.6	35.3
MT9	Clean sand (column)	CIU	1570.6	2210.2	34.8
MT10	Clean sand (column)	CIU	1638.6	2326.9	35.0
MT11	Clean sand (column)	CID	210.6	327.4	38.1
MT12	Infiltrated sand (column)	CIU	1359.4	1941.1	35.2
MT13	Infiltrated sand (column)	CIU	1541.3	2275.7	36.3
MT14	Infiltrated sand (column)	CIU	1626.8	2314.8	35.1
MT15	Infiltrated sand (column)	CID	230.0	386.2	41.0
MT16	Remoulded sand–slurry mixture (wet tamping)	CIU	1153.9	1599.1	34.3
MT17	Remoulded sand–slurry mixture (wet tamping)	CIU	1336.1	1862.2	34.4
MT18	Remoulded sand–slurry mixture (wet tamping)	CIU	1509.1	2116.2	34.6
MT19	Remoulded sand–slurry mixture (wet tamping)	CID	213.7	339.6	38.9
MT20	Remoulded sand–slurry mixture (wet tamping)	CID	422.8	669.2	38.8

Table 6.4 compares the mean peak friction angles from the CIU tests with the critical-state friction angles derived from the CSL fits. The mean CIU peak friction angles exceed the critical-state friction angles by roughly 4–5°, which reflects the contribution of dilatancy during shearing after the peak. Importantly, the critical-state friction angle itself is essentially unaffected by specimen preparation or bentonite placement. Clean sand (column), infiltrated sand (column), and remoulded sand–slurry mixture (wet tamping) specimens all converge to $\varphi'_{cs} \approx 30°$–$31°$ at large strains, indicating that the large-strain strength is governed primarily by the sand skeleton. Differences observed at peak therefore mainly reflect state and fabric effects during shear rather than changes in the intrinsic critical-state friction angle of the material.

Table 6.4: Comparison of mean CIU peak friction angles derived from maximum stress states and critical-state friction angles obtained from CSL fitting.

Specimen type	Mean ϕ'_{peak} (CIU) [°]	ϕ'_{cs} [°]
Clean sand (column)	35.0	30.4
Infiltrated sand (column)	35.6	30.7
Remoulded sand–slurry mixture (wet tamping)	34.4	30.4

During CIU shearing, the dilative tendency of the specimens generated negative excess pore-water pressure ($\Delta u < 0$), thereby increasing p' and contributing to the high deviatoric stress mobilised near peak. The maximum q did not, however, coincide systematically with the pore-water pressure becoming negative relative to atmospheric pressure; the peak is therefore interpreted as a coupled stress–dilatancy response rather than as a consequence of crossing $u = 0$. Because p' was calculated from the measured pore-water pressure, this undrained response is already represented in the derived peak friction angles. The critical-state angles were estimated from stable terminal q/p' ratios and were not governed by the transient peak pore-pressure response.

6.4.3 Influence of bentonite concentration

Figure 6.5 shows undrained monotonic tests at $p'_0 = 100$ kPa for clean sand and slurry-infiltrated sand with approximately 2%, 4%, 6%, and 8% bentonite. In the effective-stress-path view (q–p'), all specimens follow a similar trajectory at small to intermediate strains and begin to separate as peak strength is approached. Within this concentration series, the clean specimen reaches the highest peak q and the largest p'. Among the infiltrated specimens, peak strength decreases from B20 to B60 and then increases slightly for B80, so the concentration trend is not strictly monotonic. In the stress–strain view (q–ε_1), the infiltrated specimens show lower peaks and earlier softening than the clean specimen; at large strains their curves are flatter.

The initial relative densities also differ appreciably across this series ($I_D = 0.64$–0.79), so part of the observed ordering may reflect initial state rather than bentonite concentration alone. The apparent contrast with Figure 6.2, where different clean and slurry-infiltrated specimens developed comparable peaks and the peaks of the slurry-infiltrated specimens were slightly higher under some conditions, should therefore not be interpreted as a contradiction. Taken together, the results indicate that the peak response depends jointly on bentonite content, initial density, and specimen-specific fabric; the isolated influence of concentration cannot be separated from the state differences in the available tests.

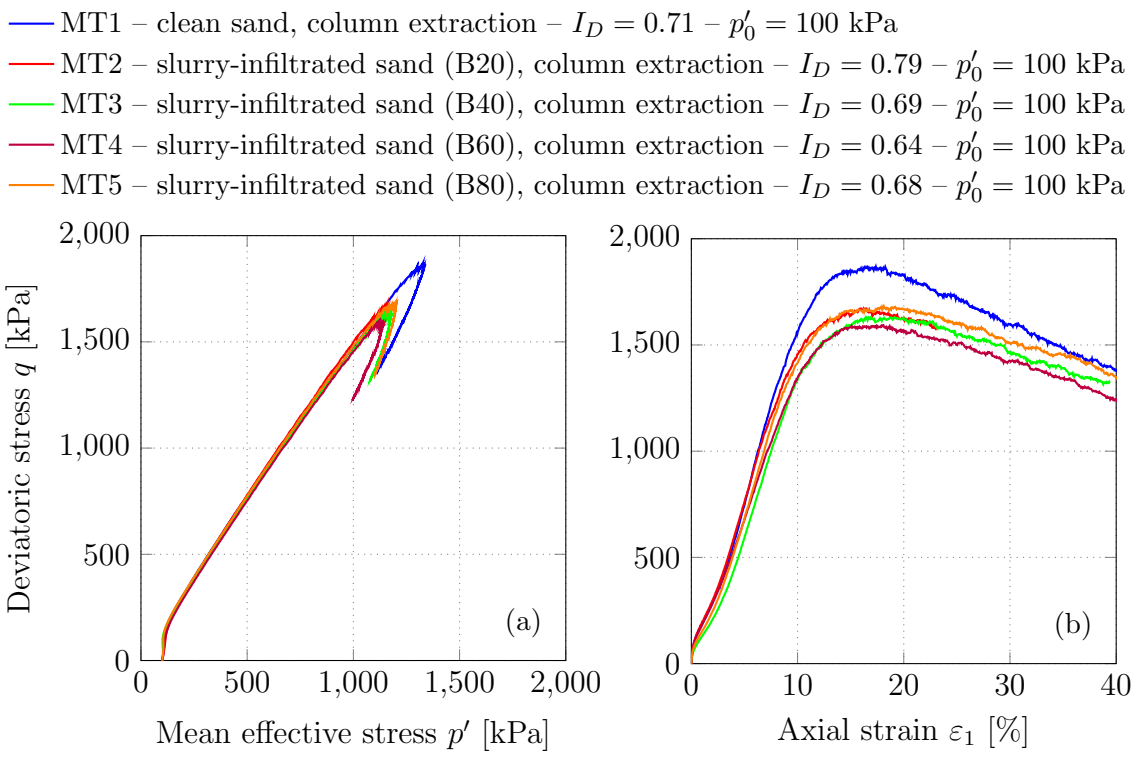

Figure 6.5: Monotonic triaxial response at $p'_0 = 100\,\text{kPa}$ for clean sand and slurry-infiltrated sand with bentonite concentrations of approximately 2–8%. Panel (a) shows the effective stress paths in the q–p' plane and panel (b) the corresponding stress–strain response in the q–ε_1 plane.

6.5 Cyclic triaxial response

The cyclic triaxial test results are presented and discussed in the following subsections. The analysis focuses on the cyclic resistance and deformation behaviour of clean sand, slurry-infiltrated sand, and remoulded sand–slurry mixtures under cyclic loading.

6.5.1 Verification of specimen saturation prior to cyclic loading

All specimens used in the cyclic tests were saturated using the protocol described in Section 3.5.4, targeting $B \geq 0.98$. To document the process, Table 6.5 reports B-values measured at four stages: $B_{200/240}$ immediately after reaching $\sigma_{\text{BP}}/\sigma_{\text{cell}} = 200/240$ kPa; $B^{\text{sat}}_{200/240}$ after a short hold at the same pressures (if recorded); $B_{600/640}$ immediately after reaching $\sigma_{\text{BP}}/\sigma_{\text{cell}} = 600/640$ kPa; and $B^{\text{final}}_{600/640}$ after a 12–24 h hold at these pressures, measured immediately before cyclic loading.

Table 6.5 shows that every specimen attained a last recorded B-value of 0.99–1.00. Achieving such high B-values is essential in undrained cyclic testing of granular soils because residual compressible air can alter pore-water-pressure development and the measured cyclic response.

Table 6.5: B-values measured at different stages of the saturation procedure prior to cyclic loading.

Test ID	Preparation method	$C_{\text{bentonite}}$ [%]	$B_{200/240}$ [-]	$B^{\text{sat}}_{200/240}$ [-]	$B_{600/640}$ [-]	$B^{\text{final}}_{600/640}$ [-]
CT1	Air pluviation	0.0	0.95	–	0.95	1.00
CT2	Air pluviation	0.0	0.95	0.97	–	0.99
CT3	Column (clean)	0.0	0.65	0.97	0.99	–
CT4	Column (clean)	0.0	0.70	0.94	0.99	0.99
CT5	Column (infiltrated)	5.2	0.82	–	–	0.99
CT6	Column (infiltrated)	5.2	0.84	–	0.96	1.00
CT7	Wet tamping (mixed)	5.1	0.73	–	–	0.99
CT8	Wet tamping (mixed)	5.3	0.75	–	0.94	0.99
CT9	Column (infiltrated)	1.8	0.76	–	0.99	–
CT10	Column (infiltrated)	3.7	0.92	–	–	0.99
CT11	Column (infiltrated)	7.1	0.89	–	–	1.00

6.5.2 Effect of specimen preparation and slurry infiltration

Figure 6.6 shows results for clean sand at the cyclic stress ratio CSR = 0.40 for two specimen preparation methods, namely air pluviation and column extraction. Panels (a) and (c) show the effective stress paths in the q–p' plane, while panels (b) and (d) present the corresponding stress–strain response in the q–ε_1 plane. The column-extracted specimen (CT3) shows a slower leftward migration of the effective stress path towards lower p' (panel c), consistent with a slower build-up of positive excess pore-water pressure. It also maintains a slightly higher mean effective stress in the final cycles than the specimen prepared by air pluviation directly in the triaxial device (CT1, panel a). The q–ε_1 curves (panels b and d) also indicate slower axial-strain accumulation for CT3. Consistently with this observation, Table 6.6 reports more cycles to the thresholds for CT3

($N_{0.9} = 28$, $N_{0.95} = 33$) than for CT1 ($N_{0.9} = 23$, $N_{0.95} = 29$). At the same CSR and p'_0, the preparation method therefore affected the response: column extraction resulted in a slightly higher cyclic resistance than air pluviation directly in the triaxial device. This behaviour is consistent with the slightly denser packing and different fabric typically produced by column extraction compared to air pluviation, which resulted in higher cyclic stability and delayed pore-pressure accumulation.

Table 6.6 and Figure 6.7 compare the cyclic responses of clean-sand specimens prepared by air pluviation and column extraction at the same initial mean effective stress. As noted above, at CSR = 0.40, CT3 required more cycles than CT1 before the defined p'-reduction thresholds were reached ($N_{0.9} = 28$, $N_{0.95} = 33$ vs. $N_{0.9} = 23$, $N_{0.95} = 29$). At the lower cyclic stress ratio, CSR = 0.30, the difference was even larger: the counts were $N_{0.9} = 132$ and $N_{0.95} = 140$ for CT4 (column extraction), compared with $N_{0.9} = 105$ and $N_{0.95} = 112$ for CT2 (air pluviation). For both CSR values, the first-five-cycle effective stress paths and stress–strain responses are shown in Figure 6.7(a), (b), (d), and (e), with broadly similar loop shapes. In these undrained tests, the response is described by effective-stress-path migration, not volumetric contraction; the early-cycle migration rate is not consistently preparation-dependent. At comparable saturation ($B \approx 1.0$) and relative density, the larger threshold-cycle counts suggest slightly higher cyclic resistance after column extraction, potentially reflecting preparation-induced fabric.

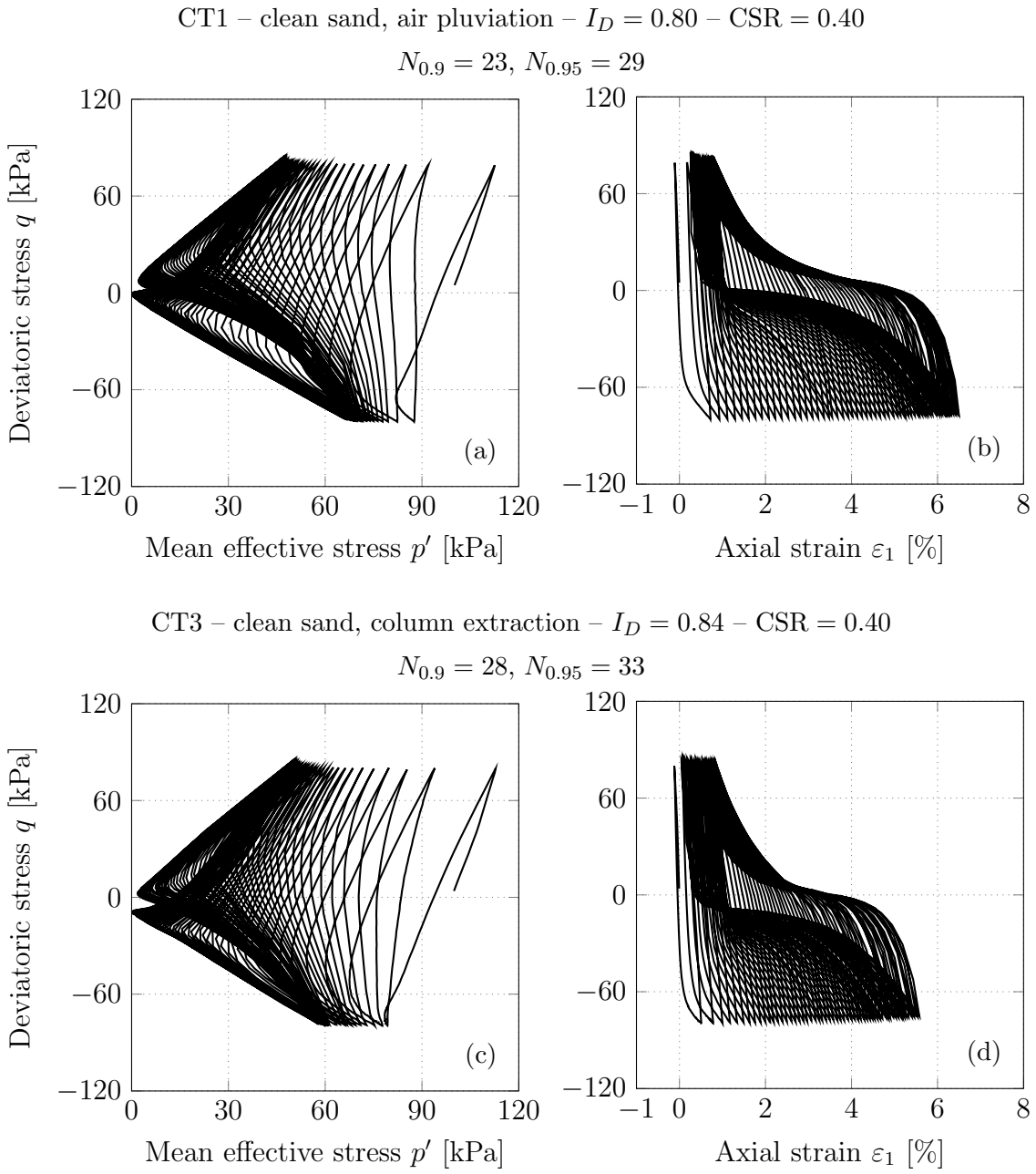

Figure 6.6: Clean sand at CSR = 0.40: CT1 (air pluviation) and CT3 (column extraction). Panels (a) and (c) present the full-cycle effective stress paths in the q–p' plane, while panels (b) and (d) show the corresponding full-cycle stress–strain response in the q–ε_1 plane (compression positive).

Table 6.7 and Figure 6.8 compare clean sand and slurry-infiltrated sand prepared using column extraction at the same initial mean effective stress. At CSR = 0.40, the slurry-infiltrated specimen CT5 required fewer loading cycles to reach the defined p'-reduction thresholds than the clean specimen CT3 ($N_{0.9} = 16$, $N_{0.95} = 21$ vs. $N_{0.9} = 28$, $N_{0.95} = 33$). A similar trend is observed at CSR = 0.30, where CT6 reached $N_{0.9} = 62$ and $N_{0.95} = 72$, compared with $N_{0.9} = 132$ and $N_{0.95} = 140$ for the corresponding clean specimen CT4. The cyclic responses during the first five cycles are shown in Figure 6.8(a), (b), (d), and (e). While the overall loop shapes remain comparable, the effective stress paths of the slurry-infiltrated specimens migrate left more rapidly towards lower p', accompanied by more rapid axial-strain accumulation. The last-cycle stress paths in panels (c) and (f) show only small, branch-dependent differences in p', with no consistent offset between the clean and infiltrated specimens; these differences should not be overinterpreted. The lower threshold-cycle counts instead suggest reduced cyclic resistance associated with slurry infiltration at comparable CSR and p'_0.

Table 6.8 and Figure 6.9 compare slurry-infiltrated sand prepared by column extraction with remoulded sand–slurry mixtures prepared by wet tamping. At CSR = 0.40, the remoulded specimen CT7 required substantially fewer loading cycles to reach the defined p'-reduction thresholds ($N_{0.9} = 5$, $N_{0.95} = 6$) than the corresponding infiltrated specimen CT5 ($N_{0.9} = 16$, $N_{0.95} = 21$). A similar difference is observed at CSR = 0.30, where the remoulded specimen CT8 reached $N_{0.9} = 16$ and $N_{0.95} = 20$, compared to $N_{0.9} = 62$ and $N_{0.95} = 72$ for the infiltrated specimen CT6. The cyclic responses during the first five cycles are shown in Figure 6.9(a), (b), (d), and (e). Compared with the infiltrated specimens, the effective stress paths of the remoulded sand–slurry mixtures migrate left more rapidly towards lower p', accompanied by faster axial-strain accumulation. The substantially smaller threshold-cycle counts therefore suggest lower cyclic resistance of the remoulded sand–slurry mixtures compared to the slurry-infiltrated sand prepared by column extraction.

Table 6.6: Summary of selected cyclic triaxial test conditions and results (CT1, CT3 at CSR = 0.40; CT2, CT4 at CSR = 0.30).

Test ID	I_D [–]	$C_{\text{bentonite}}$ [%]	CSR	$N_{0.9}$	$N_{0.95}$	B-value
CT1	0.80	0.0	0.40	23	29	1.00
CT3	0.84	0.0	0.40	28	33	0.99
CT2	0.82	0.0	0.30	105	112	0.99
CT4	0.80	0.0	0.30	132	140	0.99

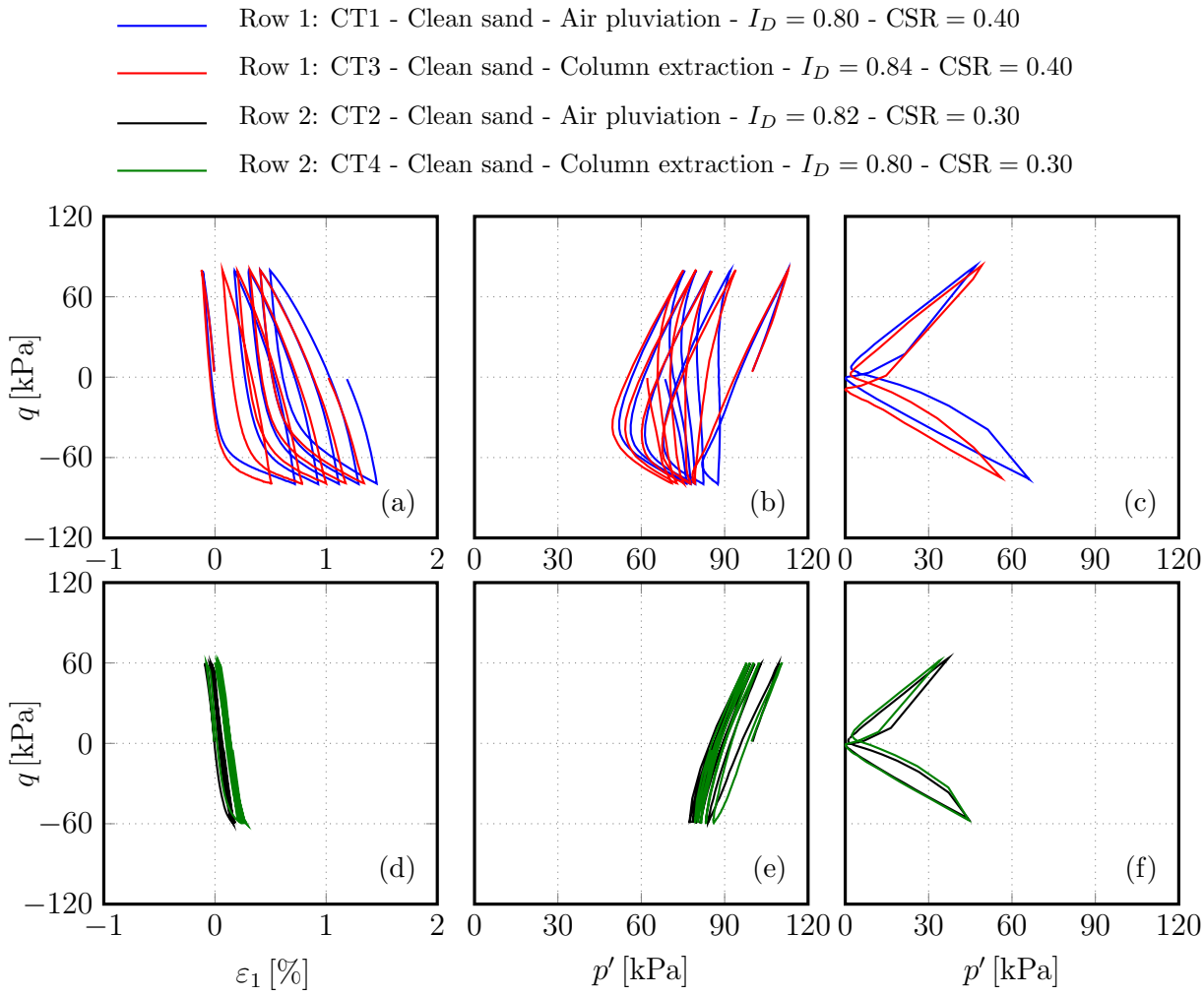

Figure 6.7: Clean sand: preparation effect at fixed p'_0. Panels (a)–(c) correspond to CSR = 0.40 and panels (d)–(f) to CSR = 0.30. Panels (a) and (d) show q–ε_1 (compression positive), panels (b) and (e) show q–p' for cycles 1–5, and panels (c) and (f) show q–p' for the last cycle.

Table 6.7: Effect of slurry infiltration: paired clean vs. infiltrated column specimens at CSR = 0.40 and 0.30.

Test ID	I_D [–]	$C_{\text{bentonite}}$ [%]	CSR	$N_{0.9}$	$N_{0.95}$	B-value
CT3	0.84	0.0	0.40	28	33	0.99
CT5	0.81	5.2	0.40	16	21	0.99
CT4	0.80	0.0	0.30	132	140	0.99
CT6	0.81	5.2	0.30	62	72	1.00

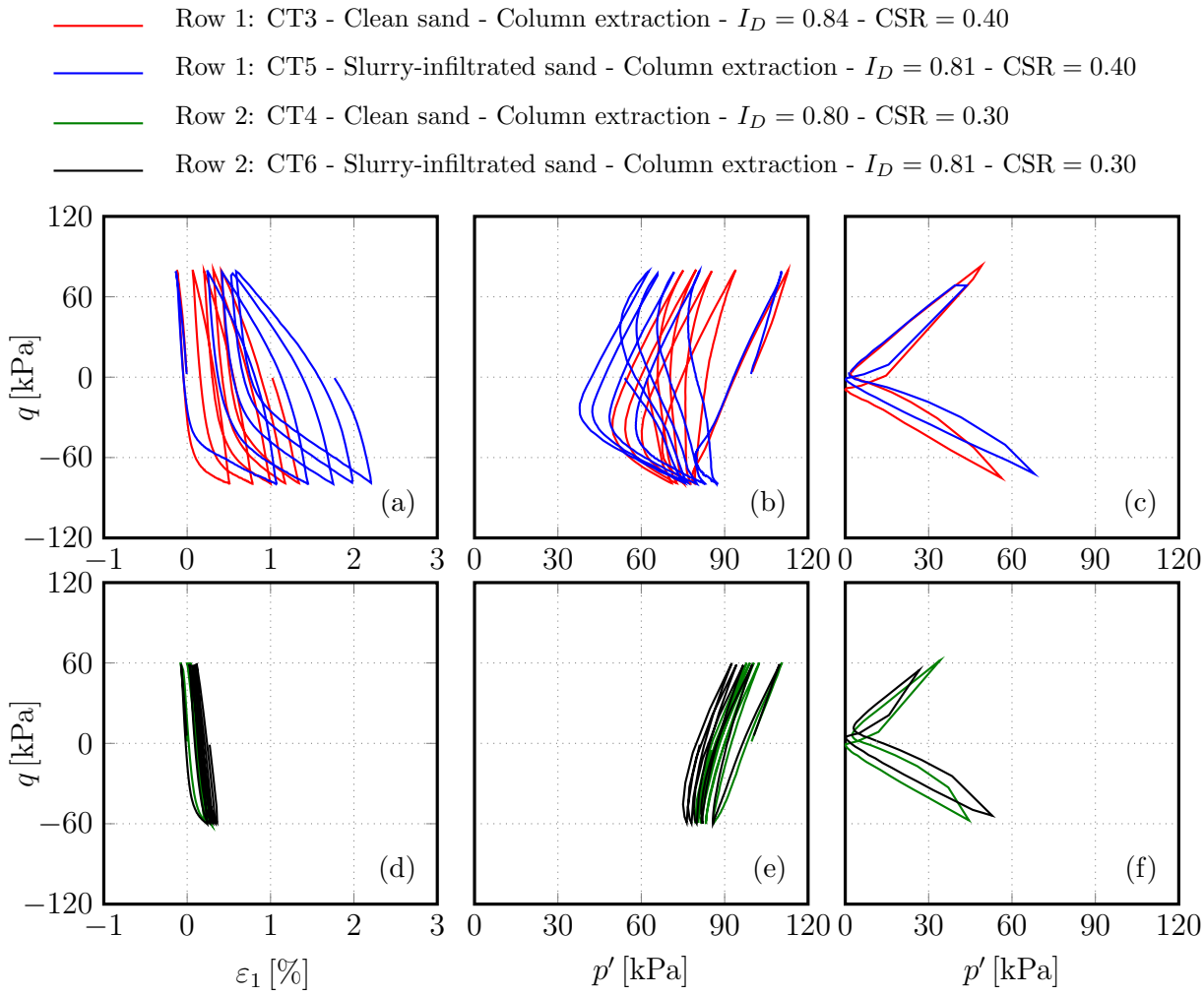

Figure 6.8: Effect of slurry infiltration. Panels (a)–(c) correspond to CSR = 0.40 and panels (d)–(f) to CSR = 0.30. Panels (a) and (d) show q–ε_1 (compression positive), panels (b) and (e) show q–p' for cycles 1–5, and panels (c) and (f) show q–p' for the last cycle.

Table 6.8: Effect of specimen preparation: slurry-infiltrated sand vs. remoulded sand–slurry mixture at CSR = 0.40 and 0.30.

Test ID	I_D [–]	$C_{\text{bentonite}}$ [%]	CSR	$N_{0.9}$	$N_{0.95}$	B-value
CT5	0.81	5.2	0.40	16	21	0.99
CT7	0.85	5.1	0.40	5	6	0.99
CT6	0.81	5.2	0.30	62	72	1.00
CT8	0.85	5.3	0.30	16	20	0.99

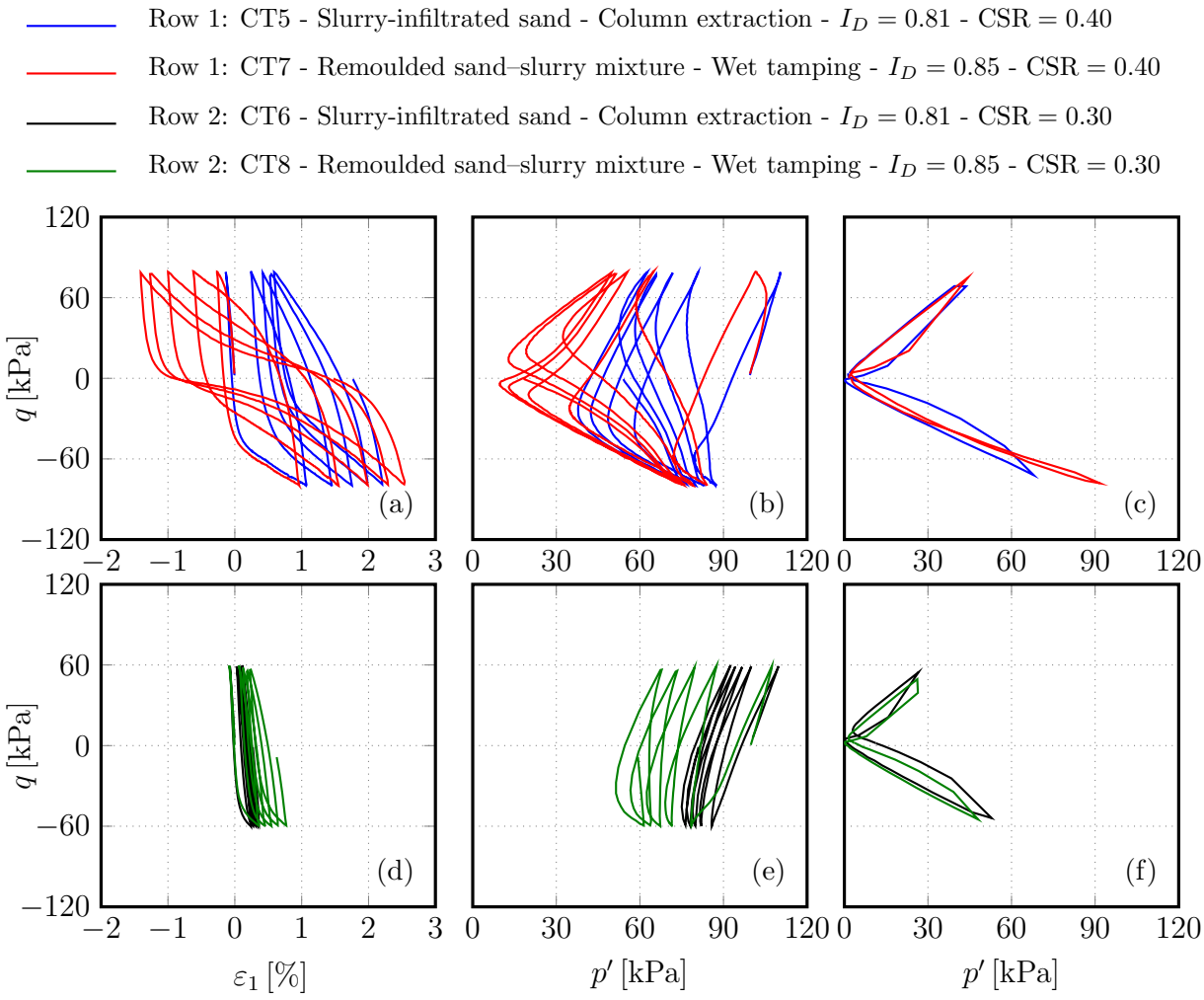

Figure 6.9: Effect of specimen preparation. Panels (a)–(c) correspond to CSR = 0.40 and panels (d)–(f) to CSR = 0.30. Panels (a) and (d) show q–ε_1 (compression positive), panels (b) and (e) show q–p' for cycles 1–5, and panels (c) and (f) show q–p' for the last cycle.

6.5.3 Effect of bentonite concentration

Table 6.9 and Figure 6.10 present the results of the slurry-infiltrated column test series with varying bentonite concentration at CSR = 0.40. The cycle counts vary within the tested range: the B40 specimen (CT10) gives the largest values, $N_{0.9} = 32$ and $N_{0.95} = 41$; B20 (CT9) and B80 (CT11) are intermediate at 27/35 and 24/31; and B60 (CT5) is lowest at 16/21. The cyclic responses during the first five cycles are shown in Figure 6.10(a,b). The loop shapes are broadly similar, but the rate of leftward migration in the q–p' plane differs: the effective stress path of B40 migrates left more slowly and retains the highest p' in the last cycle, whereas that of B60 migrates left more rapidly and reaches the lowest p'. The q–ε_1 curves in panel (a) show a similar tendency, with B40 accumulating axial strain more slowly and B60 more rapidly. Within this setup the response is non-monotonic, with an intermediate maximum near B40. Because only one specimen was tested at each concentration and the initial relative densities differ slightly ($I_D = 0.81$–0.85), the apparent concentration dependence cannot be separated reliably from specimen-to-specimen scatter. The high B-values ($B \approx 0.99$–1.00) make incomplete saturation an unlikely explanation for the differences, but repeat tests would be required to establish a concentration effect.

Table 6.9: Effect of bentonite concentration (CSR = 0.40): slurry-infiltrated column specimens with varying bentonite level.

Test ID	I_D [–]	$C_{\text{bentonite}}$ [%]	CSR	$N_{0.9}$	$N_{0.95}$	B-value
CT9	0.81	1.8	0.40	27	35	0.99
CT10	0.85	3.7	0.40	32	41	0.99
CT5	0.81	5.2	0.40	16	21	0.99
CT11	0.82	7.1	0.40	24	31	1.00

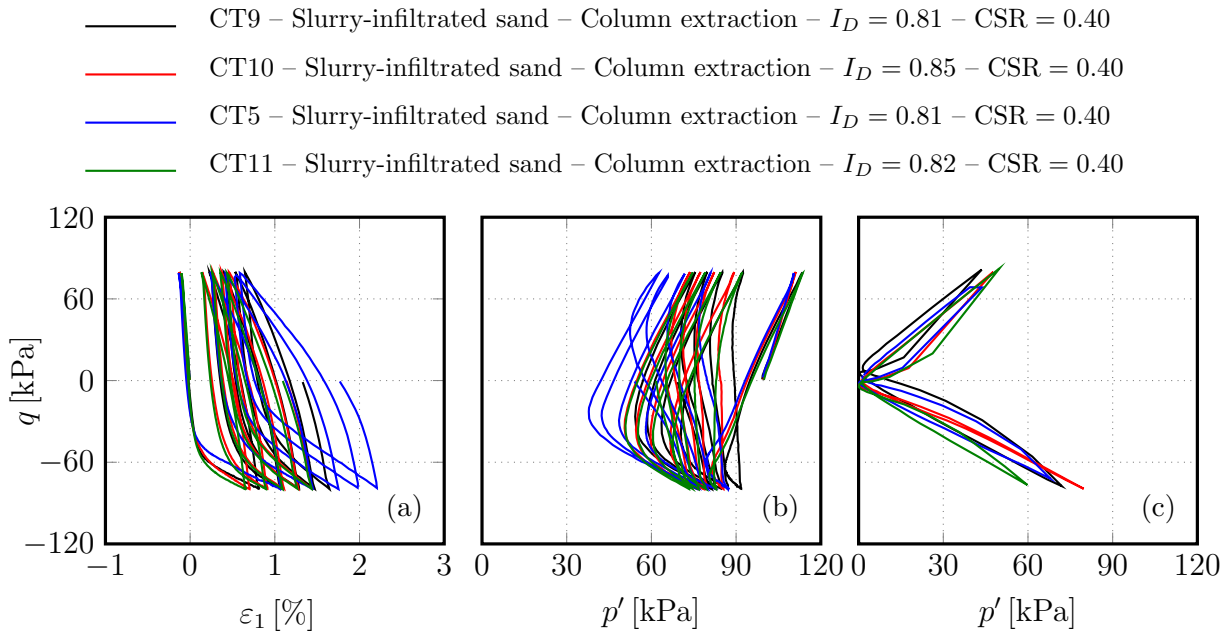

Figure 6.10: Effect of bentonite concentration at CSR = 0.40. Panels (a)–(c) show q–ε_1 (compression positive), q–p' for cycles 1–5, and q–p' for the last cycle, respectively.

6.5.4 Cycles to thresholds as functions of bentonite concentration, specimen preparation method and amplitude

Figure 6.11 plots the numbers of cycles needed to reach the two defined thresholds against bentonite concentration for the infiltrated column series at CSR = 0.40. No clear monotonic trend is evident in either $N_{0.9}$ or $N_{0.95}$: the B40 specimen ($C_{\text{bentonite}} = 3.7\%$) shows the largest values, whereas B60 ($C_{\text{bentonite}} = 5.2\%$) gives the lowest counts; the B20 and B80 specimens ($C_{\text{bentonite}} = 1.8\%$ and 7.1%, respectively) lie between these limits. The tested bentonite concentrations are generally small and the initial states are similar, so minor differences in I_D or small disturbances during preparation and handling may mask a weak concentration effect. A firmer relation would require additional data points at several densities and over a wider range of concentrations. This was not practical here because maintaining identical conditions was demanding, and a single usable dataset often required several attempts due to issues such as membrane leakage or incomplete saturation.

Figure 6.12 shows the effect of loading amplitude for the different specimen preparation methods. When CSR decreases from 0.40 to 0.30, the number of cycles increases by roughly a factor of three to five across all preparation methods. In the paired B60 comparisons, the ranking remains consistent at both levels: clean sand prepared by column extraction exhibits the highest resistance, slurry-infiltrated column specimens exhibit lower resistance, and remoulded sand–slurry mixtures prepared by wet tamping exhibit the lowest resistance; clean sand prepared by air pluviation lies between the clean-column and infiltrated responses. This behaviour is consistent with the cyclic loop plots: specimens showing a stronger contractive tendency during the early cycles exhibit more rapid leftward migration of their effective stress paths in the q–p' plane and consequently reach the defined thresholds sooner. Additional tests at higher, intermediate, and lower CSR values would help better define the slope of the CSR–N curves and verify whether the same ordering persists over a broader range of cyclic loading amplitudes.

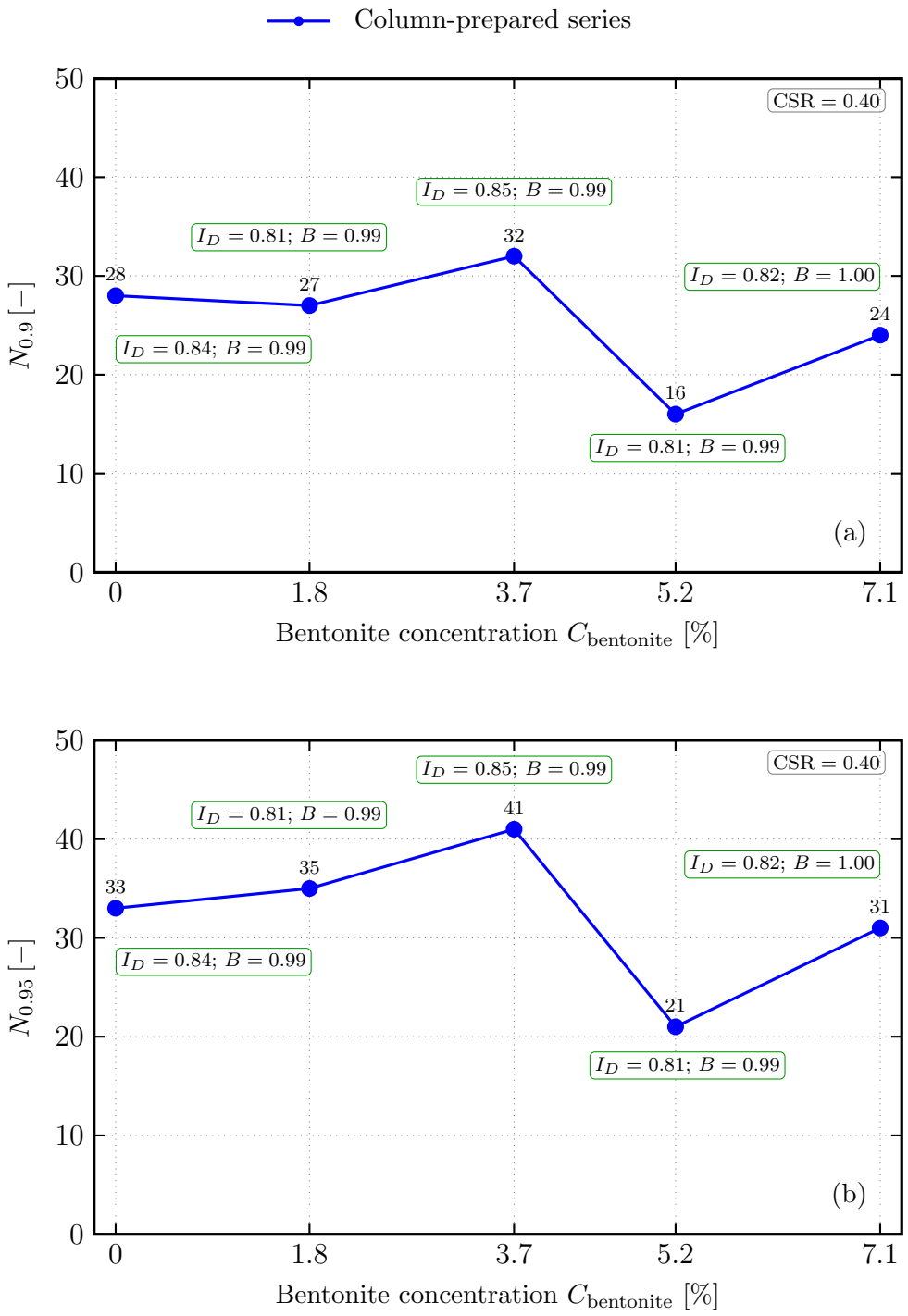

Figure 6.11: Number of cycles needed to reach the two defined thresholds versus bentonite concentration at CSR = 0.40 for the column-prepared series. The point at $C_{\text{bentonite}} = 0\%$ corresponds to clean sand prepared by column extraction. Panels (a) and (b) show $N_{0.9}$ and $N_{0.95}$, respectively.

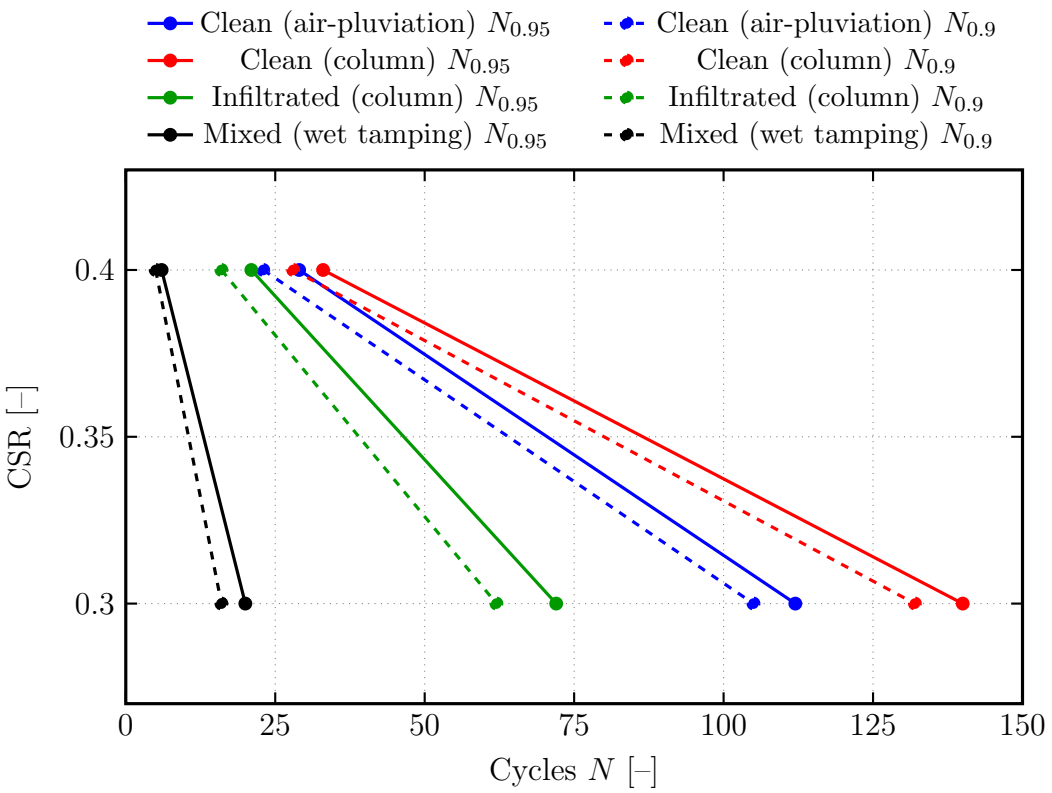

Figure 6.12: CSR versus the number of cycles required to reach the defined thresholds. For each preparation method, the solid line connects $N_{0.95}$ at CSR = 0.40 and 0.30, and the dashed line connects $N_{0.9}$.

6.5.5 Post-test bentonite mass balance

After selected cyclic tests, the specimen was removed with care to retain every grain. The membrane was peeled, the sample transferred to a clean tray, and the top and bottom porous stones, end platens, caps, and the membrane were rinsed thoroughly. The sand itself was washed with water until no visible bentonite remained attached to the grains. All rinse water and washings were collected in one container. The washings were oven-dried at 105 °C for more than 48 h until constant mass, and the remaining dry residue was weighed. As the sand grains were removed before drying, the residue consisted primarily of bentonite recovered from the washings, together with possible trace fines originating from the sand.

The theoretical bentonite mass was estimated from the specimen pore volume determined during specimen installation before saturation and loading, based on the measured specimen dimensions, and from the moisture-corrected slurry concentration used during infiltration:

$$m_{b,\mathrm{theoretical}} = \frac{C_{\mathrm{bentonite}}}{100}\,\rho_w\,V_{\mathrm{pore}}, \tag{6.7}$$

where ρ_w is the water density and V_{pore} is the pore volume determined during specimen installation. For this approximate inventory calculation, the specimen pore volume is taken as initially filled with inlet slurry and $\rho_w V_{\mathrm{pore}}$ is used as the corresponding mixing-water mass. This approximation is used only for the recovery check. Table 6.10 lists the theoretical and measured masses for the tested CT series.

The recovered dry-residue masses were broadly comparable with the theoretical bentonite masses. During cyclic loading, the closed drainage lines prevented external bentonite discharge, although redistribution within the specimen or into the adjacent porous stones remained possible. The mass balance therefore provides an approximate check on dosing and post-test recovery rather than evidence of bentonite retention during undrained cycling. Deviations from the theoretical values may reflect trace sand fines, incomplete initial slurry filling, or incomplete recovery from wetted components.

Table 6.10: Post-test bentonite mass balance. Theoretical mass from specimen pore volume and moisture-corrected slurry concentration using Equation (6.7); measured mass from oven-dried washings after testing.

Test ID	Specimen type	Theoretical [g]	Measured [g]
CT5	Slurry-infiltrated sand (column extraction, B60)	3.9	3.7
CT6	Slurry-infiltrated sand (column extraction, B60)	3.9	3.6
CT7	Remoulded sand–slurry mixture (wet tamping, B60)	3.6	3.5
CT8	Remoulded sand–slurry mixture (wet tamping, B60)	3.8	3.8
CT9	Slurry-infiltrated sand (column extraction, B20)	1.3	1.7
CT10	Slurry-infiltrated sand (column extraction, B40)	2.7	3.2
CT11	Slurry-infiltrated sand (column extraction, B80)	5.4	5.0

6.6 Response mechanisms

The results from the monotonic and cyclic triaxial tests provide a consistent picture of the mechanisms controlling the behaviour of the investigated sand–slurry systems. In the

monotonic tests, clean sand and slurry-infiltrated sand prepared by column extraction show nearly identical critical-state friction angles φ'_{cs} of 30.4° and 30.7°, respectively.

The corresponding value for the remoulded sand–slurry mixture prepared by wet tamping is 30.4°, which lies slightly below the infiltrated value and equals the clean-sand value at the reported precision. This indicates that the sand skeleton primarily governs the critical-state friction angle, while bentonite in the pore space mainly influences dilation around peak rather than the ultimate critical-state friction.

For fixed values of the cyclic stress ratio CSR and initial mean effective stress p'_0, specimens that exhibit a more contractive tendency during the early cycles show more rapid leftward migration of their effective stress paths in the q–p' plane, accumulate axial strain sooner, and reach the $N_{0.9}$ and $N_{0.95}$ thresholds in fewer cycles. The consistent ordering observed in the paired B60 tests—clean sand prepared by column extraction showing the highest cyclic resistance, slurry-infiltrated sand lower resistance, and remoulded sand–slurry mixtures the lowest—suggests a state–fabric effect in which bentonite placement modifies the stress–dilatancy response and leads to a faster loss of mean effective stress during cyclic loading. This interpretation is consistent with critical-state concepts, where the distance to the CSL and the initial tendency to contract influence the cyclic response.

The Cryo-BIB-SEM observations presented in Chapter 5 qualitatively support this interpretation of how preparation affects fabric. In the infiltrated material, the sand skeleton remains distinguishable and bentonite occurs as bridges within the intergranular pore space (Figure 5.4), whereas the remoulded reference contains quartz grains dispersed within a more continuous bentonite matrix without the organised bentonite bridges between grains observed after infiltration (Figure 5.5). These separate microstructural specimens do not resolve the load-bearing contact network and therefore cannot establish whether bentonite occupies individual force-carrying grain contacts in the triaxial specimens. It is nevertheless plausible that wet tamping places bentonite at or near a larger fraction of contacts and reduces direct sand–sand interlocking. This mechanism is consistent with, but does not by itself prove, the more gradual development of dilation observed for the wet-tamped specimen in the CID comparison and the faster loss of p' under undrained cyclic loading.

6.7 Implications for slurry-shield tunnelling

At the tunnel face of slurry-shield machines, chamber pressure and cutterhead forces show low-frequency cyclic components linked to cutterhead rotation and muck transport. Field

observations and modelling studies report such cyclic variations in face loading (Bezuijen et al., 2005; Park et al., 2021). The cyclic triaxial results presented here can therefore be interpreted as a laboratory analogue of this face loading.

In the paired B60 comparisons, for a given initial mean effective stress p'_0 and cyclic stress ratio CSR, clean sand prepared by column extraction sustained the highest number of cycles to the adopted thresholds, slurry-infiltrated column specimens showed a lower resistance, and remoulded sand–slurry mixtures prepared by wet tamping the lowest. This ordering reflects differences in specimen fabric: column extraction preserves an intact sand skeleton, whereas wet tamping remoulds the structure and leads to lower cyclic resistance.

Reducing CSR from 0.40 to 0.30 increased the number of cycles needed to reach the defined thresholds by roughly a factor of three to five across the different specimen preparation methods while preserving the same ranking. Within the infiltrated series at CSR = 0.40, the cycle counts varied non-monotonically across the tested bentonite concentrations. This variation should not be overinterpreted because only one specimen was tested at each concentration and small differences in initial state or specimen fabric may have influenced the ordering.

From an operational perspective, the paired B60 tests show that, at the same laboratory p'_0 and CSR, the slurry-infiltrated column specimens reached $N_{0.9}$ and $N_{0.95}$ in fewer cycles than the corresponding clean-column specimens. Here, cyclic resistance is defined solely by the number of cycles required to reach these adopted mean-effective-stress-reduction thresholds. The results obtained at the different bentonite concentrations showed a non-monotonic trend, however, and do not support a general statement that a higher bentonite concentration leads to a lower liquefaction resistance. For mechanized tunnelling projects, the paired B60 results therefore indicate that cyclic face-loading conditions and the fabric of slurry-infiltrated ground should be considered together when assessing susceptibility to cyclic loss of mean effective stress. However, laboratory p'_0 and CSR are not direct equivalents of field support pressure and its fluctuations. Accordingly, the measured thresholds should not be translated directly into field support-pressure criteria.

6.8 Limitations and scope

The test results presented herein apply to 50 × 100 mm triaxial specimens enclosed in a 0.7 mm membrane with smoothed end platens. This geometry permitted large axial strains without premature barreling, but it limits direct upscaling to field volume elements. The cyclic loading protocol was selected as a laboratory analogue of low-frequency fluc-

tuations in tunnel-face support pressure. Strength in this chapter is discussed within the critical-state framework: the CSL slope M and the corresponding critical-state friction angle φ'_{cs} are expressed in terms of effective stresses, and no intrinsic cohesion is inferred for the sands studied.

The preparation of the samples used here represents one way of placing bentonite in the pore space. Other preparation methods or different slurry rheologies could change how bentonite particles are distributed within the soil skeleton and, in turn, influence the measured response during cyclic loading. Particle-size filtering effects may also affect how bentonite is retained within the sand structure. The cyclic thresholds $N_{0.9}$ and $N_{0.95}$ are operational definitions used to compare tests at the same p'_0 and CSR; they should not be interpreted as universal indicators outside the present boundary conditions.

6.9 Summary

The CSL fits to the CIU tests yield tightly clustered effective critical-state friction angles φ'_{cs}: 30.4° for clean sand and 30.7° for slurry-infiltrated sand prepared by column extraction, while the corresponding value for the remoulded sand–slurry mixture prepared by wet tamping is 30.4°. The mean peak friction angles from the CIU tests were likewise narrowly clustered, ranging from 34.4° to 35.6°, and exceeded the critical-state values by approximately 4°–5°, consistent with dilation near peak.

The cyclic triaxial tests under undrained conditions with CSR control show an ordering of resistance. For the paired B60 comparisons at a given CSR and initial mean effective stress p'_0, the number of cycles required to reach the adopted thresholds follows the ranking: clean sand prepared by column extraction > slurry-infiltrated sand > remoulded sand–slurry mixture prepared by wet tamping. Decreasing the cyclic loading level (lower CSR, corresponding to smaller q_{amp}) increases the number of cycles to liquefaction substantially for all specimen types. Within the slurry-infiltrated series at CSR = 0.40, the cycle counts vary non-monotonically across the tested bentonite concentrations; because only one specimen was tested at each concentration, this result should not be interpreted as a definitive concentration trend.

Taken together, the monotonic and cyclic results are consistent with a state–fabric interpretation. Bentonite located in the pore space does not significantly change the critical-state friction angle governed by the sand skeleton, but it modifies the dilative and contractive tendencies of the soil during loading. The magnitude of this effect depends on how bentonite is distributed within the pore network and how it interacts with the sand structure during shearing.

7 Modelling slurry infiltration in porous media

In this chapter, bentonite slurry infiltration into saturated granular soils is described using a continuum mixture model. The modelling framework is implemented in COMSOL Multiphysics and verified against a published one-dimensional reference solution. The model is then extended and calibrated using the infiltration column experiments presented in Chapter 4. Finally, the model is applied to investigate infiltration behaviour under different conditions and to illustrate its applicability in a three-dimensional example.

7.1 Objectives

This chapter develops and evaluates a numerical model for bentonite slurry infiltration into saturated granular soils. The published one-dimensional infiltration model of Schaufler et al. (2013) is first implemented and verified against the reference formulation. The model is then extended to represent bentonite slurry infiltration by incorporating experimentally calibrated relations for slurry density $\rho_f(c)$ and viscosity $\mu_f(c)$ together with a concentration-dependent deposition coefficient $\lambda(c)$ and gravity in the one-dimensional setting.

The extended model is calibrated using one infiltration column test for each of the investigated sands and subsequently applied, without recalibration, to predict infiltration behaviour under different injection pressures. A parametric study is then performed to examine sensitivities and penetration trends and to assess the scope of applicability of the formulation. Finally, a simplified three-dimensional example based on the Schaufler formulation is presented to demonstrate the feasibility of extending the approach under gravity.

Principal symbols

Symbol	Unit	Meaning
c	–	Dimensionless normalized bentonite concentration used in the calibrated one-dimensional model
c_v	–	Volumetric fines concentration used only in the Schaufler reference calculations and three-dimensional proof-of-concept
$n_\alpha,\ n_f,\ n_{f0}$	–	Constituent volume fraction, porosity, and initial porosity
$\mathbf{q},\ \mathbf{v}_f$	$\mathrm{m\,s^{-1}}$	Darcy (superficial) and intrinsic pore-fluid velocities
p_f	Pa	Mobile pore-fluid pressure
$P_{\mathrm{inj}},\ \Delta P$	kPa	Prescribed inlet–outlet pressure difference
$k(n_f),\ k_0$	$\mathrm{m^2}$	Evolving and initial intrinsic permeability
$\rho_f(c),\ \rho_w$	$\mathrm{kg\,m^{-3}}$	Slurry/pore-fluid and water densities
$\mu_f(c),\ \mu_w$	Pa s	Slurry/pore-fluid and water dynamic viscosities
$\lambda(c),\ \lambda_0$	$\mathrm{m^{-1}}$	Concentration-dependent and baseline deposition coefficients
$\alpha_{100},\ \alpha_{\mathrm{ini}},\ \alpha_{\max}$	$\mathrm{m^{-1}}$	Pressure-reference, run-specific lower, and upper logistic scales
$n,\ \beta$	–	Pressure-scaling exponent and logistic curve parameter
$\widehat{n}_{bf\to bs}$	$\mathrm{s^{-1}}$	Constituent-volume transfer rate in the reference formulation and effective deposition/porosity-loss rate in the calibrated simulations
$\mathbf{g},\ g$	$\mathrm{m\,s^{-2}}$	Gravitational acceleration vector and magnitude
$L,\ \mathbf{x},\ x,\ z$	m	Model length and spatial coordinates
$t,\ T,\ t_{\mathrm{end}}$	s	Time, total simulation time, and end time

7.2 Modelling framework and assumptions

A fully saturated, rigid granular medium infiltrated by bentonite slurry is considered at the representative elementary volume (REV) scale (Bear, 1972; Whitaker, 1999). Four constituents are present—water (w), fluidized bentonite fines (bf), attached bentonite fines (bs), and soil grains (g). Fluidized fines remain suspended in the pore liquid and

move with the fluid phase, whereas attached fines are immobilized on the grain skeleton, for example on grain surfaces or within pore throats, and are therefore treated as part of the solid phase. Attachment transfers bentonite from the mobile bf constituent to the retained bs constituent and correspondingly reduces the fluid-filled pore volume. Their volume fractions are defined as $n_\alpha = V_\alpha/V$ with

$$n_f = n_w + n_{bf}, \tag{7.1a}$$

$$n_s = n_g + n_{bs} = 1 - n_f. \tag{7.1b}$$

For the Schaufler reference formulation, the volumetric concentration of fluidized fines within the pore-fluid phase is denoted by c_v:

$$c_v = \frac{n_{bf}}{n_f}, \tag{7.2}$$

because $n_{bf} = V_{bf}/V$ and $n_f = V_f/V$, with $V_f = V_w + V_{bf}$. Consequently, $c_v = V_{bf}/V_f$ is the fraction of the fluid-filled pore volume occupied by mobile bentonite fines and is not itself the porosity, as commonly used in suspension-filtration models (Herzig et al., 1970; Tien and Payatakes, 1979; Sharma and Yortsos, 1987). Thus, c_v varies with position and time. For brevity, it is written simply as c_v rather than $c_v(\mathbf{x}, t)$ where the dependence is clear.

Notation. The original notation of Schaufler et al. (2013) is retained when the reference formulation is stated: ϕ and ϕ_0 denote porosity and initial porosity, $k_s(\phi)$ and k_s^0 denote intrinsic permeability and its initial value, and $\eta_l(c_v)$ denotes the liquid viscosity. In the present model, the corresponding symbols are n_f, n_{f0}, $k(n_f)$, k_0, and $\mu_f(c)$, respectively. Thus, the symbol correspondence is $\phi \leftrightarrow n_f$, $\phi_0 \leftrightarrow n_{f0}$, $k_s(\phi) \leftrightarrow k(n_f)$, $k_s^0 \leftrightarrow k_0$, and $\eta_l(c_v) \leftrightarrow \mu_f(c)$; the constitutive forms used in the present model are stated separately below. The calibrated simulations use the dimensionless concentration c, whereas c_v is reserved for the Schaufler reference calculations.

Concentration convention. Consistent with the lowercase notation used in the preceding chapters, the calibrated model uses a single concentration symbol, c. Experimental bentonite-concentration values reported in Chapter 4 in $\mathrm{g\,L^{-1}}$ are normalized once before being used in the model:

$$c = \frac{\text{experimental bentonite concentration}}{1000\ \mathrm{g\,L^{-1}}}.$$

Accordingly, $53.3\ \mathrm{g\,L^{-1}}$ corresponds to $c = 0.0533$. Throughout the presentation of the calibrated one-dimensional model and its results, c denotes this dimensionless normalized

concentration; its prescribed value at the inlet is stated directly as a boundary value of c, without introducing a second concentration variable. In the Schaufler verification subsection and the three-dimensional proof-of-concept, c_v retains the volumetric definition used in the original reference formulation.

The Darcy (superficial, or filter) velocity $\mathbf{q}$ is the volumetric flow rate per unit bulk cross-sectional area and therefore has units of velocity, not volume. For the stationary skeleton considered here, it is related to the intrinsic pore-fluid velocity $\mathbf{v}_f$ by $\mathbf{q} = n_f\,\mathbf{v}_f$ (Bear, 1972; Schaufler et al., 2013). The vector $\mathbf{g}$ denotes gravitational acceleration. The hydraulic unknown $p_f(\mathbf{x}, t)$ is the pressure of the mobile pore-fluid/slurry phase; its spatial gradient, together with the body-force term $\rho_f(c)\mathbf{g}$, provides the hydraulic driving term in Darcy's law, Eq. (7.3a).

7.2.1 Kinematic assumptions

The granular skeleton is assumed rigid and stationary, and attached bentonite fines are immobilized on this skeleton. Water and fluidized fines move together with the pore-fluid velocity $\mathbf{v}_f$. All constituents are materially incompressible. In one dimension, mixture mass conservation therefore gives $\partial_x \mathbf{q} = 0$, meaning that the Darcy velocity remains spatially uniform at each time. The same relation is used in the reference formulation (Schaufler et al., 2013, Eq. 17).

7.2.2 Flow law

Laminar flow is described by Darcy's law with porosity-dependent intrinsic permeability and concentration-dependent viscosity. When activated, gravity and concentration-dependent density are included:

$$\mathbf{q} = \frac{k(n_f)}{\mu_f(c)}\big(\rho_f(c)\,\mathbf{g} - \nabla p_f\big), \tag{7.3a}$$

$$\nabla\cdot\,\mathbf{q} = 0, \tag{7.3b}$$

where boldface denotes vectors. Here, $k(n_f)$ is the intrinsic permeability of the evolving porous skeleton: it characterizes the connected pore geometry and is not a property of either water or the slurry (Bear, 1972). Fluid-phase effects enter separately through the concentration-dependent viscosity $\mu_f(c)$ and density $\rho_f(c)$. Neglecting body forces and assuming constant ρ_f recovers the baseline reference form $\mathbf{q} = -\,k_s(\phi)\,\eta_l^{-1}(c_v)\,\nabla p_f$, stated

here in the original notation of Schaufler et al. (2013, Eq. 22). The intrinsic permeability is related to porosity through a Kozeny–Carman-type relation, while the suspension viscosity depends on concentration (see Section 7.4; cf. (Kozeny, 1927; Carman, 1937, 1956)).

7.2.3 Attachment and porosity evolution

Attachment is written separately for the two concentration conventions. In the Schaufler reference formulation it is a constituent-volume transfer based on c_v; in the calibrated simulations it is an effective deposition and porosity-loss law based on c:

$$\widehat{n}_{bf\to bs} = \lambda_0\, c_v\, |\mathbf{q}| \qquad \text{(Schaufler reference)}, \tag{7.4a}$$

$$\widehat{n}_{bf\to bs} = \lambda(c)\, c\, |\mathbf{q}| \qquad \text{(calibrated model)}, \tag{7.4b}$$

$$\partial_t n_f = -\,\widehat{n}_{bf\to bs}. \tag{7.4c}$$

Here, λ denotes the deposition coefficient. In the baseline formulation of Schaufler et al. (2013) it is treated as the constant λ_0, whereas in the present work $\lambda(c)$ depends on the evolving local concentration. Its run-specific coefficient α_{ini} is fixed from the prescribed injection pressure before time integration. The superposed hat identifies $\widehat{n}_{bf\to bs}$ as a constituent-volume transfer rate in the reference formulation and as an effective deposition/porosity-loss rate in the calibrated simulations. Because both c_v and c are dimensionless, $\widehat{n}_{bf\to bs}$ has units of s^{-1}; with $|\mathbf{q}|$ in $\mathrm{m\,s}^{-1}$, Eqs. (7.4a) and (7.4b) therefore require λ_0 and the coefficients defining $\lambda(c)$ to have units of m^{-1}. Gravity modifies $\mathbf{q}$ through the body-force term in Darcy's law but does not alter the form or dimensions of the attachment law. This structure follows deep-bed filtration formulations, where the deposition rate scales with the particle flux and leads to a reduction of porosity as particles accumulate within the pore space (Herzig et al., 1970; Tien and Payatakes, 1979; Sharma and Yortsos, 1987).

The kinematic assumptions, flow relation, and attachment formulation introduced above define the physical processes governing slurry infiltration in the porous medium. Based on these assumptions, the conservation equations for the individual constituents and the coupled pressure–transport system are derived in the following section.

7.3 Governing equations

7.3.1 Phase balances and transport

For the Schaufler reference formulation, the local balances for materially incompressible constituents are written in volume form (Schaufler et al., 2013; Whitaker, 1999):

$$\partial_t n_w + \nabla\cdot\big((1-c_v)\,\mathbf{q}\big) = 0, \tag{7.5a}$$

$$\partial_t n_{bf} + \nabla\cdot\big(c_v\,\mathbf{q}\big) + \widehat{n}_{bf\to bs} = 0, \tag{7.5b}$$

$$\partial_t n_{bs} - \widehat{n}_{bf\to bs} = 0. \tag{7.5c}$$

Here $\mathbf{q} = n_f\,\mathbf{v}_f$ denotes the Darcy (superficial) velocity, $n_f = n_w + n_{bf}$ is the porosity, and $\widehat{n}_{bf\to bs}$ is the volumetric production term for attachment.

Summing Eqs. (7.5) and using $n_f + n_s = 1$ yields the mixture continuity

$$\nabla\cdot\mathbf{q} = 0,$$

(cf. Eq. (7.3b); Schaufler et al. 2013). The flow is laminar and described by Darcy's law (Eq. (7.3a)).

From Eq. (7.5c) and $n_s = n_g + n_{bs} = 1 - n_f$ follows the porosity evolution

$$\partial_t n_f = -\,\widehat{n}_{bf\to bs}. \tag{7.6}$$

Material incompressibility fixes the constituent densities, not their local volume fractions. Since $n_w = (1-c_v)n_f$ and $\mathbf{q} = n_f\mathbf{v}_f$, the water flux in Eq. (7.5a) is $n_w\mathbf{v}_f = (1-c_v)\mathbf{q}$, and n_w may therefore evolve through transport. Equation (7.6) governs the total fluid-filled porosity n_f; it does not imply that the constituent water fraction n_w is constant.

Using $n_{bf} = n_f c_v$ in Eq. (7.5b) together with Eq. (7.6) gives the fines transport equation, corresponding to the expanded form of $\partial_t(n_f c_v) + \nabla\cdot(c_v\,\mathbf{q}) = \widehat{n}_a$ in the reference model (Schaufler et al., 2013, Eq. 16):

$$n_f\,\partial_t c_v + \nabla\cdot(c_v\,\mathbf{q}) + (1-c_v)\,\widehat{n}_{bf\to bs} = 0. \tag{7.7}$$

7.3.2 Coupled pressure–transport system

Equations (7.3b) and (7.7) define the Schaufler reference structure in terms of c_v. For the calibrated one-dimensional formulation, the same algebraic structure is written in terms

of the normalized concentration c, with $\rho_f(c)$, $\mu_f(c)$, and the deposition and porosity-loss terms treated as effective calibrated quantities. Eliminating $\mathbf{q}$ via Eq. (7.3a) yields the two partial differential equations used for the calibrated model:

$$\nabla\cdot\Big(\frac{k(n_f)}{\mu_f(c)}\big(\rho_f(c)\,\mathbf{g}-\nabla p_f\big)\Big)=0, \tag{7.8a}$$

$$n_f\,\partial_t c+\nabla\cdot\Big(c\,\frac{k(n_f)}{\mu_f(c)}\big(\rho_f(c)\,\mathbf{g}-\nabla p_f\big)\Big)+(1-c)\,\widehat{n}_{bf\to bs}=0. \tag{7.8b}$$

Equation (7.8a) is the pressure equation (PDE A); Eq. (7.8b) is the transport and deposition equation (PDE B). In general, the production term is

$$\widehat{n}_{bf\to bs}=\lambda(c)\,c\,|\mathbf{q}|. \tag{7.9}$$

Notation. The notation $|\mathbf{q}|\equiv\|\mathbf{q}\|_2$ is used, where $\|\mathbf{q}\|_2$ denotes the Euclidean magnitude of the Darcy flux $\mathbf{q}$ defined by Eq. (7.3a). The reference attachment term scales with $c_v|\mathbf{q}|$, whereas the calibrated effective term scales with $c|\mathbf{q}|$. This structure is consistent with the reference formulation (Schaufler et al., 2013, Eq. 26) and with deep-bed filtration models in which deposition scales with particle flux and reduces porosity accordingly (Herzig et al., 1970; Tien and Payatakes, 1979; Sharma and Yortsos, 1987). Specific forms for $k(n_f)$, $\mu_f(c)$, $\rho_f(c)$, and $\lambda(c)$ are given in Section 7.4.

7.4 Constitutive relations (baseline and calibrated)

7.4.1 Hydraulic properties

The intrinsic permeability is related to porosity through a Kozeny–Carman form,

$$k(n_f)=k_0\left(\frac{n_f^3}{(1-n_f)^2}\right)\left(\frac{(1-n_{f0})^2}{n_{f0}^3}\right), \tag{7.10}$$

so that $k(n_{f0})=k_0$ in the initial state.

For the reference reproduction, the slurry properties follow the baseline assumptions

$$\mu_f(c_v)=\mu_w\left(1+\frac{5}{2}\,c_v\right), \tag{7.11}$$

$$\rho_f(c_v)\equiv\rho_w, \tag{7.12}$$

$$\lambda(c_v)\equiv\lambda_0. \tag{7.13}$$

The viscosity relation in Eq. (7.11) is Einstein's dilute-suspension expression for non-interacting rigid spherical particles (Einstein, 1906, 1911). It is adopted here solely to reproduce the baseline model of Schaufler et al. (2013, Eq. 24) and is not used for the calibrated bentonite-slurry simulations. Gravity may be neglected in the baseline runs to match the reference setting.

For the calibrated model, the following empirically derived relations are used:

$$\rho_f(c) = \rho_w + 580\, c, \tag{7.14}$$

$$\mu_f(c) = \mu_w + 271.7\, c^{2.2}. \tag{7.15}$$

Because c is dimensionless, the coefficients 580 and 271.7 have units of $\mathrm{kg\,m^{-3}}$ and $\mathrm{Pa\,s}$, respectively. The relations were obtained from the measurements described in Chapter 3; $\mu_f(c)$ uses the apparent viscosity at $\dot{\gamma} = 50\ \mathrm{s^{-1}}$, so shear rate is not a separate model variable. The fitted coefficients are specific to the dimensionless normalized concentration c defined above.

7.4.2 Deposition law and model constraints

For each simulation, the deposition coefficient is evaluated as a function of the local concentration c, with the run-specific coefficient α_{ini} assigned from the prescribed injection pressure P_{inj} before time integration:

$$\lambda(c) = \alpha_{\mathrm{ini}} + \frac{\alpha_{\max} - \alpha_{\mathrm{ini}}}{1 + \exp(\beta c)}, \tag{7.16}$$

$$\alpha_{\mathrm{ini}} = \alpha_{100} \left(\frac{P_{\mathrm{inj}}}{100\ \mathrm{kPa}} \right)^{-n}, \qquad \alpha_{100} = 0.0346\ \mathrm{m^{-1}},\ n = 3.80. \tag{7.17}$$

Here $P_{\mathrm{inj}} := |\bar{p}_0 - \bar{p}_L|$ is the prescribed inlet–outlet pressure difference, treated as a positive, time-independent scalar for each simulation rather than the pore-fluid pressure field $p_f(\mathbf{x}, t)$. It is evaluated once before time integration to assign α_{ini}; thereafter, $\lambda = \lambda(c)$ varies only through the evolving local concentration. The parameters α_{100}, α_{ini}, and $\alpha_{\max}$ have units of $\mathrm{m^{-1}}$. Here, α_{100} is the value of α_{ini} at $P_{\mathrm{inj}} = 100$ kPa, n is the dimensionless pressure-scaling exponent, and β is the dimensionless parameter controlling the steepness of the concentration dependence in $\lambda(c)$. In this relation, α_{ini} is the pressure-scaled lower asymptotic level, not the value of λ at the initial time or at $c = 0$; specifically, $\lambda(0) = (\alpha_{\max} + \alpha_{\mathrm{ini}})/2$. The parameter $\alpha_{\max}$ defines the upper logistic scale. When gravity is activated, it enters Darcy's law through the body-force term $\rho_f(c)\mathbf{g}$.

Bounds enforced in calibration and simulation are

$$0 \leq c < 1, \qquad 0 < n_f < 1, \qquad k(n_f) \geq 0, \qquad \mu_f(c) > 0, \qquad \lambda(c) \geq 0. \tag{7.18}$$

For the calibrated simulations, $c < 1$ restricts the normalized concentration to the adopted model range. In the Schaufler reference calculations, the corresponding physical bound is $0 \leq c_v < 1$.

With these bounds, the effective deposition law gives $\partial_t n_f \leq 0$; in the calibrated simulations, this evolution represents deposition-induced reduction of the effective hydraulic porosity.

Equations (7.10)–(7.17) are substituted into the system of governing equations derived in Section 7.3. Gravity acts through the body-force term in Darcy's law, and no additional field equation is introduced.

7.5 Initial and boundary conditions, and numerical implementation

7.5.1 Initial and boundary conditions

The system of governing equations in Section 7.3 is posed on a spatial domain $\Omega \subset \mathbb{R}^d$ ($d = 1$ or 3) and a time interval $t \in (0, T]$. The geometry and principal model inputs used for the simplified three-dimensional realization are described in Section 7.11. The boundary $\partial\Omega$ is partitioned into a Dirichlet part Γ_D and a Neumann part Γ_N for the hydraulic subproblem (pressure or normal flux), consistent with the initial–boundary value formulation in the reference model (Schaufler et al., 2013, Sec. 2).

7.5.2 Initial conditions

Initial fields are prescribed as

$$p_f(\mathbf{x}, 0) = p_{f0}(\mathbf{x}), \tag{7.19a}$$

$$c(\mathbf{x}, 0) = 0, \tag{7.19b}$$

$$n_f(\mathbf{x}, 0) = n_{f0}(\mathbf{x}). \tag{7.19c}$$

Here n_{f0} defines the initial porosity field, and the normalized concentration c is initially zero in the soil domain before infiltration. An initial pressure p_{f0} may be supplied for completeness, although Eqs. (7.3a)–(7.3b) form a stationary (elliptic) subproblem for p_f at each time step (Bear, 1972). The initial pressure field $p_{f0}(\mathbf{x})$ is distinct from P_{inj}, which denotes the prescribed inlet–outlet pressure difference for a simulation.

7.5.3 Boundary conditions

For the hydraulic subproblem, either pressure (Dirichlet) or normal flux (Neumann) is prescribed:

$$p_f(\mathbf{x}, t) = \bar{p}(\mathbf{x}, t) \qquad \text{on } \Gamma_D \times (0, T], \tag{7.20a}$$

$$\mathbf{q}(\mathbf{x}, t) \cdot \mathbf{n} = \bar{q}(\mathbf{x}, t) \qquad \text{on } \Gamma_N \times (0, T]. \tag{7.20b}$$

Here $\mathbf{n}$ denotes the unit outward normal, and the overbar denotes prescribed boundary data rather than averaging: $\bar{p}(\mathbf{x}, t)$ is the prescribed pore-fluid pressure on Γ_D, while $\bar{q}(\mathbf{x}, t)$ is the prescribed outward-normal Darcy (superficial) flux per unit area on Γ_N. These conditions correspond to the boundary counterparts of Darcy flow and mixture continuity (cf. Eqs. (7.3a)–(7.3b); Schaufler et al. 2013).

Because diffusion or dispersion is neglected, the concentration is prescribed only on the inflow part of the boundary,

$$c(\mathbf{x}, t)|_{\Gamma_{\text{in}}(t)} = \text{prescribed value}, \qquad \Gamma_{\text{in}}(t) := \{\mathbf{x} \in \partial\Omega \mid \mathbf{q}(\mathbf{x}, t) \cdot \mathbf{n} < 0\}, \tag{7.21}$$

while no additional condition is imposed on outflow ($\mathbf{q} \cdot \mathbf{n} \geq 0$). This choice is consistent with an advection-only transport model and avoids prescribing c where characteristics leave the domain.

For the one-dimensional column simulations used for calibration and prediction, the domain length is L and flow occurs from $x = 0$ to $x = L$. The boundary conditions are therefore

$$p_f(0, t) = \bar{p}_0, \qquad p_f(L, t) = \bar{p}_L, \tag{7.22a}$$

$$c(0, t) = \text{prescribed value for each run}, \tag{7.22b}$$

$$c(L, t) \quad \text{free (convective outflow)}. \tag{7.22c}$$

For these simulations, the value of c prescribed at $x = 0$ is constant within each run and is listed directly in the corresponding input table. For the Schaufler verification and the three-dimensional proof-of-concept, the same boundary form applies to c_v.

The prescribed pressure difference P_{inj}, defined in Section 7.4, is evaluated once for each simulation to assign the run-specific α_{ini}.

For the one-dimensional vertical columns, x increases upward from the inlet at $x = 0$ to the outlet at $x = L$. Accordingly, when gravity is activated in Darcy's law (Eq. (7.3a)), $\mathbf{g} = -g\,\mathbf{e}_x$, where $g > 0$ is the gravitational acceleration; the imposed flow is therefore upward against gravity. The boundary conditions remain unchanged, and buoyancy enters the governing equations through the term $\rho_f(c)\mathbf{g}$ in Eqs. (7.8a)–(7.8b).

7.6 Numerical implementation (1-D)

7.6.1 Flow and transport formulation

The Darcy interface supplies the Darcy (superficial) velocity $\mathbf{q}$. Within the Darcy operator, the intrinsic permeability and porosity inputs are $k(n_f)$ and n_f, respectively, while the density and dynamic-viscosity inputs are $\rho_f(c)$ and $\mu_f(c)$. The constitutive relations are given by Eqs. (7.10), (7.14), and (7.15).

The flow subproblem is solved with gravity activated using

$$\nabla\cdot\,\mathbf{q} = 0, \qquad \mathbf{q} = \frac{k(n_f)}{\mu_f(c)}\big(\rho_f(c)\,\mathbf{g} - \nabla p_f\big),$$

which corresponds to Eq. (7.8a).

Transport and deposition are solved using the *Transport of Diluted Species in Porous Media* interface without diffusion. The dependent variable is the dimensionless normalized concentration c with porous scaling,

$$\partial_t(n_f c) + \nabla\cdot\,(c\,\mathbf{q}) = R, \qquad R = -\,(1-c)\,\lambda(c)\,c\,|\mathbf{q}|,$$

which reproduces Eq. (7.8b). For the calibrated simulations, R is interpreted as an effective empirical concentration sink. The sink term R is implemented as a reaction term, with the Darcy-speed magnitude $|\mathbf{q}|$ represented in COMSOL by `dl.U`. A global parameter `Pinj` (kPa) is prescribed for each simulation and used before time integration to compute the constant coefficient α_{ini} from Eq. (7.17). During the solution, $\lambda(c)$ therefore varies only with the evolving local concentration. Consistent stabilization in COMSOL, combining streamline-diffusion and crosswind-diffusion, is used to suppress oscillations under advection-only transport. The implementation uses these built-in COMSOL interfaces, coupled through user-defined variables, constitutive expressions, and the state-variable update described below; no external user subroutines are used.

7.6.2 Numerical realization and boundary data

The effective hydraulic porosity field is updated according to

$$\partial_t n_f = -\,\lambda(c)\, c\, |\mathbf{q}|,$$

consistent with Eq. (7.6). In the implementation, this evolution is represented by the state variable `d_epsi`, updated after each time step, while the resulting porosity $n_f =$ `epsi_ini`$-$`d_epsi` is supplied to the Darcy and transport interfaces. The updated porosity controls the permeability $k(n_f)$ in the Darcy operator and the porous scaling in the transport equation.

For the one-dimensional column domain $x \in [0, L]$, the boundary data are

$$p_f(0,t) = \bar{p}_0, \qquad p_f(L,t) = \bar{p}_L, \qquad c(0,t) = \text{prescribed value for each run},$$

while the outlet concentration at $x = L$ is treated as convective outflow (no Dirichlet condition). The prescribed pressure difference P_{inj}, defined in Section 7.4, is used once before time integration to assign the constant α_{ini}.

Initial fields are prescribed as

$$p_f(x,0) = p_{f0}(x), \qquad c(x,0) = 0 \text{ in the soil}, \qquad n_f(x,0) = n_{f0}(x).$$

The one-dimensional column domain was discretized into 100 uniform line elements, with quadratic interpolation for pressure and linear interpolation for concentration.

7.7 Verification (1-D)

To verify the implementation, the one-dimensional infiltration benchmark reported by Schaufler et al. (2013) was reproduced using the same modelling ingredients as the reference: Darcy flow with a porosity-dependent intrinsic permeability (Kozeny–Carman), a concentration-dependent suspension viscosity (Einstein), and a deposition (production) term proportional to the convective flux. To distinguish the reference deposition parameter k from the intrinsic permeability $k(n_f)$ used in this chapter, it is denoted here by the constant λ_0:

$$\widehat{n}_a = -\,\lambda_0\, c_v\, |\mathbf{q}|.$$

Boundary and initial data follow the reference setup: column length $L = 20$ m; pressures $p_0 = 6.38$ kPa at $x = 0$ and $p_L = 0$ at $x = L$; prescribed inlet value $c_v = 0.1$; initial

porosity $\phi_0 = 0.32$; initial intrinsic permeability $k_s^0 = 8.57 \times 10^{-10}$ m^2 (equivalently, $n_{f0} = 0.32$ and $k_0 = 8.57 \times 10^{-10}$ m^2 in the present notation); and total time $T = 10^5$ s. With a small deposition coefficient $\lambda_0 = 10^{-4}$ m^{-1}, the computation produces the normalized-porosity map shown in Fig. 7.1(b). Figure 7.1 directly compares the published reference result in panel (a) with the present reproduction in panel (b); the reference notation ϕ/ϕ_0 is equivalent to n_f/n_{f0} in the present notation. Both panels use the dimensionless coordinates x/L and t/T and the same normalized-porosity range. The comparison reproduces the rapid porosity reduction near the inlet at early times, the smooth recovery downstream, and the progressive flattening of the contours. Minor offsets between individual isolines, most evident at later normalized times toward the outlet, are attributable to discretization and interpolation. The close agreement in the overall contour pattern supports the implementation of the coupled pressure–transport equations and deposition law in one dimension.

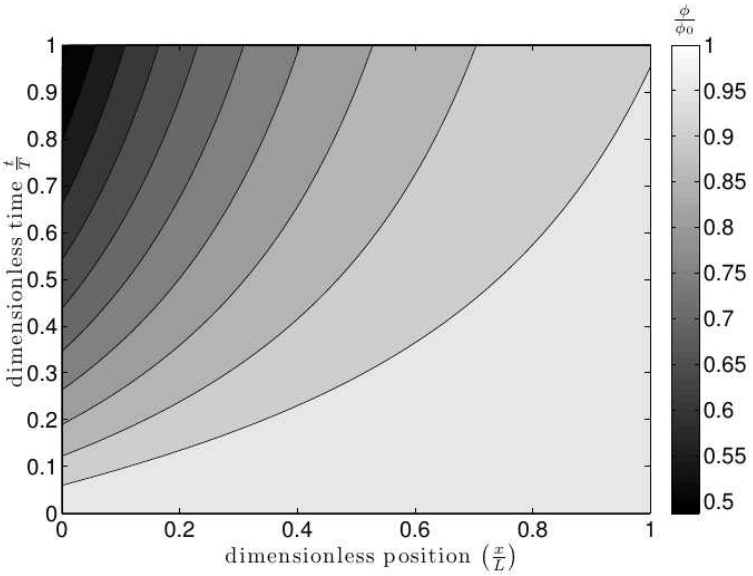

(a) Published reference result

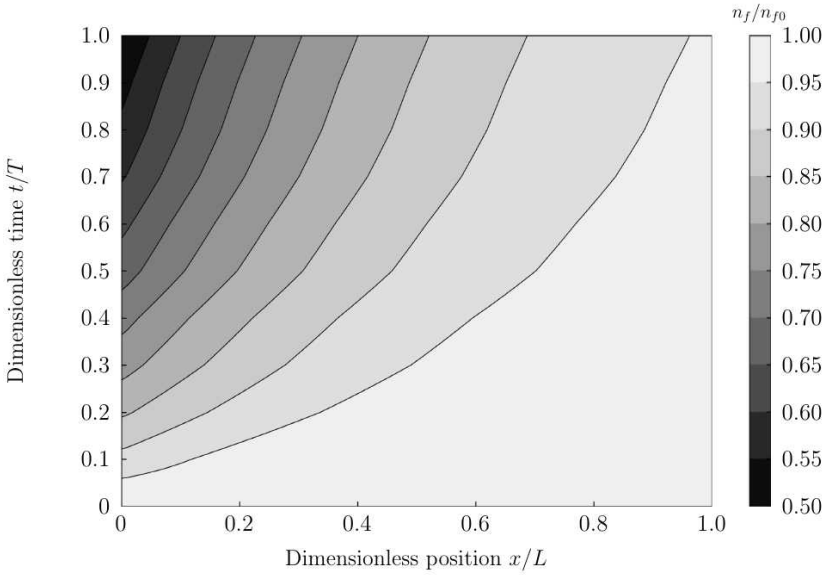

(b) Present COMSOL reproduction

Figure 7.1: Direct comparison of simulation results with the published one-dimensional benchmark. (a) Normalized-porosity contours reported by Schaufler et al. (2013, Fig. 3), expressed as ϕ/ϕ_0. (b) Present COMSOL reproduction, expressed as n_f/n_{f0}, where $\phi/\phi_0 \equiv n_f/n_{f0}$. Both panels use the dimensionless coordinates $(x/L, t/T)$ and the normalized-porosity range 0.50–1.00 (deposition coefficient $\lambda_0 = 10^{-4}$ m^{-1}).

7.8 Calibration protocol (1–D)

For each sand gradation (S 0.1–0.5 mm, S 0.5–1.0 mm, and S 1.0–2.0 mm), a single parameter set $\boldsymbol{\theta} = \{\alpha_{\mathrm{ini}}, \alpha_{\max}, \beta\}$ was calibrated using the column test conducted at the prescribed pressure difference $P_{\mathrm{inj}} = 50$ kPa. The governing equations and constitutive relations were those defined in the previous subsection; only $\boldsymbol{\theta}$ was adjusted. All other inputs were adopted from or approximated from the corresponding column test and kept fixed throughout the calibration, namely the column geometry, initial intrinsic permeability k_0 measured from the column experiments, initial porosity n_{f0}, the prescribed inlet value of c, and fluid properties. Calibration targeted the end-of-test dimensionless concentration profile c: $\boldsymbol{\theta}$ was adjusted until the simulated profile $c(z, t_{\mathrm{end}}; \boldsymbol{\theta})$ reproduced the normalized measurements $\widehat{c}(z_i)$ at the sampling elevations z_i. The agreement is shown by overlaying simulated and measured end-of-test profiles.

With the calibrated parameter set $\boldsymbol{\theta}$ fixed for each sand, the model was subsequently run at prescribed pressure differences $P_{\mathrm{inj}} = 30$, 100, and 200 kPa by modifying only the pressure boundary conditions. All other inputs (measured k_0, n_{f0}, the prescribed inlet value of c, geometry, and fluid properties) were adopted from the corresponding column tests and kept unchanged. The predicted end-of-test c profiles are compared with the normalized measurements for each pressure level. For the 1–2 mm sand, only a test at $P_{\mathrm{inj}} = 50$ kPa was available; therefore cross-pressure validation was not possible for that gradation.

Table 7.1 lists the fixed inputs from the 50 kPa column test together with the calibrated parameters. Figure 7.2(a) compares the end-of-test dimensionless concentration profile c with the model prediction, while Fig. 7.2(b) presents the corresponding pore-fluid pressure profiles. The same optimum parameter set is used in the pore-fluid pressure comparisons presented below.

The same calibration procedure was applied to the other sands. For S 0.5–1.0 mm, the inputs and calibrated parameters are summarised in Table 7.2, with the corresponding results shown in Fig. 7.3(a) for the end-of-test c profile and Fig. 7.3(b) for the pore-fluid pressure profiles. For S 1.0–2.0 mm, the inputs and optimum parameters are listed in Table 7.3, with the corresponding comparisons shown in Fig. 7.4(a) and Fig. 7.4(b). In each case the calibrated parameter set is used unchanged in the pore-fluid pressure comparisons.

For the fine and medium sands, which exhibited internal filter-cake formation, Eq. (7.17) was evaluated once before each run to assign the constant α_{ini} from the prescribed pressure. Within that run, $\lambda(c)$ varied only with the evolving concentration.

Table 7.1: Fixed inputs and calibrated parameters for the S 0.1–0.5 mm sand column test at $P_{\text{inj}} = 50$ kPa.

Quantity	**Symbol**	**Value**
Model length	L	0.326 m
Inlet pressure	p_0	50 kPa
Outlet pressure	p_L	0 kPa
Initial porosity	n_{f0}	0.42
Prescribed inlet value of c	$c(0,t)$	0.0533
Initial intrinsic permeability	k_0	4.06×10^{-11} m^2
Water dynamic viscosity	μ_w	1×10^{-3} Pa s
Slurry density	ρ_{slurry}	1032 kg m^{-3}
Pressure-scaling reference at 100 kPa	α_{100}	0.0346 m^{-1}
Pressure exponent	n	3.80
Pressure-scaled baseline at 50 kPa (used)	$\alpha_{\text{ini}}(50\,\text{kPa})$	0.48 m^{-1}
Upper logistic scale	$\alpha_{\max}$	330 m^{-1}
Curve parameter	β	101.5

Notes: α_{100}, α_{ini}, $\alpha_{\max}$ in m^{-1}; n, β, and c are dimensionless.

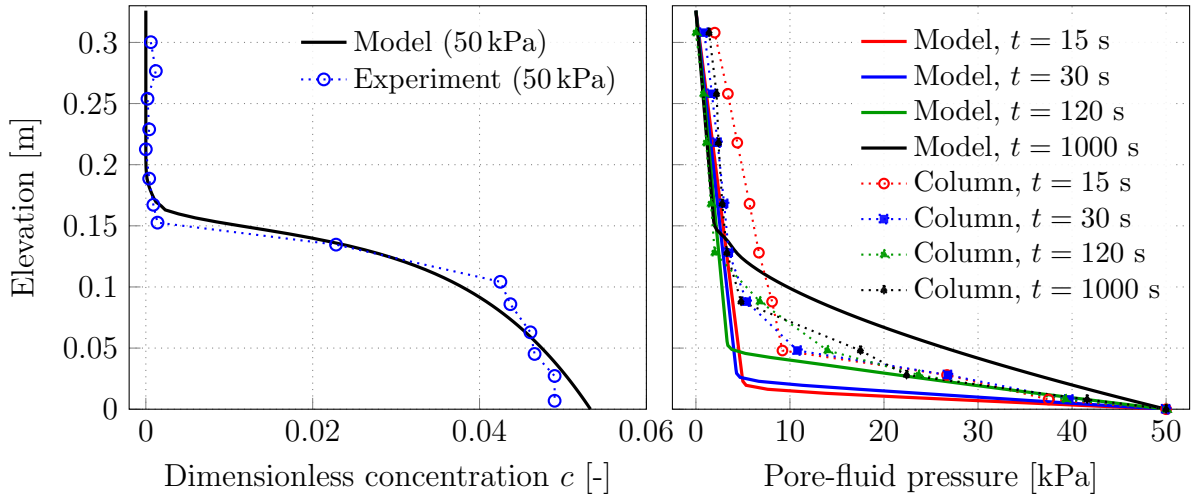

Figure 7.2: Column test on S 0.1–0.5 mm sand at the prescribed pressure difference $P_{\text{inj}} = 50$ kPa. (a) End-of-test dimensionless concentration profile c - model vs. experiment. (b) Pore-fluid pressure profiles at $t = 15, 30, 120, 1000$ s - model (solid) vs. experiment (dotted).

Table 7.2: Fixed inputs and calibrated parameters for the S 0.5–1.0 mm sand column test at $P_{\text{inj}} = 50$ kPa.

Quantity	**Symbol**	**Value**
Model length	L	0.328 m
Inlet pressure	p_0	50 kPa
Outlet pressure	p_L	0 kPa
Initial porosity	n_{f0}	0.40
Prescribed inlet value of c	$c(0,t)$	0.0500
Initial intrinsic permeability	k_0	7.32×10^{-11} m^2
Water dynamic viscosity	μ_w	1×10^{-3} Pa s
Slurry density	ρ_{slurry}	1032 kg m^{-3}
Pressure-scaling reference at 100 kPa	α_{100}	0.0346 m^{-1}
Pressure exponent	n	3.80
Pressure-scaled baseline at 50 kPa (used)	$\alpha_{\text{ini}}(50\,\text{kPa})$	0.48 m^{-1}
Upper logistic scale	$\alpha_{\max}$	330 m^{-1}
Curve parameter	β	127

Notes: α_{100}, α_{ini}, $\alpha_{\max}$ in m^{-1}; n, β, and c are dimensionless.

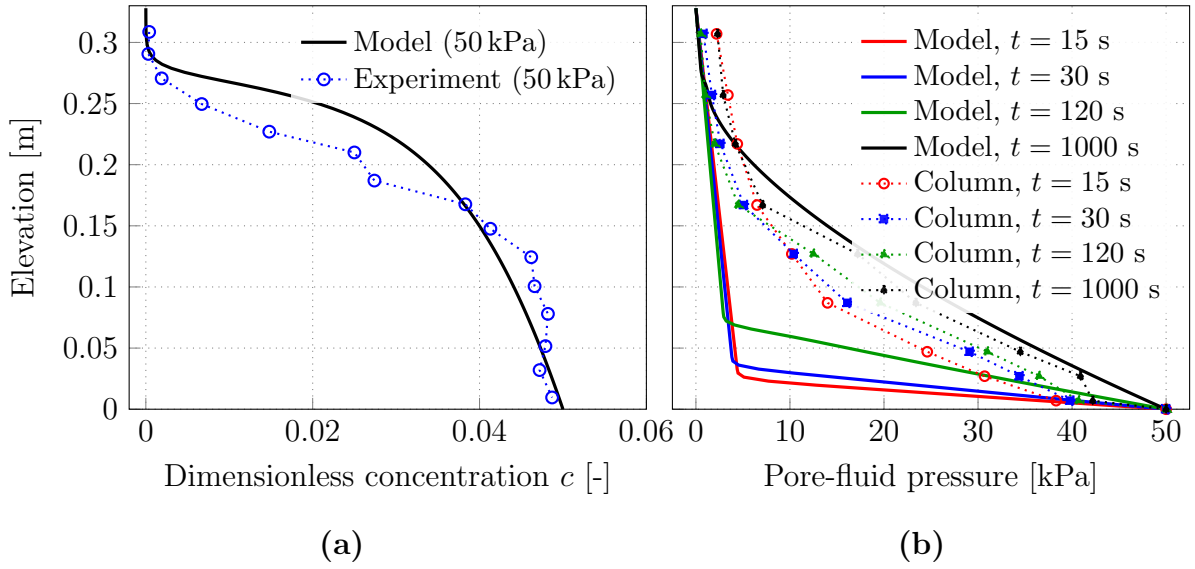

Figure 7.3: Column test on S 0.5–1.0 mm sand at the prescribed pressure difference $P_{\text{inj}} = 50$ kPa. (a) End-of-test dimensionless concentration profile c - model vs. experiment. (b) Pore-fluid pressure profiles at $t = 15, 30, 120, 1000$ s - model (solid) vs. experiment (dotted).

Table 7.3: Fixed inputs and calibrated parameters for the S 1.0–2.0 mm sand column test at $P_{\text{inj}} = 50$ kPa.

Quantity	**Symbol**	**Value**
Model length	L	0.330 m
Inlet pressure	p_0	50 kPa
Outlet pressure	p_L	0 kPa
Initial porosity	n_{f0}	0.41
Prescribed inlet value of c	$c(0,t)$	0.0533
Initial intrinsic permeability	k_0	1.065×10^{-10} m^2
Water dynamic viscosity	μ_w	1×10^{-3} Pa s
Slurry density	ρ_{slurry}	1031.8 kg m^{-3}
Prescribed baseline at 50 kPa (used)	$\alpha_{\text{ini}}(50\,\text{kPa})$	0.10 m^{-1}
Upper logistic scale	$\alpha_{\max}$	1.0 m^{-1}
Curve parameter	β	1

Notes: α_{ini} and $\alpha_{\max}$ are in m^{-1}; β and c are dimensionless.

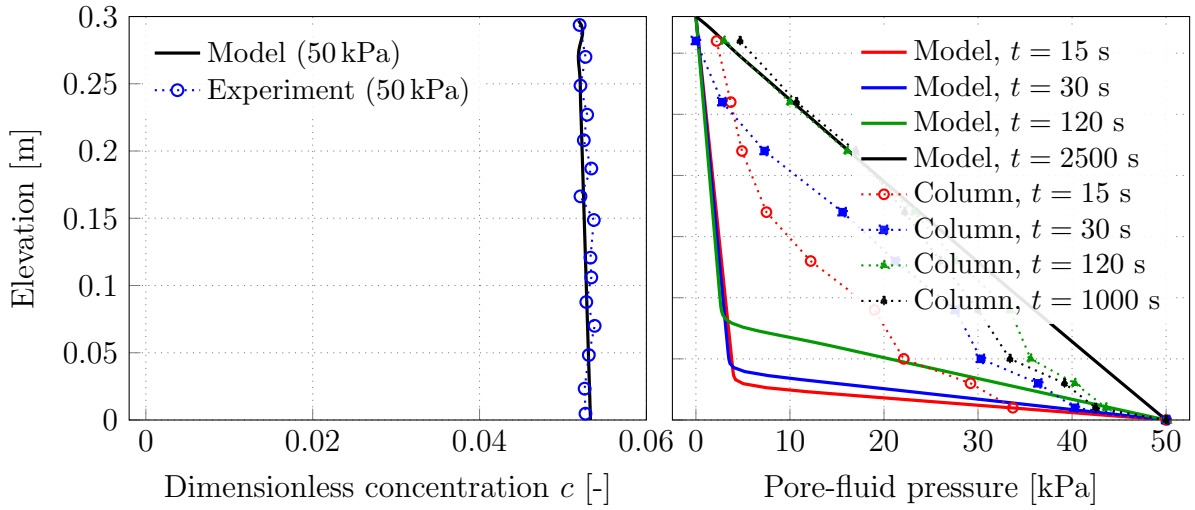

Figure 7.4: Column test on S 1.0–2.0 mm sand at the prescribed pressure difference $P_{\text{inj}} = 50$ kPa. (a) End-of-test dimensionless concentration profile c - model vs. experiment. (b) Pore-fluid pressure profiles - model at $t = 15, 30, 120, 2500$ s (solid) vs. experiment at $t = 15, 30, 120, 1000$ s (dotted).

For the S 0.5–1.0 mm calibration at $P_{\text{inj}} = 50$ kPa shown in Fig. 7.3, the model reproduces the measured end-of-test concentration and final pressure profiles reasonably well.

At $t = 15$, 30, and 120 s, however, it predicts a more localized pressure drop near the inlet and underestimates the measured pressures over most of the column. The calibration therefore captures the final state more closely than the transient pressure development, which was not included in the calibration target.

For the coarse sand S 1.0–2.0 mm, where slurry penetration occurred without internal cake formation, α_{ini} was prescribed directly as a constant (Table 7.3). This assumption may also be adopted for other sands exhibiting full penetration without internal filter-cake formation.

In Fig. 7.4(b), the equal-time model profiles at $t = 15$, 30, and 120 s underpredict the measured pore-fluid pressures over most of the column and show a more localized pressure drop near the inlet. For the final-state comparison, the simulated profile at $t = 2500$ s is shown against the experimental profile at $t = 1000$ s; these profiles agree more closely in their overall spatial distribution. The model therefore captures the developed pressure profile more closely than the transient evolution, which was not included in the calibration target.

7.9 Predictive validation under changed boundary conditions (1–D)

The parameter set identified at 50 kPa for S 0.1–0.5 mm was carried over to 30, 100 and 200 kPa without any retuning. The simulation results are compared with the experimental data in Figures 7.5–7.7. Each figure pairs the end-of-test concentration profile (Fig. 7.5(a), Fig. 7.6(a), and Fig. 7.7(a)) with the pore-fluid pressure profiles (Fig. 7.5(b), Fig. 7.6(b), and Fig. 7.7(b)) at $t = 15, 30, 120, 1000$ s.

At $P_{\mathrm{inj}} = 30$ kPa (Fig. 7.5), the simulated end-of-test concentration profile reproduces the measured front depth and the overall curvature in the lower part of the column, although the simulated transition is slightly sharper than the experimental profile in Fig. 7.5(a). In Fig. 7.5(b), the final measured pore-fluid pressure profile ($t = 1000$ s) is reproduced reasonably well. At $t = 15$ and 30 s, however, the model substantially underpredicts the measured pressures over most of the column, and the temporal evolution near the inlet is not reproduced consistently. The model therefore captures the final spatial distribution more closely than the early-time development.

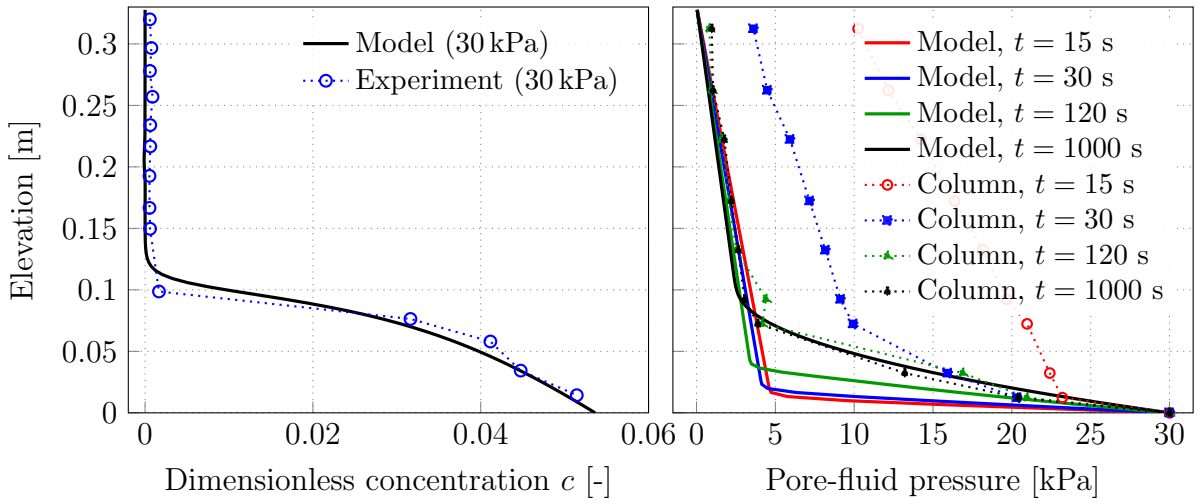

Figure 7.5: Column test on S 0.1–0.5 mm sand at the prescribed pressure difference $P_{\text{inj}} = 30$ kPa. (a) End-of-test dimensionless concentration profile c - model vs. experiment. (b) Pore-fluid pressure profiles at $t = 15, 30, 120, 1000$ s - model (solid) vs. experiment (dotted).

At $P_{\text{inj}} = 100$ kPa (Fig. 7.6), the simulated end-of-test concentration profile in Fig. 7.6(a) follows the experimental profile reasonably well in overall shape and front position, although local deviations remain. In Fig. 7.6(b), the simulated pore-fluid pressure profiles reproduce the overall decrease in pressure with elevation, but appreciable differences in magnitude and gradient persist in the lower part of the column at all four observation times.

At $P_{\text{inj}} = 200$ kPa (Fig. 7.7), the model reproduces the end-of-test concentration front in Fig. 7.7(a), but not the earlier-time pore-fluid pressure response in Fig. 7.7(b). Across the comparisons at $t = 15$, 30, and 120 s, the experimental near-inlet pressure gradient becomes steeper with time, whereas the simulated gradient weakens as the high-pressure zone extends farther up the column. The predicted temporal evolution is therefore opposite to the measured trend. Discrepancies are largest over approximately the lower 0.12 m and remain pronounced at $t = 120$ s. The final plotted curves also remain separated over most of the column.

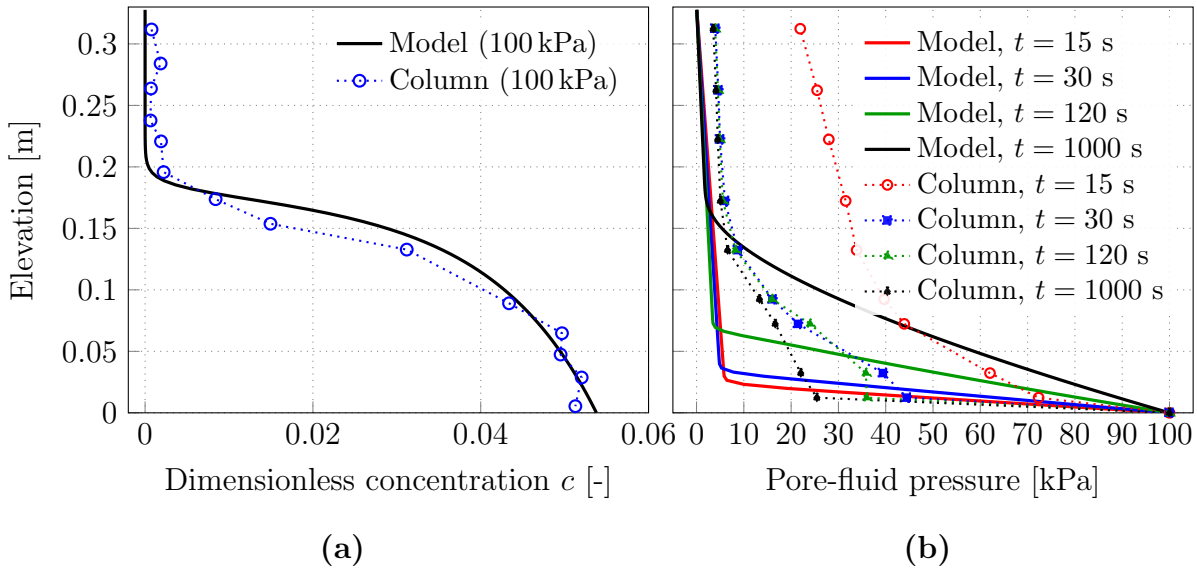

Figure 7.6: Column test on S 0.1–0.5 mm sand at the prescribed pressure difference $P_{\text{inj}} = 100$ kPa. (a) End-of-test dimensionless concentration profile c - model vs. experiment. (b) Pore-fluid pressure profiles at $t = 15, 30, 120, 1000$ s - model (solid) vs. experiment (dotted).

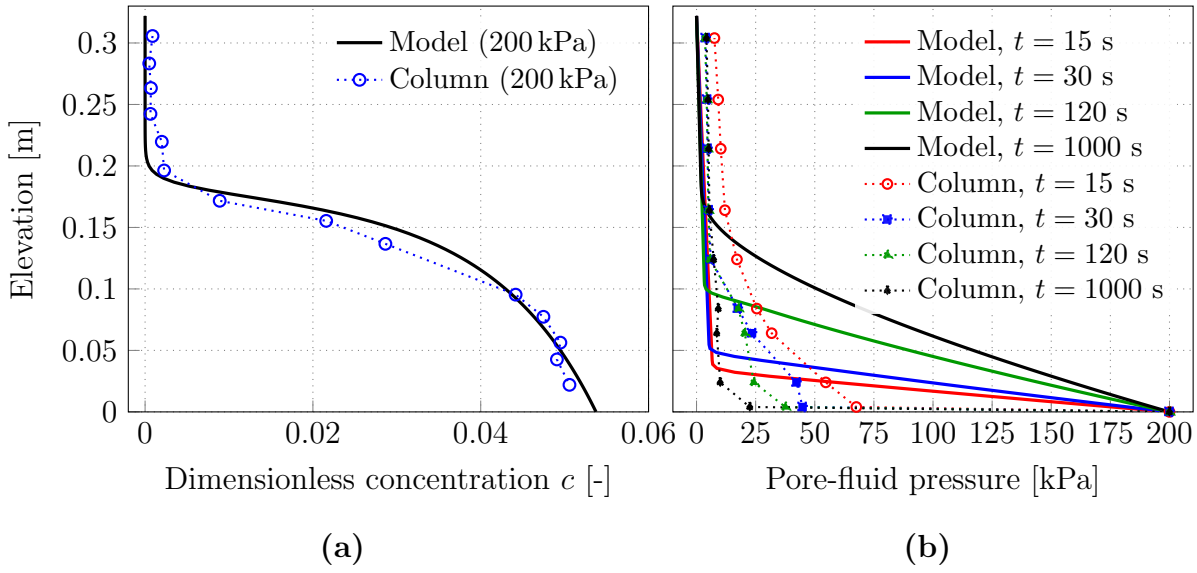

Figure 7.7: Column test on S 0.1–0.5 mm sand at the prescribed pressure difference $P_{\text{inj}} = 200$ kPa. (a) End-of-test dimensionless concentration profile c - model vs. experiment. (b) Pore-fluid pressure profiles at $t = 15, 30, 120, 1000$ s - model (solid) vs. experiment (dotted).

Overall, the 50 kPa calibration transfers more successfully for the terminal concentration profiles than for the transient pore-fluid pressure profiles: concentration shape and front position are reproduced reasonably across the 30–200 kPa range without retuning, whereas

pressure agreement depends on pressure level and time, with substantial discrepancies at 200 kPa.

Using the parameter set calibrated at 50 kPa for S 0.5–1.0 mm (Table 7.2), the model was run at 30, 100, and 200 kPa without any retuning. Figures 7.8 to 7.10 compare the predicted concentration profiles at the end of each test (Figs. 7.8(a), 7.9(a), 7.10(a)) and the transient pore-fluid pressure profiles (Figs. 7.8(b), 7.9(b), 7.10(b)) with the column data.

At 30 kPa (Fig. 7.8), the predicted concentration profile in Fig. 7.8(a) captures the measured shape over approximately 0.15–0.30 m elevation and the position of the sharp decrease in concentration. Within approximately 0–0.15 m elevation, the predicted profile gives lower concentrations than the experimental data over most of the range, but higher concentrations near its upper end. The pore-fluid pressure profiles in Fig. 7.8(b) show that the final plotted pair agrees reasonably well in overall magnitude and shape. At earlier times, however, the temporal evolution of the near-inlet gradient is opposite to the experiment: the experimental gradient generally strengthens, whereas the predicted gradient weakens as the pressure field develops. The pressures predicted for $t = 15$, 30, and 120 s are lower than the measured values over most of the column.

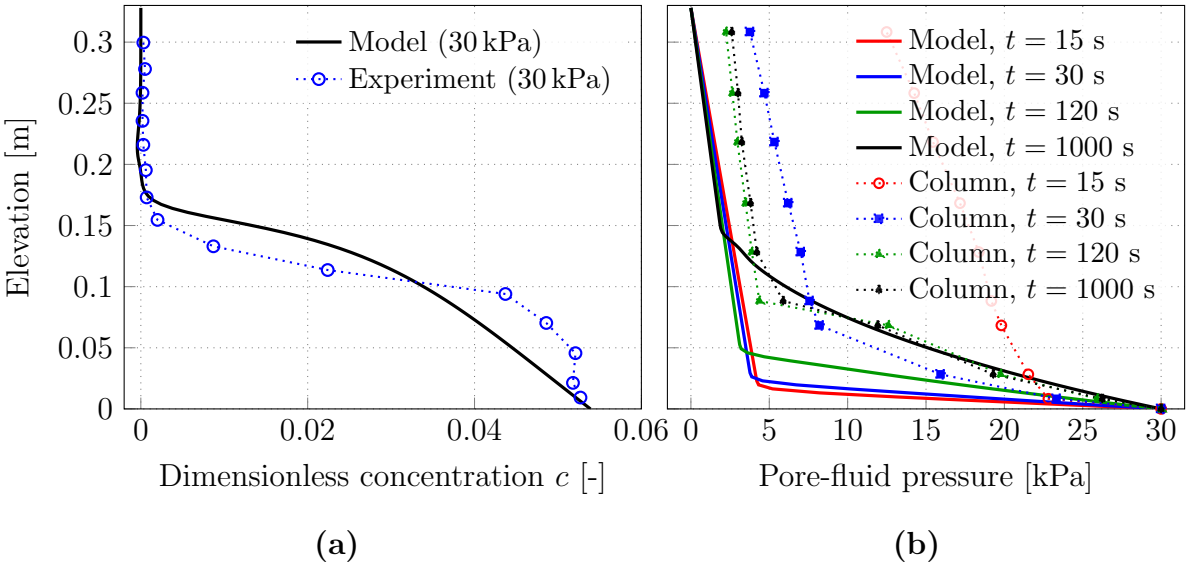

Figure 7.8: Column test on S 0.5–1.0 mm sand at the prescribed pressure difference $P_{\text{inj}} = 30$ kPa. (a) End-of-test dimensionless concentration profile c - model vs. experiment. (b) Pore-fluid pressure profiles at $t = 15, 30, 120, 1000$ s - model (solid) vs. experiment (dotted).

At 100 kPa (Fig. 7.9), the end-of-test concentration profile in Fig. 7.9(a) remains close to the measured concentration range, although the model shows a stronger decrease with

elevation. The pore-fluid pressure profiles in Fig. 7.9(b) reproduce the vertical decay, but the model underpredicts the measured pressures at $t = 15$, 30, and 120 s over most of the column. Agreement is closer for the final plotted pair.

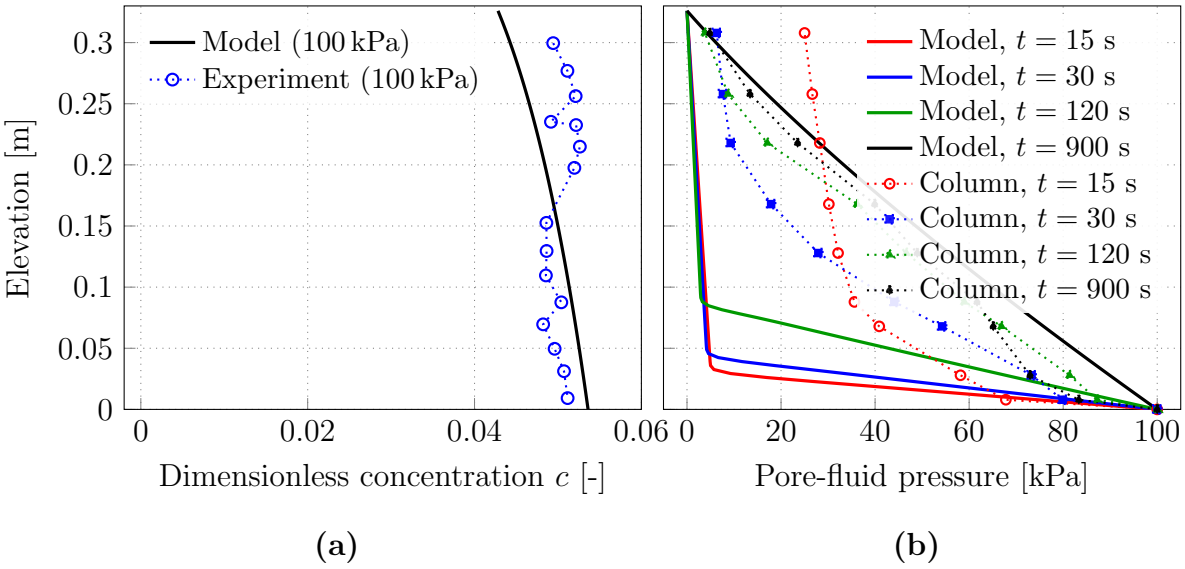

Figure 7.9: Column test on S 0.5–1.0 mm sand at the prescribed pressure difference $P_{\text{inj}} = 100$ kPa. (a) End-of-test dimensionless concentration profile c - model vs. experiment. (b) Pore-fluid pressure profiles at $t = 15, 30, 120, 900$ s - model (solid) vs. experiment (dotted).

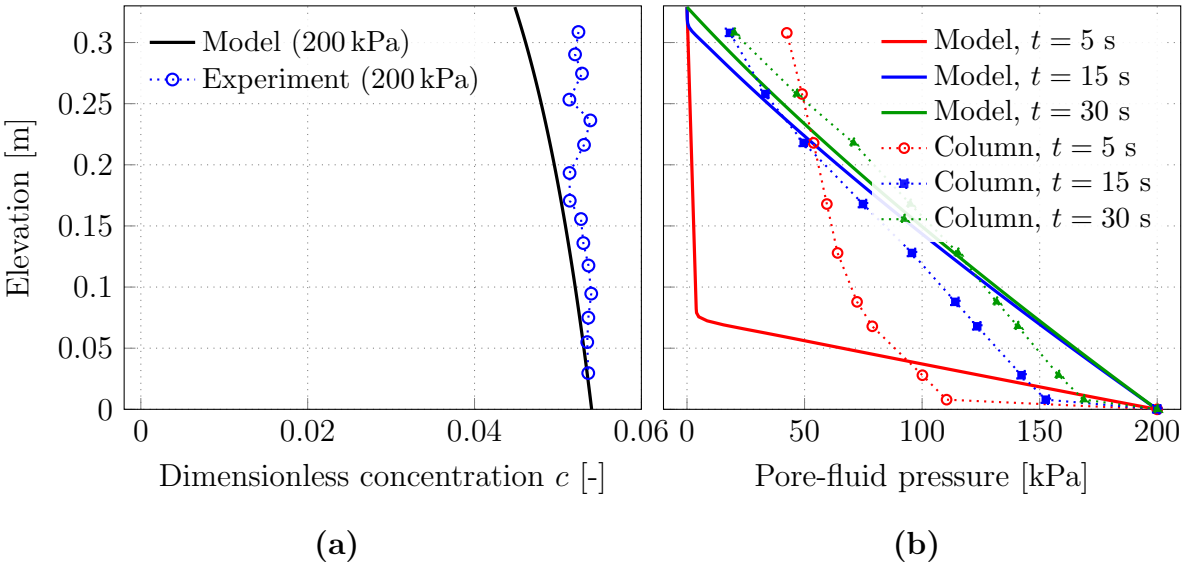

Figure 7.10: S 0.5–1.0 mm sand at 200 kPa. (a) End-of-test dimensionless concentration profile c—model vs. experiment. (b) Pore-fluid pressure profiles at $t = 5, 15, 30$ s—model (solid) vs. column (dotted).

At $P_{\mathrm{inj}} = 200\,\mathrm{kPa}$ (Fig. 7.10), both the simulated and experimental end-of-test concentration profiles extend throughout the full column height, indicating full penetration. The simulation predicts a somewhat stronger decrease in concentration with elevation but reproduces the observed penetration extent. The pore-fluid pressure data from the column experiment extend only to about 30 s, so the comparison uses $t = \{5, 15, 30\}\,\mathrm{s}$ and the simulation was limited to the same duration. The predicted pore-fluid pressure profiles in Fig. 7.10(b) show marked time-dependent differences from the measurements. At $t = 5\,\mathrm{s}$, the simulation substantially underpredicts the measured pore-fluid pressure, particularly in the upper part of the column. Agreement is closer at $t = 15$ and 30 s, although deviations remain over much of the column height.

Overall, the 50 kPa calibration was also evaluated across the investigated pressure range of 30–200 kPa for S 0.5–1.0 mm without additional parameter tuning. The main discrepancies occur during the first tens of seconds, including underprediction of the 15 and 30 s pore-fluid pressure profiles at 30 kPa and substantial underprediction of the 5 s profile at 200 kPa. The end-of-test concentration profiles and later-time pore-fluid pressure distributions generally agree more closely than the early-time pressure response, but the agreement is not uniform across all validation conditions.

7.10 Parametric study

A one-dimensional parametric study was carried out on S 0.5–1.0 mm to examine model behaviour below and above the ranges used in the validation subsection. The slurry injection pressure ΔP and the prescribed inlet value of c were varied, while the governing equations, constitutive relations, and numerical settings (Darcy flow with gravity; advection-only transport with streamline and crosswind stabilization) remained unchanged. Here $\Delta P \equiv P_{\mathrm{inj}}$ denotes the same prescribed pressure difference defined in Section 7.4. Initial intrinsic permeability k_0 and initial porosity n_{f0} were kept at their calibrated values. The relations $\rho_f(c)$, $\mu_f(c)$, and $\lambda(c)$ retained their calibrated forms and coefficients. The dimensionless values of c were prescribed directly at $x = 0$. For each imposed ΔP, α_{ini} was assigned once from Eq. (7.17); within that run, $\lambda(c)$ varied only through the evolving concentration. Across the imposed inlet values of c and ΔP, the simulations produced different concentration-front positions and pressure-gradient patterns for S 0.5–1.0 mm. Separate lower and higher ranges of both ΔP and the prescribed inlet value of c were considered, as summarized in Table 7.4.

Table 7.4: Parameter ranges used in the 1-D parametric study on S 0.5–1.0 mm. Pressure variations were performed at the calibrated prescribed inlet value of c, while concentration variations were carried out at $\Delta P = 50$ kPa.

Quantity	Levels tested
Slurry injection pressure ΔP	10, 15, 20, 25 kPa; 100, 150, 250, 300, 400, 500 kPa
Prescribed inlet value of c	0.002, 0.005, 0.010, 0.020; 0.100, 0.150, 0.200, 0.300
Held fixed (calibrated)	k_0, n_{f0}, geometry; forms and coefficients of $\rho_f(c)$, $\mu_f(c)$, $\lambda(c)$

Here $\Delta P = p_{\text{in}} - p_{\text{out}}$ is the total prescribed inlet–outlet pressure difference. The pressure boundary is therefore

$$p_{\text{in}} = p_{\text{out}} + \Delta P. \tag{7.23}$$

Gravity is included separately through the body-force term in Darcy's law. With $L = 0.328$ m, $\rho_w = 1000\ \text{kg m}^{-3}$, and $g = 9.81\ \text{m s}^{-2}$, the initial threshold for a positive upward driving force is

$$\Delta P_{\min} = \rho_w\, g\, L = 1000 \cdot 9.81 \cdot 0.328\ \text{Pa} \approx 3.22\ \text{kPa}. \tag{7.24}$$

As ΔP approaches $\Delta P_{\min}$ from above, the net upward driving head and the upward Darcy flux approach zero, and the coupled problem becomes numerically ill-conditioned. All runs with $\Delta P \geq 8$ kPa converged, whereas runs at lower pressure differences did not converge. At the beginning of infiltration, the pore fluid in the column is water, so Eq. (7.24) applies with ρ_w. As infiltration progresses, the local concentration-dependent slurry density $\rho_f(c)$ becomes relevant through the gravitational body-force term. For a spatially uniform fluid of density ρ_f, the corresponding threshold is $\Delta P_{\min} = \rho_f g L$. No analogous convergence limitation was observed over the tested concentration range.

7.10.1 Effect of the prescribed inlet value of c at $\Delta P = 50$ kPa

At fixed $\Delta P = 50$ kPa, the simulations showed different response patterns in the low- and high-concentration ranges; the two ranges are therefore discussed separately.

For low prescribed inlet values ($c < 0.030$; Fig. 7.11), the pore-fluid pressure profiles in Fig. 7.11(b) are approximately linear over most of the column for $c = 0.002$, 0.005, and 0.010 at the inlet, whereas the $c = 0.020$ case exhibits a pronounced pressure gradient near the column entrance. The end-of-test c profiles in Fig. 7.11(a) remain confined

to approximately the first 0.05 m above the inlet; the plotted cases therefore do not demonstrate full penetration. Instead, they indicate localized deposition and inner or near-face filter-cake formation over this concentration range.

For high prescribed inlet values ($c \geq 0.100$; Fig. 7.12), a large pressure drop is concentrated within the lower half of the column, at elevations up to approximately 0.15 m (Fig. 7.12(b)). The end-of-test c profiles in Fig. 7.12(a) form a sharp front that moves downward toward the inlet as the prescribed inlet value of c increases from 0.100 to 0.300. The response is consistent with higher slurry viscosity and faster deposition at larger prescribed inlet values of c, which reduce permeability near the column entrance and localize the flow. This pattern—shallow, sharp front with concentrated pressure loss near the column entrance—is indicative of inner or near-face filter-cake formation. Curves in this range were lightly smoothed at the front to remove numerical kinks; the front locations and overall trends were unaffected. Because $c = 0.100$–0.300 lies above the experimentally investigated normalized range of 0.0178–0.0712, these simulations illustrate extrapolated model behaviour rather than validated physical predictions.

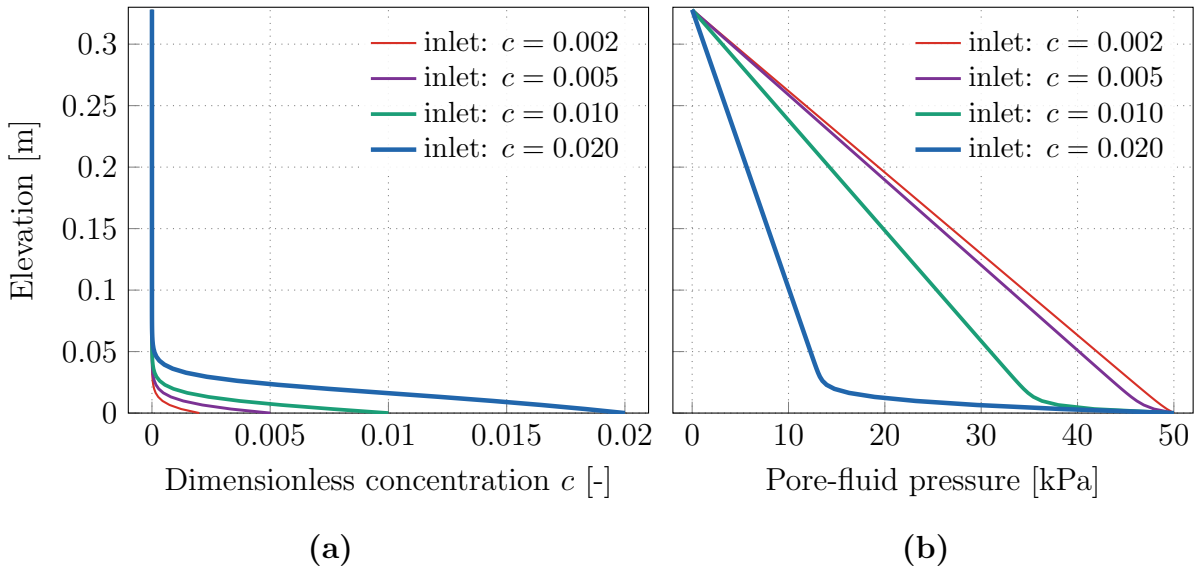

Figure 7.11: Effect of a low prescribed inlet value of c ($c < 0.030$) for S 0.5–1.0 mm sand in the 1-D model at $\Delta P = 50$ kPa. (a) Dimensionless concentration c vs. elevation. (b) Pore-fluid pressure vs. elevation. Colors run red (thin, low inlet c) → blue (thick, high inlet c).

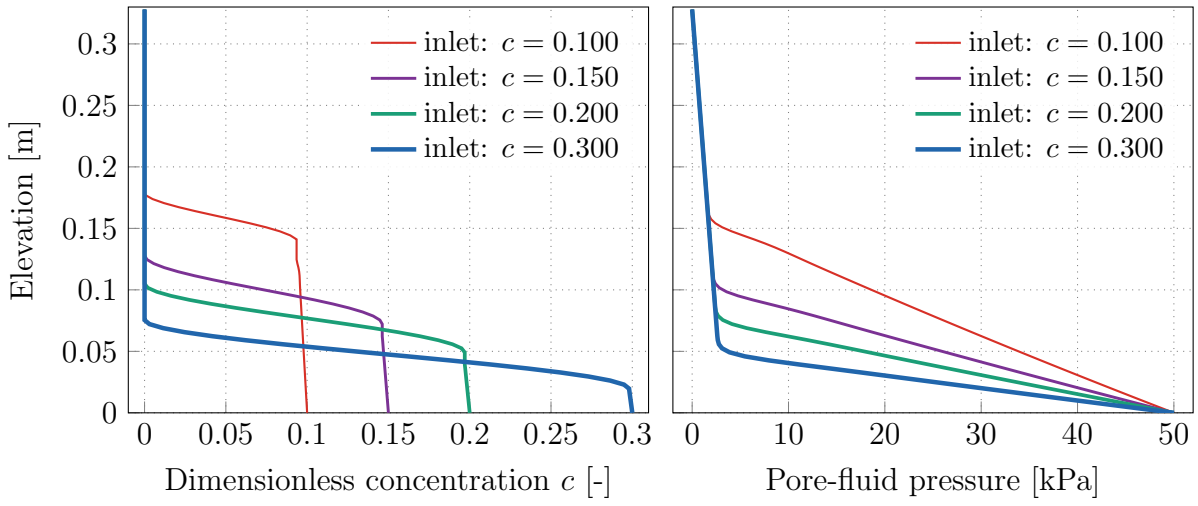

Figure 7.12: Effect of a high prescribed inlet value of c ($c \geq 0.100$) for S 0.5–1.0 mm sand in the 1-D model at $\Delta P = 50$ kPa. (a) Dimensionless concentration c vs. elevation. (b) Pore-fluid pressure vs. elevation. Colors run red (thinnest, low inlet c) $\rightarrow$ blue (thickest, high inlet c).

In summary, none of the concentration-sweep simulations at $\Delta P = 50$ kPa demonstrates full penetration over the complete column height. Within the high-concentration range, increasing the prescribed inlet value of c shifts the concentration front downward toward the inlet and localizes the pressure loss. The concentration profiles of the low-concentration simulations likewise remain localized within approximately 0.05 m of the inlet and therefore do not establish a full-penetration regime.

7.10.2 Effect of slurry injection pressure at inlet $c = 0.0500$

At fixed inlet $c = 0.0500$, a clear trend with ΔP was observed: higher ΔP led to deeper penetration and a smaller share of the pressure loss concentrated near the column entrance. The sensitivity was strong at low ΔP and became weak once ΔP was large.

For low injection pressures ($10 - 25$ kPa; Fig. 7.13), the pore-fluid pressure profiles in Fig. 7.13(a) show that the pressure drop is concentrated within the lower few centimetres at $\Delta P = 10$ kPa and becomes progressively more distributed as ΔP increases to 25 kPa. The end-of-test concentration profiles in Fig. 7.13(b) indicate that the concentration front moves distinctly upward, away from the inlet, over this range. The shallow front and the

localized pressure loss at the lowest ΔP are indicative of an inner or near-face filter-cake tendency, whereas the deeper fronts at 20–25 kPa are consistent with partial penetration.

For high injection pressures (100−500 kPa; Fig. 7.14), the pressure profiles in Fig. 7.14(a) increase with ΔP over the whole depth, while the end-of-test concentration profiles in Fig. 7.14(b) respond only weakly. The profile at 100 kPa is slightly shallower, whereas the curves for 150–500 kPa nearly coincide, with almost identical front positions and curvature. This limited sensitivity of the concentration response at high ΔP is consistent with the column tests, where the measured concentration profiles at 100 and 200 kPa were very similar (see Figs. 7.6 and 7.7). The behaviour suggests that deposition-induced permeability reduction limits further front advance at sufficiently large driving pressure, so increasing ΔP further changes the end-of-test concentration profile only slightly.

In summary, increasing ΔP at inlet $c = 0.0500$ produces a deeper concentration front and a more distributed pressure loss along the column. Low ΔP is associated with shallow fronts and near-face filter-cake behaviour, whereas higher ΔP shifts the response toward partial penetration. Beyond approximately 150 kPa the concentration profiles change only marginally and may overlap.

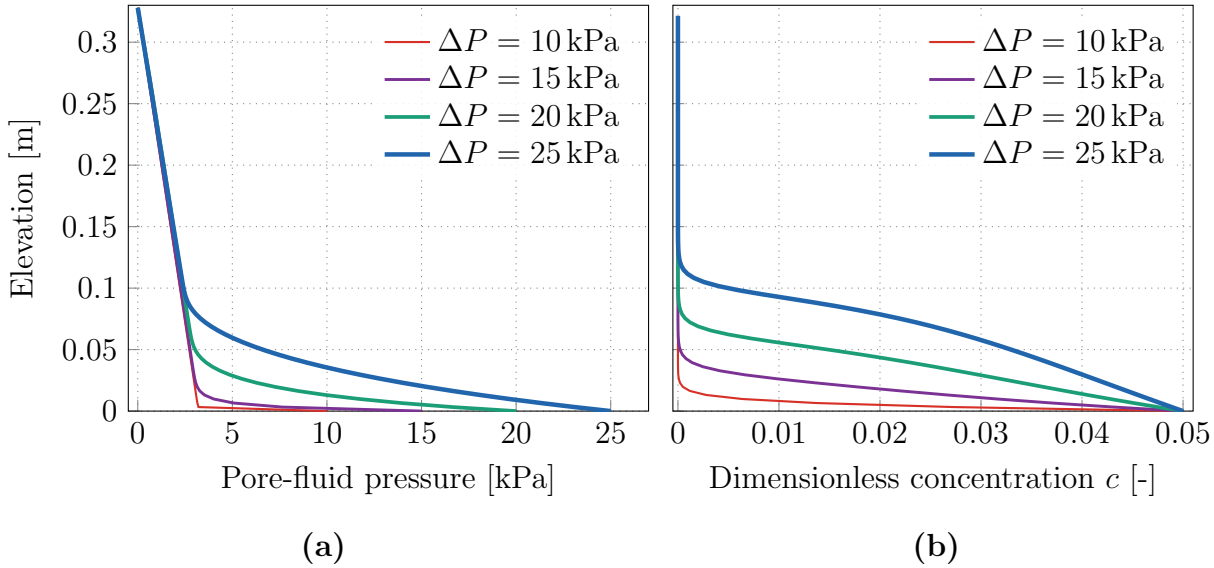

(a) **(b)**

Figure 7.13: Effect of slurry injection pressure ($\Delta P < 30$ kPa) for S 0.5–1.0 mm sand in the 1-D model. (a) Pore-fluid pressure vs. elevation. (b) Dimensionless concentration c vs. elevation. Colors run red (thin, lower ΔP) → blue (thick, higher ΔP).

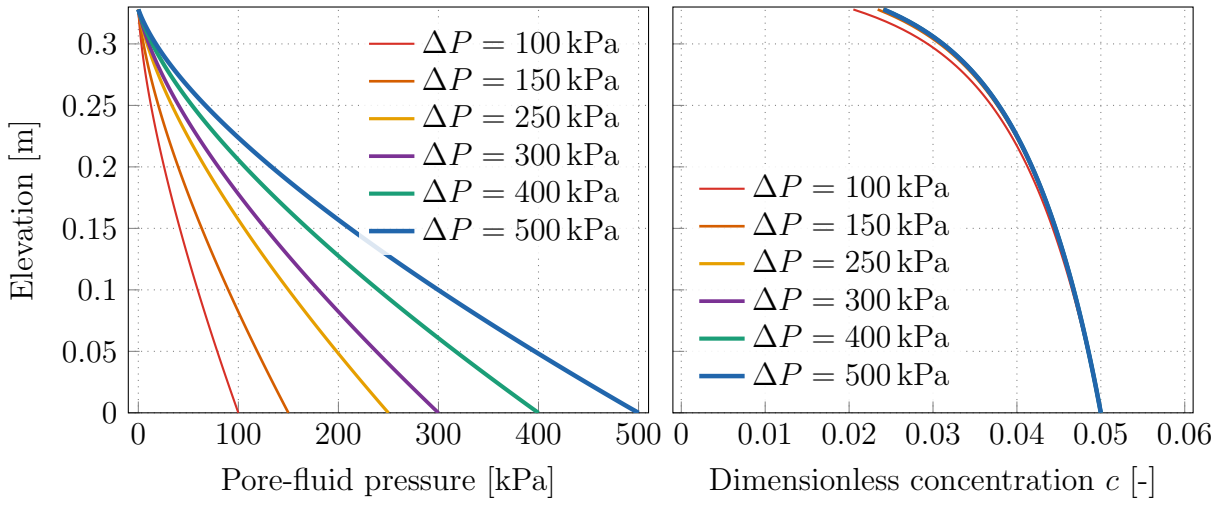

(a) **(b)**

Figure 7.14: Effect of slurry injection pressure ($\Delta P \geq 100$ kPa) for S 0.5–1.0 mm sand in the 1-D model. (a) Pore-fluid pressure vs. elevation. (b) Dimensionless concentration c vs. elevation. Red/thin denotes lower and blue/thick higher ΔP.

7.11 Three-dimensional extension

The three-dimensional COMSOL model used the baseline Schaufler formulation with constant λ_0 and activated gravity. Gravity affected the Darcy flux through the body-force term, while λ_0 retained its original unit of m^{-1}. No new constitutive relation or calibration was introduced. The $100 \times 100 \times 100$ m cube contained a 20 m-diameter, 10 m-deep cylindrical tunnel cavity extending inward from the centre of its left face, with vertical gravity and a prescribed pressure boundary on the tunnel surface. The proof-of-concept represented no experimentally investigated sand gradation. It retained $n_{f0} = 0.32$, $k_0 = 8.57 \times 10^{-10}$ m^2, and $T = 10^5$ s from the baseline one-dimensional Schaufler verification (Section 7.7); the prescribed inlet value was $c_v = 0.06$, while $\rho_w = 997$ kg m^{-3}, $\mu_w = 1.0 \times 10^{-3}$ Pa s, and $P_0 = 6.83 \times 10^4$ Pa were prescribed separately.

The three-dimensional domain was discretized in COMSOL using a physics-controlled "Finer" free-tetrahedral mesh comprising 101,543 elements. Quadratic interpolation for pressure and linear interpolation for concentration were retained.

Two values of the constant deposition coefficient in the Schaufler formulation were examined using the baseline notation λ_0:

$$\lambda_0 = 10^{-4}\ \mathrm{m}^{-1} \quad \text{(weak attachment)}, \qquad \lambda_0 = 10^{-1}\ \mathrm{m}^{-1} \quad \text{(strong attachment)}.$$

Mid-plane volumetric-concentration c_v slices are shown in Fig. 7.15. For $\lambda_0 = 10^{-4}\ \mathrm{m}^{-1}$ the bentonite slurry plume spans most of the domain and the front extends well away from the tunnel opening, consistent with full (or near-full) penetration. For $\lambda_0 = 10^{-1}\ \mathrm{m}^{-1}$ the concentration is confined to a shallow region adjacent to the tunnel with a sharp transition—behaviour indicative of inner or near-face filter-cake formation. These three-dimensional patterns mirror the one-dimensional trends: weaker attachment favours penetration, whereas stronger attachment localizes the front near the tunnel face.

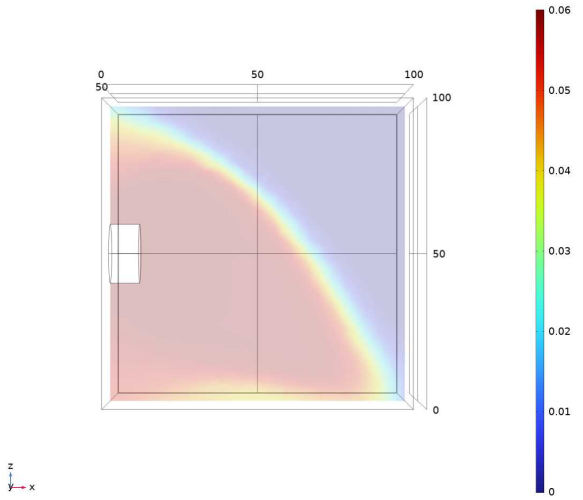

(a) $\lambda_0 = 10^{-4}\,\mathrm{m}^{-1}$: full penetration regime.

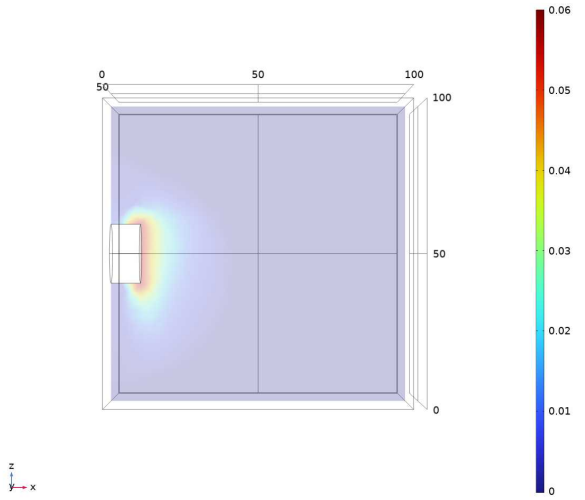

(b) $\lambda_0 = 10^{-1}\,\mathrm{m}^{-1}$: inner or near-face filter-cake formation regime.

Figure 7.15: Three-dimensional extension with gravity: mid-plane volumetric-concentration c_v slices for two values of the constant deposition coefficient λ_0 in the baseline Schaufler formulation. The baseline Schaufler formulation and its material parameters were retained with gravity activated; the calibrated parameter sets from the preceding one-dimensional column simulations were not used, and no three-dimensional calibration was performed.

The three-dimensional exercise was intended only to demonstrate feasibility and qualitative regimes; systematic three-dimensional calibration and validation, as well as alternative boundary conditions, are left to future work.

7.12 Limitations

The modelling framework adopted in this study is based on a continuum mixture. Within this formulation, grain motion, deformation of the soil skeleton, and consolidation effects of the granular matrix were not considered. The model therefore represents slurry infiltration through a rigid porous medium and does not capture potential coupling between slurry infiltration and mechanical deformation of the soil structure.

Transport was treated as advection-dominated. Diffusion and mechanical dispersion were not included, and the resulting infiltration front is therefore governed by the discretization and stabilization settings applied in the numerical solution. Streamline and crosswind stabilization were used to control numerical oscillations, but the apparent thickness and shape of the infiltration front may depend on the chosen discretization and stabilization parameters.

In the calibrated one-dimensional simulations, the constitutive relations for slurry density $\rho_f(c)$, viscosity $\mu_f(c)$, and the deposition coefficient $\lambda(c)$ depend on concentration. Here, c is the dimensionless normalized concentration defined at the beginning of the chapter; the calibrated constitutive relations and effective deposition/porosity-loss parameters are specific to this convention. For each simulation, the run-specific constant α_{ini} in $\lambda(c)$ was assigned from the prescribed injection pressure before time integration. These relations represent empirical descriptions derived from the available experimental data. The three-dimensional demonstration instead retained the constant baseline coefficient λ_0 and was not recalibrated. Potential influences of shear rate, non-Newtonian rheological behaviour of the slurry, and temperature-dependent effects were not included. Likewise, the permeability–porosity relation $k(n_f)$ was prescribed and assumed isotropic and homogeneous, so that local heterogeneity or anisotropy of the granular structure was not represented explicitly.

Filter-cake formation was represented implicitly through deposition-induced porosity reduction in the pore space. A distinct surface or inner filter-cake layer with its own hydraulic resistance was not introduced as a separate model component. Consequently, the model captures the hydraulic effect of deposition through progressive permeability reduction rather than through an explicit representation of a discrete filter-cake interface.

The parametric analysis was performed using a one-dimensional vertical column geometry, which is appropriate for controlled laboratory conditions but cannot capture lateral flow redistribution or channelization effects that may occur in more complex geometries. The total inlet–outlet pressure difference ΔP was prescribed at the boundaries according to

Eq. (7.23), while gravity acted separately through Darcy's law. Consequently, simulations with ΔP approaching the hydrostatic contribution $\rho_f g L$ may suffer from numerical ill-conditioning because the effective upward driving head becomes small.

Finally, calibration was performed using three sand gradations (S 0.1–0.5 mm, S 0.5–1.0 mm, and S 1.0–2.0 mm), while the extended parametric study was carried out for the intermediate sand S 0.5–1.0 mm. Although the results show qualitatively plausible model responses across wider ranges of dimensionless concentration c and injection pressure, a systematic calibration and sensitivity analysis was not carried out. In particular, the $c = 0.100$–0.300 sweep extends above the experimentally investigated normalized range of 0.0178–0.0712 and should be interpreted as an exploration of model behaviour.

7.13 Summary and outlook

A continuum mixture model for bentonite slurry infiltration into saturated sands was implemented and verified against a published one-dimensional benchmark. The one-dimensional formulation was extended by incorporating calibrated relations for slurry density and viscosity together with a concentration-dependent deposition coefficient $\lambda(c)$, whose run-specific α_{ini} was assigned from the prescribed injection pressure, and gravity. For each studied sand gradation (S 0.1–0.5 mm, S 0.5–1.0 mm, and S 1.0–2.0 mm), a single calibration at 50 kPa was used to predict infiltration behaviour at other pressures without re-calibration. Across the validation pressures of 30–200 kPa, the model reproduced the overall shape and penetration extent of the end-of-test concentration profiles reasonably well. The final or later-time pore-fluid pressure profiles were captured only partly, with closer agreement at 30 and 100 kPa than at 200 kPa. The main discrepancies concerned the early-time pore-fluid pressure response: pressures were underpredicted at 30 kPa, while at 200 kPa the fine-sand transient trend was not reproduced and the 5 s medium-sand profile was substantially underpredicted. The results indicate that particle attachment and permeability reduction, together with the concentration-dependent slurry density and viscosity, govern both the spatial dimensionless concentration c and pressure profiles and the time scale of infiltration.

A focused one-dimensional parametric study examined the influence of the prescribed inlet value of c and slurry injection pressure ΔP. At $\Delta P = 50$ kPa, the concentration-sweep simulations did not demonstrate full penetration. Within the high-concentration range, increasing the prescribed inlet value of c shifted the front toward the inlet and localized the pressure loss, whereas the low-concentration range did not show a monotonic transition

toward full penetration. Increasing ΔP promoted deeper penetration, while the c profiles changed only marginally once ΔP became sufficiently large.

A three-dimensional proof-of-concept simulation of a tunnel, using the constant baseline coefficient λ_0, demonstrated that the Schaufler formulation can reproduce the two qualitative regimes observed in the one-dimensional analyses, namely full (or near-full) penetration and inner or near-face filter-cake formation, in a realistic geometry with gravity.

The three-dimensional proof-of-concept demonstrates feasibility in a simplified tunnel geometry, but it was not calibrated or validated for project-representative tunnelling conditions. Further work should extend the calibrated formulation to realistic tunnel-face geometries, boundary conditions, and soil–slurry parameters, resolving the evolution of slurry concentration c, porosity n_f, and permeability $k(n_f)$ around the excavation boundary.

Such studies should investigate how variations in the prescribed inlet value of c and slurry injection pressure ΔP influence filter-cake formation at the tunnel face and its resulting hydraulic sealing capacity.

8 Conclusions and recommendations

This thesis investigated the infiltration of bentonite slurry into saturated granular soils and its implications for pressure transfer and filter-cake formation in slurry shield tunnelling. Laboratory experiments, microstructural observations, mechanical testing, and numerical modelling were combined to analyse slurry penetration, deposition processes, and their influence on the hydraulic and mechanical behaviour. The main findings of the study are summarised below.

8.1 Main findings

The principal findings obtained from the experimental investigations and modelling analyses presented in the preceding chapters are summarised below.

Slurry infiltration behaviour

Laboratory infiltration experiments demonstrated that slurry penetration into granular soils depends strongly on grain size and slurry concentration. In addition to pore-water pressure measurements, depth-resolved bentonite concentration profiles were obtained along the column height, allowing the spatial distribution of slurry infiltration to be quantified directly. The measured concentration profiles showed that coarse sands permit deep slurry penetration, resulting in nearly uniform bentonite concentrations and almost linear pore-water pressure distributions along the column. In contrast, finer sands exhibited rapid particle deposition and the development of internal filter-cake zones. In these cases, the concentration profiles displayed sharp decreases in bentonite content with depth, which coincided with distinct changes in the pore-water pressure gradient. This correspondence between penetration depth and pore-water pressure response provides a direct indication of the location where slurry deposition reduces permeability and pressure transfer becomes localized. These observations demonstrate that slurry infiltration may transition from deep penetration to deposition-controlled behaviour depending on soil grading and slurry properties. At $\Delta P = 50$ kPa, the B20, B40, and B60 slurries

penetrated throughout the S 1.0–2.0 mm column, whereas B80 formed an internal filter cake at approximately 8–15 cm from the inlet, indicating that a sufficiently high bentonite concentration promotes earlier filtration and shallower penetration. At a fixed nominal B60 grade, increasing ΔP generally delayed filtration and extended penetration: S 0.5–1.0 mm transitioned from internal filtration at 30–50 kPa to full penetration at 100–200 kPa, while S 0.1–0.5 mm retained internal filtration at all tested pressures but with a front that generally moved farther from the inlet.

Microstructural observations

Cryo-BIB-SEM imaging provided direct observations of the bentonite–sand microstructure in samples taken from different locations within the infiltration columns. The analysed samples revealed the presence of bentonite particles within the pore space of the sand matrix and their accumulation in specific zones of the specimen. In several samples, bentonite platelets were observed to occupy pore throats and locally reduce the available flow paths within the granular structure.

These observations indicate that slurry infiltration is accompanied by progressive particle deposition within the pore space. The resulting reduction in effective pore size can be related to the permeability decrease inferred from the infiltration experiments, although the permeability change was not quantified directly. Together with the measured concentration profiles and pore-water pressure responses, the microstructural evidence supports the interpretation that filter-cake development originates from progressive particle deposition within the granular matrix.

Hydro-mechanical behaviour of infiltration-conditioned sands

Monotonic and cyclic triaxial tests showed that bentonite infiltration modifies the mechanical response of sands, particularly under cyclic loading. The tested conditions comprised column-extracted clean sand, column-extracted slurry-infiltrated sand, and remoulded sand–slurry mixtures prepared by wet tamping. The critical-state friction angle remained essentially unchanged across these conditions, indicating that the fundamental shear strength of the sand skeleton is not significantly altered by the presence of bentonite.

In the paired B60 comparisons at the same initial mean effective stress p'_0 and cyclic stress ratio CSR, slurry infiltration was associated with a systematic decrease in cyclic resistance and faster axial-strain accumulation compared to clean column specimens. The more rapid migration of the effective-stress paths towards lower p' is consistent with faster development of positive excess pore-water pressure in the slurry-infiltrated specimens.

The experiments also showed that the mechanical behaviour depends not only on the presence of bentonite but also on the method by which it is introduced into the soil. Specimens conditioned by slurry infiltration exhibited different responses compared to specimens prepared by direct slurry mixing. In particular, at both tested CSR levels, the remoulded sand–slurry mixtures prepared by wet tamping showed lower cyclic resistance than the slurry-infiltrated column specimens. This difference reflects the spatial distribution of bentonite within the soil structure. In infiltration-conditioned samples, bentonite particles primarily occupy the pore space, whereas in slurry-mixed specimens bentonite can also be present at grain–grain contact points. The presence of bentonite at these contacts modifies the contact conditions between sand grains and thereby affects the deformation behaviour of the soil.

Continuum modelling of slurry infiltration

A continuum mixture model describing slurry transport and bentonite particle deposition in granular soils was implemented and verified against a published one-dimensional benchmark. The formulation was extended by incorporating calibrated relations for concentration-dependent slurry density and viscosity together with a concentration-dependent deposition coefficient $\lambda(c)$ and gravity. For the fine and medium sands, the run-specific coefficient α_{ini} was assigned before time integration from the prescribed injection pressure; for the coarse sand, α_{ini} was prescribed directly for the sole available 50 kPa test. Calibration against a single column-infiltration test for each sand type allowed the model to reproduce the measured infiltration behaviour of that test. For the fine and medium sands, the resulting parameter sets predicted penetration reasonably well under other injection pressures without additional adjustment.

Parametric simulations showed that the prescribed inlet value of c and slurry injection pressure ΔP exert distinct influences on infiltration behaviour. Within the high-concentration range, increasing the prescribed inlet value of c shifted the front towards the inlet and localized the pressure loss, whereas the low-concentration range did not show a monotonic transition towards full penetration. Increasing ΔP initially promoted deeper penetration, while further increases led to only minor changes in the concentration profiles once ΔP became sufficiently large.

A three-dimensional proof-of-concept simulation of a tunnel excavation demonstrated that the formulation can reproduce both full penetration and inner or near-face filter-cake formation regimes in a simplified geometry with gravity.

8.2 Scientific contributions

The work presented in this thesis contributes to the understanding of bentonite slurry infiltration into granular soils and its implications for pressure transfer and filter-cake formation in slurry shield tunnelling. The principal scientific contributions of the study are summarized below.

First, the thesis introduces an experimental methodology that enables depth-resolved measurement of bentonite concentration within infiltration columns. Combined with pore-water pressure monitoring, these measurements provide new insight into the relationship between slurry penetration depth, bentonite deposition, and the resulting pressure transfer behaviour.

Second, the study provides microstructural observations of bentonite-conditioned sands using Cryo-BIB-SEM imaging. By analysing samples taken from different locations within the infiltration columns, the investigation reveals how bentonite particles accumulate within the pore space and progressively modify the pore structure. These observations offer insight into the mechanisms governing permeability reduction during slurry infiltration.

Third, the thesis establishes a methodology for preparing and testing near-intact sand specimens conditioned by slurry infiltration while preserving the deposited bentonite within their pore space. This approach enables the mechanical behaviour of soils affected by slurry infiltration to be investigated without replacing the infiltration process with artificial sand–slurry mixing. The results show that the monotonic shear behaviour of the sand remains largely unchanged, whereas the cyclic response is modified by the presence and spatial distribution of bentonite within the pore space. This finding is particularly relevant for slurry shield tunnelling, where cyclic loading occurs due to cutterhead rotation.

Fourth, a continuum modelling framework for bentonite slurry infiltration in granular soils was developed and verified. The model incorporates experimentally determined relations for concentration-dependent slurry density and viscosity, together with gradation-specific deposition parameters calibrated against the measured end-of-test concentration profile from one column test at $\Delta P = 50$ kPa for each investigated sand gradation. For the fine and medium sands, the calibrated parameter sets were subsequently applied without further adjustment at other injection pressures and reproduced the main penetration trends reasonably well. The influence of the prescribed inlet value of c was examined separately through a parametric study.

8.3 Future research

The results of this thesis suggest several directions for further investigation. One important aspect concerns the influence of fines-loaded slurries and controlled injection-pressure sequences, including step changes, ramps, and oscillations, on slurry infiltration and pressure transfer. Future experiments combining synchronized pore-water pressure measurements with depth-resolved concentration profiles could help to further clarify the mechanisms governing slurry loss, particle deposition, and filter-cake formation under these conditions.

Another direction involves strengthening the link between microstructure and hydraulic behaviour. Three-dimensional characterization of the pore structure, for example using tomographic imaging techniques, could provide quantitative information on pore-throat geometry and its evolution during slurry infiltration.

From a modelling perspective, future work should build on the simplified tunnel proof-of-concept presented in Chapter 7, which already demonstrates the formulation in three dimensions. The calibrated formulation should then be extended and validated for project-representative tunnel-face geometries, boundary conditions, and soil–slurry parameters. This would allow the spatial evolution of slurry concentration, porosity, and permeability around the excavation boundary to be analysed and the hydraulic sealing capacity of the filter cake to be evaluated under realistic conditions.

Bibliography

G. Anagnostou and K. Kovári. The face stability of slurry-shield-driven tunnels. *Tunnelling and Underground Space Technology*, 9(2):165–174, 1994. doi: 10.1016/0886-7798(94)90028-0.

H. A. Barnes. Thixotropy—a review. *Journal of Non-Newtonian Fluid Mechanics*, 70: 1–33, 1997. doi: 10.1016/S0377-0257(97)00004-9.

J. Bear. *Dynamics of Fluids in Porous Media*. American Elsevier, New York, 1972.

K. Been and M. G. Jefferies. A state parameter for sands. *Géotechnique*, 35(2):99–112, 1985. doi: 10.1680/geot.1985.35.2.99.

H. Ben Rhaiem, C. H. Pons, and D. Tessier. Factors affecting the microstructure of smectites: role of cation and history of applied stresses. In L. G. Schultz, H. van Olphen, and F. A. Mumpton, editors, *Proceedings of the International Clay Conference, Denver, 1985*, pages 292–297, Bloomington, Indiana, 1987. The Clay Minerals Society. doi: 10.1346/CMS-ICC-1.41.

A. Bezuijen. Influence of pore pressure at tunnel face. In *BAW Workshop: Tunnelling in Soft Ground*, Karlsruhe, 2004.

A. Bezuijen and A. M. Talmon. Processes around a TBM: pore pressures, plastering and grout. In C. W. W. Ng, H. W. Huang, and G. B. Liu, editors, *Geotechnical Aspects of Underground Construction in Soft Ground (IS–Shanghai 2008)*, pages 1–11, Shanghai, China, 2008. Tongji University/ISSMGE.

A. Bezuijen, A. M. Talmon, J. F. W. Joustra, and B. Grote. Pressure gradients and muck properties at the face of an epb. In *Geotechnical Aspects of Underground Construction in Soft Ground (IS–Amsterdam 2005)*, Amsterdam, 2005. ISSMGE.

A. Bezuijen, J. P. Pruiksma, and H. H. van Meerten. Pore pressures in front of a tunnel: measurements, calculations and consequences for face stability. In A. Bezuijen and

H. van Lottum, editors, *Tunnelling: A Decade of Progress*, pages 27–33. Taylor & Francis, London, 2006.

Bosche GmbH & Co. KG. *S40S S-shaped Load Cell*. Damme, Germany, 2020. Technical documentation for S40S load cells.

P. C. Carman. Fluid flow through granular beds. *Transactions of the Institution of Chemical Engineers*, 15:150–166, 1937.

P. C. Carman. *Flow of Gases Through Porous Media*. Butterworths, London, 1956.

J. A. H. Carraro, M. Prezzi, and R. Salgado. Shear strength and stiffness of sands containing plastic or nonplastic fines. *Journal of Geotechnical and Geoenvironmental Engineering*, 135(9):1167–1178, 2009. doi: 10.1061/(ASCE)1090-0241(2009)135:9(1167).

F. Chen, H. Xiong, Z. Y. Yin, and X. Chen. Impermeable and mechanical stability of filter cake under different infiltration conditions via CFD–DEM. *Acta Geotechnica*, 18 (8):4115–4140, 2023. doi: 10.1007/s11440-023-01805-8.

DAUB. Recommendations for face support pressure calculations for shield tunnelling in soft ground. Technical report, German Tunnelling Committee (DAUB), Germany, 2016.

A. Deirieh, I. Y. Chang, M. L. Whittaker, S. Weigand, D. Keane, J. Rix, J. T. Germaine, D. Joester, and P. B. Flemings. Particle arrangements in clay slurries: The case against the honeycomb structure. *Applied Clay Science*, 152:166–172, 2018. doi: 10.1016/j.clay.2017.11.010.

G. Desbois, J. L. Urai, F. Pérez-Willard, Z. Radi, S. Offern, I. Burkart, P. A. Kukla, and U. Wollenberg. Argon broad ion beam tomography in a cryogenic scanning electron microscope: a novel tool for the investigation of representative microstructures in sedimentary rocks containing pore fluid. *Journal of Microscopy*, 249(3):215–235, 2013. doi: 10.1111/jmi.12011.

DIN Deutsches Institut für Normung e. V. Erd- und Grundbau – Prüfverfahren für Stützflüssigkeiten im Schlitzwandbau und für deren Ausgangsstoffe. DIN 4127:2014-02, Feb. 2014. 28 pages; German standard.

A. Einstein. Eine neue Bestimmung der Moleküldimensionen. *Annalen der Physik*, 324 (2):289–306, 1906. doi: 10.1002/andp.19063240204.

A. Einstein. Berichtigung zu meiner Arbeit: „Eine neue Bestimmung der Moleküldimensionen“. *Annalen der Physik*, 339(3):591–592, 1911. doi: 10.1002/andp.19113390313.

C. S. El Mohtar, J. Clarke, A. Bobet, M. Santagata, V. Drnevich, and C. Johnston. Cyclic response of a sand with thixotropic pore fluid. In *Geotechnical Earthquake Engineering and Soil Dynamics IV*. American Society of Civil Engineers, 2012. doi: 10.1061/40975(318)63.

R. J. Fannin. Karl Terzaghi: From theory to practice in geotechnical filter design. *Journal of Geotechnical and Geoenvironmental Engineering*, 134(3):267–276, 2008. doi: 10.1061/(ASCE)1090-0241(2008)134:3(267).

Federation of Piling Specialists. *Bentonite Support Fluids in Civil Engineering*. Federation of Piling Specialists, Bromley, UK, 2nd edition, Jan. 2006.

Graphtec Corporation. *Midi Logger GL820: User Manual*. Yokohama, Japan, 2020. User manual for Graphtec GL820 data logger.

R. E. Grim. *Clay Mineralogy*. McGraw-Hill, New York, 2nd edition, 1968. ISBN 0070248362.

S. M. Hassanizadeh and W. G. Gray. General conservation equations for multi-phase systems: 1. Averaging procedure. *Advances in Water Resources*, 2(3):131–144, 1979a. doi: 10.1016/0309-1708(79)90025-3.

S. M. Hassanizadeh and W. G. Gray. General conservation equations for multi-phase systems: 2. Mass, momenta, energy, and entropy equations. *Advances in Water Resources*, 2(4):191–203, 1979b. doi: 10.1016/0309-1708(79)90035-6.

S. M. Hassanizadeh and W. G. Gray. General conservation equations for multi-phase systems: 3. Constitutive theory for porous media flow. *Advances in Water Resources*, 3(1):25–40, 1980. doi: 10.1016/0309-1708(80)90016-0.

S. M. Hassanizadeh and W. G. Gray. Mechanics and thermodynamics of multiphase flow in porous media including interphase boundaries. *Advances in Water Resources*, 13(4): 169–186, 1990. doi: 10.1016/0309-1708(90)90040-B.

S. Hemes, G. Desbois, J. L. Urai, B. Schröppel, and J.-O. Schwarz. Multi-scale characterization of porosity in Boom Clay (HADES-level, Mol, Belgium) using a combination of X-ray µ-CT, 2D BIB-SEM and FIB-SEM tomography. *Microporous and Mesoporous Materials*, 208:1–20, 2015. doi: 10.1016/j.micromeso.2015.01.022.

J. P. Herzig, D. M. Leclerc, and P. Le Goff. Flow of suspensions through porous media—application to deep filtration. *Industrial & Engineering Chemistry*, 62(5):8–35, 1970. doi: 10.1021/ie50725a003.

L. Holzer and M. Cantoni. Review of FIB–SEM cross-sectioning artefacts in porous solids. *Microscopy Today*, 20(4):34–39, 2012. doi: 10.1017/S1551929512000994.

T. Huisman. On the determination of the penetration length of bentonite slurry into sand for face support calculations. Technical report, Delft University of Technology, Delft, The Netherlands, 1998.

M. Jiang, C. Rößler, E. Wellmann, J. Klaver, F. Kleiner, and J. Schmatz. Workflow for high-resolution phase segmentation of cement clinker from combined BSE image and EDX spectral data. *Journal of Microscopy*, 286(2):85–91, 2022. doi: 10.1111/jmi.13072.

Keller AG. *Piezoresistive Pressure Sensor Series 21Y: Operating Instructions*. Winterthur, Switzerland, 2020. Technical documentation for Keller 21Y piezoresistive pressure sensors.

A. Kirsch. Experimental investigation of the face stability of shallow tunnels in sand. *Acta Geotechnica*, 5(1):43–62, 2010. doi: 10.1007/s11440-010-0110-7.

J. Kozeny. Über kapillare Leitung des Wassers im Boden. (Aufstieg, Versickerung und Anwendung auf die Bewässerung). *Sitzungsberichte der Akademie der Wissenschaften in Wien, Mathematisch-Naturwissenschaftliche Klasse, Abteilung IIa*, 136(2a):271–306, 1927.

T. Krause. *Schildvortrieb mit flüssigkeits- und erdgestützter Ortsbrust*. Dissertation, Technische Universität Braunschweig, Braunschweig, Germany, 1987. Mitteilungen des Instituts für Grundbau und Bodenmechanik, Heft 24.

S. Kube, B. Schößer, and M. Thewes. Penetration behaviour of slurry in saturated soil – analysis of particle deposition on the basis of electrical resistance. In *WTC 2023: Expanding Underground. Abstract Book*, Athens, 2023. World Tunnel Congress; abstract/proceedings.

A. A. Lavasan, C. Zhao, T. Barciaga, A. Schaufler, H. Steeb, and T. Schanz. Numerical investigation of tunneling in saturated soil: the role of construction and operation periods. *Acta Geotechnica*, 13:671–691, 2018. doi: 10.1007/s11440-017-0595-4.

Y. Lin, Y. Fang, C. He, and W. Wang. Experimental study on degree of match between slurry and ground based on particle retention rate. *Tunnelling and Underground Space Technology*, 116:104105, 2021. doi: 10.1016/j.tust.2021.104105.

Z. Lu, W.-H. Zhou, Z.-Y. Yin, and J. Yang. Numerical modeling of viscous slurry infiltration in sand. *Computers and Geotechnics*, 146:104745, 2022. doi: 10.1016/j.compgeo.2022.104745.

P. F. Luckham and S. Rossi. The colloidal and rheological properties of bentonite suspensions. *Advances in Colloid and Interface Science*, 82(1–3):43–92, 1999. doi: 10.1016/S0001-8686(99)00005-6.

B. Maidl, M. Herrenknecht, U. Maidl, and G. Wehrmeyer. *Mechanised Shield Tunnelling*. Ernst & Sohn, Berlin, 2nd edition, 2012. ISBN 978-3-433-02995-4. doi: 10.1002/9783433601051. Translated by D. S. Sturge.

J. Mewis and N. J. Wagner. *Colloidal Suspension Rheology*. Cambridge University Press, Cambridge, 2012. doi: 10.1017/CBO9780511977978.

F. Min, W. Zhu, and X. Han. Filter cake formation for slurry shield tunneling in highly permeable sand. *Tunnelling and Underground Space Technology*, 38:423–430, 2013. doi: 10.1016/j.tust.2013.07.024.

S. Miura and S. Toki. A sample preparation method and its effect on static and cyclic deformation-strength properties of sand. *Soils and Foundations*, 22(1):61–77, 1982. doi: 10.3208/sandf1972.22.61.

H. Müller-Kirchenbauer. Stability of slurry trenches. In *Proceedings of the 5th European Conference on Soil Mechanics and Foundation Engineering*, pages 543–553, Madrid, Spain, 1972. Sociedad Española de Mecánica del Suelo y Cimentaciones.

J. Olivier, J. Vaxelaire, and E. Vorobiev. Modelling of cake filtration: An overview. *Separation Science and Technology*, 42(8):1667–1700, 2007. doi: 10.1080/01496390701242186.

T. Omar and A. Sadrekarimi. Effects of multiple corrections on triaxial compression testing of sands. *Journal of GeoEngineering*, 9(2):75–83, 2014. doi: 10.6310/jog.2014.9(2).3.

D.-H. Park, I.-M. Lee, B.-Y. Choi, Y.-G. Kang, and S.-M. Chang. Quantitative analysis and classification of rotational harmonics of TBM drive system. *Geomechanics and Engineering*, 25(4):375–386, 2021. doi: 10.12989/gae.2021.25.4.375.

C. P. Polito and J. R. Martin. Effects of nonplastic fines on the liquefaction resistance of sands. *Journal of Geotechnical and Geoenvironmental Engineering*, 127(5):408–415, 2001. doi: 10.1061/(ASCE)1090-0241(2001)127:5(408).

S. Praetorius and B. Schößer. *Bentonite Handbook: Lubrication for Pipe Jacking*. John Wiley & Sons, Hoboken, 2017.

S. Qin, Y. Cheng, and W.-H. Zhou. State-of-the-art review on pressure infiltration behavior of bentonite slurry into saturated sand for TBM tunneling. *Smart Construction and Sustainable Cities*, 1:14, 2023. doi: 10.1007/s44268-023-00018-y.

B. F. Ruth. Studies in filtration. III. Derivation of general filtration equations. *Industrial & Engineering Chemistry*, 27(6):708–723, 1935. doi: 10.1021/ie50306a024.

T. Schanz and P. A. Vermeer. Angles of friction and dilatancy of sand. *Géotechnique*, 46 (1):145–151, 1996. doi: 10.1680/geot.1996.46.1.145.

A. Schaufler, C. Becker, and H. Steeb. Infiltration processes in cohesionless soils. *ZAMM – Journal of Applied Mathematics and Mechanics / Zeitschrift für Angewandte Mathematik und Mechanik*, 93(2-3):138–146, 2013. doi: 10.1002/zamm.201200047.

J. Schmatz, J. Klaver, M. Jiang, and J. L. Urai. Nanoscale morphology of brine/oil/mineral contacts in connected pores of carbonate reservoirs: Insights on wettability from Cryo-BIB-SEM. *SPE Journal*, 22(5):1374–1384, 2017. doi: 10.2118/180049-PA.

A. N. Schofield and C. P. Wroth. *Critical State Soil Mechanics*. McGraw-Hill, London, 1968.

B. Schößer, M. Thewes, and S. Kube. Face support, soil conditioning and material transport in earth pressure balance and hydro shield machines. In G. Meschke and M. Thewes, editors, *Interaction Modeling in Mechanized Tunneling*. Springer, Cham, 2023. doi: 10.1007/978-3-031-24066-9_4.

M. M. Sharma and Y. C. Yortsos. Transport of particulate suspensions in porous media: Model formulation. *AIChE Journal*, 33(10):1636–1643, 1987. doi: 10.1002/aic.690331007.

C. J. A. Sinn, J. Klaver, R. Fink, M. Jiang, J. Schmatz, R. Littke, and J. L. Urai. Using BIB-SEM imaging for permeability prediction in heterogeneous shales. *Geofluids*, 2017: 4709064, 2017. doi: 10.1155/2017/4709064.

A. M. Talmon, D. R. Mastbergen, and M. Huisman. Invasion of pressurized clay suspensions into granular soil. *Journal of Porous Media*, 16(4):351–365, 2013. doi: 10.1615/JPorMedia.v16.i4.70.

F. Tatsuoka, K. Ochi, S. Fujii, and M. Okamoto. Cyclic undrained triaxial and torsional shear strength of sands for different sample preparation methods. *Soils and Foundations*, 26(3):23–41, 1986a. doi: 10.3208/sandf1972.26.3_23.

F. Tatsuoka, S. Toki, S. Miura, H. Kato, M. Okamoto, S. Yamada, S. Yasuda, and F. Tanizawa. Some factors affecting cyclic undrained triaxial strength of sand. *Soils and Foundations*, 26(3):99–116, 1986b. doi: 10.3208/sandf1972.26.3_99.

M. Thewes, B. Schößer, and Z. Žižka. Transient face support in slurry shield tunnelling due to different time scales for excavation and penetration. In *Proc. World Tunnel Congress*, San Francisco, 2016.

C. Tien and R. Bai. An assessment of the conventional cake filtration theory. *Chemical Engineering Science*, 58(7):1323–1336, 2003. doi: 10.1016/S0009-2509(02)00655-3.

C. Tien and A. C. Payatakes. Advances in deep bed filtration. *AIChE Journal*, 25(5): 737–759, 1979. doi: 10.1002/aic.690250502.

F. M. Tiller and H. R. Cooper. The role of porosity in filtration: IV. Constant pressure filtration. *AIChE Journal*, 6(4):595–601, 1960. doi: 10.1002/aic.690060418.

Y. P. Vaid and S. Sivathayalan. Fundamental factors affecting liquefaction susceptibility of sands. *Canadian Geotechnical Journal*, 37(3):592–606, 2000. doi: 10.1139/t00-040.

H. van Olphen. Internal mutual flocculation in clay suspensions. *Journal of Colloid Science*, 19(4):313–322, 1964. doi: 10.1016/0095-8522(64)90033-9.

H. van Olphen. *An Introduction to Clay Colloid Chemistry*. John Wiley & Sons, New York, 2nd edition, 1977. ISBN 978-0-471-01463-8.

D. Wanatowski and J. Chu. Effect of specimen preparation method on the stress-strain behavior of sand in plane-strain compression tests. *Geotechnical Testing Journal*, 31 (4):308–320, 2008. doi: 10.1520/GTJ101307.

Z. Wang, Y. Wang, D. Feng, J. Zhang, and S. Liu. Effects of slurry viscosity and particle additive size on filter cake formation in highly permeable sand. *Underground Space*, 7 (2):151–161, 2022. doi: 10.1016/j.undsp.2021.06.002.

S. Whitaker. *The Method of Volume Averaging*. Kluwer Academic Publishers, Dordrecht, 1999.

T. Wichtmann. *Explicit accumulation model for non-cohesive soils under cyclic loading*. PhD thesis, Ruhr-University Bochum, Bochum, 2005. Publications of the Institute of Soil Mechanics and Foundation Engineering, Issue No. 38.

T. Wichtmann, A. Niemunis, and T. Triantafyllidis. Strain accumulation in sand due to cyclic loading: Drained triaxial tests. *Soil Dynamics and Earthquake Engineering*, 25 (12):967–979, 2005. doi: 10.1016/j.soildyn.2005.06.005.

T. Wichtmann, K. Steller, and T. Triantafyllidis. On the influence of the sample preparation method on strain accumulation in sand under high-cyclic loading. *Soil Dynamics and Earthquake Engineering*, 131:106028, 2020. ISSN 0267-7261. doi: 10.1016/j.soildyn.2019.106028.

T. Xu and A. Bezuijen. Analytical methods in predicting excess pore water pressure in front of slurry shield in saturated sandy ground. *Tunnelling and Underground Space Technology*, 73:203–211, 2018. doi: 10.1016/j.tust.2017.12.011.

T. Xu and A. Bezuijen. Bentonite slurry infiltration into sand: filter cake formation under various conditions. *Géotechnique*, 69(12):1095–1106, 2019. doi: 10.1680/jgeot.18.P.094.

T. Yin, Z. Zhang, X. Huang, T. Shire, and K. J. Hanley. On the morphology and pressure-filtration characteristics of filter cake formation: Insight from coupled CFD–DEM simulations. *Tunnelling and Underground Space Technology*, 111:103856, 2021. doi: 10.1016/j.tust.2021.103856.

X. S. Yin, R. P. Chen, Y. C. Li, and S. Qi. A column system for modeling bentonite slurry infiltration in sands. *Journal of Zhejiang University – Science A*, 17(10):818–827, 2016. doi: 10.1631/jzus.A1500290.

M. Yoshimine, K. Ishihara, and W. Vargas. Effects of principal stress direction and intermediate principal stress on undrained cyclic behaviour of sand. *Soils and Foundations*, 38(3):179–188, 1998. doi: 10.3208/sandf.38.3_179.

Z. Zhang and T. Yin. A coupled CFD–DEM simulation of slurry infiltration and filter cake formation during slurry shield tunneling. *Infrastructures*, 3(2):15, 2018. doi: 10.3390/infrastructures3020015.

Z. Zhang, T. Yin, X. Huang, and D. Dias. Slurry filtration process and filter cake formation during shield tunnelling: Insight from coupled CFD–DEM simulations of slurry filtration column test. *Tunnelling and Underground Space Technology*, 87:64–77, 2019. doi: 10.1016/j.tust.2019.02.001.

C. Zhao, Z. Žižka, B. Schößer, M. Thewes, and A. A. Lavasan. Support pressure transfer at a slurry supported tunnel face due to time dependent decrease of soil permeability. In M. Elshafie, G. Viggiani, and R. Mair, editors, *Geotechnical Aspects of Underground Construction in Soft Ground*, London, 2023. ISSMGE. doi: 10.1201/9781003355595-59.

S. Zhou, X. Zhang, D. Wu, and H. Di. Mathematical modeling of slurry infiltration and particle dispersion in saturated sand. *Transport in Porous Media*, 124(1):91–116, 2018. doi: 10.1007/s11242-018-1054-x.

Z. Žižka. *Stability of slurry supported tunnel face considering the transient support mechanism during excavation in non-cohesive soil.* PhD thesis, Ruhr-Universität Bochum, Bochum, 2019. Published by Shaker Verlag, Düren, in Schriftenreihe des Instituts für Konstruktiven Ingenieurbau, Heft 2019,3; ISBN 978-3-8440-6940-2; DOI 10.13154/294-6514.

Z. Žižka, M. Thewes, and I. Popović. Analysis of slurry pressure transfer on the tunnel face during excavation. In *Proc. ITA-AITES World Tunnel Congress 2015*, Dubrovnik, Croatia, 2015.

Z. Žižka, B. Schößer, M. Thewes, and T. Schanz. Slurry shield tunneling: New methodology for simplified prediction of increased pore pressures resulting from slurry infiltration at the tunnel face under cyclic excavation processes. *International Journal of Civil Engineering*, 17(1):113–130, 2019. doi: 10.1007/s40999-018-0303-2.

Schriftenreihe des Instituts für Grundbau, Wasserwesen und Verkehrswesen der Ruhr-Universität Bochum

Herausgeber: H.L. Jessberger

1 (1979) **Hans Ludwig Jessberger**
Grundbau und Bodenmechanik an der Ruhr-Universität Bochum

2 (1978) **Joachim Klein**
Nichtlineares Kriechen von künstlich gefrorenem Emschermergel

3 (1979) **Heinz-Joachim Gödecke**
Die Dynamische Intensivverdichtung wenig wasserdurchlässiger Böden

4 (1979) **Poul V. Lade**
Three Dimensional Stress-Strain Behaviour and Modeling of Soils

5 (1979) **Roland Pusch**
Creep of soils

6 (1979) **Norbert Diekmann**
Zeitabhängiges, nichtlineares Spannungs-Verformungsverhalten von gefrorenem Schluff unter triaxialer Belastung

7 (1979) **Rudolf Dörr**
Zeitabhängiges Setzungsverhalten von Gründungen in Schnee, Firn und Eis der Antarktis am Beispiel der deutschen Georg-von-Neumayer- und Filchner-Station

8 (1984) **Ulrich Güttler**
Beurteilung des Steifigkeits- und Nachverdichtungsverhaltens von ungebundenen Mineralstoffen

9 (1986) **Peter Jordan**
Einfluss der Belastungsfrequenz und der partiellen Entwässerungsmöglichkeiten auf die Verflüssigung von Feinsand

10 (1986) **Eugen Makowski**
Modellierung der künstlichen Bodenvereisung im grundwasserdurchströmten Untergrund mit der Methode der finiten Elemente

11 (1986) **Reinhard A. Beine**
Verdichtungswirkung der Fallmasse auf Lastausbreitung in nichtbindigem Boden bei der Dynamischen Intensivverdichtung

12 (1986) **Wolfgang Ebel**
Einfluss des Spannungspfades auf das Spannungs-Verformungsverhalten von gefrorenem Schluff im Hinblick auf die Berechnung von Gefrierschächten

13 (1987) **Uwe Stoffers**
Berechnungen und Zentrifugen-Modellversuche zur Verformungsabhängigkeit der Ausbaubeanspruchung von Tunnelausbauten in Lockergestein

14 (1988) **Gerhard Thiel**
Steifigkeit und Dämpfung von wassergesättigtem Feinsand unter Erdbebenbelastung

15 (1991) **Mahmud Thaher**
Tragverhalten von Pfahl-Platten-Gründungen im bindigen Baugrund,
Berechnungsmodelle und Zentrifugen-Modellversuche

Schriftenreihe des Instituts für Grundbau der Ruhr-Universität Bochum

Herausgeber: H.L. Jessberger

16 (1992) **Rainer Scherbeck**
Geotechnisches Verhalten mineralischer Deponieabdichtungsschichten
bei ungleichförmiger Verformungswirkung

17 (1992) **Martin M. Bizialiele**
Torsional Cyclic Loading Response of a Single Pile in Sand

18 (1993) **Michael Kotthaus**
Zum Tragverhalten von horizontal belasteten Pfahlreihen aus langen Pfählen in Sand

19 (1993) **Ulrich Mann**
Stofftransport durch mineralische Deponieabdichtungen:
Versuchsmethodik und Berechnungsverfahren

20 (1992) **Festschrift anlässlich des 60. Geburtstages von**
Prof. Dr.-Ing. H. L. Jessberger
20 Jahre Grundbau und Bodenmechanik an der Ruhr-Universität Bochum

21 (1993) **Stephan Demmert**
Analyse des Emissionsverhaltens einer Kombinationsabdichtung im Rahmen der
Risikobetrachtung von Abfalldeponien

22 (1994) **Diethard König**
Beanspruchung von Tunnel- und Schachtausbauten in kohäsionslosem Lockergestein
unter Berücksichtigung der Verformung im Boden

23 (1995) **Thomas Neteler**
Bewertungsmodell für die nutzungsbezogene Auswahl von Verfahren zur Altlastensanierung

24 (1995) **Ralph Kockel**
Scherfestigkeit von Mischabfall im Hinblick auf die Standsicherheit von Deponien

25 (1996) **Jan Laue**
Zur Setzung von Flachfundamenten auf Sand unter wiederholten Lastereignissen

26 (1996) **Gunnar Heibrock**
Zur Rissbildung durch Austrocknung in mineralischen Abdichtungsschichten
an der Basis von Deponien

27 (1996) **Thomas Siemer**
Zentrifugen-Modellversuche zur dynamischen Wechselwirkung zwischen Bauwerken
und Baugrund infolge stoßartiger Belastung

28 (1996) **Viswanadham V. S. Bhamidipati**
Geosynthetic Reinforced Mineral Sealing Layers of Landfills

29 (1997) **Frank Trappmann**
Abschätzung von technischem Risiko und Energiebedarf bei Sanierungsmaßnahmen für Altlasten

30 (1997) **André Schürmann**
Zum Erddruck auf unverankerte flexible Verbauwände

31 (1997) **Jessberger, H. L. (Herausgeber)**
Environment Geotechnics, Report of ISSMGE Technical Committee TC 5 on Environmental Geotechnics

Schriftenreihe des Instituts für Grundbau und Bodenmechanik der Ruhr-Universität Bochum

Herausgeber: Th. Triantafyllidis

32 (2000) **Triantafyllidis, Th. (Herausgeber)**
Boden unter fast zyklischer Belastung: Erfahrung und Forschungsergebnisse (Workshop)

33 (2002) **Christof Gehle**
Bruch- und Scherverhalten von Gesteinstrennflächen mit dazwischenliegenden Materialbrücken

34 (2003) **Andrzej Niemunis**
Extended hypoplastic models for soils

35 (2004) **Christiane Hof**
Über das Verpressankertragverhalten unter kalklösendem Kohlensäureangriff

36 (2004) **René Schäfer**
Einfluss der Herstellungsmethode auf das Verformungsverhalten von Schlitzwänden in weichen bindigen Böden

37 (2005) **Henning Wolf**
Zur Scherfugenbänderung granularer Materialien unter Extensionsbeanspruchung

38 (2005) **Torsten Wichtmann**
Explicit accumulation model for non-cohesive soils under cyclic loading

39 (2008) **Christoph M. Loreck**
Die Entwicklung des Frischbetondruckes bei der Herstellung von Schlitzwänden

40 (2008) **Igor Arsic**
Über die Bettung von Rohrleitungen in Flüssigböden

41 (2009) **Anna Arwanitaki**
Über das Kontaktverhalten zwischen einer Zweiphasenschlitzwand und nichtbindigen Böden

Schriftenreihe des Lehrstuhls für Grundbau, Boden- und Felsmechanik der Ruhr-Universität Bochum

Herausgeber: T. Schanz

42 (2009) **Yvonne Lins**
Hydro-Mechanical Properties of Partially Saturated Sand

43 (2010) **Tom Schanz (Herausgeber)**
Geotechnische Herausforderungen beim Umbau des Emscher-Systems
Beiträge zum RuhrGeo Tag 2010

44 (2010) **Jamal Alabdullah**
Testing Unsaturated Soil for Plane Strain Conditions: A New Double-Wall Biaxial Device

45 (2011) **Lars Röchter**
Systeme paralleler Scherbänder unter Extension im ebenen Verformungszustand

46 (2011) **Yasir Al-Badran**
Volumetric Yielding Behavior of Unsaturated Fine-Grained Soils

47 (2011) **Usque ad finem**
Selected research papers

48 (2012) **Muhammad Ibrar Khan**
Hydraulic Conductivity of Moderate and Highly Dense Expansive Clays

49 (2014) **Long Nguyen-Tuan**
Coupled Thermo-Hydro-Mechanical Analysis: Experimental and Back Analysis

50 (2014) **Tom Schanz (Herausgeber)**
Ende des Steinkohlenbergbaus im Ruhrrevier: Realität und Perspektiven
für die Geotechnik
Beiträge zum RuhrGeo Tag 2014

51 (2014) **Usque ad finem**
Selected research papers

52 (2014) **Houman Soleimani Fard**
Study on the Hydro-Mechanical Behavior of Fiber Reinforced Fine Grained Soils,
with Application to the Preservation of Historical Monuments

53 (2014) **Wiebke Baille**
Hydro-Mechanical Behaviour of Clays - Significance of Mineralogy

54 (2014) **Qasim Abdulkarem Jassim Al-Obaidi**
Hydro-Mechanical Behavior of Collapsible Soils

55 (2015) **Veselin Zarev**
Model Identification for the Adaption of Numerical Simulation Models -
Application to Mechanized Shield Tunneling

56 (2015) **Meisam Goudarzy**
Micro and Macro Mechanical Assessment of Small and Intermediate Strain
Properties of Granular Material

57 (2016) **Oliver Detert**
Analyse einer selbstregulierenden interaktiven Membrangründung für Schüttkörper auf geringtragfähigen Böden

58 (2016) **Yang Yang**
Analyses of Heat Transfer and Temperature-induced Behaviour in Geotechnics

59 (2016) **Alborz Pourzargar**
Application of suction stress concept to partially saturated compacted soils

60 (2017) **Hanna Haase**
Multiscale Analysis of Clay-Polymer Composites for Geoenvironmental Applications

61 (2017) **Kavan Khaledi**
Constitutive modeling of rock salt with application to energy storage caverns

62 (2017) **Nina Silvia Müthing**
On the consolidation behaviour of fine-grained soils under cyclic loading

63 (2017) **Elham Mahmoudi**
Probabilistic analysis of a rock salt cavern with application to energy storage systems

64 (2017) **Negar Rahemi**
Evaluation of liquefaction behavior of sandy soils using critical state soil mechanics and instability concept

65 (2018) **Chenyang Zhao**
Numerical Modeling of Mechanized Tunnel Excavation:
Effects of Sub-systems and Advanced Process Simulation

66 (2018) **Tom Schanz (Herausgeber)**
Innovationen im Spezialtiefbau und in der Umweltgeotechnik
Beiträge zum RuhrGeo Tag 2018

67 (2019) **Linzhi Lang**
Hydro-Mechanical Behaviour of Bentonite-Based Materials Used for Disposal of Radioactive Wastes

68 (2019) **Usama Al-Anbaki**
Hydraulic Interaction of Soil and Nonwoven Geotextiles under Unsaturated Conditions

69 (2019) **Abhishek Rawat**
Coupled Hydro-mechanical Behavior of a Compacted Bentonite-Sand Mixture:
Experimental and Numerical Investigations

Schriftenreihe des Lehrstuhls für Bodenmechanik, Grundbau und Umweltgeotechnik der Ruhr-Universität Bochum

Herausgeber: T. Wichtmann

70 (2019) **Mahmoud Qarmout**
Tunnel face stability using Kinematical Element Method (KEM)

71 (2021) **Raoul Hölter**
Optimal Experimental Design in Geotechnical Engineering

72 (2022) **Wolfgang Lieske**
Impact of polymer constitution on the hydro-mechanical behaviour of modified bentonite for the application in geotechnical and geoenvironmental engineering

73 (2022) **Patrick Staubach**
Contributions to the numerical modelling of pile installation processes and high-cyclic loading of soils

74 (2022) **Lingyun Li**
On the hydromechanical behaviour of loess and its effect on slope stability under rainfall infiltration

75 (2022) **Debdeep Sarkar**
Influence of particle characteristics on the behaviour of granular materials under static, cyclic and dynamic loading

76 (2023) **Torsten Wichtmann (Herausgeber)**
Umbau des Emscher-Systems - Geotechnische Erfahrungen
Beiträge zum RuhrGeo Tag 2023

77 (2023) **Abbas Farhat**
Fluidization and erosion of cemented granular materials. Experimental characterization and micromechanical simulation

78 (2023) **Andrea Geppetti**
Experimental and numerical investigations on the behaviour of tailing storage facilities under seismic loading

79 (2023) **Mohammad Hassan Sanayei**
Micromechanical modelling for the analysis of piping erosion in cemented soils for suction-assisted offshore foundations

80 (2024) **Christoph Schmüdderich**
Contributions to the stability assessment of slopes subjected to seismic loading

81 (2024) **Thomas Barciaga**
Constitutive modeling of natural clay with application to mechanized tunneling

82 (2024) **Cristian Rodriguez**
Contributions to the modelling of large deformations of soils: A particle-based approach

83 (2025) **Florian Christ**
Experimental investigations on the hydro-mechanical behaviour of clay shales for tunnelling relevant boundary conditions

84 (2025) **Alireza Jebeli**
On the influence of a heterogeneous pore structure on collapse behavior of sandy soils

85 (2025) **Maximilian Schoen**
Numerical analysis of tunnel excavation in swellable clay shales

86 (2025) **Qian Gu**
On the effects of grain shape, gradation, fabric and stress state on the small-strain stiffness of granular soils

87 (2025) **Manh Cuong Le**
Experimental validation of the effective stress concept in unsaturated soils using the suction stress approach across multiple test types and a wide suction range

88 (2025) **Firas Hussain Ali Ghrairi**
Numerical simulation of flexible granular inclusions with special focus on the installation process

89 (2026) **Torsten Wichtmann (Herausgeber)**
Innovationen in der Geotechnik
Beiträge zum RuhrGeo Tag 2026

90 (2026) **Antonia Therese Nitsch**
A novel framework for the numerical modelling of the hydro-mechanical behaviour of expansive soils

91 (2026) **Peyman Mianji**
Bentonite slurry infiltration in granular soils and its implications for hydroshield tunnelling